STUDY OF LI-RICH K GIANTS

A THESIS

SUBMITTED FOR THE DEGREE OF

DOCTOR OF PHILOSOPHY

IN

THE FACULTY OF SCIENCE

CALICUT UNIVERSITY

BY

BHARAT KUMAR YERRA

INDIAN INSTITUTE OF ASTROPHYSICS
BANGALORE - 560 034, INDIA

AUGUST 2011

To my parents and friends...

For my part I know nothing with any certainty, but the sight of the stars makes me dream.

DECLARATION

I hereby declare that the matter contained in the thesis entitled **"Study of Li-rich K Giants"** is the result of investigations carried out by me at the Indian Institute of Astrophysics under the supervision of Dr. B. Eswar Reddy. This thesis has not been submitted for the award of any degree, diploma, associateship, fellowship etc. of any University or Institute.

Bharat Kumar Yerra
(Candidate)

Indian Institute of Astrophysics
Bangalore-560034, India

CERTIFICATE

This is to certify that the matter contained in the thesis entitled "**Study of Li-rich K Giants**" submitted to Calicut University by **Mr. Bharat Kumar Yerra** for the award of the degree of Doctor of Philosophy in the Faculty of Science, is based on the results of investigations carried out by him under my supervision and guidance, at the Indian Institute of Astrophysics. This thesis has not been submitted for the award of any degree, diploma, associateship, fellowship etc. of any University or Institute.

Dr. B. Eswar Reddy
(Supervisor)

Indian Institute of Astrophysics
Bangalore-560034, India

ACKNOWLEDGEMENTS

This dissertation would not have been possible without the guidance and the help of several individuals who in one way or another contributed and extended their valuable assistance in the preparation and completion of this study.

First and foremost, my utmost gratitude to my thesis supervisor Dr. B. Eswar Reddy whose guidance, sincerity, and encouragement i never forget. It has been an honour to be his first Ph.D student. He has taught me, both conciously and unconciously, how good astronomical spectroscopy is done.

I express my sincere gratitude to the role model for stellar spectroscopist in the world, Prof. David L. Lambert, for being my collobarotor, for providing the spectra, and for his suggestions and fruitful discussions, without which this thesis would not have possible. I am thankful to Dr. Muthumariappan for his encouragement and fruitful discussions.

I am grateful to the Director of Indian Institute of Astrophysics, Prof. S. S. Hasan for giving me the opportunity to work in this institute and providing all the support and facilities required for research work. I thank all the members of the Board of Graduate Studies for the help and support that have been provided throughout the course of my work. I am grateful to the instructors who light the passion for astronomy during the course work. I am grateful to the members of my doctoral committee, Dr. Biman N. Nath, Prof. A. V. Raveendran, Prof. R .T. Gangadhara, Dr. Gajendra Pandey for useful comments and suggestions which imporved my research work. I express my sincere thanks to IIA faculities, Dr. Gajendra pandey, Dr. Annapurni, Dr. Anupama, Dr. Sivarani, Dr. Sunetra, Dr. Aruna, Dr. Sushma, Prof. Mallik, Prof. N. K. Rao for their friendly approch which enabled me to have fruitful discussions. I am thankful to IIA library staff, and the Librarian Ms. Christina Birdie for providing all the assistance required in making the books and journals available for reference. I thank the staff members of Administrative division of IIA for the required assistance and help they have provided in time at each steps during my fellowship period. My sincere thanks to all the technical staff including Dr. Baba, Mr. Fayaz and Mr. Ashok for helping with computer related issues.

I thank Prof. B. R. S. Babu, Dr. M. M. Musthafa and all the faculty of Department of Physics, Calicut university for their valuable advice and suggestions. My sincere thanks goes to the administrative staff of the department and CDC for helping me during registration and submission. I would like to take this opportunity to thank the faculty in MSc Period, Prof. Bolanath padhy, and my teachers from school and college days whose valuable tips and encouragement provided me a platform to write this thesis.

I thank the faculty and present/former staff of CREST, Dr. D. K. Sahu, Dr. P. Parihar, Dr. B. C. Bhatt, Dr. Shanti kumar, Mahalakshmi, Aman, Ravi, Ramya, Sasikumar, Ritu, and Manjunath for the help and guidance they provided for observations with HCT through out the research period. I thank all the staff of VBO Kavalur, Dr. Muneer (former observatory incharge), Dr. Muthu mariappan, Mr. Anbazhagan, Mr. Ravi, Mr. Srinivasa Rao, Mr. Ramachandran, Mr. Pukhalendhi, Mr. Murthy, Mr. Appakutty, Mr. Jayakumar, Mr. Velu, Mr. Kuppusamy, Mr. Selvakumar, Mr. Sivakumar, Mr. Dinakaran, Mr. Ramachandran and Mr. Ramesh for the help and guidance they provided for observations with VBT and 1-m telescope through out the research period.

For reading the manuscript of this thesis I would like to express my heartiest thanks to Ms. Sandra Rajiva and also to my friends, Pradeep and Vigeesh for their time and helpful comments. I thank Avijeet and Prasanth for helping me in Mathematica.

My time at IIA and Bhaskara was made enjoyable in large part due to many friends and groups that became a part of my life. I dont say just thanks to Vigeesh, Blesson, Ramya and Uday as i never forget their love, caring and support. I miss you guys a lot. I thank Pradeep and Suresh for their support in final days. I thank my batchmate friends, Ramya, Ananta, Tapan, Rumpa, and Girjesh for their wonderful company in first and subsequent years. I still remember those course work days when we used to have maggi in mid nights etc. I would like to thank my senior friends: Nagu, Malay, Ravi, Mahesh, Nataraj, and Veeresh for their encouragement in intial days in IIA. I extend my heartfelt thanks to my junior friends: Sreeja, Smitha, Indu, Sindhu, Drisya, Hema, Madhu, Sumangala, Anusha, Anantha Chandu, Krishna, Sudhakar, Arun, Sam, Ratnu, sugar, subham, Sajal for making my stay at IIA and Bhaskara memorable.

Where would I be without my family? My parents deserve special mention for their inseparable support and prayers. My mother, Lakshmi, and father, Lakshmana Rao, are the one who sincerely raised me with their caring and gently love. Bujji, thanks for being supportive and caring sibling. My brother-in-law, Devi prasad, whose words are inspirational, thanks for the encouragement. Naughty and cute niece, Kavya, is the one whose cheerful smile driven me till the end of the thesis.

It is a pleasure to thank my old (gold) friends: Bhanu, Chandu, Durga, Ganesh, Jaggu, Krishna mama, Kshitish, Kiran (K, A, Ch) , Simadri, Sudheer, Surya for their encouragement and belief that driven me to complete this thesis.

Finally, I would like to thank everybody who was important to the successful realization of thesis, as well as expressing my apology that if I could not mention personally one by one.

TABLE OF CONTENTS

SUMMARY

Lithium (Li), with atomic number 3, is the lightest and the least dense solid element. Also, like other alkali metals (Na, K etc.,) Li is very reactive. In nature Li is found in two stable isotopes: ^{6}Li and ^{7}Li. ^{7}Li is the most dominant isotope contributing to about 93% of Li and rest being the ^{6}Li. For its properties of light and fragile, Li plays an important role in astrophysics to understand both the chemical and physical processes that operate in systems ranging from Big Bang to galaxies and to stars.

The Big Bang Nucleosynthesis (BBN) calculations predict Li production at the time of Big Bang along with other light elements: Deuterium, He, and to some extent Be and B. BBN model predicts primordial Li at log ϵ (Li) = 2.72 dex relative to H which is 12 on logarithmic scale. However, the predicted Li amount is in dispute with the measured Li in old metal-poor stars with log ϵ (Li) = 2.27 dex which is considered as primordial Li. Predicted Li is by a factor of 2-3 more than the observed value. Solution to this dispute is a significant step to understand the input physics involved in BBN models and also to understand Li depletion process in stars. The current Li amount as measured in interstellar medium (ISM) and in the young stellar objects is log ϵ (Li) = 3.2 dex (e.g., Lambert & Reddy 2004). The evolution of Li from its primordial value of log ϵ (Li) = 2.3 (2.6) dex to the present ISM value of log ϵ (Li) = 3.2 dex is of great importance to our understanding of the chemical evolution in the universe: from the earliest to the present epochs.

The processes that are responsible for increase from the primordial to the present Li value are not clearly understood. However, a small amount of Li is produced via cosmic ray spallation from heavier elements (Lemoine et al. 1998), supernovae of Type II (Woosley et al. 1990; Woosley & Weaver 1995), classical novae (Starrfield et al. 1978), AGB stars (Sackmann & Boothroyd 1992), and by some low-mass giants. In this study, we focus on low mass red giants as source of Li in the Galaxy and the process that drives Li production and mixing.

Galactic evolutionary models use Li contribution from low mass giants that vary from

1 to 30% to match the present Li in the Galaxy. The actual contribution of Li from low mass giants needs to be estimated to understand the evolution of Li in our Galaxy. There are a few low mass giants (G and K giants) whose atmospheres are highly enriched with Li. A few among Li-rich giants are found to have Li as high as ISM value. High values of Li are contrary to what one would expect in low mass giants where convective envelopes reach deep inside destroying remaining Li from the main sequence phase. The high value of Li in K giants was first discovered three decades ago by Wallerstein & Sneden (1982). Since then the puzzle of anomalous Li in K giants remained with a very little progress. Over the years sample of Li-rich giants increased but the clear understanding of high Li origin remained elusive.

The amount of Li present and absent in the stellar photosphere is often ascribed to stellar evolutionary phase and the associated mixing processes. Standard stellar first dredge-up predicts Li reduction in the low mass giants ($\leq 2.5 M_{\odot}$) by an order of 1-2 magnitudes, by the end of first dredge-up on the RGB phase. We assume that the progenitors of K giants evolved off the main sequence with maximum initial Li of about $\log \epsilon(\mathrm{Li}) = 3.28$. The amount of Li one would expect, depending on the mass, metallicity and the amount of Li on the main sequence, for a low mass K giant is $\log \epsilon(\mathrm{Li}) \leq 1.4$ dex (Iben 1967a, 1967b). The consensus among the investigators of Li in RGB stars is that a K giant with $\log \epsilon(\mathrm{Li}) > 1.4$ can be termed as Li-rich, and a giant with $\log \epsilon(\mathrm{Li}) \geq 3.28$ (ISM value) is termed as super Li-rich.

Li-rich K giants (LRKG) are rare. Most of the LRKGs show high rotation and infrared excess. Similar to high Li, high rotation and IR excess are anomalous properties. Relation among three properties need to be looked at carefully to understand the clues for high Li origin in K giants. In the literature, one finds three principle suggestions for the origin of Li enhancement; a) preservation of Li from the main-sequence phase, b) addition of Li-rich material through planet engulfment, c) production of Li in the stellar interiors and some sort of mixing mechanism.

As part of this thesis, we have attempted to substantially increase the LRKGs and to understand the origin of anomalous Li in K giants. In this direction, a systematic survey was initiated to search for LRKGs. A large ($\approx$2000) number of sample stars along the red giant branch were selected. Main aim was to obtain low resolution spectra for the entire sample using facilities available locally. Spectra of sample stars were taken from 2 m Himalaya Chandra Telescope, Vainu Bappu Telescope, and 1 m Zeiss Telescope. Li abundances were estimated from the relative strength of Li resonance line at 6707.7 Å to the nearby Ca I line at 6717.6 Å and an empirical relation that was deduced from the

known LRKGs. The survey resulted 15 new LRKGs including 4 new super Li-rich K giants which doubled the number of known LRKGs. Importantly, survey showed that the Li-rich phenomenon among K giants is rare, just under 1%, in the solar neighbourhood. Entire new sample along with the known Li-rich sample was subjected to high resolution spectroscopic study.

High resolution spectra of new LRKGs, from this study, as well as the known sample, collected from literature, were obtained from VBT and 2.7 m Harlan J. Smith telescope. Atmospheric parameters like temperature, gravity, metallicity were derived using equivalent widths of Fe I and Fe II lines measured from spectra, model atmospheres from Kurucz database, and line synthesis code MOOG. Li abundances were derived by matching the synthetic spectra of Li profiles at 6707 Å and 6103 Å. Results confirm the Li-richness in new LRKGS estimated from low resolution spectra. High resolution spectra were analyzed to determine carbon isotopic ratios and other elemental abundances. Carbon isotopic ratios ($^{12}C/^{13}C$) of sample sources were obtained by matching computed spectra with that of observed spectra of CN region at 8003 . $^{12}C/^{13}C$ ratios of LRKG are much lower than predicted values for post first-dredge phase indicating extra mixing. From our survey we found three super LRKGs with anomalously low $^{12}C/^{13}C$ ratio that is closer to CN equilibrium value. The low isotopic ratios of carbon among LRKGs indicate that the atmospheres of these stars are mixed well, and which rules out the possibility of K giants retaining their main sequence Li due to suppressed depletion.

The entire sample was studied with the help of Hertzsprung-Russel Diagram (HR diagram). The position of Li-normal and Li-rich giants in the H-R diagram allowed us to determine a stage on RGB at which Li enrichment occurs. We also made use of 644 sample giants from Brown et al (1989). Brown et al survey supplements our study in that they covered mostly upper part of the RGB. In this study we showed that all the LRKGs occupy a particular position, with a very narrow range of luminosities, on the RGB phase which coincides with luminosity bump and/or clump in the H-R diagram. We did not find any K giant with Li-excess below or above the bump and clump position. This is a major finding which points to the source of Li-excess in K giants to the internal nucleosynthesis during the RGB bump evolution and/or He core flash at RGB tip. At the same time, our results suggest possibility of planet engulfment or other external sources as origin for Li-excess in K giants seems to be unlikely.

Other properties of the LRKGs that are considered as anomalous are: rotational velocity and infrared excess. In this thesis, we have made an attempt to understand whether all of these properties are related to each other. Rotational velocity (*vsini*) of LRKG are

obtained from the synthesis of the Fe I profiles at 6703 Å and 6705 Å. Atmospheric parameters, abundances obtained from equivalent widths, macroturbulance, limb-darkening coefficient are kept fixed, and *vsini* is varied to match the observed profile. We found most of the LRKGs are slow (3 km/s) rotators consistent with the expected values for K giants. However, a few of them are rapid rotators.

Also, we have studied infrared properties of sample stars (≈2000) in our survey. The entire sample was divided into four groups: pre-bump, bump, post-bump and clump giants. Far infrared (FIR) colors for the sample giants were derived from the fluxes taken from IRAS catalog. A colour-colour diagram was made to understand the infrared excess. The computed tracks of mass loss and far-IR colours were over plotted with the samples. Results indicate that pre-bump stars show no excess but stars at and above the bump show excess flux in 60μ band. Also, most of the LRKGs are found to have FIR excess. Mass-loss rates obtained from the spectral energy distribution (SED) confirm that LRKGs have higher mass-loss rates than the rates expected for normal K giants. The distribution of dust around stars was studied using dust emissitivity index which shows that the dust distribution is spherical among Li-normal giants and non-spherical in at least a few LRKGs indicates a dust shell with truncated polar caps. The evolutionary timescales of the dust shells are in the order of 10^4 to 10^5 yrs suggesting IR excess seen in K giants is a short duration phenomena compared to the life time of RGB bump which is about a couple of million years, and the duration of clump which is a few tens of million years. Results suggest that the excess mass loss in LRKGs is indeed connected to Li enhancement. The study also suggests that Li-rich phenomenon is a transient lasting for a few thousand years or much less than the duration of either bump or clump evolution periods.

The outline of the thesis is as follows:

CHAPTER 1: Here, we provide a brief introduction to the Li-rich K giants (LRKG). LRKGs are rare, just one in every hundred K giants in solar neighbourhood. Origin of high Li among K giants has been a subject of study ever since it was discovered three decades ago. Over the years, sample of K giants having Li-excess grew but remained insufficient to prove various proposals for its origin of high Li.

CHAPTER 2: In this chapter we provide details of observations, reduction techniques, and description of observational facilities and instruments.

CHAPTER 3: Here we deal with the main issue of the study: survey for LRKGs. Sample selection criteria, source of the sample (Hipparcos catalog) and observational strategy were discussed in brief. Also, we provide full description of estimating Li abundances in K giants using low resolution spectra. Results from low resolution spectra are presented.

CHAPTER 4: In this chapter we discuss the entire Li-rich sample which includes the LRKGs found in this study and the ones taken from literature. Description of data analysis of high resolution spectra obtained from 2.3m VBT , Kavalur, and 2.7-m Harlan J. Smith telescope, McDonald Observatory, USA is presented here. Here, we also provide detailed description of deriving stellar atmospheric parameters, abundances and isotopic ratios, and the required inputs like atomic line list, oscillator strengths, stellar model atmospheres, and radiative transfer code

CHAPTER 5: Here we discuss three super Li-rich giants with anomalous low $^{12}C/^{13}C$ that are presented in Chapter 4. These are: HD 77361, HD 10437, and HD 8676.

CHAPTER 6: In this chapter we dealt with the study of IR-excess and mass-loss on RGB. Optical, near-IR and far-IR fluxes were collected from respective catalogues. Spectral energy distributions (SEDs) were constructed to estimate IR-excess and mass-loss. Just 1% of the sample stars seems to have IR-excess and most of them are indeed LRKGs. With the help of DUSTY code, we have constructed far-IR colour-color diagram from which we have derived evolutionary timescales for dust envelopes. The connection between Li-excess and IR-excess has been discussed.

CHAPTER 7: Here, we describe our investigation to find out the possible cause for Li enrichment in K giants. Our survey sample of 2000 K giants was supplemented by Brown et al survey sample of about 650 G- and K-giants. For the entire sample, luminosities and effective temperaturs are derived in the same way. In this chapter, we have discussed two main observational results: a) finding of all the LRKGs in a very narrow luminosity region in the HR diagram which coincides with the positions of luminosity bump on the RGB or the red clump, b) finding no LRKGs below or above this region.

CHAPTER 8: Here, we have provided in brief the summary of the thesis highlighting important results. We have concluded the study with a few suggestions for further studies in this direction.

LIST OF PUBLICATIONS

REFEREED JOURNALS

Kumar, Y. Bharat ; Reddy, B. E., Lambert, D. L., *Origin of lithium enrichment in K giants*, 2011, ApJ (Letters), 730, L12

Kumar, Y. Bharat ; Reddy, B. E., *HD 77361: A new case of super Li-rich K giant with anomalous low $^{12}C/^{13}C$ ratio*, 2009, ApJ (Letters), 703, L46

CONFERENCE PROCEEDINGS

Kumar, Y. Bharat ; Reddy, B. E., *Survey for Li-rich K Giants*, 2010, IAUS, 268, 327

Kumar, Y. Bharat ; Reddy, B. E., *Investigation of anomalous high Li in K Giants*, 2008, BASIP, 25, 57

UNDER PREPARATION

Kumar, Y. Bharat ; Muthumariappan, C.; Reddy, B. E., *Study of Far-IR Excess in K Giants: Connection with Li-enhancement at RGB Bump*

Kumar, Y. Bharat ; Reddy, B. E., *Search for Li-rich K Giants: Low resolution spectroscopic survey along the Red Giant Branch*

Kumar, Y. Bharat ; Reddy, B. E., Lambert, D. L., *Detailed Analysis of New Li-rich K Giants*

Kumar, Y. Bharat ; Reddy, B. E., *Planet Hosting K Giant with anomalous high Lithium*

LIST OF FIGURES

LIST OF TABLES

CHAPTER 1

REVIEW OF LITERATURE

1.1 GENERAL INTRODUCTION

The splendor and grandeur of the night sky always fascinated the humankind. The artful patterns of stars and planets, and their passage across the night sky inspired many, since the beginning of human race, to ponder over the dazzling, and yet a systematic and largely a periodic phenomenon. The periodic appearance and disappearance of celestial objects helped societies and cultures to define time, track seasons, harvest crops, invent navigational tools, and devise calendars for their day-to-day activities. Astronomy, therefore, is considered as the oldest branch of natural sciences. The systematic observations and the human quest to understand the great importance of the physical universe has led to a remarkable spectrum of inventions and discoveries. From years of careful watching of the night sky with naked eye, centuries before the dawn of the telescope, our ancestors observed that some stars move in the night sky with respect to the others. The moving stars were called planets. This led to the idea of solar system where the Sun, Earth, and other planets are different from rest of the stars in the sky. In around 140AD, Greek astronomer Ptolemy developed the theory of geocentric universe where everything else in the universe goes around the Earth. About fourteen hundred years later, the geocentric theory was discarded with much better and accurate observational data on planetary motions accumulated by Tycho Brahe, and the data helped Jonathan Kepler to formulate the famous laws of planetary motions. These observations gave foundation to Isaac Newton to formulate the famous universal theory of gravitation.

With the advent of the telescope in early 1600AD, the new era began in astronomy. Galileo Galilee was the first to use the telescope in 1609AD and made landmark discoveries such as four moons revolving around the planet Jupiter which shattered the myth

that our earth is unique in the universe. This also gave an idea that there is much more to discover in the universe with better and larger aperture telescopes. A race to make bigger and better telescopes began. With it came the rapid change the way the universe was viewed.

In the early part of 1900s, Edwin Hubble using the observations of galaxies with the 2.5m Hooker telescope, Mount Wilson Observatory, made a remarkable discovery of the expansion of the universe. Farther the galaxies faster they appeared to recede from us. The immediate implication of Hubble's discovery was that our universe was much more compact in the past and must have had beginning in time. This, later became an active area of research, the big bang cosmology. The big bang interpretation was supported by the discovery of astonishingly smooth microwave background radiation in the universe. In the last 100 years, astronomers with the aid of sophisticated telescopes and instruments made stupendous progress in understanding many aspects of our observable universe. The findings include; development of stellar evolution theory, understanding of synthesis of elements in stars, discovery of dark matter, evidence of the accelerated expansion of the universe probably due to an unknown form of energy known as dark energy, finding of exo-planetary systems etc.

Studies of the stars and stellar systems played important roles in our understanding of the universe and its evolution. Stars are the building blocks of the galaxies which in turn make-up the universe. Detailed understanding of the stars, their internal structure, evolution, and chemical composition is essential to decipher the birth and the evolutionary sequence of the galaxies. Much of current understanding of stellar structure and evolution could easily be traced back to early and mid 1900s research of eminent astrophysicists like A. Emden, James Jeans, A.S. Eddington, S. Chandrasekhar, M. Schwarzschild, Ico Iben and many others. Though the basic stellar physics is on sound foundations, there are still many outstanding issues which need to be probed for better clarity. For example, still there is no clear consensus on how exactly stars form out of collapsing clouds and their early evolution. Also, gaps exist in our understanding of different phases of stellar evolution: Main Sequence (MS), Red Giant Branch (RGB), Horizontal Branch (HB), Asymptotic Giant Branch (AGB), post-AGB, Planetary Nebulae (PNe), and the transition to the final phase such as white dwarf, neutron stars or black holes. Since the thesis is concerned about a particular phase of stellar evolution (RGB phase), a brief description of evolution of the stars at various phases of their life is provided.

1.2 EVOLUTION OF STARS AND THE HR DIAGRAM

Star's evolution is mainly dictated by its initial mass. Stars with higher mass will evolve much faster compared to lower mass stars. The evolution of a star is characterized by its change in effective temperature ($T_{\rm eff}$), surface gravity (g), and chemical composition. In other words, as the star evolves it continuously changes its color and brightness which are generally represented by (B-V) and luminosity (log $L/L_{\odot}$), respectively. Depending on their initial mass, evolution of stars are classified into three mass categories: low-mass (up to about $2M_{\odot}$), intermediate mass (2 - $10M_{\odot}$) and massive stars evolution.

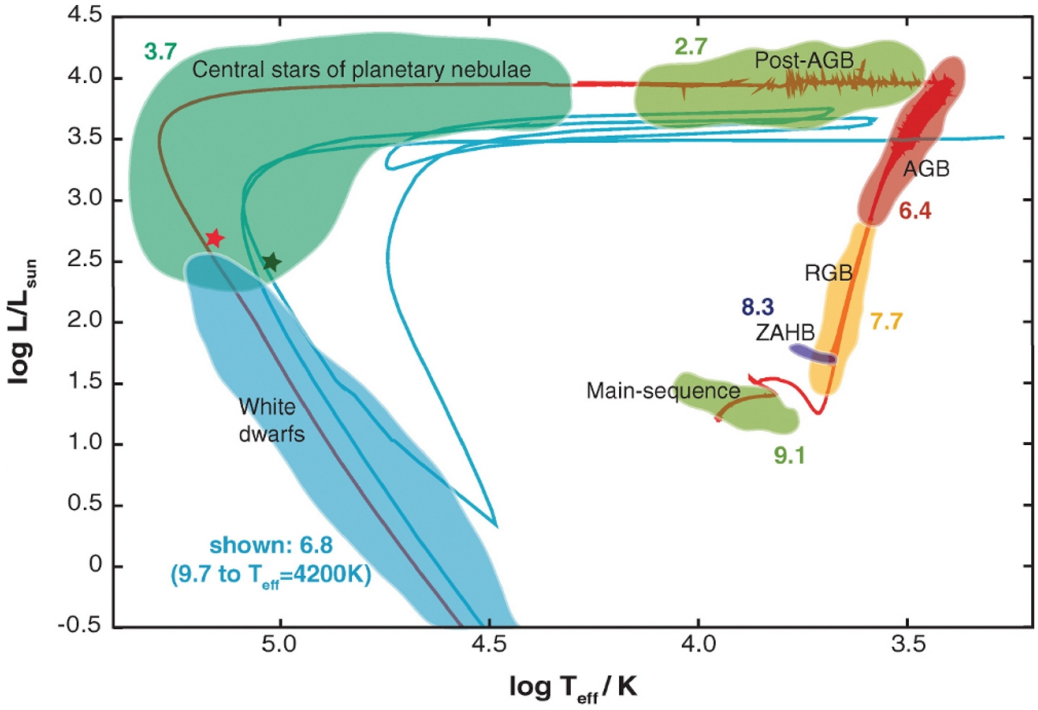

Figure 1.1: Evolution of 2 $M_{\odot}$ star is shown in H-R diagram. Various phases are also highlighted. Courtesy: Herwig (2005)

The changes in the star's life are conveniently shown in a diagram of luminosity versus color (or $T_{\rm eff}$) which is the famous Hertzsprung-Russel diagram or HRD after the two famous astronomers Ejnar Hertzsprung and Henry Norris Russel who independently realized the usefulness of such a diagram. The main stages of star's evolution for a $2M_{\odot}$ star is illustrated in Figure 1.1. Below we describe each of these stages in more detail. Emphasis is given to low- and intermediate mass star's evolution.

1.2.1 PRE-MAIN SEQUENCE PHASE

Star's evolution from its birth in the molecular clouds to the main sequence is called as pre-main sequence phase. In general, star formation or the cloud collapse process begins, as suggested by Jeans (1928), with small density fluctuations which steadily grow by gravity. When the fluctuations exceed some critical intensity, cloud becomes gravity dominated, the collapse begins, a process known as gravitational instability. Thus, the gravity is the fundamental driving force in the star formation process. Star formation can occur only where the gas becomes dense enough for its self-gravity to over come the effects such as thermal pressure, turbulence, magnetic fields etc. This sets a limit on a minimum mass, called Jean's mass, that a cloud must have to collapse under its gravity. Thus, an isothermal cloud of certain mass and temperature of the order of 6-10 K begins to collapse under its own gravity. As the collapse continues central density increases which increases optical depth. Hence center becomes opaque and as a result radiative cooling becomes unimportant. The cloud becomes adiabatic leading to a rapid raise in temperatures at the center. Thermal pressure builds up at the center halting further collapse. However, the core keeps growing in mass by accreting material that is left behind during the collapse. At about 2000 K, hydrogen molecules begin to dissociate making the core unstable again. Further rapid collapse ensures a complete ionisation of H at the center and a complete halt to collapse, a protostar is formed at the center with hydrostatic equilibrium. The accreting protostar becomes a normal pre-main sequence star, which by then has acquired nearly all of its mass by accretion from the envelop.

Further, protostar becomes hotter and increases its brightness while shrinking in size. As the protostar evolves temperature of the core reaches to burn hydrogen through nuclear fusion. Finally, stars are in hydrostatic equilibrium, outward radiation pressure is balanced by the inward gravity force, settle on the Zero-age main sequence (ZAMS). In our Galaxy, observations show that much of the star formation occurs in the spiral arms and also in the central regions. T-Tauri stars are the youngest (about 1 Myr) visible stars, and these are pre-main sequence stars that have not yet become hot enough at their centers to burn hydrogen and begin the main-sequence phase of evolution.

1.2.2 MAIN SEQUENCE

After reaching hydrostatic equilibrium protostars arrive at the most stable and long lasting phase of their evolution, the main sequence phase or MS. Obviously, the MS phase in the HRD, as shown in Figure 1.1, is the most populated, and the width of the MS suggests

stars on the MS do evolve but very slowly. Width can also partly be due to differences in chemical composition and mass. Stars on the MS survive by burning hydrogen into helium in their cores, and the resulting energy provides radiation pressure. Depending on star's mass and central temperature, star's hydrogen fusion into helium occurs in the core through two different process: proto-proton (PP) chain reaction and CNO reaction where CNO nuclei are intermediaries. Stars less massive than of about 1.5 $M_\odot$ burn hydrogen mostly through PP chain reaction and stars above that mass mostly through CNO reaction. The CNO reaction is very sensitive to the temperature compared to PP chain i.e with raising temperature CNO reaction processes more material at the center. Thus, high mass stars exhaust hydrogen in the core much faster and evolve off the MS. For example, the Sun has been on the MS for about 4.5 Gyrs and it may live another 4 - 5 Gyrs. On the other hand stars with mass about $10M_\odot$ spend just 20 - 30Myrs. The sequence of PP and CNO reactions are shown in Figures 1.2 & 1.3.

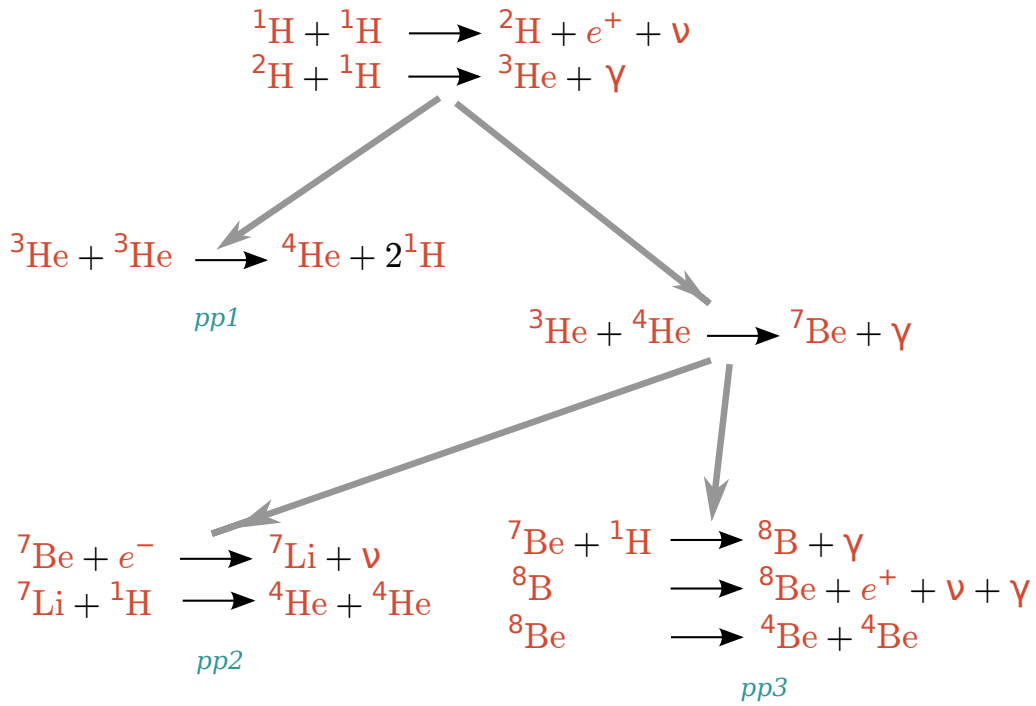

Figure 1.2: PP Chain reactions

However, the material with the changed composition in the center is not yet mixed with the outer surface or photosphere. The photosphere of MS stars still represent initial composition that was acquired from the ISM at the time of their birth. Thus, MS stars are often the subject of Galactic chemical evolution studies. The continued burning depletes hydrogen and forms He core at the center. The hydrogen burning slowly moves outward

forming a ring like structure (H-shell) around the He ash core. Once the entire H is burnt the structural changes in the interior ensure stars evolve off the MS towards right (cooler T_{eff}) in the HRD. Stars grow in size, become cooler and brighter, a beginning of a new phase in their evolution.

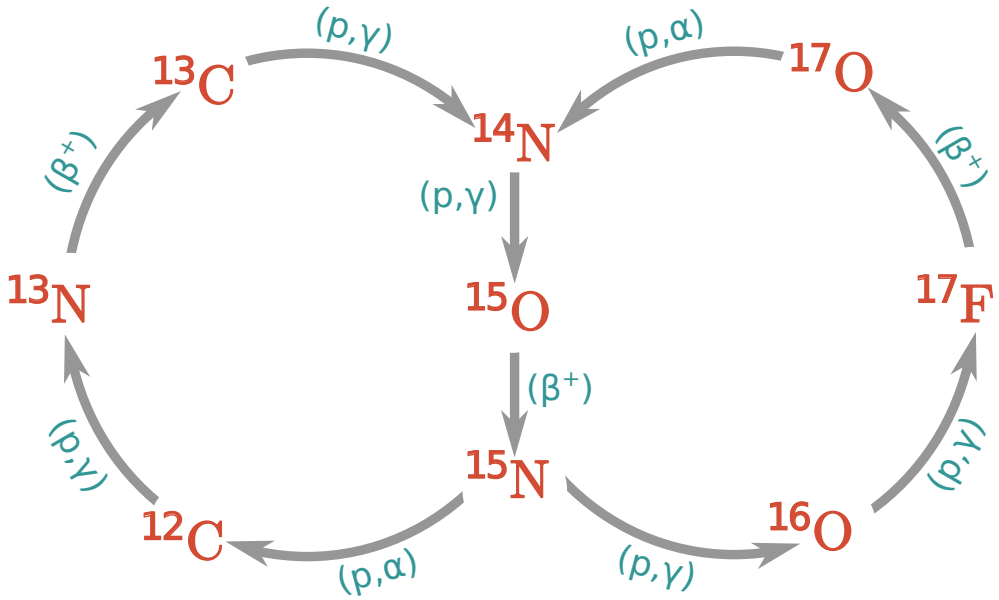

Figure 1.3: CNO reactions

1.2.3 POST-MAIN SEQUENCE

The post-main sequence (Post-MS) evolution of a stars depends on their initial mass which controls the central temperature. The post-MS evolution of the low- and intermediate stars has a few significant phases which play greater roles in the chemical enrichment history of the Galaxy. These are: The red giant branch (RGB), Horizontal branch (HB), Asymptotic giant branch (AGB), post-AGB and Planetary Nebulae (PNe). Of course, depending on the initial stellar mass stars end their lives either as white dwarfs (low- and intermediate mass stars), neutron stars or black holes (massive stars). Here, we briefly describe salient features of each of these phases.

RED GIANT BRANCH

As the He-core contracts star evolves off the MS and hydrogen starts to burn in a shell. The increased energy production in the interior results in star's overall expansion, and also rapid reduction in surface temperature. By the time the star reaches the base of RGB the

convection reaches its maximum extension in mass (Salaris et al. 2002) and extends all the way to the hydrogen burning shell. For the first time, the processed interior material gets exposed to the surface. The mixing of interior material with the outer surface will alter the photospheric chemical composition. This phenomenon in RGB stars is called the "first dredge-up". The first dredge-up brings up the material with reduced ^{12}C, increased ^{14}N, ^{3}He and ^{13}C. Also, a significant reduction in Li abundance is observed. The Li evolution in RGB stars seems to be a complex phenomenon. A more detailed description of Li in RGB stars is provided later in this chapter.

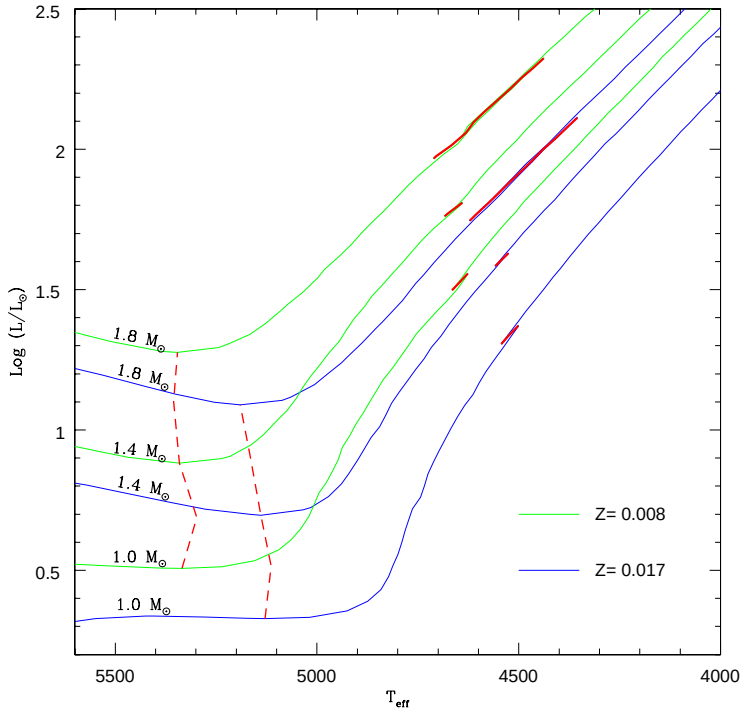

Figure 1.4: Evolutionary tracks of 1.0 and 1.8 $M_{\odot}$ computed for Z = 0.017 and Z = 0.004 are shown in blue and green lines, respectively. Base of the RGB in red broken line and RGB bump in red kinks are also shown.

In the case of low mass ($\leq$ 2.25 $M_{\odot}$) RGB stars, core is a degenerate He gas (Iben 1968; Bertelli et al. 2008). As the H-burning shell continues to deposit He, the density of the core increases and hence the temperature. Stars move-up on the RGB rapidly with large increase in luminosity. As they moves-up the convection zone begins to retreat from the deepest point of penetration leaving H-discontinuity between H-burning shell and the base of convective zone. At this point as models suggest (Iben 1968) the H-burning shell moves upward until it encounters the H-discontinuity that was created at the time

of first-dredge up. At the encounter, H-burning shell is provided with more H fuel which temporarily cools the central temperature leading to reduced luminosity. This creates a kink on the RGB known as RGB luminosity bump (see Figure 1.4). The bump seems to happen for only low mass stars which have degenerate He-core. The bump occurs, depending on mass, in the luminosity range $\log L/L_{\odot}$ = 1.3 - 2.4 (Bertelli et al. 2008). This internal mechanism in the evolution of RGB effects its evolution. The slowing down of evolution at the bump is manifested over density of stars at the RGB bump region. Observations of open and globular clusters (Di Cecco et al. 2010 and references there in) , dwarf spheroidal galaxies (Bellazzini et al. 2005), LMC and SMC, show (see Figure 1.5) evidence of such luminosity bump.

After a while equilibrium is established in the interior, and the stars starts again climbing-up towards the tip of RGB (TRGB). The continued depositing of He from H-burning increases the core density which raises its temperature sharply. The thermal run away occurs in the He degenerate core, due to the continued rise in temperature resulting in He-flash. He-flash lifts the degeneracy and the core expands and outer layers shrink in size. Stars climb down in luminosity with slight increase in T_{eff}. As shown in Figure 1.5, stars post-He flash, probably, end up as HB stars. Stars in the horizontal branch burn He in the core under non-degenerate conditions and H-burning in the shell. A new phase of evolution has begun which is also known as He-main sequence for He-burning at the center.

HORIZONTAL BRANCH

Stars on horizontal branch (HB) are analogues to the main sequence stars. The difference being in HB stars are He-core with H-burning in a shell. Much earlier Hoyle & Schwarzschild (1955) identified that the HB stars are nothing but the stars evolved from the RGB. Evolution from the tip of the RGB, after He-flash, to the stable HB is quite rapid and is not well understood. All the low and intermediate mass stars evolve to HB. Stars on the HB stay for a longer period with almost same luminosity but with a range of temperatures. Evolutionary time scales on HB are subject to their initial mass and also composition. Stars that are massive enough would undergo He fusion through 3α-reaction. The by-product is carbon which gets deposited at center. As He-burns, core contracts and stars make structural adjustments to maintain hydrostatic equilibrium. As a result stars shrink in radius which ensures almost constant luminosity with rise in temperature.

Once the He burning gets over at the center, and moves to shell He-burning HB stars

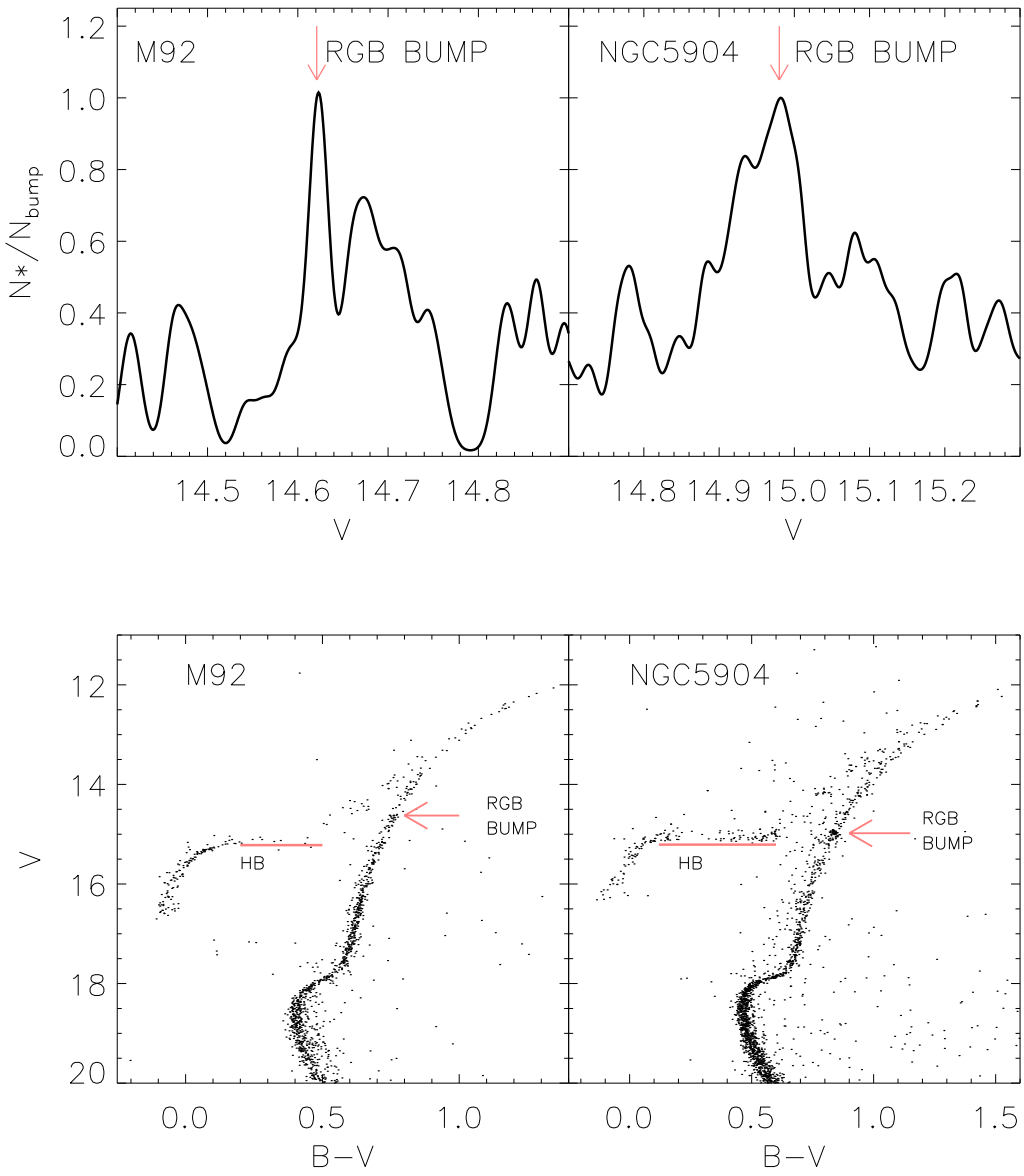

Figure 1.5: CMD of M92 and M5 globular clusters are shown. Red giant bump is marked in red line.

begin to ascend once again towards higher luminosity. The second ascent phase is known as asymptotic giant branch. All the HB stars may not ascend second time. Low mass stars depending on their chemical composition or heavy mass loss during the RGB end up as hot extreme HB stars (e.g. Möhler 2004).

ASYMPTOTIC GIANT BRANCH

All low and intermediate stars of about 1-10$M_{\odot}$ experience the AGB phase. AGB stars are the final evolutionary stage of low- and intermediate-mass stars driven by nuclear burning. This phase of evolution is characterized by nuclear burning of hydrogen and helium in thin shells on top of the electron-degenerate core of carbon and oxygen (See Figure 1.6). In the case of the most massive ($\sim$ 8 - 10 $M_{\odot}$) AGB stars core is of oxygen, neon, and magnesium. AGB phase is characterized by series of thermal pulses as a result of competing energy sources of He- and H- burning shells creating deep convective envelope. AGB stars expand significantly and they are as large as R$\sim$100$R_{\odot}$. As a result of large size and thermal pulses AGB stars lose mass heavily. It is estimated that about 70% of the dust in the Galaxy is due to the AGB stars. Also, they provide a rich environment for nuclear production. The primary C- and N-, and much of the *s*-process elements (Y, Ba, Nd, etc.) in the universe are mainly produced in the interiors of the AGB stars. The new element rich material is brought up to the photosphere as a result of deep convective zone and recurring thermal pulses, phenomenon known as 3rd dredge-up. Depending on the initial mass, AGB stars either become C-rich or O or N-rich stars. Stars with initial mass less than about 4 $M_{\odot}$, become C-rich (C/O $\geq$ 1) as fresh C, result of He-triple alpha reaction, is pumped-up to the surface. The more massive AGB stars (above 4 $M_{\odot}$) become O-rich (or N-rich stars) due to hot bottom burning (HBB). In more massive stars it is found that nucleosythesis occurs in the convective zone where the CNO reaction converts much of the primary carbon into nitrogen. This would reduce amount of carbon in the envelope and hence star becomes O-rich (C/O < 1) or highly N enhanced AGB star.

Due to heavy mass-loss towards the tip of the AGB, stars are obscured by heavy dust and invisible in optical wavelengths. These stars are mostly studied in IR and millimeter observations. Stars in this phase are also called OH/IR stars. The continued mass loss depletes mass of the H-envelope, and when a star reaches some critical value (about $10^{-3}M_{\odot}yr^{-1}$), it ends the AGB phase and moves left, in the HR diagram, towards planetary nebulae (PNe) phase. There are quite a good number of reviews on AGB star evolution in the literature (e.g; Iben & Renzini 1983; Herwig 2005).

POST-AGB EVOLUTION

Evolutionary phase of stars between AGB and PNe is known as post-AGB or some times proto-planetary nebula (pPNe) phase. Time scales of post-AGB phase are relatively very small of the order of a few tens of thousand years. All the low- and intermediate- mass

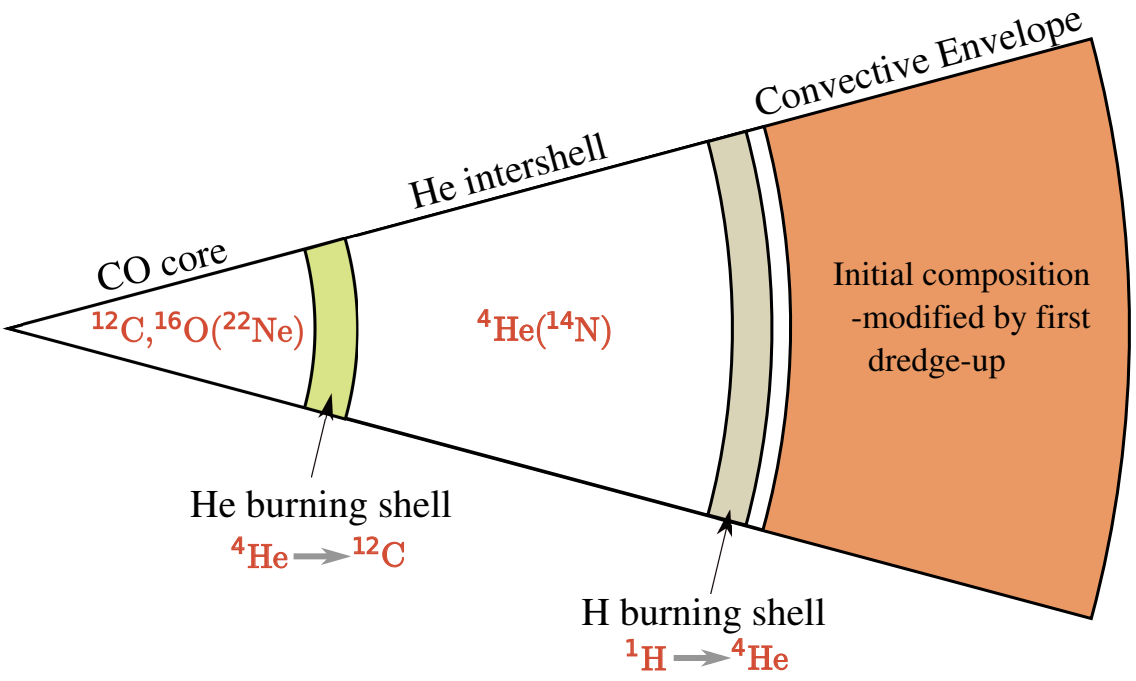

Figure 1.6: Structure of AGB star.

stars go through this phase. Post-AGB stars evolve from right to left (AGB to PNe) with constant luminosity and increasing surface temperature. Identification of post-AGB stars is difficult as they evolve much faster and also they appear like population I supergiants in the visible wavelengths. Number of post-AGB stars were discovered following the IRAS mission in 1983. Post-AGB stars show characteristic of far-IR colours with dust temperatures ranging between 100 - 300 K. The surface abundances of post-AGB stars reflect the nucleosynthesis and dredge-up process that occurred during the star's AGB evolution. The dust envelope that was created during the AGB phase slowly moves away from the central star. In slightly massive stars surface temperature rises fast enough to ionize the dust which appears as nebula. Stars enter into PNe phase. In the case of low mass stars, evolution is slow and the dust envelope dissipates by the time surface temperature rises enough to ionize the dust.

PLANETARY NEBULAE

PNe harbour a very hot compact star at their center and surrounded by dense torus of material presumably ejected earlier in the life of the AGB star. The morphologies of PNe are found to be complicated, and are categorised into three major types: round, elliptical, and bipolar. Normally, all PNes show reflection symmetry about their major and minor

axes (e.g. HST image of Cat's Eye Nebulae (Harrington & Borkowski 1994) given in Fig (ref), showed the shape of the PNe and jet-like structures). PNe's occupy the top left corner in the HRD, shown in Figure 1.1 The central stars of PNe are classified into two types: hydrogen normal and hydrogen deficient. (e.g R Coronae Boriolis star). The origin of H-deficiency in these stars are not well understood. There are few explanations existing in the literature: e.g. Born-again star scenario, in which a postAGB star (or WD) reignites helium-shell burning and transforms the star back into an AGB star (See the green star in Figure 1.1). The temperatures of the central stars are in the order of 10^4 which ionizes the nebular material and makes it visible. The abundances of nebular material is rich with heavier elements that have been synthesized inside the stars during their early evolution. The nebula expands to a great extent and merges into ISM, and the fully exposed core of the central star enters into white dwarf phase. In this way stars add heavier elements to its intital material and return back to ISM. Hence PNe play a crucial role in chemical evolution of the Galaxy. The intrinsic brightness of all PNe's are similar hence these are potential standard candles for the measurements of extragalactic distances.

WHITE DWARFS

White dwarf is the end state of stars ($< 4M_{\odot}$) which is highly densed object supported by degenrate-electron pressure. White dwarfs are very hot with temperatures of the order 10^5. Since there is no source of energy, it radiates all the energy and cools down. These are called cold black dwarfs. Similarly, the stars with higher masses ($> 4\ M_{\odot}$) evolve through various phases and ends their lives as neutron stars or blackholes (See Figure 1.7)

1.3 LITHIUM IN THE UNIVERSE

Li is one of the light elements with atomic number 3. It is found in two flavors: ^{7}Li and ^{6}Li. It is fragile, and gets destroyed at about 2-2.5 $\times$ 10^6K, such temperatures are common in stellar interiors. Hence its evolution is found to be a complex phenomenon. It is important to understand its evolution in the universe, in general, and in our Galaxy and in stars, in particular. Its study would enhance our understanding of the nucleosynthesis at the time of big bang and its evolution since then. In the case of stars, Li study would help to better constrain theoretical models dealing with the internal structure and dredge-up process. Thus, Li is considered as a crucial element to validate Big Bang nucleosynthesis models and an important diagnostic of standard and non-standard stellar evolutionary theories. Though our study is primarily focused on Li in RGB stars, we thought, it would

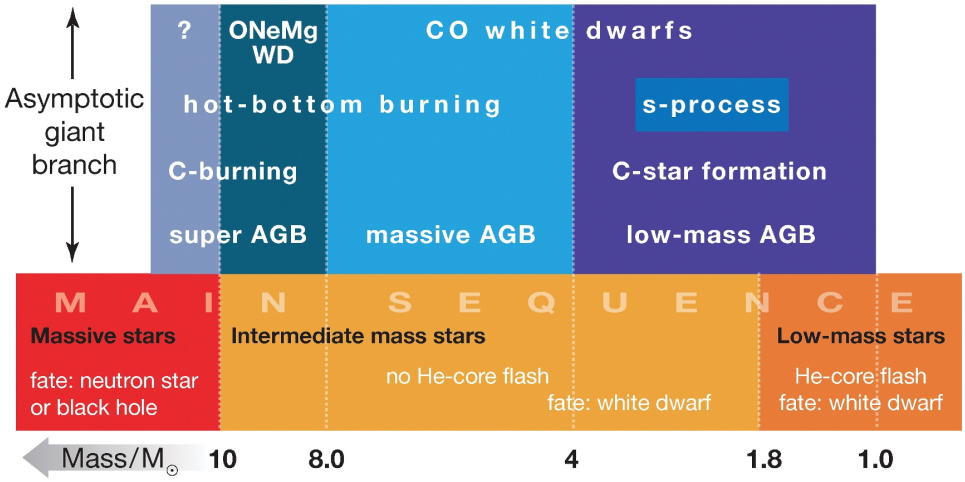

Figure 1.7: Evolution of low, intermediate, and high mass stars. Various phases in the evolution are also shown. Coutesy: Herwig (2005)

be relevant to provide an overview of Li content in various systems: old-metal poor stars (primordial value), ISM, and stars in the current epoch.

1.3.1 PRIMORDIAL LITHIUM

What is the primordial Lithium abundance? This question prevailed for quite some time and was debated in numerous studies. Yet, the answer seems to be not in sight. The discrepancy between the predictions made by big bang nucleosynthesis (BBN) models and the Li measurements made in metal-poor stars is too significant to be reconciled with. The main isotope of lithium (^{7}Li) along with other light elements hydrogen, Deuterium (D), ^{3}He, and He are known to have been produced during the big bang nucleosynthesis. The standard big bang nucleosynthesis (SBBN) models predict abundances of these four nuclei if the baryon-to-photon ratio (η) or a cosmological baryon density ($\Omega_b h^2$), a free parameter in SBBN, is fixed. The η value can be measured either by measuring the relative abundances of any two of the four nuclei or by measuring microwave background (CMB) with experiments such as WMAP (e.g; Dunkley et al. 2009). The current best values for ($\Omega_b h^2$) are 0.02273 ± 0.00062 (Dunkley et al. 2009) and 0.0214 ± 0.0020 (Kirkman et al. 2003) measured by five years WMAP data and by using D/H ratios measured in QSO absorption systems, respectively (see Figure 1.8) . These values correspond SBBN prediction of ^{7}Li abundance of log ϵ (Li) =2.72 ± 0.06 dex (Cyburt et al. 2008).

In the case of observations, Li abundance derived in hot (more than about 5800 K)

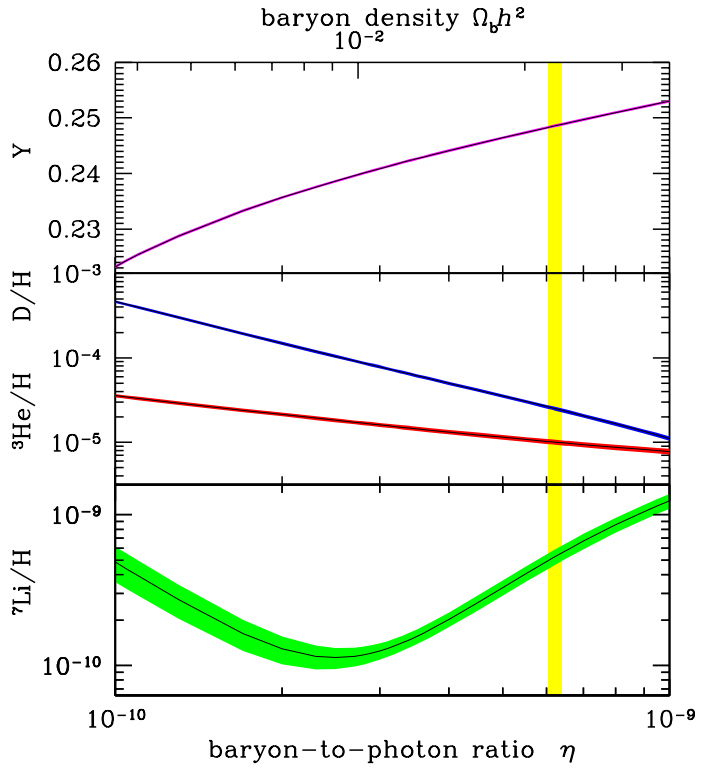

Figure 1.8: Comparison of predicted and measured abundance of four light nuclei as a function of baryon density parameter.

population II stars is interpreted as primordial value. Spite & Spite (1982) were the first to report almost a constant Li abundance, in warm metal-poor stars, over a range of metallicity ([Fe/H]) and $T_{\rm eff}$. This later came to be well known as Spite Plateau. Since then a number of studies are devoted to Li measurement in metal-poor stars (e.g. Ryan et al. 2000; Asplund et al. 2006; Bonifacio et al. 2007; Hosford et al. 2009; Aoki et al. 2009. In an attempt to put stringent constraints on the observed Li abundances, Ryan et al. (2000), after taking into account effects such as Galactic chemical evolution, possible depletion, and errors (systematic and random) in the measurements have derived log ϵ (Li)=2.08 ± 0.04 dex. Values derived in other studies are not too different from the value measured by Ryan et al. (2000). In summary, the observed Li value is about 4 times smaller than the predicted value from the best measured baryon-to-photon ratio and the SBBN model. This discrepancy between SBBN and observations is the cosmological Li problem and which is now well defined, thanks to improved observations in Li measurements and accurate η value from WMAP. In Table 1.1 below, recently measured Li abundances from

Pop II stars and the values computed from SBBN are given, where logϵ(Li) = log(Li/H) + 12.

Table 1.1: Primordial Lithium abundance

	Source	A(Li)[a]	Ref
Predicted	SBBN+WMAP	2.72±0.06	Cyburt et al. (2008)
Observed	Spite Plateau	2.05±0.15	Spite & Spite (1982)
	Halo stars	2.08±0.04	Ryan et al. (2000)
		2.10±0.09	Bonifacio et al. (2007)
		2.18±0.04	Hosford et al. (2009)
	Globular clusters	2.34±0.06	Bonifacio et al. (2002)
		2.24±0.05	Korn et al. (2006)
	Average Li	2.27±0.03	Lind et al. (2009)

[a] A(Li) = log ϵ(Li) = log(Li/H) + 12

As the problem is well defined, studies turned to look for other reasons for the discrepancy. Assuming that SBBN value and also the measured Li abundance in stars are correct one would make a suggestion that the primordial Li has been severely destroyed in the Galaxy before the formation of old metal-poor stars by astration of matter in massive Pop III stars (Piau et al. 2006). Also, it could be that the original Li in Pop II stars might have been depleted due to internal processes such as atomic diffusion and mixing (Richard et al. 2005; Korn et al. 2006; Lind et al. 2009). Also, one can't rule out the possibilities of uncertainties in the input parameters of SBBN. Some of these may be nuclear reaction rates and cross sections (Cyburt et al. 2008). However, to the present knowledge, the discrepancy between the predictions and observations of primordial Li, shown in Figure 1.9, is a challenge that need to be tackled.

1.3.2 GALACTIC LITHIUM

Young open clusters and the the main sequence pop I stars have been found to have a maximum Li abundance of log ϵ (Li) = 3.2 dex. This is in good agreement with the measured Li value in different molecular clouds which represents ISM value (See Table 1.2). From this, one can safely draw a conclusion that the maximum Li abundance found in main sequence (e.g; Lambert & Reddy 2004) stars and in ISM is the value that represents Li in current epoch or the cosmic Li abundance. The current Li abundance is about an order of magnitude more than the observed Li abundance, believed to be a primordial value, in pop II dwarfs. Understanding of enrichment history of Li from Spite plateau value to the

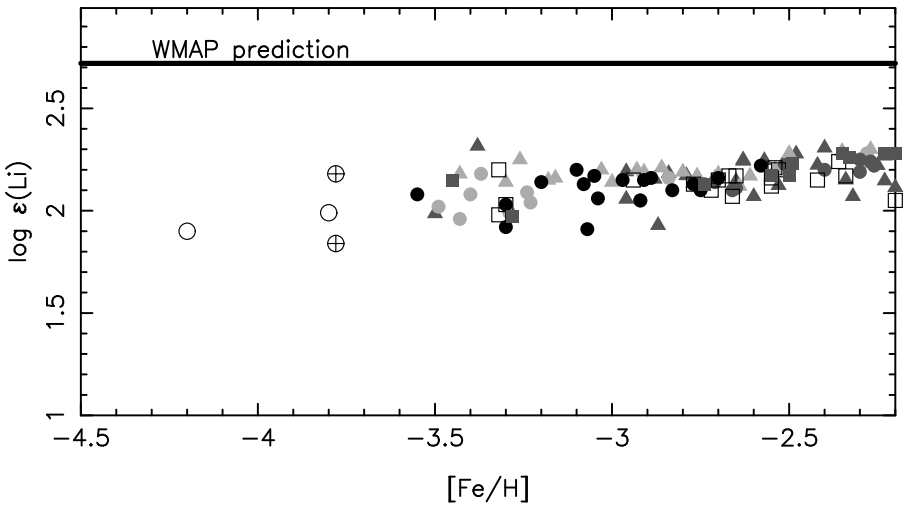

Figure 1.9: Discrepancy between the predicted and observed value of primordial Li.

current ISM value is one of the most interesting and challenging aspects in astrophysics. A number of sources have been proposed for Li contribution in the Galaxy. Some of them are: cosmic ray spallation from heavier nuclei (Lemoine et al. 1998), supernovae (e.g; Woosley & Weaver 1995), novae (Jose & Hernanz 1998) and the nucleosynthesis in stars (Sackmann & Boothroyd 1999). Important aspects of each of these Li sources are outlined below.

Table 1.2: Li abundance in our Galaxy

	A(Li)	Ref
$\text{Primodial}_{\text{WMAP}}$	2.72±0.06	Cyburt et al. (2008)
$\text{Primodial}_{\text{Obs}}$	2.27±0.03	Lind et al. (2009)
Age of Universe	13.7±0.13 Gyr	WMAP
	13.8±1.1 Gyr	Gratton et al. (2003)
Young stars	3.2	Lambert & Reddy (2004)
ISM	3.25	Knauth et al. (2000, 2003)
Meteroitic	3.28	Lodders (2003)

COSMIC RAY SPALLATION

Cosmic ray spallation is a form of nucleosynthesis where the lighter elements (LiBeB) are produced through nuclear fission from the impact of cosmic rays on higher elements (A > 11). ^{14}N,^{16}O, and ^{12}C are abundant in the interstellar space for the spallation process to work and to contribute to light elements. The isotopes of Li are produced via

spallation reactions (Reeves 1970; Meneguzzi et al. 1971) when Galactic Cosmic Rays (GCR), mainly protons, interact with C,N, and O nuclei in the interstellar medium. It is believed that the amount of ^{6}Li present in the universe is entirely produced through cosmic ray spallation, whereas only small fraction of ^{7}Li is understood to be produced. The evidence for ^{7}Li production in the GCR has been inferred using the Be and B abundances that are seen in Pop II stars (Olive & Schramm 1992). Be and B abundances do not show plateau unlike ^{7}Li suggesting B and B are mainly from GCR and ^{7}Li must be from big bang. Lemoine et al. (1998) calculated the amount of ^{7}Li produced by GCR. However, the observational evidence of ^{7}Li production through GCR process is not well tested. The detection of a significantly high amount of ^{6}Li (^{6}Li/^{7}Li $\approx$ 0.05) in some of the Pop II stars is one of the evidences that Li gets produced in the GCR through α-α fusion reactions (Smith et al. 1993; Asplund et al. 2006).

SUPERNOVAE NUCLEOSYNTHESIS

The core of massive stars collapses to form a neutron star and explode as supernovae. Most of the gravitational energy released at the explosion is carried away by neutrinos ($\sim 10^{58}$) emitted from the central remnant. Although cross section of neutrino-nucleus reactions are very small, such a large number of neutrinos enable to contribute the increase in the yields of some species of light nuclei. This process is called ν-nucelosynthesis (Woosley et al. 1990). During the formation of the neutron star in the pre-explosion phase, SNe II II can produce ^{7}Li in the He-shell by excitation of ^{4}He by μ- and τ- neutrinos followed by de-excitation with emission of a proton or neutron, via ^{4}He(ν,$\nu^{'}$n)^{3}He, which in turn reacts with α particle and forms ^{7}Li via Be-transport mechanism.Woosley & Weaver (1995) calculated the detailed ^{7}Li yields from SNe II as functions of initial stellar metallicity. Unfortunately, the theoretical suggestion of possible Li production through ν-process is not confirmed by observations.

NOVAE SYNTHESIS

Classical novae could also in principle be ^{7}Li producers. Della Valle et al. (2002) were the first to report the detection of ^{7}Li in a nova. The novae explosion occurs when the hydrogen rich envelope on the white dwarf reaches some critical mass by accretion from its low mass companion. The explosion results in exposing the stellar regions in which the hydrogen burning via PP chain is incomplete. Hence, ^{3}He is accumulated in the envelope (e.g. Dantona & Mazzitelli 1982). Arnould & Norgaard (1975) proposed that the Cameron-Fowler mechanism, acting at the nova outburst, would produce Li abun-

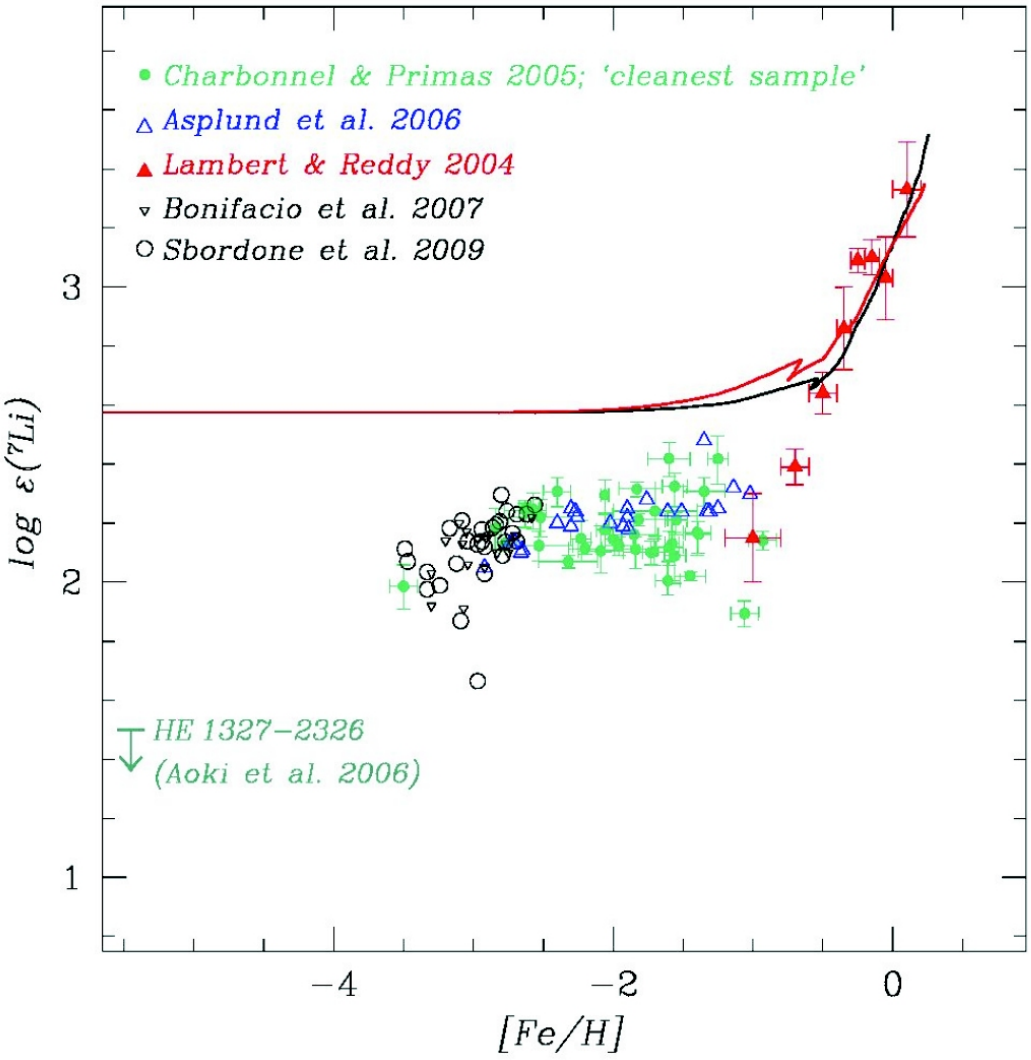

Figure 1.10: Galactic chemical evolutionary models. Courtesy: Matteucci (2010)

dance proportional to the ^{3}He abundance in the nova envelope. Starrfield et al. (1978) showed that the mechanism could be efficient for outburst temperatures > 150 MK, and the fast ejection of the ^{7}Be rich nova shell leads to ^{7}Li production. D'Antona & Matteucci (1991) linked the Li abundance produced in the outburst to the "delay time" between the formation of the white dwarf and the occurrence of nova outbursts. As a result, novae containing white dwarf and ^{3}He-rich low mass companion, contribute to the galactic production of lithium. Hernanz et al. (1996) and Jose & Hernanz (1998) modeled with an implicit hydro-code including a full reaction network, showed the white dwarfs having carbon-oxygen cores are more efficient in lithium production than oxygen-neon cores.

Table 1.3: Contributions from various sources in Galactic evolutionary models.

Source	Romano(2001) %	Travaglio(2001) %
Galactic Cosmic Rays (GCR)	25	10-20
Supernovae Type II (SNeII)	9	10
Novae	18	10
AGB stars	0.5	40
Low mass stars	41	20

AGB STARS

During the evolution of AGB stars the bottom of the convective envelope reaches the H-shell burning layers, and the nuclear products are transported to the surface by convection. This is the perfect site for lithium production through the Cameron-Fowler mechanism (Cameron & Fowler 1971; Iben 1973; Sackmann et al. 1974). The envelope models of AGB stars (Scalo et al. 1975; Sackmann & Boothroyd 1992), show that the temperature (T_{bce}) of the bottom of convective envelope reaches as high as 40×10^6 K sufficient to produce lithium via ^{3}He(α,γ)^{7}Be(e$^-$,ν)^{7}Li chain. These models were able to explain the high lithium abundance found in some luminous red giants. The process is known as Hot Bottom Burning (HBB). HBB models of AGB stars (Sackmann & Boothroyd 1999) suggest that the stars in the mass range (4 - 6 $M_\odot$) can produce significant quantities of ^{7}Li (A(Li) $\sim$ 4 - 4.5) which are seen in Galactic C- and S- stars as well as M-stars in Magellanic Clouds (Smith & Lambert 1989, 1990; Smith et al. 1995). The consequence of HBB or the nucleosynthesis in the convective envelope is that stars are not only enriched in ^{7}Li but also become O-rich (C/O $<$ 1.0) as the CNO reaction converts most of the fresh C into N. As given in the earlier paragraphs, AGB stars lose mass heavily (10^{-7} - 10^{-5} $M_\odot yr^{-1}$) due to thermal pulses. Therefore AGB stars are thought to be one of the significant ^{7}Li contributors to the Galactic Li enrichment. The amount of contribution is not well known and there are a few studies which predict significant different values: Romano et al. (2001) predicts considerably less contribution and Travaglio et al. (2001) suggests AGB stars contribute as much as 40% of Li to the Galaxy (See Table 1.3).

LOW MASS GIANTS

Low mass giants are known to have, in general, low Li in their atmospheres and negligible mass-loss, 10^{-11} - 10^{-9} $M_\odot yr^{-1}$. However, there are a small class of stars which are found to have anomalously high Li abundances and are known to have significant mass loss

10^{-9} - 10^{-7} $M_{\odot}yr^{-1}$. Their contribution to the Li enrichment of the Galaxy is not well understood due to a paucity of stars with high lithium. The issue of Li in stars, in general, and in low mass giants, in particular, is described below in detail.

1.4 LITHIUM IN STARS

Li is a sensitive indicator of mixing mechanism, and therefore, a good tracer of stellar evolutionary phase. The amount of Li presence and absence in the stellar photosphere is often ascribed to stellar evolutionary phase and the associated mixing processes. Li has been crucial to test models of cool stars at all possible stages of evolution, from pre-main sequence to the post-AGB. Li in stars is measured conveniently by the resonance doublet at 6707.8 Å. In general, Li that originated from the natal clouds gets destroyed in stars. The destruction begins right through the pre-main sequence (PMS) to the AGB. The high temperature in the interior regions and the deep convection are the two main parameters that control Li in stellar photospheres. The level of convection again is a function of mass and metallicity. Low mass stars develop relatively a deep convective envelope, thereby depleting Li much more compared to massive stars by the time they arrive at the main sequence. This was amply demonstrated from the Li observation of open clusters (e.g; Randich et al. (2001)). They have shown clearly high rate of depletion in PMS stars of mass less than $1M_{\odot}$ compared to PMS stars of mass more than $1M_{\odot}$. The observed Li abundance of the sun ($\log\epsilon(\mathrm{Li}) \approx 1$) is two orders of magnitude less from its original values of ISM. Observations of solar type stars in open clusters (Sestito & Randich 2005; Randich et al. 2005; Pallavicini et al. 2006) strongly suggest that the solar Li content is not a typical one. The observed main sequence depletion of stars may be due to mixing of upper Li rich material with that of material in the inner regions where Li has been destroyed. This is normally explained by turbulent mixing or meridional circulation, although diffusion can also lead to lithium reduction. Understanding when and how Li depletion occurs in Pop I main-sequence stars of different masses is still a major challenge and several unsolved problems exist (See Figure 1.11). e.g. "Lithium dip", a sharp decrease of Li abundance in a very narrow temperature range around 6500 K, first discovered in the Hyades by Boesgaard & Tripicco (1986) and then found in several other clusters older than a few hundred Myr. This is a well known Boesgaard dip .

As the stars evolve off the main sequence, one would expect further dilution of Li as a result of further deepening of convective envelope. Standard stellar evolutionary

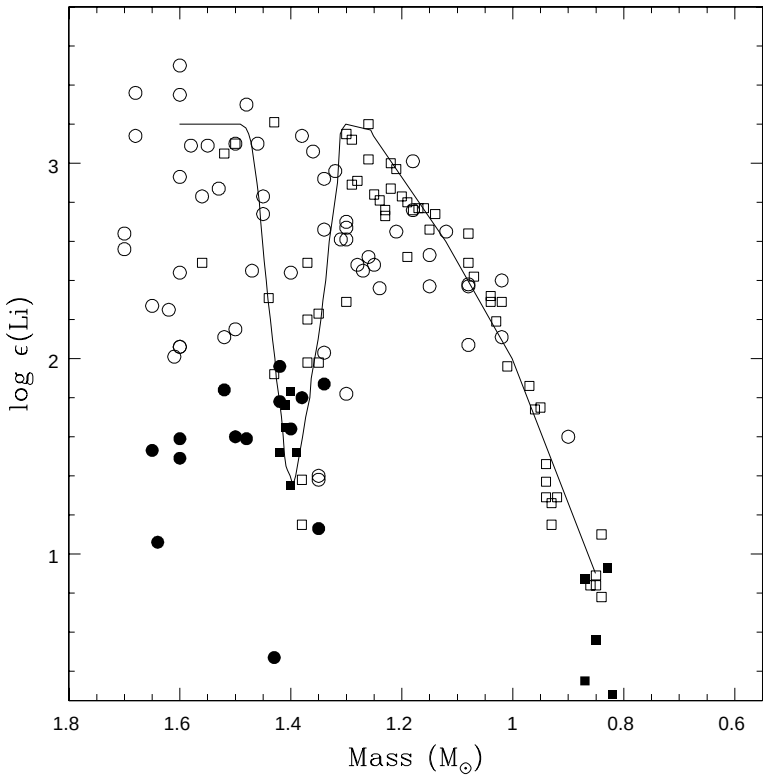

Figure 1.11: Li abundance in main sequence dwarfs.

models predict Li reductions in the low mass stars ($\leq$ 2.5 M$\odot$) by an order of 1 - 2 magnitudes, by the end of 1st dredge-up on the RGB phase. Assuming that the progenitors of K giants evolved off the main sequence with an initial Li of about log ϵ(Li) = 3.2 (e.g.,Lambert & Reddy 2004), the maximum amount of Li one would expect, depending on mass, metallicity and the amount of Li on the main sequence, for a low mass K giant is log ϵ(Li) $\leq$ 1.4 dex (Iben 1967a,b). Observations suggest that the value is much smaller than the predicted value as most of the stars are depleted in Li during their evolution on PMS and MS.

Lambert et al. (1980) obtained lithium abundance for the Hyades giants, with a turn-off mass of 2.2 M$\odot$, in rough agreement with standard theoretical predictions. Li abundance obtained in some more old open clusters (M67, NGC 752, and NGC 7789), with a range of turn-off mass (M $\sim$ 1.2, 1.6, and 1.8 M$_\odot$), are also in good agreement with the standard theoretical expectations (Pilachowski 1986; Pilachowski et al. 1988). Many of the G- and K- giants in the field, as well as in clusters, are found to have lithium which is a factor of 10 less than the expected value (Brown et al. 1989; Pilachowski et al. 1988).

In fact, Li is observed in a wide range, -1 ≤ logϵ(Li) ≤ 1, in Pop I red giants (Lambert et al. 1980; Brown et al. 1989; Mallik 1999). Much lower Li abundance than the value predicted by standard models has been one of the major issues in the literature, and was attributed to extra-mixing in giants (Sweigart & Mengel 1979; Charbonnel 1995; Palacios et al. 2006; Eggleton et al. 2008).

So far we have talked about Li depletion in stars which act as sinks of Li in the Galaxy. If this is the situation one would expect an overall reduction in Li content in the universe or at least same as the primordial value unless the GCR production rate of Li is much higher compared to the depletion of Li through stellar process. But this is not the case, as we have already mentioned that Li in the Galaxy is enriched by a factor of 15 from its original value of big bang and the GCR alone may not account for such increase. Therefore, one needs to look for other sources. Stars seems to be also sources of Li apart from sinks in certain special conditions. Below we briefly describe such rare group of stars in the post-main sequence where Li is found to be much higher compared to the predictions.

1.4.1 ACTIVE STARS

There is a small class of stars which are chromospherically active and high abundances of Li. For example the RS Cvn binaries with periods ranging from one to fifteen days show high abundances of Li. It is not very clear whether there is a relation between activity and the high Li abundances. Recent study by Mishenina et al. (2010) suggest that frequency of stars with observed high lithium is significantly higher among active stars than the non-active stars.

1.4.2 SUPERGIANTS

Supergiants are the high mass post main sequence stars. These stars evolve off the main sequence to the right and pass through the instability strip in the HR diagram, reaching temperatures as low as 4000 K. Under normal conditions, one may not expect enhanced Li on their outer surfaces as they develop deep convective envelope resulting considerable amount of Li depletion. However, two of the supergiants were found to have much more Li than that expected (Luck 1982). One of these stars (HD 172365) has been studied in detail by Andrievsky et al. (1999). Later, one more star Cepheid HV 5497 in LMC was found to be Li-rich (Luck & Lambert 1992). Of course these findings were mere accidents, and the studies were not meant for finding Li-rich supergiants. It is impor-

tant to undertake survey of supergiants in the instability strip to see whether the high Li abundance is linked to oscillations or some other physical phenomenon.

1.4.3 AGB STARS

The observation of strong Li line in a carbon star, WZ Cas, by McKeller 1940, suggested that AGB stars could have high lithium abundance. Followed by this finding, a survey of 30 disk carbon stars was undertaken by Torres-Peimbert & Wallerstein (1966). This study resulted 16 AGB stars with substantially strong Li line. Later, this was extended to S-stars where large amount of Li has been measured (Keenan 1967; Boesgaard 1970) S-stars are AGB stars with enhanced carbon and s-process elemental abundances, but with C/0 still less than 1.0. These stars showed Li abundance ($\log\epsilon$(Li) $\sim$ 4.0) as high as one order of magnitude more than the value measured in ISM. Recent findings of high Li in very luminous Galactic AGB stars that are enriched in *s*-process are in conformity with the finding of high Li in luminous O-rich and *s*-process elements enhanced AGB stars in large and small Magellanic clouds (Smith & Lambert 1989, 1990; Plez et al. 1993; Smith et al. 1995). These results clearly suggest that the high Li abundances are in fact related to the mass of the AGB stars. The high Li in the AGB stars was explained as due to Hot Bottom Burning (HBB) which according to models happen only in massive AGB stars ($\geq$ 4 - 6$M_{\odot}$) (Scalo et al. 1975; Sackmann & Boothroyd 1992). In massive AGB stars the bottom of the convective envelope is hot enough to operate PP, CN reactions, and Cameron-Fowler Li synthesis mechanism. The ^{7}Be produced ($^{3}He\ (^{4}He,\gamma)^{7}Be$) gets transported to cooler regions where it ($^{7}Be\ (e^{-},\nu)^{7}Li$) has time to get converted to ^{7}Li before it gets destroyed by proton capture ($^{7}Li(^{1}H,^{4}He)^{4}He$). The Li-rich material somehow brought-up through the third dredge-up process.

1.4.4 WEAK G-BAND STARS

The weak G-band stars are G and K giants whose spectra show very weak or absent G-bands of CH $A^{2}\Delta$ - $X^{2}\Pi$ system at 4300 Å. Weak G-band stars as a class was identified by Bidelman (1951). Chemical composition studies (Sneden et al. 1978; Cottrell & Norris 1978) revealed that they are underabundant in carbon and over abundant in nitrogen, and nearly normal abundance of oxygen. Also, they are found to have enriched with carbon isotope ^{13}C with near equilibrium value of $^{12}C/^{13}C = 4$ (Sneden et al. 1978). The weak G-band or the CH-band and CNO abundance observations indicate that the weak G-band is due to underabundance of carbon (Rao 1978; Hartoog et al. 1977; Sneden &

Pilachowski 1984). The results of chemical composition studies suggest the existence of large amounts of CN cycle processed material in the atmosphere of weak G-band G and K giants. An apparent contradiction to the simple CN cycle production and efficient mixing is the observation of very high Li abundances in several weak G-band stars. Their very low carbon abundance and high nitrogen abundance and very low $^{12}C/^{13}C$ ratio clearly indicate that they are evolved and material being well mixed. Origin of high Li in these stars is not well understood, and from the very limited observational studies one may suggest weak G-band phenomenon seems to be happening only in stars of masses greater than 2.5 $M_{\odot}$. (Lambert & Sawyer 1984; Parthasarathy & Rao 1980)

1.4.5 G- AND K- GIANTS

The discovery of Li-rich K giant by Wallerstein & Sneden (1982) has challenged the evolution of lithium along the first ascent giant branch. Since then a few more Li-rich K giants were reported e.g; Hanni (1984); Gratton & D'Antona (1989). All of these Li-rich K giants were discovered serendipitously. The first systematic survey to search for Li-rich giants was undertaken by Brown et al. (1989) who selected 644 bright giants, not necessarily K giants, from the catalog of McClure & Forrester (1981). The survey resulted in findings of one super Li-rich K giant, and 9 additional Li-rich giants. Results from the survey suggested that high Li among K giants is a rare phenomenon, and such stars account just under 1% of giant stars in the solar neighborhood. Some of the Li-rich giants were found to be associated with rapid rotation ($vsini \geq 8\ km\ s^{-1}$) and chromospheric activity which added the other anomalies to Li-rich giants (e.g. HD 9746 (Brown et al. 1989), HD 33798 (Fekel & Marschall 1991)). Gregorio-Hetem et al. (1993) survey (PDS or Pico Dias Survey) to search for young T-Tauri stars based on infrared colors resulted in the discovery of a few Li-rich K giant candidates. Some of these were studied in detail e.g; Reddy et al. (2002); Drake et al. (2002). Note, the above surveys are pre-hipparcos. The sample data lacks accurate astrometry resulting in large uncertainties in luminosity. A few Li-rich K giants are also found in other studies (e.g; Mishenina et al. 2006; Luck & Heiter 2007). Currently there are about two dozen Li-rich K giants and five of them are super Li-rich (Balachandran et al. 2000; Reddy & Lambert 2005). Recently, Monaco et al. (2011) added a few more Li-rich giants including one super Li-rich K giant. This survey was done among thick disk population of the Galactic disk. A handful of Li-rich giants are also discovered in bulge, open clusters (Hill & Pasquini 1999), globular clusters (Kraft et al. 1999) and dwarf spheroidal galaxies (Domínguez et al. 2004; Monaco & Bonifacio 2008). Another important study was by Gonzalez et al. (2009) who initiated a survey,

among 400 red giants, to search for Li-rich K giants in Galactic bulge which resulted in finding two giants with Li abundance of near cosmic value (A(Li) > 2.6) and six giants with Li more than 1.4 dex. Results from Gonzalez's survey combine with Brown's results suggested that Li-rich giants are only of 1% in the Galaxy.

There are some theoretical and observational studies regarding the origin of anamolous high Li in these rare group of K giants and its connection with other peculiarities. The three principal suggestions for explaining the high Li are as follows : a) preservation of Li from the main-sequence phase due to inefficient mixing b) addition of Li-rich material through planet engulfment, c) production of Li in the stellar interiors (Cameron & Fowler 1971) and some sort of mixing mechanism (Sweigart & Mengel 1979; Palacios et al. 2006; Eggleton et al. 2008). These suggestions are discussed in detail in Chapter 5. There are few attempts to understand the relation between Li and other peculiarites: (i) Fekel(1993) suggested a scenario linking the Li and high rotation via chromospheric activity. In this scenario, the surface convection zone reaches the rapidly rotating core and dredges up the highly angular momentum material to the surface including the freshly synthesized Lithium. Rapid rotation of these giants which results in the chromospheric activity via the dynamo process. But the study of *vsini* in large number of evolved stars suggested that single K giants are very slow rotators having mean *vsini* value of order of 2 km s^{-1} (De Medeiros et al. 2000). For a selected group of Li-rich giants de Medeiros et al. (1996) found no correlation between Li and rotation. (ii) There are two arguments regarding the relation between Li and infrared excess that are following: (a) The model developed by de La Reza et al. (1996) suggested a relation between Li enhancement and infrared excess. The model proposed that all normal K giants become Li-rich during a short interval in their RGB phase. The observational study on K giants by de La Reza et al. (1997) supported the above scenario. (b) Observational studies by Fekel & Watson (1998) and Jasniewicz et al. (1999) found that the number of Li-rich giants with circumstellar shell is less than normal giants with dust, suggested that no relation between Li enhancement and the association of infrared excess, and the reason for CS may be due to heated up of debris disk on RGB. Still the association of these pecularities with Li-rich giants are uncertain and the relation with Li enhancement is not well understood.

1.5 OUTLINE OF THESIS

The puzzle of origin of anomalous high Li, by a factor of 10 to 100 compared to theoretical predictions, in a small group of K giants remained unsolved and its connection with

other peculiarities, rapid rotaion and infrared excess, still need to be explained. In this thesis, we have investigated the rare group of Li-rich K giants to understand the associated anomalies and their connections with each other. The study of Li-rich giants is in three folds: (i) To increase the sample of Li-rich giants and determine the fractional content of them among K giants in our Galaxy, a systematic search for Li-rich giants was performed among large sample of low mass giants starting from the base to the post luminosity bump of RGB to study the evolution of Li in K giants . (b) To pin down the source of Li in K giants from the three principal suggestions, we have studied the physical parameters and chemical composition of Li-rich giants in detail. (c) To understand the relation between Li and other peculiarities, we studied the infrared properties of K giants along the RGB and the rotational evolution from the mainsequence stars to post bump stars in the HRD.

Chapter 1 gives a brief introduction to various stellar evolutionary phases in the H-R diagram, sources and sinks of Li in the universe, and Li-rich stars which are the main study of interest in this thesis. **Chapter 2** describes the observations, data reduction procedures, and description of observational facilities and instruments. It also provides the details of few other tools that are used in analysis techniques.

Chapter 3 deals with the survey for Li-rich K giants which is main issue of the study. It briefly discusses the criteria of sample selection, source of the sample (Hipparcos catalog) and observational strategy. It also provides full description of estimating Li abundances in K giants using low resolution spectra. The results obtained from low resolution spectra of sample stars are discussed. The entire Li-rich sample which includes the new candidates found from the survey and the ones taken from literature are discussed in **Chapter 4**. It provides description of the data analysis of high resolution spectra obtained from 2.3-m VBT , Kavalur, and 2.7-m Harlan J. Smith telescope, McDonald Observatory, USA. It also provides detailed description of deriving stellar atmospheric parameters, abundances and isotopic ratios. The three super Li-rich giants with anomalous low $^{12}C/^{13}C$ ratios resulted from the Li abundance and carbon istopes are discussed in **Chapter 5**. It also discusses the Li origin in the context of preservation and planet engulfment scenario.

Chapter 6 deals with the study of IR-excess and mass-loss on RGB. Optical, near-IR and far-IR fluxes were collected from respective catalogues. Spectral energy distributions (SEDs) were constructed to estimate IR-excess and mass-loss. Just 1% of the sample stars seems to have IR-excess and most of them are indeed Li-rich K giants. With the help of DUSTY code, we have constructed far-IR color-color diagram from which we have derived evolutionary timescales for dust envelopes. The connection between Li-excess

and IR-excess has been discussed.

Chapter 7 describes our investigation to find out the possible cause for Li enrichment in K giants. Our survey sample of 2000 K giants was supplemented by Brown et al. survey sample of about 644 G- and K giants. For the entire sample, luminosities and effective temperatures are derived in the same way. For Li-rich K giants, both new and old, Li abundances and isotopic ratios are presented. This chapter discuss the two main observational results: a) finding of all the Li-rich K giants in a very narrow luminosity region in the HR diagram which coincides with the positions of luminosity bump on the RGB or the red clump, b) finding no Li-rich K giants below or above this region.

Chapter 8 provides summary and conclusion of the thesis highlighting important results. It also provides few suggestions for further studies in this direction.

CHAPTER 2

DATA RESOURCES AND ANALYSIS TOOLS

The study in this thesis is mainly based on extensive use of stellar spectroscopic observations and techniques. In this chapter, we describe low, medium and high resolution spectroscopic observations and reduction procedures. We discuss in brief the computational methods and analysis techniques involved in the study of spectra. We also discuss the various other tools that are used in our study.

2.1 ASTRONOMICAL SPECTRA

Spectrum is a fingerprint of an object and a collection of photons of different wavelengths and fluxes in which lies the information regarding star's birth, evolution and its chemical makeup. The spectra of astronomical objects are obtained from spectroscopic observations that require a dedicated system containing telescope, spectrograph, and a detector. A brief description of each part of the systems is given below.

TELESCOPE

Telescopes collect light from distant astronomical sources and brings it to a focus. The focused light is viewed or utilized from eye-piece. Lenses are used in refracting telescopes and mirrors in reflecting telescopes. Modern telescopes are of reflecting type consisting of primary and secondary mirrors. In general, the light gathering capacity of a telescope is directly proportional to the square of the diameter of the primary mirror.

SPECTROGRAPH

The main function of the spectrograph is the decomposition of star's light into finite colors or spectral features. This has four important parts: (i) Entrance aperture where light enters, generally called **slit**, which ideally should be smaller than that of the seeing disk. The slit sets a reference point in the spectrograph and also blocks unwanted light from the sky and other nearby sources. The spectral resolution is a function of slit width i.e., narrowing the slit would help increase the resolution but also increase light loss.
(ii) **Collimator** is the element which converts a diverging beam of white light from the slit to a parallel beam. The focal ratio of the collimator must be matched to the effective focal ratio of the telescope. The diameter of the collimator determines the diameter of the light beam in the spectrograph. The size of the collimator affects the size of the "slit image" on the detector. Bigger, longer focal length cameras reduce the size of the slit image, and increase the resolution of the spectrograph.
(iii) **Dispersing element** disperses the light. The disperser elements that are used in the low resolution spectrographs are Prism, Grating, and Grism. A prism disperses the channeled spectrum more in blue than in red and hence red fringes are crowded. It works on refraction and used for very low resolution spectroscopy. Its dispersion is non linear. A grating disperses the light through diffraction and produces the crowded blue fringes. It can be used in low and medium resolution spectroscopy. Its dispersion is almost linear. A Grism disperses the spectrum so that the channeled fringes are equally spaced across the detector. It gives linear dispersion. It can be used in both low and medium resolution spectrographs. To get the high resolution, Echelle gratings are used in the spectrographs.
(iv) **Camera** converts a parallel beam into a converging beam. There are two types of camera, transmission camera and reflecting camera or schmidt camera. Schmidt camera has broad wavelength coverage but there is a central obstruction due to its on- of off- axis. Transmission camera has lenses which are generally on-axis so that no central obstruction, but multiple elements are required to get the broad wavelength coverage.

DETECTORS

Detectors record the dispersed spectra that come from the spectrograph. The examples are photographic plates, CCD, IR array, etc. Photographic Plates are the light-sensitive emulsion of silver halide that are applied to the glass plates. These were used before the invention of Charge couple device (CCD) in 1980s. Since then CCDs became part of observational astronomy and replaced photographic plates altogether.

The CCD chip is an array of Metal-Oxide-Semiconductor capacitors (MOS capacitors), each capacitor represents a pixel. CCDs are typically fabricated on a p-type substrate. A thin n-type region is formed on its surface. A insulator, in the form of a silicon dioxide layer is grown on top of the n-region. The capacitor is finished off by placing one or more electrodes, also called gates, on top of the insulating silicon dioxide. These electrodes could be metal, but in general these are heavily doped polycrystalline silicon conducting layers.

CCDs are worked based on the principle of photoelectric effect. Light photons create a small charge each time they strike a capacitor. The more photons that strike a capacitor, the more charge that builds up in it, so that the total charge is proportional to the light intensity at that point. When the exposure period is finished, the process of transferring the charges off the grid begins. The CCD is essentially an analogue shift register. In one edge row, the charge in each capacitor is shifted along until it reaches the corner capacitor, where the voltage is measured and transferred to memory by an analogue-to-digital converter. This shifting process is controlled by a gate driver and a clock signal. Once all the capacitor voltages in the row have been measured, the charges in other rows are shifted towards the edge row. Millions of capacitors are sampled in a fraction of a second by this method.

2.1.1 OBSERVING FACILITIES

The main requirement for this study is the spectroscopic data of low and high resolution for a selected sample of K giants. The following instruments at the different facilities were made use of:

- HFOSC mounted on Himalayan chandra telescope (HCT) with a CCD of size 2K $\times$ 4K CCD
- OMRS attached to the 2.34-m Vainu Bappu telescope (VBT) with a CCD of size 1K $\times$ 1K CCD
- UAGS mounted on 1-m Carl Zeiss telescope (CZT) with a CCD of size 1K $\times$ 1K CCD

High resolution spectroscopic data have been obtained from two different spectrographs. These are:

- fiber-fed echelle spectrograph attached to the 2.34-m VBT with a CCD of size 2K $\times$ 4K CCD,

- coude spectrometer attached to the 2.7-m Harlan J. Smith telescope (HJST) with a CCD of 2K $\times$ 2K CCD.

The telescope facilities, 2-m HCT, 1-m CZT, and 2.34-m VBT are operated by Indian institute of Astrophysics, India, and 2.7-m HJST is operated by University of Texas, Austin, USA. A brief description of each of these facilities is given below.

HIMALAYA CHANDRA TELESCOPE

Himalaya Chandra Telescope (HCT) is a 2 m aperture optical-infrared alt-azimuth telescope installed at Indian Astronomical Observatory (IAO) located in Hanle, Ladak. The latitude (32d46m46s North) of this site enables to observe the objects in the whole of northern hemisphere. The altitude (4500) of the site enables to access the near infrared and near UV part of the electromagnetic spectrum and also offers significant number of clear nights in a year. The telescope is remotely operated through a dedicated link from CREST, Hosakote which is about 40 km from the main campus of IIA, Bangalore. The telescope is equipped with three science instruments, Himalaya Faint Object Spectrograph Camera (HFOSC), the near-infrared (NIR) imager, and the optical CCD imager, which are mounted at the cassegrain focus of the telescope. For this project, we have extensively used HFOSC. HFOSC is an optical imager with spectrograph which allows a wide field coverage for a given CCD, and also low and medium resolution grism spectroscopy. The instrument has four wheels in which slits, filters, grisms, and calibrated mirrors are housed. For imaging, Bessels broad band filters (UBVRI) and narrow band filters (Hβ, O at 5007,Hα, and Ca at 6724) containing 10 Å bandwidth. For spectroscopy, short and long slits from 67 μ to 1340 μ and 10 various grisms available which gives the wavelength coverage of 3500 Å - 10500 Å. It has an option of cross dispersed (echelle) mode from which maximum resolution available is R$\approx$3500. Various combination of slits and grisms give the range of resolutions starting from 200 to 3500.

1-m Carl Zeiss Telescope

Carl Zeiss Telescope (CZT) is 102-cm aperture optical telescope that was developed and built in German Democrat Republic during 1970s which was installed at the Vainu Bappu Observatory (VBO), Kavalur. It accommodates science instruments both at cassegrain focus (f/13) and coude focus (f/30). It is equipped with two science instruments at cassegrain focus : Imaging camera and Medium resolution zeiss Universal Astro Grating Spectrograph (UAGS) and Echelle spectrograph at coude focus. Echelle spectrograph

is installed in a separate chamber which gives the spectral resolution of nearly R ~ 20,000.

2.34-m Vainu Bappu Telescope

Vainu Bappu Telescope (VBT) is a 2.34-m classical telescope with equatorial mount. This was built over the years 1978-1985 and was named in honor of Prof. M. K. Vainu Bappu. VBT is the largest optical facility in India which was built indegenously. Telescope was installed at VBO, kavalur which is in Tamilnadu state and about 160 km from IIA, Bangalore. The location of the observatory (12 degree north) enables to access most of the southern sky upto −65 degrees. The telescope is equipped with three science instruments at prime and cassegrain focus. (i)Imaging Camera with a 3-element Wynne corrector is mounted on prime focus which is equipped with 1K X 1K 24-micron CCD camera, with a gain of 5.9 e/ADU and readout noise of 8-9 e. The FOV is 10 X 10 arcmin with a scale of 0.6 arcsec/pixel. (ii) Medium resolution Optometrics Research Spectrograph (OMRS) is mounted on cassegrain F/13 focus. (iii) Fiber-fed echelle spectrograph is located in a separate chamber which is connected through a fiber from prime focus.

OMR spectrograph was designed and built by the Optomechanics Research Inc., Vail, Arizona, USA which is available at the Cassegrain focus of the 2.3m VBT (Prabhu et al. 1998). It has a 25 mm long slit with a minimum width of 40μ and a maximum width of 950μ. There is a set of four gratings which can be manually changed as per requirement. Short and long camera focii are available, both with clear aperture of 100 mm, with focal length 150 mm and 450 mm, respectively. Gratings available are : 150 l/mm with R ~ 21.2 and 8.0 , 300 l/mm with R ~ 10.6 and 4 , 600 l/mm with 5.3 and 2.0 , and 1200 l/mm with 2.7 & 1.0 . It has two wavelength comparison sources, Fe-Ne and Fe-Ar, and one flat-field, Tungsten-Halogen Quartz lamp.

The centering of the objects on the slit and guiding on or off the slit is accomplished by a peltier-cooled Star I CCD with liquid circulator which can achieve an operating temperature of -40 C nominally. The CCD system obtained from Photometrics Ltd., Tucson, has a scientific grade Thomson TH7883 chip of 23 μ pixel size and 384 X 576 format.

Fiber fed echelle spectrometer for the VBT is designed, built and commissioned in 2003. The spectrometer sits on a vibration isolation optical table and housed in a separate enclosure called coude laboratory, and linked to the VBT with the help of optical fibre of 100μ core size. It has an echelle grating which works at a large blaze angles (theta of 63 to 70 degrees) operated in higher diffracted orders and hence the spectrometer achieves higher resolution (R~ 30,000 - 105,000) with large wavelength coverage from 4000 to

10000 Å. It has a CCD chip of 12μ pixel size and 4K×4K format. It has an adjustable slit from 30 to 100μ. The optimum resolution of the spectrograph is set for R~ 70,000 (~ 4 km s^{-1}) by keeping the slit width of 60μ.

2.7-m Harlan. J. Smith Telescope

Harlan. J. Smith Telescope (HJST) was constructed between 1966 and 1968 with 2.72-meter (107-inch) mirror, which was the third largest telescope in the world when it was bulit. It was installed at McDonald Observatory located atop Mount Locke and Mount Fowlkes in the Davis Mountains of West Texas, which offers significant number of dark nights in any year. It has Ritchey-Chretien optics with prime and cassegrain focus: F/3.93, F/8.8 and F17.7. The coude focus is at F32.5. The telescope is equipped with three science instruments at cassegrain and coude focus. The instruments that are mounted on cassegrain F/8.8 Ritchey-Chretien focus are: (i) Visible Integral-field Replicable Unit Spectrograph - Prototype (VIRUS-P) (Hill 2008) offers low (5.3)to moderate resolution (1.0 Å) spectra for multiple objects in a 2.82 square arcmin field of view. The wavelength coverage of the instrument is 3400 - 6850 Å. The IFU consists of 246 fibers and the spectrograph have four gratings. (ii) CCD WHT Camera is the only instrument which offers CCD imaging in usual optical-band filters. (iii) Imaging Grism Instrument (IGI) has two modes: imaging and spectroscopy. It has a grism which covers wavelength range from 0.4 to 1.0 micron at low resolution (12-20 Å).

There are two science instruments available at coude F32.5 : (i) Tull spectrograph (TS1), which has two separate foci available for two cameras, 6-foot camera (TS11) and long focus camera (TS12). It has five gratings and two echelles covering 0.3 to 1.2 micron for variety of resolutions. The maximum resolving power for TS11 and TS12 are 200,000 and 400,000. (ii) Cross-Dispersed echelle spectrograph (TS2), which we used for our observations, is a high resolution spectrometer. The high-resolution spectra (R=60,000) for a few fainter stars have been obtained using coude cross-dispersed echelle spectrometer which is mounted to 2.7 m Harlan J. Smith Telescope in McDonald Observatory, USA. The spectrometer is available with TK3, a thin, grade 1, Tektronix 2048 x 2048 CCD. Two-pixel resolving powers in its two modes of operation are 60,000 and 240,000. Two echelle gratings offer minimum inter-order separations of 10.5 and 15.5 arcsec. At R=60,000, data from the full bandwidth of 3,400 - 10,900 Å are collected with the TK2048 CCD in as few as two exposures.

2.1.2 DATA ACQUISITION

Astronomical observations of night sky needs attention and patience. Observations of our program stars were carried out during 2006-2010 using the above facilities. Observational setup including the quality of the image are checked in the day time by taking the lab (comparison) spectra and solar spectra before every observations. The images that are acquired during the observations are calibrated frames, comparison frames, program star frames, hot star frames, and standard star frames. The calibrated frames are basically, bias, dark and flat. (i) A Bias frame is the raw CCD frames taken with no light incident upon the detector implies "Zero" exposure time. (ii) A dark frame is an exposure taken under the same conditions as the light exposure, but with no light striking the detector (ii) A Flat frame is one illuminated with some uniform source on the detector, used to determine the relative sensitivity of the pixel elements. Tungsten and halogen lamps are used as source for flat. (iii) Comparison frames are the spectra taken from known source, typically an arc lamp, which are used as a reference for modeling the pixel number to wavelength scale. Fe-Ne, Fe-Ar, and Th-Ar lamps are used as a source for comparison. (iv) Standard stars are known stars whose atmospheric parameters are well studied which are used as reference for flux calibrations and to check radial velocity variation in program stars. (V) Hot star is basically an early spectral type star whose rotational velocities are in the order of 100 to 300 km s^{-1}. The photospheric lines of stars are smeared out due to high rotation and the absorption lines from our earth atmosphere is present in the spectra. This spectra can be used to remove the telluric contamination in program star spectra.

Normally one takes a large number of calibration and comparison frame in a given night at regular intervals to improve the statistical importance of calibration frames. Examining of the frame would suggest performance of the detector and the spectrograph. In a given night couple of hot stars were observed for identification and removal of telluric lines from the program stars spectra.

2.2 DATA REDUCTIONS

The raw two dimensional spectra are recorded on a CCD and stored in a digitized format, called FITS (Flexible Image Transport System). The data storage of the present CCD processors are in 16 bit file format, which is a binary file that can save 2^{16} bytes of instructions. There are two types of formats in which digitized data are saved: (i) SHORT holds signed 16 bit/pixel (2-byte) integers in value from -32,768 through 32,767. (ii) USHORT holds unsigned 16-bit/pixel (2-byte) integers ranging in value from 0 through

65,535. It cannot represent a negative value. The spectra acquired from VBT and CZT are saved as SHORT format whereas HCT spectra is in USHORT format.

Image reduction fixes the small defects in the CCD and optical system. Proper calibration is of much importance in producing good quality images. CCD sensors operate for a fixed voltage level (bias), sensitivity to temperature (dark current), and sensitivity to light. These effects not only vary from CCD to CCD but also from pixel to pixel in the same CCD. Each of these effects corrupts the intensity represented in every pixel of the image in a specific way. The variations due to these effects can be removed from the proper calibration. The three basic calibration steps are bias, dark, and flat-field.

Bias is an offset that occurs when a pixel is read from the CCD. Unfortunately, bias can vary across the image. Each pixel will have a slightly different value, but except for a small amount of noise, the value for any one pixel will be consistent from image to image. Since the bias is consistent from image to image it can be subtracted. The bias frame itself contains a small amount of readout noise. This readout noise is produced inside the electronics that read the pixels. This noise can be easily suppressed by combining a number of bias frames together. It is possible to perform accurate calibration using dark frames and without using bias frames. Every camera detector produces a certain amount of dark current, which accumulates in the pixels during an exposure. The dark current is produced by heat. The main problem with dark current is that it accumulates at a different rate in every pixel. Some pixels are ”hot” and others are ”cold”. The effect of hot and cold pixels can be easily removed by subtracting a dark frame from the program frame by pixel-by-pixel. The hot pixels which are not able to be removed by dark frame can be replaced with the average of the surrounding pixels. Each pixel in the camera has a slightly different sensitivity to light which adds another noise component to the image known as flat-field error. The flat-field frame is renormalized by dividing each pixel into the average value in the array. Any pixel that is more sensitive will be assigned a number slightly below 1; any pixel that is less sensitive will be assigned a number slightly above 1. When this frame is multiplied by a raw image, it removes the sensitivity variations.

IRAF is a general Image Reduction and Analysis Facility provides a wide range of image processing tools to process the raw two dimensional data into a one dimensional data for further analysis. IRAF is a product of the National Optical Astronomy Observatories (NOAO) and was developed for the astronomical community. IRAF contains various packages to process the image. We briefly describe here the data processing using IRAF below.

IRAF

Low resolution spectroscopic data are acquired in long slit mode and high resolution spectra in narrow slit mode. The basic reduction procedures are same for low and high resolution spectra. The only difference is removing scattered light from high resolution spectra. The basic steps and the tasks that are used in processing the raw spectra are given below.

The data in USHORT format are unsigned using *chpix*. Bad and hot pixels are removed using *ccdproc*. Noise dominated edges of the image are trimmed using *ccdproc*. These steps are required for initial processing and are performed for all the frames. Now all the frames are corrected for dead pixels and noise dominated edges. The next step is to remove the CCD characterstics.

Bias frames are combined to create master bias using *zerocombine*. Bias is removed from the rest of frames using two methods: mean counts are subtracted using *imarith* and subtracted frame to frame using *ccdproc*. We found frame to frame subtraction is the best way to remove bias as it performs pixel to pixel operation. Bias subtracted flat frames are added to create master flat using $flatcombine$. The master flat frame is corrected for scattered light using $apscatter$. To process this task, the reference apertures are required, so apertures of a bright star are selected using $apall$. Scattered light corrected master flat is normalized using $apflatten$. Flat field correction is applied to all the object frames by dividing with normalized flat using *ccdproc*. The scatter light also modeled and removed from the object frames using $apscatter$. Further, the raw data is processed from two dimensional spectra to one dimensional spectra.

The information is extracted from the raw spectra using $apall$. Previously selected apertures are used as reference and traced the orders by fitting poynomials. The extracted spectra contains counts vs pixels. Thus, pixels are converted into wavelengths by using the arc spectra for which the rest wavelengths are known. Bias subtracted arc frame is extracted using $apall$. The spectral lines in the arc spectra are identified using $identify$ (for single order spectra) or ecidentify (for echelle spectra) with the help of available identification charts. We fit the polynomials or splines to the identified points and found out the errors in the identification which are less than 10% per pixel. Using the above wavelength identified/calibrated arc spectra as a reference using $refspec$, the object frames are corrected for the dispersion using $dispcor$, and hence the spectra are wavelength calibrated. The continuum of these spectra are modeled using *continuum*. The final continuum fitted spectra are corrected for the telluric lines contamination (due to earth atmosphere) using *telluric*.

2.3 DATA ANALYSIS

The spectral line can be used to understand various parameters in stellar atmospheres which are: temperature, surface gravity, radial velocity, rotational velocity, chemical composition, ages, etc. One would extract information such as temperature, surface gravity and composition by analysis the relative intensities of various line profiles combined with the radiative transfer computer codes and stellar atmospheric models. Radial velocities are measured by measuring the actual shift of the line profiles relative to the rest wavelengths of those profiles. Rotation measurement are a bit cumbersome to measure which require information such as abundance and instrument contributions, also line profiles get broadened by things like magnetic fields (Zeeman broadening), microturbulence and macroturbulence. All of these parameters are further discussed elsewhere in this study.

The radial velocity of a star is measured using the shift as given below:

$$\frac{\Delta\lambda}{\lambda_c} = \frac{v}{c} \tag{2.1}$$

where $\Delta\lambda$ = λ_c - λ_o, λ_c is rest wavelength and λ_o is observed wavelength. c is the speed of light and v is the light of sight velocity.

In the case of rotational velocity, one would measure FWHM of a line which includes all the effects which are mentioned in the above para. Rotational velocity can be measured from the FWHM of the line using the equations,

$$W_s = \sqrt{FWHM^2 - W_i^2} \tag{2.2}$$

where W_s is intrinsic stellar broadening and W_i is instrumental broadening. Now it is in Å and it can be converted into km s^{-1} by solving the polynomials,

$$W_s = 0.04082 + 0.02509X + 0.00014X^2 \tag{2.3}$$

where X is equivalent of W_s in units of km s^{-1}. The rotational velocity of the star then calculated from the equation,

$$v = \sqrt{X^2 - {v_m}^2} \tag{2.4}$$

where v_m is macroturbulance.

EQUIVALENT WIDTH

For the current study extraction of the composition is the principal aim. This information is coded in the spectral line strength which in the abundance studies is known as equivalent width with units in Å. The equivalent width is defined as the width of a rectangular spectral line whose area is equal to the integrated area of a spectral line below the continuum flux level (See Figure 2.1). In the Figure, λ_0 represents the central wavelength of the spectral line. The width of the rectangle represents the Full width at half maximum (FWHM) of a spectral line. The definition is as follows:

$$W_\lambda = \int_{line} \frac{F_{\lambda_c} - F_\lambda}{F_{\lambda_c}} \tag{2.5}$$

where W_λ is the equivalent width for a given λ and F_{λ_c} is the continuum flux.

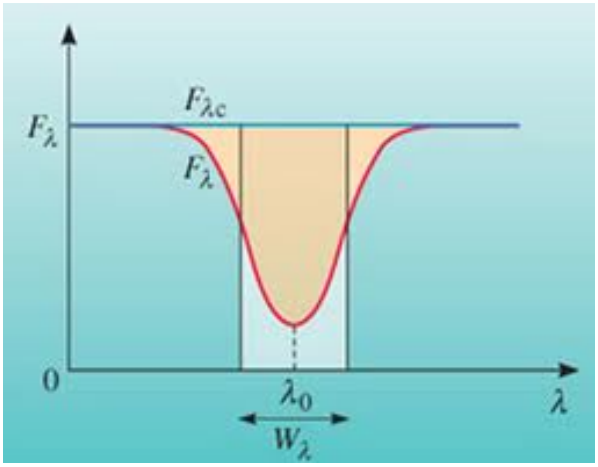

Figure 2.1: Equivalent width of a spectral line

The spectral line information (λ_o, FWHM, and W_λ) in the observed spectra are measured using the two most suited options depending on the situation of the spectral profile: SPLOT task in IRAF and/or GAUSSFIT subroutine in IDL. The isolated and clean lines are measured by fitting the single gaussian profile. In some cases, multiple guassian profiles are computed to deblend the contaminated profiles in the required observed profile. In case of few lines we measured area under the curve of a line profile directly. The final equivalent widths considered for the analysis are from the mean of two measurements.

The equivalent widths are used to obtain atmospheric parameters and chemical composition of star. Star's T_{eff}, microturbulance, abundance can be obtained from this equation.

$$log\left(\frac{W_\lambda}{\lambda}\right) + log(\frac{v}{c}) = log(gf\lambda) - \left(\frac{5040}{T_{exc}}\right)\chi_l - 1.826 + log(N) - log(\kappa_\lambda U(T)v) \quad (2.6)$$

where $v^2 = 2KT/m + \xi^2$, ξ is microturbulence. The λ is central wavelength of a given spectral line and W_λ is the equivalent width of a given λ which are measurable quantities from the spectra. gf is oscillator strength and χ_l is lower excitation potential which are atomic data of given spectral line. U(T) is a partition function and κ_λ is opacity which are distribution function parameters. T_exc is excitation temperature and N is the number of atoms which are atmospheric parameters.

The Saha ionization is used to measure the ionization temperature and surface gravity,

$$log\left(\frac{N_1}{N_0}\right)P_e = 2.5log(T_{ion}) - \frac{5040}{T_{ion}} + log\left(\frac{U_1}{U_0}\right) - 0.1762 \quad (2.7)$$

Where N_0 and N_1 are the abundance of particular element in ground state and first excited state,respectively. U_0 and U_1 are the partition function of corresponding states. T_{ion} and I are the ionization temperature and ionization potential, respectively. P_e is the electron pressure which is proportional to gravity ($g^{1/3}$).

At present, the radiative transfer codes are available where these basic equations are incorporated by assuming the stellar atmospheres in LTE conditions. Determination of atmospheric parameters and chemical composition using radiative transfer codes required atomic data and model atmospheres. A brief description of each tool is given below.

2.3.1 ATOMIC DATA

The spectral lines are principally characterized by three quantities: their wavelengths associated spectroscopic classifications; the energies of their upper and lower atomic levels; and their oscillator strengths or atomic transition probabilities. The spectral lines that are formed in the dense gas or plasma depend on additional quantities : line shape and line shift parameters. Of the three principal quantities, atomic transition probabilities are much less known than either wavelengths or energy levels. Even for a small percentage of lines for which they are reliably known, the accuracy of the available transition probability data is usually not very high and a number of discrepancies between various data are encountered.

The spectral lines of Iron, neutral and singly ionized, are abundant in the entire optical region of the spectra for which atomic data with accurate log gf values are available in

the literature: Fuhr & Wiese (2006), NIST database, VALD database, etc. In this case, we have freedom to choose isolated and clean absorption lines which are suitable for measurements. For the other elements, due to scarcity, we chose the lines with good atomic data.

2.3.2 MODEL ATMOSPHERES

The atmosphere of a star is defined as the layer that is sufficiently close to the surface that some photons can escape. It is a transition from dense stellar interior to interstellar medium. The primary layers in the stellar atmosphere are, photosphere, chromosphere, corona, and stellar wind. The atmosphere is the region that produces the stellar spectrum. The physical depths in the atmosphere where the spectral features form depend on the atmospheric conditions: temperature, density, level populations, optical depth etc. The theory of stellar atmospheres involves constructing models of the photosphere that take into account the effective temperature, T_{eff}, gravity, g, and elemental abundances. The assumptions and limitations in the model atmospheres are:

- The thickness of the photosphere is much lesser than the radius of the star, and hence plane parallel geometry. The gravity also constant through out the photosphere. The optical depth ($\tau \sim$ infinity) is deep in the atmosphere and $\tau \sim 0$ at the photospheric surface. The plane-parallel approximation breaks down for luminous, low surface gravity stars, with extended envelope atmospheres.
- The atmosphere is homogeneous and hence ignores the structures like granulation, starspots etc.
- The outward pressure gradients exactly balances the gravity and hence hydrostatic equilibrium.
- It is in a steady state so the properties do not change with time. The equation of radiative transfer is independent of time. The atoms and molecules are in statistical equilibrium. Models assume no rotation, pulsation, expanding envelopes, winds, shocks, and variable magnetic fields etc.
- All energy transport by radiative processes and hence radiative equilibrium. Transport by convectionis neglected. Also, neglects the hydrodynamic effects. But there is much evidence for the existence of velocity fields in the solar atmosphere and mass motions, including convection, are significant in stellar atmospheres, particularly in luminous giants.

- Under LTE, all the microscopic processes are in detailed balance and the densities of energy states are calculated from the Maxwell, Boltzmann, and Saha relations.

An extensive grid of stellar photospheric models was calculated using the ATLAS9 stellar atmosphere code which was originally written and developed by Robert. L. Kurucz (Kurucz 1970, 1993). The grid covers a range of effective temperatures from 8000 K to 35000 K at steps of 250 K and a range of surface gravities (log(g)) from 2.25 dex to 6.25 dex at steps of 0.25 dex. ATLAS9 makes a standard set of assumptions, that are described above, in modeling. The models were calculated using the standard solar metallicity ODFs (Opacity Distribution Functions). The abundances of each model are explicitly set to the solar values for each element. Overall, the differences between the models calculated at [M/H] = 0 versus other metallicities are not very significant to make any difference in the abundance analysis. This version of the ATLAS9 code employs the Castelli et al. (1997b,a) convection correction. All models were calculated with a constant microturbulent velocity. A velocity of 5 km s^{-1} was used in models hotter than 9000 K and a velocity of 2 km s^{-1} was used in cooler models. A lower value was employed in the cooler models because higher values exceed the thermal velocity of hydrogen in the upper layers of the model, causing instabilities. The microturbulence value used to calculate the models does not significantly perturb the abundances calculated from equivalent widths.

2.3.3 MOOG

The study of chemical composition include both Fine analysis and Spectrum Synthesis methods depending on the quality of available data. Equivalent widths were converted to abundances in Fine analysis and line profiles were synthesized to fit the observed profiles in spectrum synthesis method. In this analysis, we used the updated version of LTE raidative transfer code, MOOG which was originally written and developed by Sneden (1973) for his PhD thesis. The version of the MOOG code used is optimized to work with cooler G and K stars. The detailed description of these codes and methods can be found in Chris. Sneden thesis and in a review article by Castelli & Hack (1990). We briefly describe here each of these methods.

FINE ANALYSIS

The method consists of comparing the measured equivalant width of a given line with the equivalent widths calculated for a given atmospheric model and atomic data. The subroutine, abfind, in MOOG solves the radiative transfer problem for spectral lines under

the LTE assumptions and calculates the equivalent widths for a given stellar atmospheric model. MOOG requires the atmospheric model and linelist as an input. The linelist consists of wavelength, ion information, excitation potential, oscillator strength/log gf value and measured equivalent width. For a given stellar model, abundance is modified until the computed equivalant width matches with that of observed equivalent width. This can be achieved by many iterations with some prefixed step value (e.g. 0.1 dex). Weak and moderate lines would be best for the determination of abundances because their equivalent widths are not affected by microturbulance and damping constants.

SPECTRUM SYNTHESIS ANALYSIS

This method consists of comparing the observed spectrum with that of the computed spectrum. In this method, fluxes are computed for closeby λ values with similar resolution as the observed spectrum which allows the direct comparison. In this synthesis, broadening mechanisms like microturbulance, instrumental broadening, limb darkening, rotational broadening and macroturbulance should be taken into account. Instrumental broadening can be represented by a guassian profile, which has the same FWHM as the instrumental profile that convolved with the observed spectrum. Macroturbulance, the large scale structures in the stellar atmospheres, is a random distribution but it can be simulated by gaussian. The rotational broadening can be taken into account by computing the Doppler shifts of the intensities coming from the different parts of the stellar disc and then integrating the Doppler shifted intensities to obtain the flux. The emergent intensity decreases from the center of the disc to the limb, known as limb darkening, can be calculated from the available empirical relations. The spectrum synthesis calculations require extensive linelist for a given region. The synthesis of a particular element requires the data of different ionized states, with accurate laboratory wavelengths, excitation potentials for lower and upper levels, and reliable transition probabilities (gf-values), and broadening parameters. A large database for both atomic and molecular lines is available from the pioneering work of Kurucz & Bell (1995).

Spectrum synthesis analysis has some advantages over fine analysis in chemical composition studies. The comparison of computed spectrum with the observed spectrum makes it possible to derive line micro and macro-turbulance, projected rotational velocity, Doppler shifts and abundances from single and blended lines. The continuum level in the observed spectra can be better estimated, particularly, in case of stars with rapid rotation and cool stars whose spectra with numerous metallic lines. The computed spectrum is used to confirm abundances of blended lines obtained with the fine analysis because the

comparison of profiles gives much more information than the comparison of equivalent widths.

We have used the "synth" subroutine in the line synthesis code, MOOG, for computing the synthesis spectra in our abundance analysis. The inputs to the MOOG are as follows: stellar atmospheric model, abundances of relevant elements, beginning and end points of the required region, step size (in wavelength) in the spectrum, width of the spectrum to be considered at each point and atomic data similar to fine analysis but without equivalent widths. For the given inputs, MOOG calculates continuum flux, point by point, separated by a given step size. The abundances are estimated from MOOG to run for several times by adjusting the input abundances of elements until the computed spectrum matches that of observed one.

ATMOSPHERIC PARAMETERS

The atmospheric parameters, T_{eff}, log g, and microturbulance, are obtained using fine analysis method by modifying the model atmospheres to satisfy the three constrains:
(1) Minimize the slope of A(Fe I) versus W_λ/λ which determine the microturbulance (ξ_t) because the adopted ξ_t has a significant effect on the abundances derived from the equivalent width of the lines. The strong lines which suffer from saturation has more effect compared to weaker lines. Therefore, we set the microturbulance of model atmosphere where the lines with the range of equivalent widths include moderate and strong show no trend.
(2) Minimize the slope of A(Fe I) versus LEP which is sensitive to the effective temperature because the predicted population in various excitation levels is a function of the excitation temperature of the stellar atmosphere
(3) The median values of A(X I) and A(X II) are equal for the requirement to maintain ionization equilibrium (e.g. A(Fe I) = A(Fe II)) which is sensitive to gravity .

METALLICITY

In astronomy, the elements that are heavier than helium are called metals. The measure of the proportion of metals that a star contains is called Metallicity. Iron is the most abundant heavy element among all the metals and is easily measured in the optical region of the spectra and hence metallicity is often referred as the relative amount of iron and hydrogen present in the star compared with solar values. Metallicity is denoted as [Fe/H] and is calculated from the following logarithmic formula.

$$[Fe/H] = log(Fe/H)_{\star} - log(Fe/H)_{\odot} \tag{2.8}$$

where $[Fe/H]_{\odot} = 0$. For example, if the metallicity [Fe/H] = -1 then the abundance of heavy elements in the star is one tenth that found in the Sun; if [Fe/H] = +1, the heavy element abundance is 10 times the solar value.

2.4 OTHER RESOURCES

There are few other resources which are extensively used in this thesis that are given in brief as follows:

HIPPARCOS CATALOG

HIPPARCOS is an acronym for High Precision Parallax Collecting Satellite. Hipparcos satellite mission was launched successfully in August 1989. It observed the celestial sphere for 3.5 years before the mission ended in March 1993. This was the first space mission dedicated to astrometry. Calculations from observations by the main instrument generated the Hipparcos Catalogue of 118,218 stars charted with the highest precision. An auxiliary star mapper pinpointed many more stars with lesser but still unprecedented accuracy, which are given in the Tycho Catalogue which consists 1,058,332 stars. The Tycho 2 Catalogue, completed in 2000, brings the total to 2,539,913 stars, and includes 99% of all stars down to magnitude 11.

Accurate measurements of the positions of stars, parallaxes and proper motions are obtained for more than 100 thousand stars from Hipparcos and released the entire data as a catalog in 1997. The data with new reduction techniques which improved the accuracy in errors in the parallaxes. The revised parallaxes were released in 2008.

EVOLUTIONARY TRACKS

The evolutionary tracks are available with Padova and yale-yonseii (YY) groups. Padova tracks computed by Girardi et al. (2000) and Bertelli et al. (2008) are used. Y2 tracks computed by yale group (Yi et al. 2003) are also used. Padova tracks have the data of the bump whereas no such data is in Y2 tracks. We utilized all these three evolutionary tracks in this study.

PUBLIC RESOURCES

This research was made use of material available in the public resources that are following: (i) the SIMBAD Database , VizieR Service, and Catalogs (access to astronomical catalogs), operated at CDS, Strasbourg, France. (ii) The SAO/NASA Astrophysics Data System (ADS), which is a Digital Library for Astronomy and Physics, operated by the Smithsonian Astrophysical Observatory (SAO) under a NASA grant. (iii) Two micron all sky survey (2MASS), which is a joint project of the University of Massachusetts and the Infrared Processing and Analysis Center/California Institute of Technology, funded by the National Aeronautics and Space Administration and the National Science Foundation. (iv) Hipparcos Catalog, data collected from the Hipparcos space mission, funded by European Space Agency (ESA). (V) The Infrared Astronomical Satellite (IRAS), which is a joint project of the US, UK and the Netherlands. (Vi) IRAF is the Image Reduction and Analysis Facility, a general purpose software system for the reduction and analysis of astronomical data. IRAF is written and supported by the IRAF programming group at the National Optical Astronomy Observatories (NOAO) in Tucson, Arizona. NOAO is operated by the Association of Universities for Research in Astronomy (AURA), Inc. under cooperative agreement with the National Science Foundation.

CHAPTER 3

SURVEY FOR LI-RICH GIANTS

3.1 INTRODUCTION

Li-rich giants are a rare group of stars. There are just about two dozen low mass K- and G- giants that are known to have an anomalously large amount of Li. Many of these were discovered accidentally (Hanni 1984). It was the study by Wallerstein & Sneden (1982) which pointed out the unexpected excess of Li in a typical RGB star HD 112127. Li excess in this giant is about 100 times more than the value one would expect from the standard theory of stellar evolution and mixing on RGB. The excess, they thought could be due to internal synthesis via Cameron & Fowler (1971) mechanism, and some sort of mixing. They have also pointed out that the suggestion of linking of excess Li to the planet engulfment (Alexander 1967) is an unlikely scenario. since then, solutions to origin of Li in giants remained largely very speculative. The main reason for that being the lack of sufficient observational data to understand various possibilities.

To address the issue, Brown et al. (1989) initiated a first systematic survey to find out a more number of Li-rich giants among 644 K- and G- giants. Their high resolution spectroscopic survey resulted in about 10 Li-rich giants which demonstrated the rarity of Li-rich giants in the solar neighborhood. Other important survey was the Pico Dias survey (PDS) by Gregorio-Hetem et al. (1993) which resulted in half a dozen Li-rich K giants (Reddy & Lambert 2005). Originally, their survey was meant to study Li profile in T Tauri stars. Though the post survey resulted in a good number of Li-rich giants, it lacked the uniformity and selection criteria that could be used to draw statistical conclusions such as a number fraction of Li-rich giants, Li correlation with other properties etc. Also, the above surveys were pre-Hipparcos leading to uncertain luminosities. As a result sample stars were contaminated by a large number of intermediate mass giants, AGB stars etc.

Also, the PDS survey was based on a sample of stars that have far-IR (IRAS) colors similar to pre-main sequence T Tauri stars. Obviously, the selection bias in the sample might have led the authors to suggest that Li excess and the IR excess are correlated. Also, some Li-rich K giants were found to have much larger rotational velocities (> 8-10 km s^{-1}) than the expected values for typical K giants (about 2 km s^{-1}). It has to be seen how the three observational properties: high Li, IR excess, and high rotation are related to each other. Or is it pure coincidental that all the three anomalous properties exist in some of the Li-rich K giants (Brown et al. 1989; Balachandran et al. 2000) Establishing such correlations will constrain theoretical modeling and help to understand the underlying physics for the excess Li and also other properties.

This requires a systematic and a well defined survey for Li-rich K giants. Hipparcos space mission was launched to measure accurate astrometry for about one lakh stars, and its full data was made available in 1997 (Perryman et al. 1997). Unfortunately, no systematic survey was taken up by any group in the post-Hipparcos period. Given the number of speculative ideas for the origin of excess Li in K giants, it became important to venture into such an uniform study to find clues about their origin. Understanding of Li in K giants also has other broader implications such as understanding the stellar structure and evolution of RGB stars, evolution of Li in our Galaxy, and the actual production of Li at the time of big bang. This study may not address all of these implications but concentrate on finding clues for its origin.

For the above mentioned reasons, we thought that the study of a controlled but unbiased survey sample of K giants would not only increase the number of K giants but also constrain different theoretical ideas for the Li excess in K giants. Therefore, we have set the following goals for the survey:

a) Adding significant number of Li-rich giants to the existing sample

b) Gathering enough evidence to support or against the hypothesis that the planet engulfment could enhance surface Li in K giants

c) Establishing the location of Li enhancement in K giants along the RGB in the HR diagram

d) Establish the fractional content of Li-rich K giants in the Galaxy

e) Understanding the relation among Li excess and other anomalies such as high rotation and infrared excess

f) Study of Li excess and its trend with other abundances like C, N, O and ^{13}C

In this chapter, we describe a set of criteria for selecting stars for the survey and an observational strategy to complete the study within a stipulated period of time for my doctoral thesis. Also, methodology of determining Li from low resolution spectra and some statistics are presented.

3.2 SAMPLE SELECTION

One of the challenges was to choose the right source catalog for sample stars. The Hipparcos (Perryman et al. 1997) catalogue contains about one hundred thousand stars for which very accurate (milli arcsecond) astrometry is available. Also, the catalog is complete upto a brightness of about 9^{th} magnitude. For each star, in the catalog, parallax, proper motion and the associated errors are provided. Also, information such as color (B-V), magnitude (V), and coordinates are available. Given the parallaxes and magnitudes, and color one could derive luminosities and effective temperatures ($T_{\rm eff}$), respectively, which are the most important parameters for the sample selection. Note that samples are field stars, and since the Hipparcos is a space mission, catalog contains stars covering both the northern and southern hemispheres.

In the beginning, sample stars were taken from the original Hipparcos catalog (Perryman et al. 1997). The catalog was later revised with better reduction and calibration techniques. Revised version (van Leeuwen 2007) was made available to public in 2007. By this time, we had started obtaining spectra for the selected samples from the original catalog. The data from the two catalogs of the survey sample were compared and difference in errors as large as 50% were found, and also, a small but non-negligible difference in the mean values of parallaxes and proper motion between the two catalogs was found. We have applied our selection criteria to the new revised Hipparcos catalog and re-selected the sample. As a result, about one fourth of the survey sample had to be re-observed to ensure all stars in the study were within the limits of our criteria.

The following criteria were applied to the Hipparcos catalog for sample stars selection: a) Stars of luminosity, log ($L/L_{\odot}$), from about 1.0 to 2.5 covering giants all the way from the base of the red giants to the well beyond the RGB bump, b) Stars with color (B-V) from 0.9 to 1.4 which translates to late G- and K-spectral types. The two criteria yielded about seven thousand giants. More conditions were applied to reduce the sample further and make it well defined: c) Stars with parallax (π) errors less than or equal to 20% were chosen, and majority of the sample stars have π with 10% error or less. This would minimize positional uncertainties in the HR diagram, d) Restrict of the samples

to distances upto 200pc to minimize uncertainties in color due to unaccounted interstellar extinction, e) Samples were restricted to magnitudes V~8.5 or brighter to avoid large errors in parallax and also to make it easy for the observations, f) Stars with declination from −60 to +80 deg were chosen to fit observing program with the facilities located at +32 degree north (2-m HCT) and +12 degree north (1-m CZT and 2.34-m VBT) latitudes, and finally, g) We have culled all the stars with mass greater than $3M_{\odot}$ and less than $0.8M_{\odot}$. We have done this by plotting computed stellar evolutionary tracks in the HR diagram and superposing the selected sample stars. The above criteria resulted in 2000 giants. A representative list of the main list is provided in Table 3.1.

3.2.1 SAMPLES ON H-R DIAGRAM

As noted earlier, positions in HR diagram represent the evolutionary stages of stars. By plotting stars and evolutionary tracks in the form of Luminosity versus $T_{\rm eff}$, one would get a fair idea of stellar mass, age, and also relative evolutionary stages. Therefore, it is important to derive luminsoity and $T_{\rm eff}$ for the entire sample stars. Since we have, for all the stars, parallaxes, apparent magnitude (m_v), and color (B-V), it is straight forward to derive $\log(L/L_{\odot})$ and $T_{\rm eff}$ using well known calibrations and a set of equations.

The basic equations used to derive luminosity are given below:

$$log(L/L_{\odot}) = 0.4(M_{bol}\odot - M_{bol}) \tag{3.1}$$

where $M_{bol}\odot$ and M_{bol} are the bolometric magnitudes of the sun and star, respectively. For $M_{bol}\odot$, we have adopted a value of 4.74 (see Allen's astrophysical quantitites (Cox 2000)).

$$M_{bol} = V_o + BC + 5log\pi + 5 \tag{3.2}$$

where V_o is the visual magnitude of a star corrected for interstellar extinction, BC is the bolometric correction and π is the parallax in arcsec. BC is derived from calibrations given Alonso et al. (1999) below:

$$BC(v) = \frac{-9.93\times10^{-2}}{x} + 2.887\times10^{-2} + 2.275x - 4.425x^2 + 0.3505x[Fe/H] \\ -5.558\times10^{-2}[Fe/H] - 5.375\times10^{-3}[Fe/H]^2 \tag{3.3}$$

where x = $log(T_{\rm eff})$ - 3.52, [Fe/H] is the metallicity of a star.

$T_{\rm eff}$ is derived from (B-V) color taken from *Hipparcos* catalog, and the calibrations

Table 3.1: Basic data of a few stars in the sample survey.

HIP No	HD No	π(arcsec)	σ_π(%)	Dist	B−V	RA	DEC	V	Sptype	T_{eff}	log(L/L$_\odot$)
2081	2261	0.0385	1.85	25.9	1.11	00 26 16.87	−42 18 18.4	2.40	K0III..	4644.8	1.849
43026	74794	0.0108	7.25	92.5	1.01	08 46 02.45	−02 02 55.6	5.70	K0III:	4619.4	1.647
28417	40460	0.0069	13.18	144.9	1.10	06 00 06.05	+27 16 20.5	6.61	K1III	4758.9	1.754
12146	16295	0.0081	15.06	122.8	1.03	02 36 33.97	−14 39 24.0	6.91	K0III	4736.0	1.795
40407	69280	0.0051	11.11	196.0	1.270	08 14 56.71	−35 41 19.6	6.80	K1/K2III	4327.5	1.957
53240	94363	0.0126	3.40	79.3	0.913	10 53 25.04	−02 15 18.0	6.12	K0III	4977.7	1.353
43388	75790	0.0067	9.53	149.2	0.980	08 50 18.94	−44 43 16.1	7.50	K0III	4840.8	1.369
45439	79917	0.0145	3.72	68.8	1.084	09 15 36.76	−38 34 11.7	4.92	K1III	4643.0	1.769
6939	9033	0.0081	12.14	122.3	1.199	01 29 23.49	+25 16 31.2	6.66	K2III	4442.6	1.785
115444	220363	0.0084	8.29	119.0	1.315	23 23 04.56	+12 18 50.2	5.09	K3III	4257.7	2.139
114449	218792	0.0064	12.55	155.5	1.330	23 10 42.62	+17 35 40.0	5.68	K4III	4234.9	2.282
37901	62902	0.0122	6.72	82.1	1.378	07 46 02.16	−06 46 20.2	5.49	K5III	4163.7	1.731
5928	6319	0.0093	5.39	106	1.08	01 16 12.62	+87 08 44.0	6.20	K2III:	4588.9	1.590
75119	136514	0.0136	6.42	73.3	1.18	15 21 02.01	00 42 56.1	5.35	K3III	4456.0	1.647
22240	30790	0.0067	9.07	149.2	1.01	04 47 06.85	−59 08 13.6	6.80	K0III	4717.1	1.759
7837	10212	0.0077	11.42	129.8	0.970	01 40 49.74	+45 01 08.7	8.13	K0III	4860.7	1.095
15677	20924	0.0079	9.04	125.7	1.152	03 21 58.79	−15 27 31.4	7.26	K0III	4522.3	1.247
12070	16202	0.0061	9.91	163.9	1.122	02 35 38.44	−14 56 41.9	6.84	K0/K1III	4574.7	1.412
84455	156362	0.0087	8.66	115.3	1.187	17 15 58.92	+27 08 03.6	6.57	K2III	4462.7	1.623
46363	81841	0.0051	14.6	194.5	1.154	09 27 14.19	−33 47 28.5	7.16	K2III	4518.9	1.826
112731	216174	0.0082	6.60	121.8	1.167	22 49 46.23	+55 54 09.7	5.43	K1III	4496.5	2.034
96014	184293	0.0071	6.56	141.6	1.274	19 31 19.36	+50 18 23.7	5.55	K1III	4321.2	2.232
52338	92354	0.00635	10.79	157.4	1.315	10 41 48.31	+68 26 36.8	5.74	K3III	4257.7	2.379

given in Alonso et al. (1999). The empirical calibrations are as follows:

$$T_{eff} = \frac{5040}{\theta_{eff}} \quad (3.4)$$

$$\theta_{eff} = 0.6177 + 0.4354(B-V) - 0.00425(B-V)^2 + 0.0524(B-V)[Fe/H] - 0.1127[Fe/H] - 0.01385[Fe/H]^2 \quad (3.5)$$

We have assumed metallicity, [Fe/H] = −0.01 for the entire sample stars. There may be a few stars with [Fe/H] either much lower or higher than the value we have adopted. The extreme values of [Fe/H], say from about +0.3 to −0.5 dex, will have impact of 80 K to 120 K in $T_{\rm eff}$. Since our sample stars are nearby, effects of interstellar extinction may be negligibly small which is not taken into account either in the determination of temperature or luminosity. However, in the extreme cases of farthest stars in particular directions, we do find extinction values as large as E(B-V) = 0.03 - 0.05 which corresponds to the underestimation of $T_{\rm eff}$ by 50 K - 100 K. However, we also found large errors in the determination of extinction within the solar neighborhood. To avoid unknown uncertainties by applying small corrections, we have opted for no extinction correction to any of the stars.

Survey sample is shown in the HR diagram (Figure 3.1) in terms of log $L/L_{\odot}$ and $T_{\rm eff}$. As shown, the sample covers a wide region in the HR diagram showing the evolution of low mass RGB stars. The base of the RGB is shown as a broken red line which marks the maximum extent of convective envelope and the 1st dredge-up. The 1st dredge-up brings up the by-products of PP and CNO nuclear reactions that operate in the H-burning shell. Stars evolve up the RGB and undergo small structural changes at the RGB bump location. This is marked by a solid red line on each of the tracks. The bump position in the HR diagram depends on the mass as illustrated in Figure 3.1. Stars while going up on the RGB experience the bump in luminosity due to outward growth of He-core which pushes the H-burning shell. The outward moving H-shell encounters the hydrogen discontinuity and gets mixed with the cool hydrogen. As a result, the star experiences a sudden drop in luminosity. After a while the star reaches its equilibrium and starts climbing up on the RGB again. As a result star's evolution gets slowed down resulting in clustering of stars at a particular position in the HR diagram. This has been shown from the luminosity function (Iben 1968).

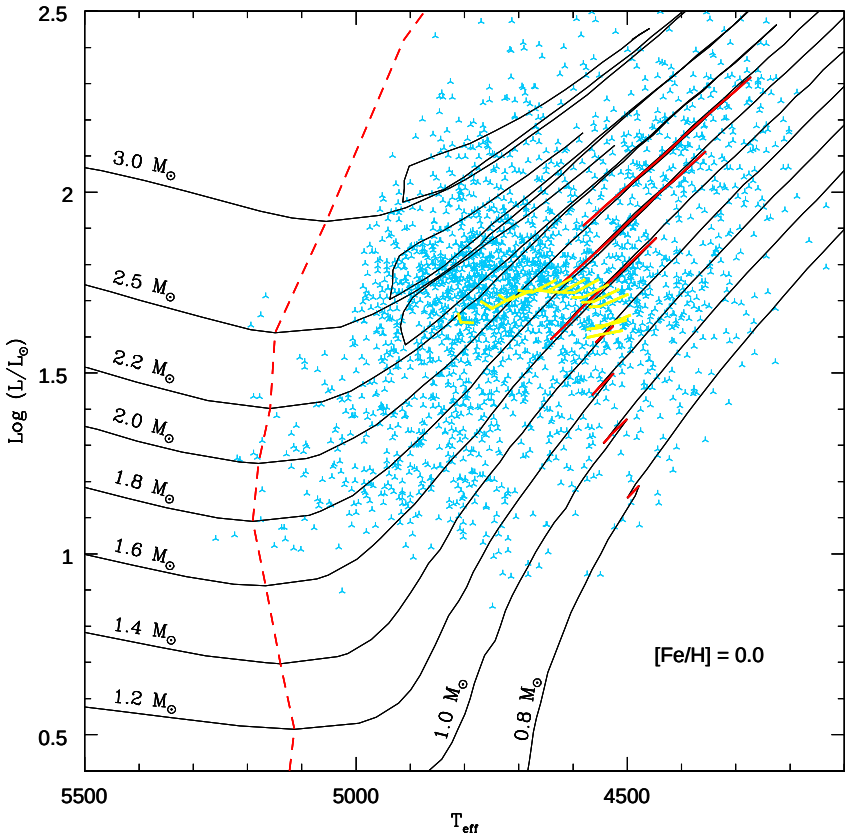

Figure 3.1: Entire sample stars of the survey are shown in the HR diagram. Evolutionary tracks of stars of masses from 0.8 to 3.0$M_{\odot}$ and of solar metallicity, [Fe/H]=0.0, computed by Bertelli et al. (2008) are also shown. The base of the RGB and the extent of RGB bump are marked as broken and solid red lines, respectively. The RGB clump region is shown as a thick yellow line.

3.3 OBSERVATIONS

A sample size of 2000 stars could be a difficult task if one has to obtain high resolution spectra. It requires a large amount of observing time on 2m class telescopes equipped with high resolution spectrographs. In India, such facility exists at VBO with 2.3-m telescope. However, clear nights are a few, and for which VBO receives a number of proposals. Given this situation, we thought of obtaining low resolution (R 2000 - 4000) spectra using spectrographs that are available on 2-m HCT, and 1-m CZT and 2.3-m VBT telescopes. The detailed description of the facilities and telescopes is provided in Chapter 2. Advantage of opting for low resolution is that we can obtain spectra relatively much faster, and also we can obtain spectra for the entire sample stars using facilities both in

northern and southern part of the country. But the disadvantage is that we will not be able to get accurate Li abundances, and also, in the low resolution, we can't have Li information in stars where Li profile is weak. We may not get the full Li distribution among the RGB stars which limits us to say something on anamolously low lithium among a group of RGB stars. Also, determination of abundances of other elements will not be possible. However, our interest in this study is primarly extracting RGB stars with excess Li and search for clues for its origin. Thus, our planned study of medium to strong Li-profile stars, and later subject, the potential high Li stars, to high resolution spectroscopy for confirmation and detailed studies is well justified.

Table 3.2: Journal of Observations

HD	RA	DEC	V	Exp time	SNR	Yr of obs
HCT + HFOSC + 67s + Gr9 + Gr11 + 1K×3K CCD						
186648	19 46 21.82	−19 45 39.2	4.87	90	250	2007
183491	19 28 57.08	+24 46 07.3	5.82	180	250	2007
198236	20 44 33.08	+69 45 06.8	6.50	260	250	2007
196912	20 39 59.83	+08 26 49.4	6.85	300	250	2007
194056	20 21 14.12	+52 24 38.0	7.61	420	250	2007
193342	20 17 00.58	+56 54 17.0	8.07	480	250	2007
224533	23 58 40.41	−03 33 20.9	4.88	100	300	2006
187614	19 49 55.81	+27 05 06.6	6.46	240	200	2007
16302	02 37 34.35	+20 34 29.8	6.92	270	200	2007
146388	16 15 28.68	+18 48 29.9	5.72	150	200	2009
22572	03 37 50.37	+00 08 28.0	7.18	360	250	2006
19551	03 09 00.94	+12 51 34.7	7.23	510	150	2006
947	00 14 22.39	+76 01 19.8	7.72	510	100	2006
1-m CZT + UAGS + 120μ + 1800lmm^{-1} + 1K×1K CCD						
23319	03 42 50.12	−37 18 48.0	4.59	900	200	2009
70002	08 18 17.39	−35 27 06.1	5.59	1200	200	2009
88399	10 10 37.70	−41 42 53.8	5.98	1500	200	2009
45984	06 27 04.14	−58 00 07.6	5.82	1800	200	2009
22663	03 37 05.68	−40 16 28.2	4.57	900	200	2006
20640	03 17 26.6	−47 45 06.3	5.84	900	150	2008
VBT + OMRS + 300μ + 1200lmm^{-1} + 1K×1K CCD						
159194	17 35 06.28	−38 47 58.3	6.76	300	300	2009
26833	04 11 58.89	−53 24 43.5	7.07	600	300	2009
77120	08 58 30.75	−50 48 25.2	7.57	720	300	2009
133904	15 09 23.25	−57 04 01.6	8.00	900	300	2009
28700	04 29 20.04	−46 30 55.3	6.13	420	350	2007

Spectra of entire sample were taken over a period of about 3 years, during 2006-2009. Our initial goal was to complete observations in over two years. However, we couldn't

accomplish partly due to sky conditions at VBO, where monsoons take away significant portion of observing time, and partly due to the revised astrometry data. The journal of observations for a sample of stars is given in Table 3.2 which contains star's identity, coordinates (RA and Dec), visual magnitude, exposure time, signal to noise ratio, and year of observations. Below, we provide a brief description of observations that were carried out with three different instruments mounted on three different telescopes.

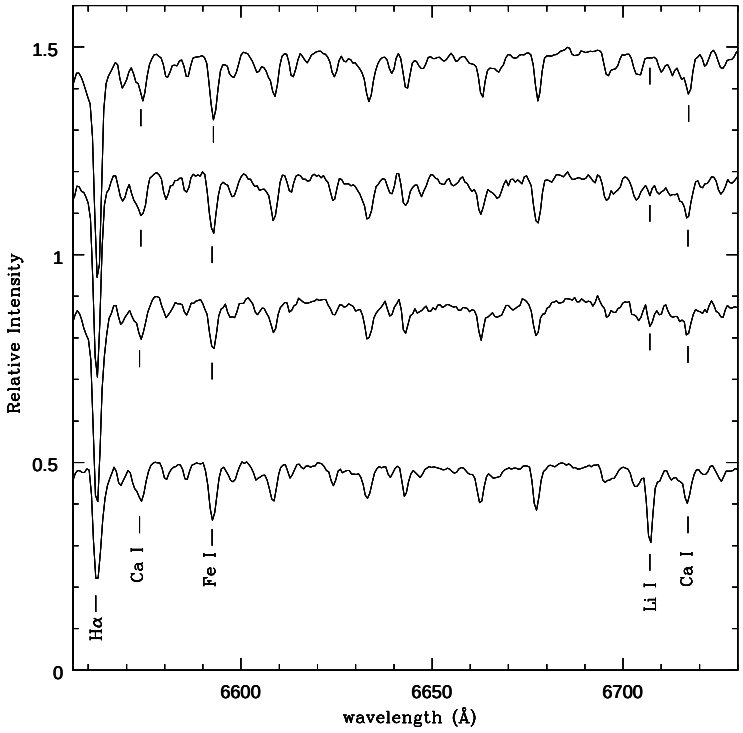

Figure 3.2: A sample spectra taken from HFOSC on 2-m HCT. Li line at 6707 Å, Ca lines at 6717 Å and 6572 Å, and Fe line 6592 Å are marked. Note the strength variation of Li line relative to other lines. All other lines including Hα vary in strength very little or no change at all.

3.3.1 SPECTRA FROM HFOSC ON 2-M HCT

Stars in the survey sample with declination between −20 to +80 deg were observed with the 2-m HCT telescope. HCT is equipped with Himalayan Faint Object Spectrograph Camera or HFOSC, a dedicated instrument for imaging and spectroscopy. It has a 2K $\times$ 4K CCD with a pixel size of 15 μ (For details see Chap 2). Spectra were obtained in Echelle mode with a combination of Grism (Gr9) and cross disperser (Gr11) combined

with slit width of 0.77″. This resulted in spectra with a resolution of R ≈ 3500 covering spectral range from 4500 Å to 9000 Å over 8 orders. Since stars are brighter we could get very good Signal-to-Noise Ratio (SNR) with exposure times as small as 5-10 minutes. All the spectra are of SNR of 200 to 300 as measured at 6700 Å.

3.3.2 SPECTRA FROM UAGS ON 1-M CZT

This aim was to obtain spectra for the entire sample stars within 2 years using the facilities that were available as the 1-m telescope. Most of the bright stars, both northern and southern stars, were observed using medium resolution Zeiss Universal Astro Grating Spectrograph (UAGS) which is available at the Cassegrain focus. Spectra were recorded on 1K × 1K CCD with a pixel size of 24 μm. We have used a grating with 1800l mm^{-1} which gives a dispersion of 0.6 Å per pixel which has a resolution of about R=5000. We have obtained spectra centered at 6700 Å which covers Ca and Hα lines apart from Li line at 6707 Å. The typical SNR for most of the spectra is about 100 or more at 6700 Å . Exposure times for a given star of same m_v is relatively much larger for UAGS compared to other two spectrographs due to its high dispersion and smaller aperture of the telescope.

3.3.3 SPECTRA FROM OMRS ON 2.3-M VBT

Other telescope that was used in this study was 2.3-m Vainu Bappu telescope (VBT) at VBO. The VBT is equipped with low resolution OMR spectrograph at the Cassegrain focus, and a Tetronix CCD of 1K × 1K with a pixel size of 24μm. We have used a grating with 1200 lmm^{-1} which gives the dispersion of 1.4 Å per pixel (R 2000) about one third of UAGS. With this resolution only strong Li profile could be detected. A few hundred spectra were obtained with the VBT and it is quite efficient with minimal overheads.

3.3.4 REDUCTIONS

Spectra were obtained with three different instruments with different resolutions and coverage, and with different modes such as echelle (orders) and long slit modes. The reduction procedure differs slightly from one set of observations to the other set. All the raw two dimensional spectra were reduced with the use of an image reduction software known as *IRAF* for *Image Reduction and Analysis Facility* developed by NOAO, USA. During observations, spectra of Fe-Ne arc lamp were obtained for wavelength calibration purpose. Fe-Ne spectrum contains a number of emission lines that have accurately

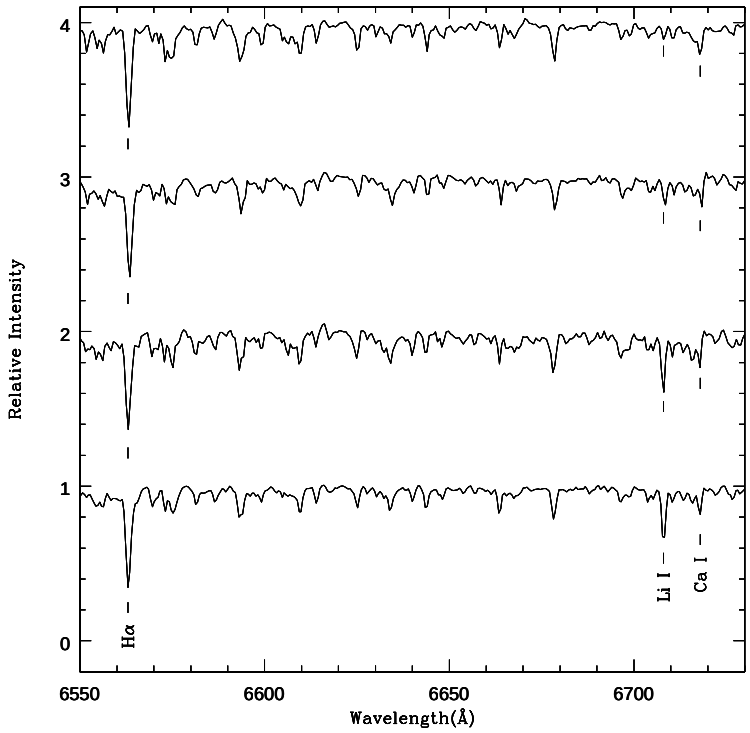

Figure 3.3: A few spectra taken from UAGS on 1-m telescope at VBO. Due to slightly higher resolution, relatively well separated lines are seen.

measured wavelengths. Also, obtained were images of dark and flat field to correct for thermal noise and pixel-to-pixel variation in the CCD, respectively.

IRAF is a full fledged software that contains number of packages with which one can accomplish all the tasks necessary to convert raw images to the one dimensional relative flux versus wavelength. As a first step, all the images were corrected for dark, and applied normalized flat images to correct for pixel-to-pixel variation. The dark and flat corrected images were reduced to one dimensional spectra, including Fe-Ne arc, using aperture extraction tools available within *IRAF*. Emission lines in Fe-Ne arc spectrum were identified and assigned wavelengths. A polynomial fit was obtained between pixel positions versus wavelength of emission features. The derived polynomial was used to convert program stars spectra into flux versus wavelengths. Two or three such polynomials were obtained for each night to see if there are any changes over the night. In general, we have found the instruments are quite stable and therefore no changes are noticed in the derived polynomials. Similar procedure was applied to all the data. Finally, to obtain relative strengths of different lines, spectra were normalized to unity i.e continuum fitting

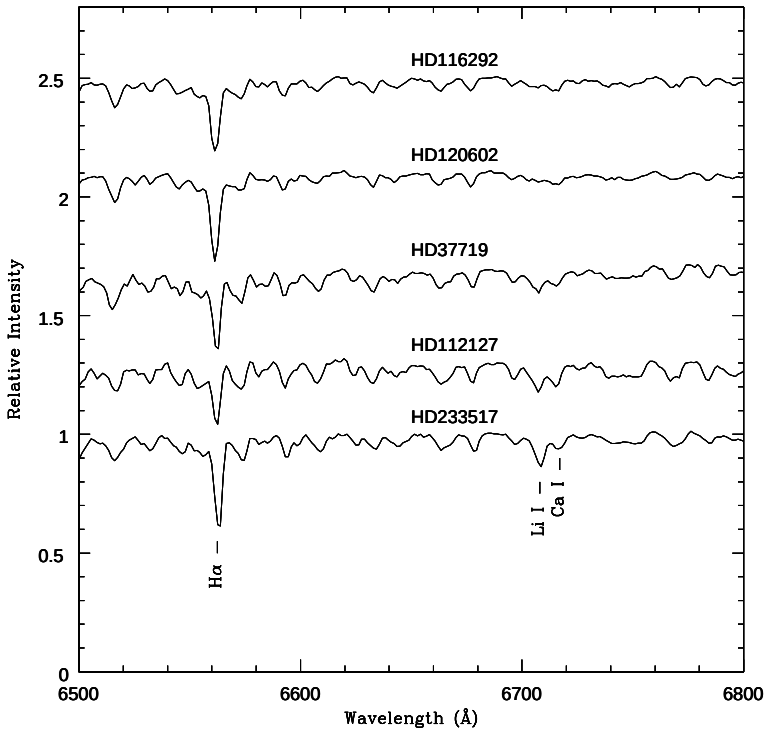

Figure 3.4: A few sample spectra taken from OMR spectrograph on 2.3-m VBT. One can easily note the effect of relatively much lower resolution (R~2000) compared to other two spectrographs. .

was done. A sample of continuum fitted spectrum of HDE 233517 obtained using all the three instruments is shown. Note that each spectrum looks different from the other. This is because of the fact that in the spectrum of relatively higher resolution lines are sharper and deeper compared to lower resolution spectra.

3.4 IDENTIFICATION OF LI-RICH GIANTS FROM LOW RESOLUTION SPECTRA

Now the question is how to measure Li abundance in a giant using low resolution spectra and identify candidates of Li-rich K giants. It is an easy task if we have a high resolution spectrum with which equivalent widths can be measured directly. Equivalent widths are used to derive Li abundance in combination with radiative transfer codes and atmospheric models. However, the concept of equivalent widths does not apply for low resolution spectrum as seen here, in which lines are blended with a number of other lines whose

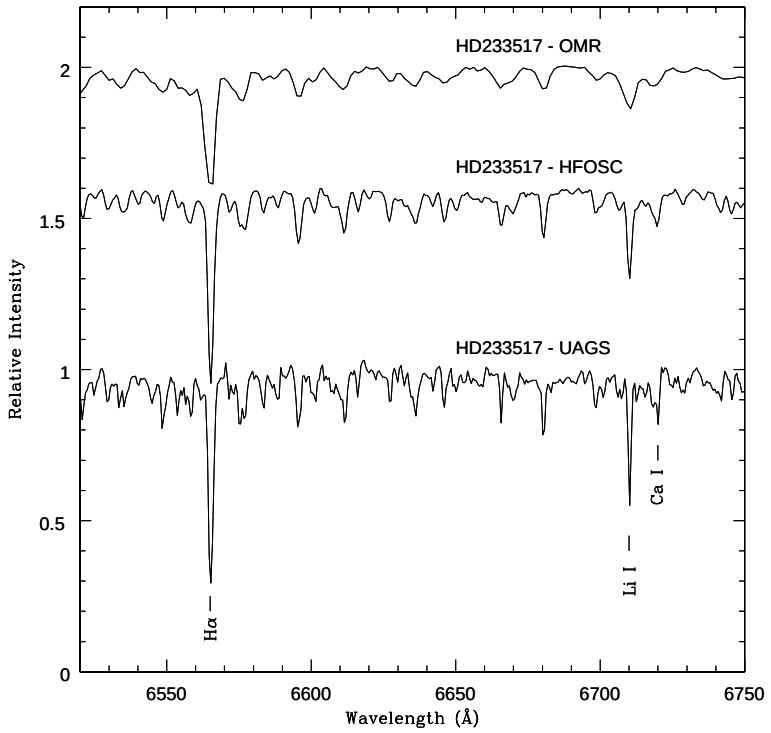

Figure 3.5: Spectra of a Li-rich giant HD 233517 taken with all the three instruments. Note the effect of resolution. Spectrum that has relatively higher resolution has sharper and deeper lines, and also the separation between the same lines is more.

identification is not known. Therefore, in this study we have developed a simple but a reliable method to quantify Li abundances using the low resolution spectra.

Strategy is to measure relative core depth of Li resonance profile with that of a line which is close to Li line in wavelength and in low excitation potential. The neutral Ca lines at 6717 Å and 6572 Å, and Fe line at 6591 Å are the ideal candidates for this purpose. Another important consideration that was taken in choosing these lines is that they are isolated and dominant transitions i.e., other blended lines may not be contributing too much to the line strength. In our observing program, we have made sure to obtain spectrum covering all the three transitions. Since the selected transitions have very similar low excitation potentials their strengths are expected to behave very similar to $T_{\rm eff}$. This is an important point as Ca line strength varies only with $T_{\rm eff}$ for a given metallicity, and mild variation with log g is expected. However, Li line strength depends on various parameters such as amount of Li present in the photosphere, mass and as well age. The amount of Li is basically independent of $T_{\rm eff}$, log g, and metallicity. Li is known to be produced or depleted by many different processes which are not well understood. The catch here is the

Table 3.3: Derived line depth ratios and Li abundances for K giants that are used in deriving relations.

HD	RA	DEC	V	A(Li)	Exp time		Li/6717			Li/6572	Li/6592
					HFOSC	UAGS	HFOSC	UAGS	OMR	HFOSC	HFOSC
787	00 12 09.986	−17 56 17.80	5.29	1.80	90	1200	0.95749	0.9392	–	0.96117	1.01321
40827	06 05 08.229	+59 23 35.56	6.32	1.60	180	900	1.00717	1.01521			
233517	08 22 46.7100	+53 04 49.19	9.70	4.22	480	2700	0.804079	0.67400	0.919216	0.81194	0.85651
108471	12 27 42.000	+08 36 37.00	6.36	2.00	180	1800	1.02286	1.07364	1.004347	1.02831	1.08613
109703	12 36 17.0811	+51 30 53.41	8.60	2.82	420	2700	0.945698	0.93822	0.978636	0.94619	1.00
112127	12 53 55.6159	+26 46 48.06	6.89	2.70	240	2400	0.894208	0.79652	0.976524	0.89317	0.95796
116292	13 23 01.2222	−17 44 05.35	5.36	2.82	90	600	1.05964	1.12853	1.014482	1.0568	1.12297
120602	13 50 24.6228	+05 29 49.69	6.01	1.90	90	600	1.01761	1.06961	1.010927	1.00763	1.06325
126868	14 28 12.5243	−02 13 40.33	4.84	2.40	60	300	1.01932	1.04382	0.999792	1.00206	1.04657
146850	16 19 00.4681	-14 52 21.881	6.018	2.00	120	600	0.95617	0.935602	...	0.95533	1.03899

assumption of constant metallicity. This is reasonable for a given sample which is located in the solar neighborhood. Our estimates based on Stromgren photometry suggest that vast majority of stars in the sample have metallicity close to solar value of [M/H]=0.0. Unfortunately, we do not have Stromgren photometry for the entire sample stars. Also, looking at the sample spectra one may notice that metallic lines such as Fe and Ca are almost constant but Li varies from one spectrum to the other (Figure 3.2). Thus, the ratio of core depths of Li at 6707 Å and other Ca I lines will provide reliable information on Li abundance for a given star.

To understand how core depth ratios of Li line at 6707 Å with Ca I lines and Fe I line relate with Li abundances, we have observed a sample of K giants, for which Li abundances are available based on high resolution spectra, with low resolution spectrographs mounted on the three facilities that were mentioned before. Empirical relations between core depth ratios and the abundances taken from the literature have been derived. The sample K giants that are used in the empirical relations include most of the known Li-rich K giants for which accurate Li abundances are available. Empirical relations derived for HCT spectra for ratios of line core depths of Li and other candidate lines core depths are given below. The linear regression fits, obtained using *SIXLIN*, show that core depth ratios are directly proportional to the amount of Li present in the atmosphere. Scatter in the fits seems to be very similar for all the three relations but the relation between Li (6707 Å)/Ca (6717 Å) and Li abundances is relatively a better fit. This might be due to the strength of Ca line at 6717 Å and hence is well seen in the low resolution spectrum.

$$A(Li) = \left(\frac{(1.201 \pm 0.02) - (Li/Ca_{6572})}{0.096 \pm 0.009} \right) \tag{3.6}$$

$$A(Li) = \left(\frac{(1.248 \pm 0.015) - (Li/Ca_{6592})}{0.094 \pm 0.072} \right) \tag{3.7}$$

$$A(Li) = \left(\frac{(1.164 \pm 0.009) - (Li/Ca_{6717})}{0.083 \pm 0.005} \right) \tag{3.8}$$

The above relations are valid for stars of constant metallicity which is closer to solar value. Also, the above relations are valid only for stars of abundances greater than 0.6 dex. This is because, in the HCT spectra, we could detect Li lines only if the Li abundance in the star is more than 0.6 dex. The empirical relations are shown in Fig 3.6 and bottom panel of Fig 3.7. A similar procedure was followed for the data collected from 1-m and 2.3-m telescopes. The derived relations are shown in top two panels of Fig 3.7. Relations derived from 2.3-m spectra have relatively more scatter due to significantly

lower resolution compared to other spectrographs. As a result, in many cases, even the strong Ca or moderate Li lines could not be properly resolved. This puts the minimum detection limit of 1.5 dex for Li abundance. This still works for us as we have defined K giant with Li abundance log ϵ (Li) $\geq$ 1.5 as the Li-rich K giant and does not voilate our goal of identifying Li-rich K giants among RGB stars.

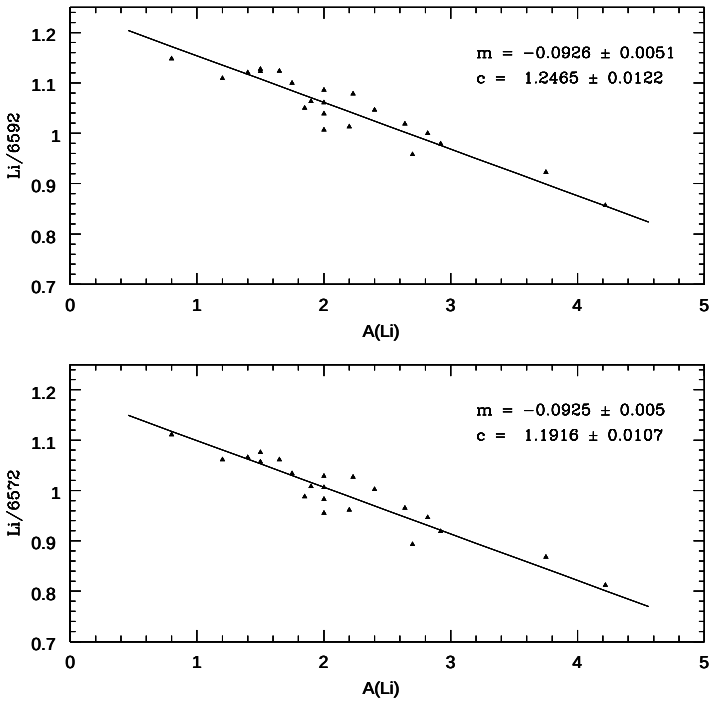

Figure 3.6: Empirical relations derived for line depth ratios and Li abundances of known Li-rich giants for spectra obtained from HCT . In the top panel, relation of core depth ratio of Li to Ca line (6572) and Li abundances is shown. The bottom panel shows relation for Li to Fe line (6592 Å). The fit coefficients are provided on top of the panels.

$$A(Li) = \left(\frac{(1.323 \pm 0.05) - (Li/Ca_{6717})}{0.16 \pm 0.019} \right) \tag{3.9}$$

$$A(Li) = \left(\frac{1.068 \pm 0.01 - (Li/Ca_{6717})}{0.0345 \pm 0.002} \right) \tag{3.10}$$

As noted earlier, we have observed the entire sample over a period of three years making use all the facilities at our disposal. Out of 2000 sample stars, spectra for 1100 stars were obtained from 2-m HCT, 500 spectra from 1-m at VBO, and the rest of the 400 stars spectra came from 2.3-m VBT telescope. Line depth ratios for the entire spectra

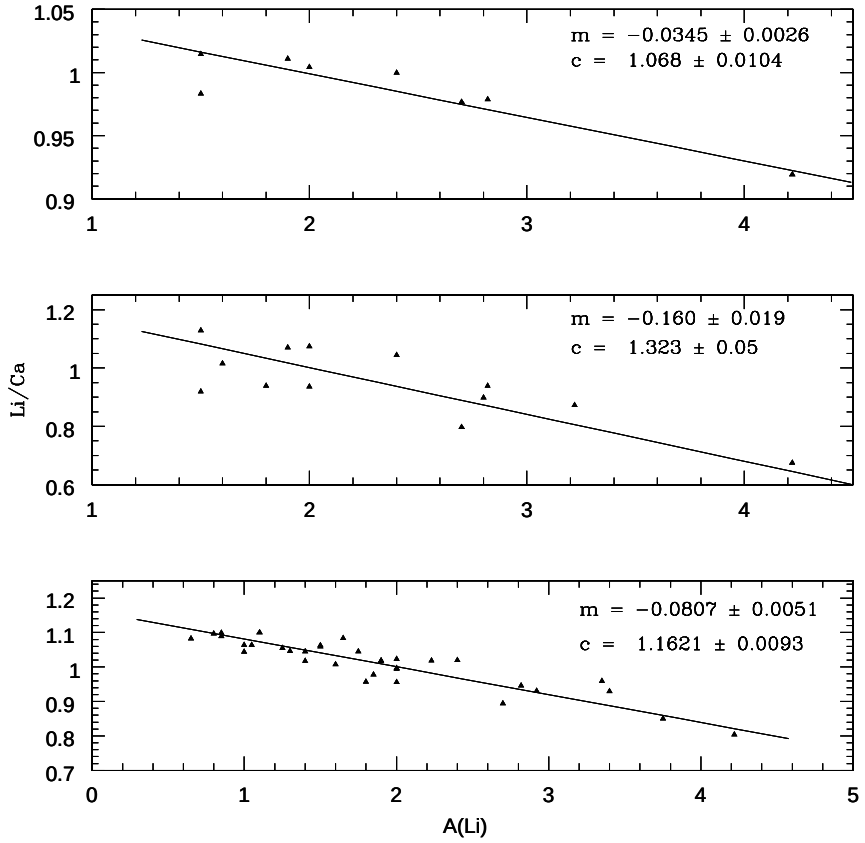

Figure 3.7: Same as Fig 3.6 but for line ratios of Li to Ca at 6717 Å. Relation derived from hct spectra is shown in bottom panel. Relation derived for the spectra obtained from OMR spectrograph on 2.3-m telescope shown in top panel. The relation derived from the spectra of Known Li-rich giants observed from 1-m CZT is shown in middle panel. The scatter is more due to the less sample points.

were measured using the tasks available in *IRAF*. A sample of measured ratios and the known Li abundances are given in Table 3.3.

As a result of different resolutions minimum limit on Li measurement varies from one data set to the other. In the case of 2-m HCT spectra, minimum Li that could be measured is 0.4 dex, and 0.2 dex from 1-m CZT spectra. For the rest 400 stars spectra are of very low resolution and we could confidently measure stars with Li abundances above 1.5 dex. However, the varying minimum limits of Li abundance will not affect the goals of this study. We are mainly interested in stars with Li abundance greater than equal to 1.5 dex and is applicable all of the data and found satisfactory.

Table 3.4: Measurements of line ratios and derived Li abundance of sample stars

Spectrograph	HD	Teff	Lum	Li/Ca	A(Li)
HFOSC	101151	4243	2.47	1.12151	0.44
	101112	4649	1.73	1.1085	0.61
	101341	4733	1.68	1.10286	0.68
	101321	4828	1.31	1.08893	0.86
	115319	4857	1.47	1.07366	1.07
	117304	4703	1.79	1.06299	1.21
	118536	4484	1.92	1.04725	1.41
	100470	4693	1.80	No detection	
	102096	4972	1.19	No detection	
	10348	4778	2.07	No detection	
UAGS	38313	4615	1.54	1.1905	0.90
	79524	4360	2.08	1.1637	1.07
	23697	4735	1.31	1.1450	1.19
	13004	4539	1.46	1.1314	1.27
	115912	4604	1.99	1.1136	1.38
	85563	4500	1.86	1.0736	1.64
OMR	51367	4655	1.78	0.9688	3.08

3.5 RESULTS AND DISCUSSION

Once the relations are established between ratio of line depths and the known Li abundances, it is now straight forward to derive Li abundance of program stars for a given line depth ratio. Relations were verified using K giants which are not used in obtaining the relations but have known Li abundances derived from independent methods. Agreement between literature abundances and the abundances derived from the relations obtained in this study are satisfactory within about ±0.3 dex in Li abundance.

Table 3.5: Statistical analysis of Sample stars

Telescope	Samples	Li detection	Li-free	Li-rich
HCT	1100	250	750	11
VBT	500	10	450	2
CZT	400	100	300	2

Respective relations are used to derive Li abundances from spectra obtained from different telescopes. Sample results are shown in Table 3.4 for each data set. In the case of HCT data set, only 25% of K giants showed detectable Li i.e., log ϵ(Li) $\geq$ 0.5. Out of 1100 K giants only 20 giants showed Li above 1.2 dex and we assign them as potential candidates that belong to Li-rich K giants group, and 11 have Li abundance more than 2.0

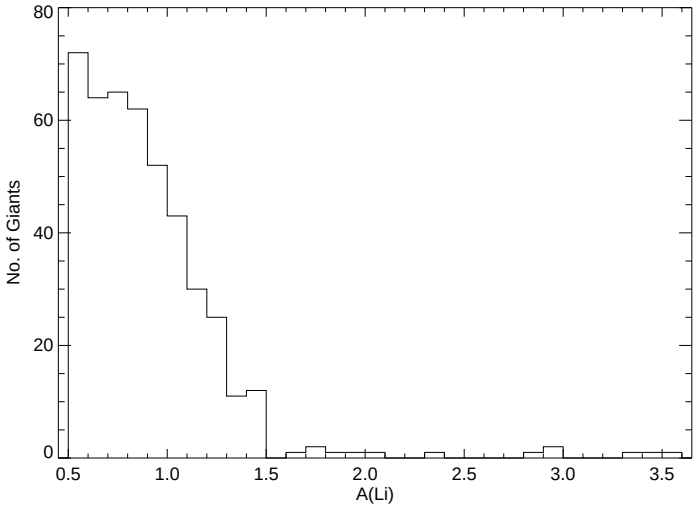

Figure 3.8: Li abundance of HCT samples are represented as Histogram. The distribution of the sample showing Gaussian with peak Li abundance at 0.6 dex. Note the Li-rich giants have occupied the tail portion.

dex which are assigned as Li-rich K giants. A distribution function of Li for HCT data set is shown in Figure 3.8. As shown in the distribution, just about 2% of giants found to have Li more than the expected value of about 1.5 dex. Rest of the K giants, with Li less than 1.5 dex, are treated as normal giants. A few more Li-rich K giants (2 from 1-m data set, 2 from 2.3-m data set) were added to the list. A consolidated Li distribution is shown in Figure 3.9. Giants with Li abundance less than the minimum detectability are excluded from the distribution i.e., giants with Li abundance more than 0.5 dex (HCT data set), 0.3 dex (1-m data set), and 1.5 dex (2.3-m data set) are only included in the distribution. The distribution for a full set of data is shown in Figure 3.9. This is very similar to the distribution for a sub-set of data given in Figure 3.8. Based on the kind of data that we have with us, we draw the following statistics: a) In about 70% of K giants, we found Li null detection. b) about 20% K giants show Li abundance between 0.6 - 0.8 dex, c) about 10% giants have Li between 0.8 - 1.4 dex, and d) about 1 - 2% of total giants have log ϵ(Li) $\geq$1.5. A total of 15 giants were assigned as Li-rich K giant candidates.

From the Li distributions shown in Figures and the statistics given above, one can make two important conclusions: 1) Very few giants are there beyond the maximum expected Li limit of 1.5 dex suggesting rarity of Li-rich K giants, and 2) Distribution peaks at about Li abundance 0.6-0.7 dex which is in good agreement with the standard theoretical model predictions. However, we can't make a suggestion or confirm, based on the data set presented here, results of anomalously low Li abundances in K giants (Brown

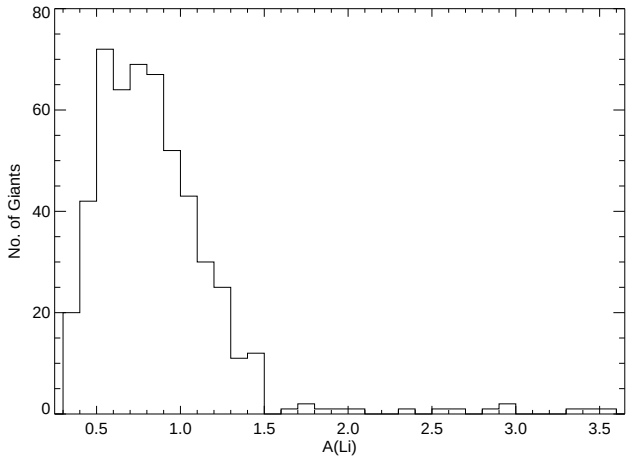

Figure 3.9: Li abundance of all samples are represented as Histogram. The distribution of the sample showing Gaussian with peak Li abundance at 0.7 ± 0.2 dex. Note the Li-rich giants have occupied the tail portion.

et al. 1989).

Table 3.6: Derived parameters of new Li-rich giants

HD	Teff	Lum	Li/Ca	A(Li)	Telescope
hd40168	4771.50	2.15802	1.0599	1.24	HCT
hd88476	4941.12	1.89466	1.02526	1.74	HCT
hd133086	4831.96	1.72413	1.02285	1.77	HCT
hd118319	4752.32	1.71014	1.00512	2.07	UAGS
hd12203	4804.46	1.71598	1.0102	1.89	HCT
hd107484	4504.67	1.80961	0.99814	2.04	HCT
hd145457	4731.41	1.63329	0.974466	2.35	HCT
hd37719	4655.10	1.77948	0.968824	3.08	OMR
hd51367	4530.49	1.61089	0.985891	2.61	OMR
hd167304	4729.52	1.95527	0.936517	2.81	HCT
hd150902	4664.27	1.85361	0.93185	2.85	HCT
hd170527	4812.28	1.71506	0.902105	3.30	HCT
hd10437	4660.60	1.79629	0.883247	3.54	HCT
hd8676	4705.07	1.70139	0.846645	3.70	HCT
hd77361	4549.62	1.69125	0.818115	3.30	UAGS

To further understand the sample, we have separated all the new Li-rich K giants from the sample and presented in Table 3.6 along with parameters such as $T_{\rm eff}$, Luminosity, line depth ratio, and derived Li abundance. Entire sample giants along with the newly identified Li-rich K giants are shown in the HR diagram. Li-rich K giants are shown as solid blue circles indicating the amount of Li with circle size. Results shown in Figure 3.10

suggest that only a few stars show Li excess and giants that have Li excess are located at a particular position in the HR diagram. The later result has much broader implications as for the origin of high Li in giants is concerned. For example, based on the 2nd result, we suggest that planet engulfment for Li origin in K giants seems to be very unlikely. If this is the case, one would expect Li enhancement all along the RGB not necessarily at a particular position in the HR diagram. This issue has been discussed in detail in Chapter 8. The location of Li-rich K giants in the HR diagram is of interest. All the Li-rich stars are close to the luminosity bump (solid red mark) and the red giant clump region (solid yellow mark). In chapters 4 & 8, we have supplemented our survey with Brown et al. survey to understand the issue in more detail.

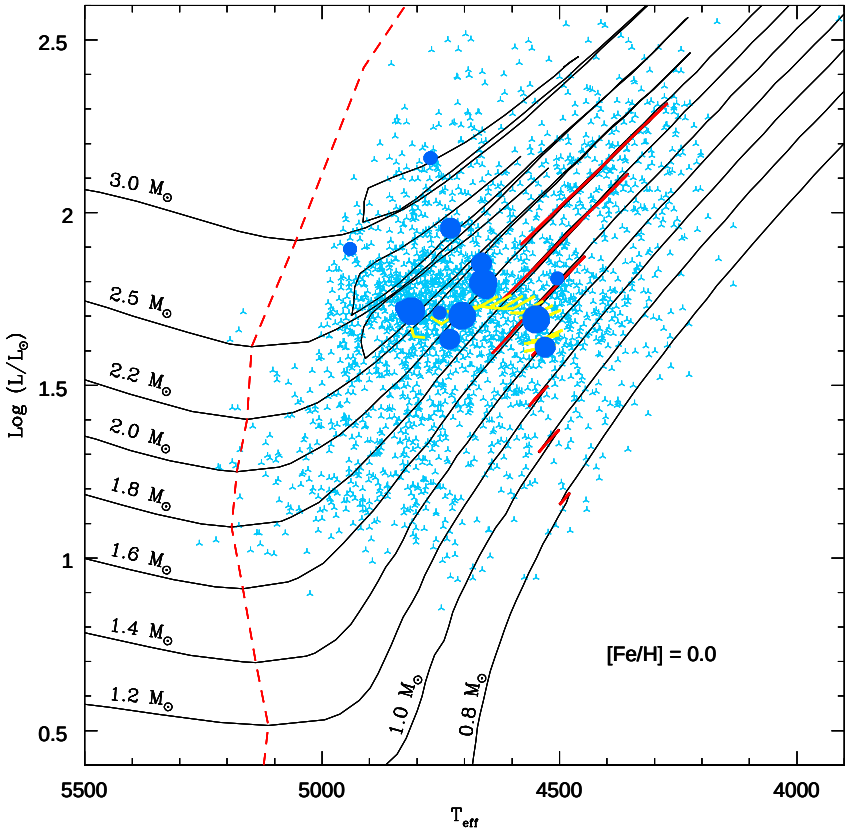

Figure 3.10: This figure is similar to the Fig 3.1. New Li-rich giants are shown as blue circles. The size of the circle represents the relative amount of Li. Note the Li-rich giants have occupied the bump and clump region in the HRD.

3.6 CONCLUSIONS

We have completed a largest survey for Li-rich K giants among RGB stars. A sample of 2000 giants were chosen from the revised Hipparcos catalogue. Color and luminosity criteria were applied to the catalogue in such a way that sample stars are of late G- and K-type, and of wide luminosity range, from the base of RGB to well beyond the luminosity bump. A novel strategy was followed to complete the entire survey program. Strategy was to obtain low resolution spectra and use relative line depth of Li line profile at 6707 Å to near by Ca or Fe lines. With this strategy we could get spectra for the entire sample in relatively shorter time.

The survey resulted in 15 new Li-rich K giants increasing the current Li-rich giants by a factor of two. Also, we confirm earlier survey by Brown et al., and establish from this study that the Li-rich stars are rare, just about 2%, in the Galaxy. Another important result is that Li-rich stars occupy a particular position in the HR diagram. The new Li-rich stars are located close to the luminosity bump and the hotter ones overlap with the red clump stars. Results suggest that planet engulfment or some external trigger is a very unlikely scenario for Li-excess in the RGB stars. We conclude from the results that Li excess is most probably triggered by events in the stellar interior at this particular evolutionary stage. In other chapters we discuss possible scenario such as Li production during bump evolution, Li production at the time of He-flash at the tip of the RGB, etc.

CHAPTER 4

HIGH RESOLUTION SPECTROSCOPY:

LI, CNO AND ^{13}C ABUNDANCES OF NEW LI-RICH GIANTS

4.1 INTRODUCTION

We have identified more than a dozen Li-rich candidate K giants from our low resolution spectroscopic survey. The procedure was discussed extensively in Chapter 3. However, to understand the mechanism of Li enhancement it is necessary to investigate Li trends with those of other elements which too are sensitive to mixing on the RGB. These are C, N and O, ^{13}C, and metallicity ([Fe/H]). None of this information can be extracted reliably from low resolution spectra. High resolution spectroscopy offers more possibilities that would help to find clues to the origin of high Li in K giants. Apart from accurately determining Li, we derive CNO and carbon isotopic ratio ^{12}C/^{13}C for all the newly identified Li-rich K giants.

Study of CNO and other isotopes along RGB has a long history, and one finds a wealth of high resolution observational studies (Harris et al. 1988; Gilroy 1989; Charbonnel et al. 1998) In general, abundances of C, N and ^{13}C are expected to have significantly different values compared to the main sequence stars. The altered composition in the interiors due to PP chain and CN reactions of main sequence dwarfs is brought up to the surface as a result of 1st dredge-up on RGB. The net effect is reduction of ^{12}C and enhancement of ^{14}N, and ^{13}C isotope. The scrutiny of vast observational data and the data predicted from the standard stellar evolution and nucleosynthesis revealed conflicts between the two. For example, theory predicted substantially higher ^{12}C/^{13}C values compared to observations for population I stars, similar to those being studied in this thesis. Similarly, observed Li abundances in vast majority of RGB stars are significantly lower than the predicted values from the standard theory. For giants of mass less than about $2M_{\odot}$ with metallicity close

to solar value, standard theory predicts $^{12}C/^{13}C$ in the range of 20-30. This is a reduction of $^{12}C/^{13}C$ ratio by a factor of about 3 from its main-sequence value of $^{12}C/^{13}C \approx 89$. However, the number of studies on open clusters and field giants show much smaller values. For example, Wallerstein & Morell (1994) 23 giants in an open cluster showed almost a constant value of $^{12}C/^{13}C \approx 12$. In some cases even much smaller values (e.g; Kumar & Reddy 2009. Reason for low values of $^{12}C/^{13}C$ and Li compared to standard theory is attributed to extra mixing of various kinds (see e.g; Boothroyd & Sackmann 1999; Palacios et al. 2006; Eggleton et al. 2008). By invoking special mixing mechanism, these models could reproduce low values observed in majority of RGB stars.

However, there are a very small group of giants which show extremely large amount of Li which is totally unexpected in K giants with such deep mixing process. Also, there are a few giants of Pop I, which have extremely low values of $^{12}C/^{13}C \approx$ 4-8. None of the models constructed so far could reach that low values. Also, it is quite necessary to develop a model that could simultaneously predict low values of $^{12}C/^{13}C$ and very high values of Li. To constrain models in this direction, it would be an important exercise for us to derive accurate Li, CNO, and $^{12}C/^{13}C$, and [Fe/H] for all the new K giants. These are the first measurements of its kind for these 15 K giants. In this chapter, we describe high resolution spectroscopic observations, abundance derivation, Li trends with other elemental abundances and isotopic ratios, and kinematics.

4.1.1 A BRIEF ACCOUNT OF NEWLY IDENTIFIED LI-RICH K GIANTS

Our survey for finding Li-rich K giants among RGB stars resulted in 15 new candidate Li-rich giants. Basic data of the program stars is given in Table 4.1. Below we provide a brief account of each of the newly identified Li-rich K giants.

HD 8676 : No previous studies on any stellar parameters including Li. No references are found in literature.

HD 10437: Pakhomov et al. (2011) study on space velocities show that this star is associated with Hercules moving group.

HD 12203: No previous studies on any stellar parameters including Li. No references are found in literature.

HD 37719: It has been checked for its binarity and found with null detection (Makarov & Kaplan 2005; Frankowski et al. 2007).

HD40168: It is a faint x-ray source with 0.06±0.01 cts/s which is listed in ROSAT All sky survey bright star catalog (RASS) (Voges et al. 1999). Haakonsen & Rutledge (2009) studied the cross association of RASS sources with 2MASS sources quantitatively and

found that P_{id} is 0.547 and P_{noid} is 0.232. Where P_{id} is the probability that the NIR source and X-ray source are uniquely associated, and P_{noid} is the probability that none of the 2MASS/PSC sources are associated with the X-ray source.

HD 51367: No previous studies on any stellar parameters including Li. No references are found in literature.

HD 77361: It is classified as a K1III CN star (Houk 1982). The variability is not found from the observations of light curves while studying the TY Pyxidis (Surendiranath et al. 1978).

HD88476: No previous studies on any stellar parameters including Li. No references are found in literature.

HD 107484: It is a Cyanogen strong star and classified as KOIII CN+2 (Schild 1973).

HD 118319: It is classified as a variable star in the SIMBAD. This star was studied in X-ray survey by Maggio et al. (1990) where they found its X-ray flux to be $2.5\times10^{-16}\mathrm{Wm}^{-2}$ and the ratio of X-ray to optical flux is -4.5.

HD 133086: It is classified as a star in double system in SIMBAD Database.

HD 145457: A planet is found to be revolving around this star (Sato et al. 2010). This star has been monitored since 2001 for radial velocity variations, which is part of a large survey for planet hunting with subaru telescope.

HD 150902: No previous studies on any stellar parameters including Li. No references are found in literature.

HD 167304: It was studied by Clarke (1964) along with Nova Herculis to check for polarization, and was found to be less than 0.3%.

HD 170527: It is classified as a variable star in SIMBAD. It has X-ray activity with counts 0.23 ± 0.01. The probability P_{id} and P_{noid} are 0.994 and 0.006 respectively (Haakonsen & Rutledge 2009). Koen & Eyer (2002) took 72 observed data points to check the variability and found 0.0169mag variation in the amplitude and classified it as unsolved variable. Guillout et al. (2009) observed strong Li line in the spectra of resolution R≈21,000, and deduced the abundance of 3.64 dex. Hence concluded the star's association with pre-main sequence.

4.2 OBSERVATIONS AND DATA REDUCTION

High resolution spectra of the program stars were taken with 2.34-m Vainu Bappu Telescope (VBT) at Vainu Bappu Observatory (VBO) and 2.7-m Harlan Smith Telescope at McDonald Observatory. The VBT is equipped with echelle spectrograph. Full details of

Table 4.1: Absolute magnitude and Luminosity of new Li-rich giants from basic data available in Hipparcos catalog

HD No	HIP No	V	Sptype	π(")	σ_π	σ_π(%)	M_v	σ_{M_v}	BC	σ_{BC}	M_{bol}	$\sigma_{M_{bol}}$	log($L/L_\odot$)	σ_L
8676	6647	7.77	K0III	4.27	0.74	14.6	0.9221	0.3769	-0.3108	0.0392	0.6114	0.3789	1.6554	0.1516
10437	8052	6.57	K1III	6.72	0.59	11.7	0.7068	0.1917	-0.3226	0.0409	0.3842	0.196	1.7463	0.0784
12203	9343	6.75	G5	6.58	0.64	9.7	0.8411	0.2122	-0.3082	0.0378	0.533	0.2155	1.6868	0.0862
37719	26499	7.62	K1III	4.23	0.63	14.9	0.7517	0.324	-0.405	0.0514	0.3467	0.3281	1.7613	0.1312
40168	28149	6.88	G5	3.75	0.64	17.0	-0.2498	0.3711	-0.3352	0.0422	-0.5851	0.3735	2.134	0.1494
51367	33298	6.99	K1/K2III	7.09	0.46	11.0	1.2432	0.1423	-0.4063	0.0524	0.8369	0.1516	1.5652	0.0607
77361	44290	6.20	K1IIICN	9.25	0.43	8.0	1.0307	0.1029	-0.4433	0.0571	0.5874	0.1177	1.665	0.0471
88476	50019	6.86	G8III	4.97	0.72	14.5	0.3418	0.3152	-0.2306	0.029	0.1112	0.3165	1.8555	0.1266
107484	60240	7.72	K0IIICN	4.06	0.75	18.4	0.7626	0.4016	-0.4115	0.053	0.3512	0.4051	1.7595	0.162
118319	66405	6.48	K0III	7.58	0.55	12.7	0.8783	0.1588	-0.4098	0.0516	0.4685	0.167	1.7126	0.0668
133086	73136	6.83	K0	6.25	0.43	6.8	0.8094	0.1507	-0.2809	0.0355	0.5285	0.1548	1.6886	0.0619
145457	79219	6.57	K0III	7.98	0.45	9.2	1.08	0.1241	-0.315	0.0394	0.765	0.1302	1.594	0.0521
150902	81156	7.93	G5	3.36	0.55	16.3	0.5617	0.356	-0.3855	0.0492	0.1762	0.3594	1.8295	0.1438
167304	89246	6.36	K0III	6.07	0.34	8.0	0.2759	0.1233	-0.3105	0.0397	-0.0345	0.1295	1.9138	0.0518
170527	90274	6.84	K0	6.31	0.40	6.3	0.8401	0.1391	-0.331	0.0417	0.5091	0.1452	1.6963	0.0581

the VBT and the spectrograph (Rao et al. 2005) are given in Chapter 2. All the spectra were taken with a slit width of 60μ which is about 4 pixels on CCD with a 15μ pixel size which gives spectral resolution R 60,000 (R=$\lambda/\Delta\lambda$). Full spectrum covers over a wide range from 4000Å to 9000Å but with large gaps between orders. Therefore, we require two set-ups to have full optical spectrum. High quality spectra with S/N 300-500 and resolution R 60,000 were obtained from 2.7-m Harlan Smith Telescope which is equipped with Coude echelle spectrograph (Tull et al. 1995). Spectra covers from 3500Å to 9500Å with small gaps between the orders beyond 5600 Å. Again to cover all the important transitions we required two wavelength set-ups. Along with program spectra, we have obtained twilight solar spectrum for easy identification of wavelengths of line profiles. For the purpose of wavelength calibration, we have obtained Th-Ar arc spectra at regular intervals. Flat field images and bias frames were obtained at the beginning and end of each night. For the purpose of identifying and removing of atmospheric lines, couple of hot stars with very high rotation were observed. The journal of observations is given in Table 4.2.

Table 4.2: Journal of Observations

HD	HIP	RA	DEC	V	Observatory	Exp time
88476	50019	10:12:42.5	+28:14:31.2	6.87	McDonald/VBT	720/2700
170527	90274	18:25:10.1	+64:50:18.3	6.87	McDonald/VBT	1200/2700
167304	89246	18:12:42.6	+41:08:48.6	6.356	McDonald/VBT	900/2700
150902	81156	16:34:30.2	+77:39:14.2	7.93	McDonald/VBT	1500/3600
133086	73136	14:56:48.4	+74:54:03.3	6.843	McDonald/VBT	1200/2700
40168	28149	05:56:54.7	-08:23:02.4	6.881	McDonald/VBT	900/2700
145457	79219	16:10:03.9	+26 44 33.9	6.584	McDonald/VBT	900/2700
51367	33298	06 55 36.5	-33 48 24.7	6.99	McDonald	1800
77361	44290	09:01:11.4	-26:39:49.3	6.206	McDonald/VBT	900/2700
8676	6647	01:25:18.2	-14:59:38.8	7.77	McDonald/VBT	1800/2700
10437	8052	01:43:21.4	+59:37:58.4	6.57	McDonald/VBT	1200/2700
107484	60240	12:21:10.1	+41:28:59.2	7.72	McDonald/VBT	900/2700
118319	66405	13:36:50.6	-34:28:03.9	6.48	VBT	2700
12203	9343	01:59:58.4	+06:02:07.7	6.76	McDonald/VBT	1200/2700
37719	26499	05:38:08.9	-47:42:51.4	7.62	VBT	2700

Entire two dimensional raw images were reduced to one dimensional flux versus wavelength using spectral image reduction tools available in *IRAF*. Images were removed off dark current using bias frames and pixel-to-pixel variation was taken off using flat field images. Details on dark and flat images are given in Chapter 2. Once the images were corrected for dark current and flat fields, images were inspected for any scattered

light. Scattered light effect is seen in the red part of McDonald spectra which was removed by fitting polynomials to the spectral orders using tasks such as "apscatter" in *IRAF*. Now the spectra is ready for extraction. The extracted spectrum is flux versus pixels. To convert pixels to wavelength we used Th-Ar comparison spectrum. Wavelengths for Th-Ar emission lines are known from the laboratory measurements. A 3rd or 4th order polynomial wavelength solution for each Th-Ar spectrum was produced for each night. Program spectra were wavelength calibrated with the Th-Ar polynomial solutions. Before making the spectra to work with we require to normalize the spectrum to unity or continuum fitted. This is because of the fact that the way the equivalent width (W_λ) has been defined. However, fitting the continuum to the cool stars such as ours is a tricky issue as one must be sure about the shallow dips. For a reference we used a very high quality and high resolution spectrum of Arcturus (Hinkle et al. 2000). A couple of continuum fitted spectra are shown in Figure 4.1. The reduced spectra are further processed to correct for the telluric contamination by dividing the object spectra with the hot star spectra. Entire spectra are brought to laboratory wavelengths by correcting radial motion of stars. The measurement of radial velocities is discussed later in this chapter.

4.3 ATMOSPHERIC AND OTHER STELLAR PARAMETERS

Stellar atmospheric parameters like $T_{\rm eff}$, log g, and microturbulence velocity (ξ_t) are necessary for the selection of representative atmospheric model and hence quantitative chemical composition of stellar photospheres are derived. Also, required are the radial and rotational velocities. Radial velocities (R_v) help to accurately identify weak transitions of trace elements and measure equivalent widths. Also, Rvs are required for computing kinetic motion to determine stellar population in the disk. Rotational velocities are important in the case of abundance determination by spectrum synthesis method. Atmospheric parameters like $T_{\rm eff}$ and log g can be derived either from photometry or from high resolution spectroscopy. Draw back in the photometric values is the uncertainty in extinction and the errors in the calibrations. However, photometric values are model independent and less cumbersome to derive. On the other hand, values derived from spectroscopy depend on model choice and accuracy in the measured equivalent widths. Here we describe how we have obtained the parameters through both photometry as well as spectroscopy. Finally, we adopt spectroscopy values since photometric temperatures are found to be more effected from extinction.

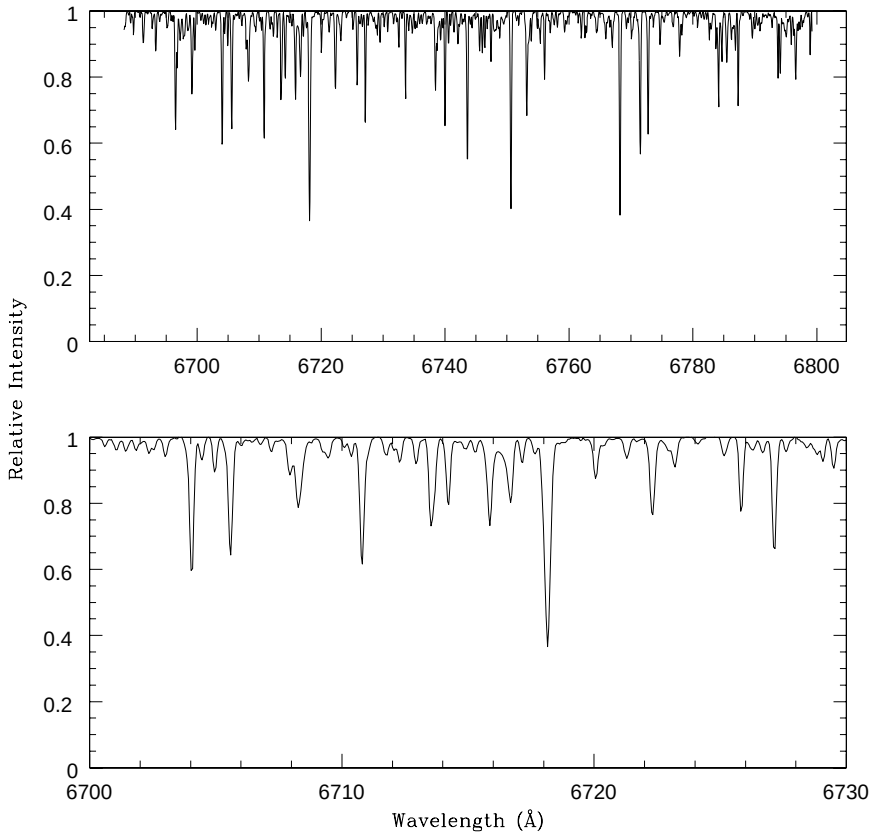

Figure 4.1: Sample reduced spectra with continuum fitted of one echelle order.

4.3.1 PHOTOMETRY

EFFECTIVE TEMPERATURE

The effective temperature ($T_{\rm eff}$) is derived from multiple ways: Johnson broadband UBVRI colors, Stromgren (uvby) narrow band colors. Based on a large set of sample stars Alonso et al. (1999) and Houdashelt et al. (2000) derived a number of relations between $T_{\rm eff}$ and the respective colors for Pop I G- to M- giants. Alonso et al. (1999) calibrations include metallicity dependency whereas Houdashelt's relations do not include [Fe/H] component. However, [Fe/H] parameter could be of much smaller significance as our stars have very narrow metallicity range near the solar value. The adopted colors of (B-V) (Hipparcos catalog ESA 1997), Stromgren photometry (Hauck & Mermilliod 1998), and of (R-I) (Monet et al. 2003) are given in Table 4.3. The corresponding $T_{\rm eff}$ derived using the empirical relations from Alonso et al. (1999). are given in the respective columns. Note that the $T_{\rm eff}$ obtained using relations between $T_{\rm eff}$ and (B-V) colors from two dif-

ferent studies with (Alonso et al. 1999) and without metallicity term (Houdashelt et al. 2000) agree very well within ±50 K suggesting very little effect of [Fe/H]. Only for a few stars (b-y) colors are available and the $T_{\rm eff}$ derived are in good agreement with the (B-V) temperatures. However, $T_{\rm eff}$ obtained from (R-I) colors are found to be systematically higher than both the (B-V) and (b-y) temperatures. The average difference is about ±120 K. One reason we can readily think of is that interstellar or circumstellar extinction which caused more absorption in Johnson "B" and "V" or stromgren "b" and "y" bands leading to estimation of cooler temperatures. Color (R-I) seems to be least affected and hence hotter temperatures.

Table 4.3: Derived temperatures from various photometric colors.

HD	B-V	err	R-I	b-y	T_{B-V} [a]	T_{B-V} [b]	T_{b-y} [b]	T_{R-I} [b]
8676	1.051	0.013	0.50	0.641	4744	4704	4710	4825
10437	1.075	0.007	0.50	0.679	4696	4659	4589	4825
12203	0.999	0.012	0.47	0.624	4850	4803	4768	4945
37719	1.078	0.012	0.51	–	4690	4654	–	4785
40168	1.016	0.010	0.47	0.660	4815	4770	4649	4946
51367	1.148	0.005	—	–	4557	4529	–	4676
77361	1.137	0.008	0.55	–	4578	4558	–	4642
88476	0.931	0.005	0.44	0.581	4995	4940	4924	5079
107484	1.163	0.005	0.55	–	4530	4503	–	4642
118319	1.026	0.006	0.47	0.640	4795	4751	4714	4946
133086	0.985	0.010	0.46	–	4880	4850	–	4989
145457	1.037	0.005	0.48	–	4772	4730	–	4904
150902	1.073	0.015	0.51	0.682	4700	4663	4580	4785
167304	1.038	0.007	0.50	–	4770	4728	–	4824
170527	0.995	0.011	0.46	–	4858	4811	–	4989

[a]Houdashelt (2000)
[b]Alonso et al. (1999)

SURFACE GRAVITY

Surface gravity (log g) of program stars has been derived from photometry as well as spectroscopy. In the case of photometry, one requires parallaxes and bolometric magnitudes. Bolometric corrections are estimated from calibrations given in Alonso et al. (1999). Basic parameters such as parallaxes, visual magnitude, absolute magnitude obtained from the distance modulus, bolometric corrections (BC), bolometric magnitudes, and the derived luminosities of the individual stars and the associated errors are summarized in Table 4.1. Errors in luminosity are mainly from the errors in parallaxes and

magnitudes. The mean error in luminosity is less than 0.1.

Now it is straight forward to determine surface gravity with standard relations involving $T_{\rm eff}$, mass, log $L/L_\odot$ i.e., $L \propto R^2\ T^4$ and $g \propto M/R^2$:

$$logg = log\frac{L}{L_\odot} + log\frac{M}{M_\odot} + 4logT_{eff} - 10.61 \tag{4.1}$$

Where T_{eff} is the mean of the temperatures given in Table 4.3. Luminosity is re-measured for the above corresponding temperature. Stellar masses are estimated using evolutionary tracks computed from Bertelli et al. (2008). The log g values are also derived from empirical calibrations (Hekker & Meléndez 2007) for giants where the relations are derived from the observations of large number of sample giants which is a function of temperature alone:

$$logg_{III} = -26.332 + 1.117{\times}10^{-2}T_{eff} - 1.064 \times 10^{-6}{T_{eff}}^2 \tag{4.2}$$

Table 4.4 summarizes log g values derived from two different methods, mean T_{eff}, luminosity and mass of a star. We see good agreement between the log g values derived from the two relations.

Table 4.4: Derived surface gravities from astrometry and photometry .

HD	T_{mean}	log($L/L_\odot$)	$M/M_\odot$	logg^a	logg^b
8676	4746	1.670	1.8	2.694	2.714
10437	4692	1.766	1.9	2.602	2.654
12203	4842	1.703	2.2	2.749	2.807
37719	4710	1.745	2.0	2.652	2.674
40168	4795	2.130	3.0	2.474	2.764
51367	4587	1.574	1.6	2.680	2.518
77361	4592	1.658	1.5	2.570	2.525
88476	4985	1.865	3.0	2.807	2.909
107484	4558	1.773	1.5	2.442	2.476
118319	4802	1.678	2.1	2.774	2.770
133086	4906	1.689	2.3	2.840	2.859
145457	4802	1.597	1.8	2.788	2.771
150902	4682	1.826	2.1	2.582	2.641
167304	4774	1.924	2.5	2.594	2.743
170527	4886	1.680	2.2	2.823	2.843

[a]From standard relation
[b]Hekker 2007

4.3.2 HIGH RESOLUTION SPECTROSCOPY

RADIAL VELOCITY

It is important to measure radial shifts in a given spectrum as the shifts are used to identify line profiles. Observed positions in terms of wavelengths for about 100 well defined and isolated lines have been recorded by fitting Gaussian. The corresponding laboratory wavelength positions of the identified lines were taken from different sources (Reddy et al. 2003; Allende Prieto et al. 2002; NIST). The differences between observed and laboratory wavelength positions are the radial shifts in wavelength. Shifts are converted to radial velocities (see Chapter 2). In Table 4.5 we provide measurements of a few lines of rest wavelength, observed wavelength, measured shift, and derived radial velocities. The mean of Rv is obtained by fitting the Gaussian distribution to the histogram of radial velocities (See Figure 4.2). The observed radial velocities are corrected for Earth's motion to get heliocentric radial velocities. In Table 4.6, we have provided star's radial velocity with respect to local standard of rest (LSR) by taking into account of Sun's motion in the space. For a few stars radial velocities exist already in the literature. The literature values are in good agreement with the values from this study within ±1 km s^{-1}. This may also suggest that these are not binaries. For some stars the values given in Table 4.6 are the first measurements.

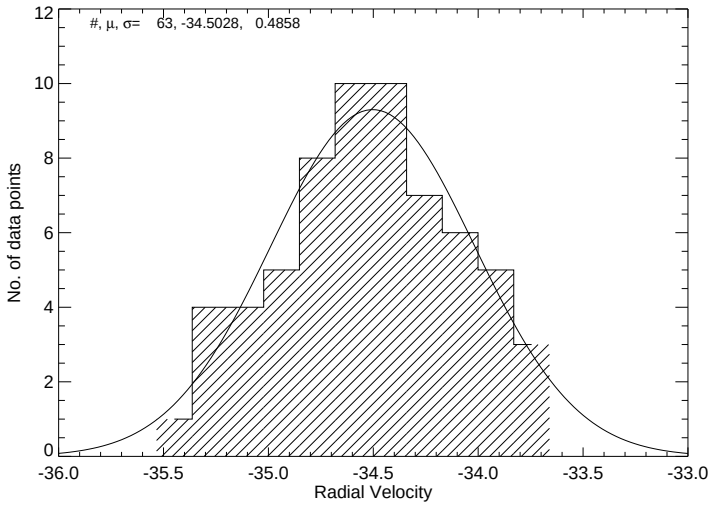

Figure 4.2: Mean radial velocity is determined by fitting the guassian to the distribution of radial velocity from various individual lines.

Table 4.5: Measurement of line shifts for few selected lines to derive radial velocity.

λ_{rest}	λ_{obs}	$\delta\lambda$	R_v
4432.566	4432.057	-0.508789	-34.4115
4481.610	4481.089	-0.520996	-34.8515
4635.850	4635.314	-0.536133	-34.6708
4656.980	4656.439	-0.541016	-34.8278
4798.265	4797.710	-0.555176	-34.687
4802.880	4802.325	-0.554688	-34.6232
5234.620	5234.021	-0.599121	-34.3123
5358.120	5357.496	-0.624023	-34.9148
5379.574	5378.957	-0.617188	-34.3946
5414.070	5413.439	-0.630859	-34.9325
5473.901	5473.271	-0.629883	-34.4972
5525.540	5524.914	-0.625977	-33.9628
5661.348	5660.693	-0.655273	-34.6995
5741.850	5741.188	-0.662109	-34.5699
5753.121	5752.462	-0.65918	-34.3495
5809.220	5808.549	-0.671387	-34.6478
5849.690	5849.009	-0.681152	-34.9086
5927.786	5927.111	-0.675293	-34.1523
5952.716	5952.037	-0.678711	-34.1814
6027.060	6026.366	-0.693848	-34.5127
6082.710	6082.006	-0.704102	-34.7024
6149.250	6148.539	-0.710938	-34.6601
6159.380	6158.666	-0.713867	-34.7457
6247.560	6246.844	-0.71582	-34.349
6271.283	6270.560	-0.723145	-34.5692
6369.460	6368.734	-0.726074	-34.1743
6496.469	6495.737	-0.732422	-33.7991
6591.330	6590.560	-0.77002	-35.0227
6699.142	6698.379	-0.763184	-34.1531
6725.360	6724.592	-0.768066	-34.2376
6793.260	6792.471	-0.788574	-34.8005
6837.009	6836.229	-0.779785	-34.1924
6857.250	6856.469	-0.780762	-34.1342
6971.936	6971.141	-0.794922	-34.1815
7112.173	7111.356	-0.816895	-34.4338
7802.510	7801.585	-0.924805	-35.5334
7807.920	7807.022	-0.897949	-34.4776

KINEMATIC MOTION AND GALACTIC ORBITAL PARAMETERS

We have computed space motion of each of the program stars to investigate whether Li-rich behavior is anyway related to their membership to either thin disk, thick disk or the halo populations (see Reddy et al. 2003, 2006). The three velocity components of space

Table 4.6: Derived radial velocities along with literature values

Star	V_r (km s^{-1})	V_{helio} (km s^{-1})	σV_r (km s^{-1})	$V_r lit$ (km s^{-1})	σV_r (km s^{-1})
8676	12.25	-7.93	0.4	—	—
10437	2.25	-1.60	0.51	-2.6	0.3
12203	-44.75	-59.78	0.5	—	—
37719	62.35	53.74	0.45	—	—
40168	66.00	42.78	0.5	—	—
51367	44.03	58.71	0.5	—	—
77361	-1.43	-23.34	0.5	-24.3	0.6
88476	31.97	4.19	0.39	4.7	0.3
107484	10.10	10.90	0.5	9.8	0.3
118319	19.20	22.68	0.5	21.8	0.6
133086	-1.76	-9.67	0.50	-9.9	0.3
145457	-23.15	-2.87	0.55	-3.6	0.3
150902	-34.52	-40.53	0.43	—	—
167304	-59.80	-49.67	0.42	-48.9	0.3
170527	-53.30	-51.72	0.5	-52.1	0.6

velocity U (velocity radially outward from the Galactic center), V (velocity along the Galactic rotation), and W (velocity perpendicular to the Galactic plane) are computed using the data from Hipparcos catalog: parallaxes and propermotions, and radial velocities given in Table 4.6. The space velocities (U,V,W) with respect to LSR are given in Table 4.7. Solar motion of U, V, W (-10,5.2,7.2) km s^{-1} derived by Dehnen & Binney (1998) is used. The Galactic orbital parameters are computed by assuming sun's distance of 8.5 kpc from the center and the derived kinematics. Probability of a star belonging to either of the three populations in the Galaxy has been computed following the details given in Reddy et al. (2006). Probability ($P_{thin}, P_{thick}, or P_{halo}$) of ≥ 0.7 is considered for a star to belong to a particular component population: thin disk, thick disk or halo. Computed probabilities are given in Table 4.7. Except HD 12203, all the giants belong to the thin disk component.

ATOMIC DATA AND EQUIVALENT WIDTHS

Atomic data such as central wavelengths, excitation potentials and oscillator strengths (log gf) are the main input data in the derivation of abundances. In case of molecules we require dissociation energies. Other important input is the line strength or equivalent widths (W_λ) of line profiles in the spectrum. In Table 4.8 we have given atomic data of selected lines: central wavelength, ion number, lower excitation potential, loggf, and measured equivalent widths.

Table 4.7: Space velocities, orbital parameters, and probability distribution in Galaxy

HD	U_{lsr}	V_{lsr}	W_{lsr}	Z_{max}	R_{apo}	R_{per}	P_{thick}	P_{thin}	P_{halo}
8676	-16.70	-4.00	12.90	0.26	8.82	7.86	0.00989	0.99008	0.00002
10437	40.50	-41.00	-14.80	0.12	9.00	5.61	0.03512	0.96476	0.00010
12203	-15.40	-49.20	59.30	0.62	8.64	5.48	**0.83065**	0.16422	0.00512
37719	17.20	-42.00	-9.60	0.14	8.59	5.76	0.02493	0.975001	0.00006
40168	24.60	-17.50	-3.60	0.08	8.92	7.16	0.01043	0.98954	0.00002
51367	22.30	-44.00	-1.30	0.03	8.65	5.63	0.02473	0.97520	0.00007
107484	18.40	-44.30	19.00	0.29	8.64	5.62	0.04045	0.95942	0.00011
118319	-23.00	-21.90	-0.60	0.06	8.65	6.63	0.01126	0.98870	0.00002
133086	-16.00	5.50	-5.80	0.11	9.02	8.30	0.00768	0.99230	0.00001
145457	13.00	9.40	15.20	0.15	9.16	8.23	0.01004	0.98993	0.00002
150902	-31.50	-38.20	6.60	0.17	8.77	5.94	0.02213	0.97780	0.00006
167304	-27.10	-48.90	-14.30	0.13	8.56	5.31	0.04283	0.95703	0.00013
170527	29.90	-53.60	1.10	0.07	8.71	5.03	0.04197	0.95789	0.00013
77361	-44.60	17.40	-5.00	0.05	10.67	7.78	0.01035	0.98961	0.00002
88476	10.40	-9.50	-4.10	0.16	8.68	7.69	0.00834	0.99163	0.00001

ATMOSPHERIC PARAMETERS

Atmospheric parameters like $T_{\rm eff}$, log g, microturbulent velocity (ξ_t) and metallicity ([M/H]) have been derived using spectral line analysis. Determination of atmospheric parameters from high resolution spectrum requires a set of well defined lines with a wide range of W_λs and low excitation potentials (LEP). The neutral (Fe I) and singly ionized (Fe II) iron lines satisfy the above criteria as Fe I lines are numerous in any given spectrum. The next best element that is represented by large number of clean lines is nickle (Ni I).

We have adopted Fe I and Fe II lines from Reddy et al. (2003) and Allende Prieto et al. (2002). They have compiled a list of FeI and FeII that are unblended (verified using solar and Arcturus spectrum) and have accurate log gf values either measured in laboratory or derived from inverting solar spectrum. For computation of theoretical W_λ we have used computer code called MOOG (version 2002) originally developed by Sneden (1973). Stellar models were taken from Kuruz data base (Kurucz 1994) which are computed from ATLAS9 code developed by Robert Kurucz. Models are based on LTE.

Effective Temperature: Abundances for a set Fe I lines were obtained for stellar models of given log g, ξ_t and [Fe/H] values but for a set of $T_{\rm eff}$s. Initial $T_{\rm eff}$ and log g are the values derived from photometry. The best value of $T_{\rm eff}$ for a given star is the one for which abundances are independent of LEPs (see Figure 4.3). To have minimal effect of ξ_t on the derivation of $T_{\rm eff}$, it is important to choose only weak lines for this purpose. In the derivation of $T_{\rm eff}$, we have used about 40 lines with LEP starting from 1.0 eV to 5.0

Table 4.8: Atomic data of selected lines and their equivalent widths for few sample Li-rich giants

λ (Å)	Ion	LEP (ev)	log gf	Ref	W$_\lambda$(mÅ)				
					8676	10437	12203	88476	133086
5778.458	26.000	2.590	-3.450	R03	70.400	75.60	58.35	51.57	66.34
5358.120	26.000	3.300	-3.160	R03	34.700	40.60	26.18	23.94	35.48
5466.990	26.000	3.573	-2.230	C02	73.800	79.80	59.40	56.83	74.12
5849.690	26.000	3.695	-2.930	R03	27.870	35.23	18.30	18.15	28.00
6857.250	26.000	4.076	-2.040	R03	52.320	58.70	40.28	38.37	52.08
6793.260	26.000	4.076	-2.330	C02	33.100	40.70	24.10	23.71	35.95
6725.360	26.000	4.103	-2.170	R03	42.390	47.39	32.42	31.72	44.26
5858.790	26.000	4.220	-2.180	R03	35.300	39.88	26.60	22.42	36.09
5705.460	26.000	4.301	-1.360	C02	68.300	71.30	57.00	57.20	67.47
5855.090	26.000	4.608	-1.480	R03	45.180	52.30	34.50	35.48	46.26
7807.920	26.000	4.990	-0.510	R03	81.200	86.99	71.20	70.38	85.69
6369.460	26.100	2.891	-4.020	R03	29.800	33.30	29.32	32.34	35.47
6149.250	26.100	3.889	-2.630	R03	45.000	48.00	41.35	47.88	50.04
6247.560	26.100	3.892	-2.270	R03	58.900	62.00	56.00	68.10	65.97
5052.150	6.000	7.680	-1.300	R03	22.30	—	24.90	20.00	17.40
5380.320	6.000	7.680	-1.610	R03	11.600	10.80	16.30	11.25	09.10

eV and line strengths below 60mÅ. Uncertainty in $T_{\rm eff}$ are estimated by changing $T_{\rm eff}$ in steps of 25 K until one notices change in the slope of abundances versus LEP plot. These are typically 75-100 K.

Surface Gravity: Log g values are obtained using neutral and singly ionized iron lines. A number of clean and moderately weak Fe II lines are quite few in cool spectra such as of K giants. We have just half a dozen of them. To derive log g we have extracted stellar models for given $T_{\rm eff}$ (derived above), ξ_t and [Fe/H] values but for a set of log g values. The best value of log g is the one for which Fe I and Fe II abundances are equal (see Figure 4.4).

Microturbulent velocity: The value of ξ_t is estimated using lines of same species but with a range of W_λ. Value of ξ_t is varied until abundances of different lines of a particular element (in this case Fe I) are same (within uncertainties) irrespective of its line strength i.e ξ_t is varied until the slope in the plot of Fe I versus W_λ/λ is zero. Uncertainties are estimated by varying ξ_t in small steps until the slope responses. Derivation of ξ_t is shown Figure 4.3.

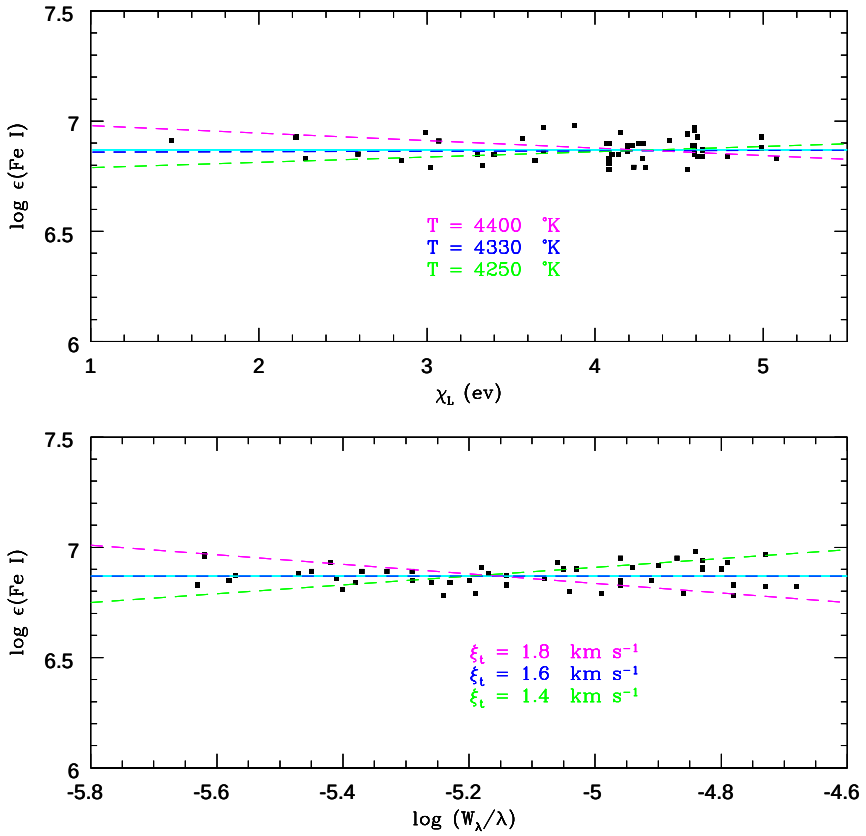

Figure 4.3: Determination of Temperature and microturbulence. Top panel shows the iron abundance is independent of LEP and bottom panel shows the abundance is independent of the strength of line.

The three parameters $T_{\rm eff}$, log g, and ξ_t are obtained certainly for a given [M/H] value. To select a right model atmosphere to represent a given stellar atmosphere, the process needs to be iterated until all the parameters are determined to give consistent abundance results. Metallicity, [Fe/H], of the star is normally represented by the mean of Fe I and Fe II abundance expressed relative to the Sun. The atmospheric parameters of all program stars are derived and are given in Table 4.9. The spectroscopic temperatures are systematically higher compared to the photometric values estimated from B-V and b-y colors. These temperatures are in good agreement with the values estimated from (R-I) color. Spectroscopic log g are in good agreement with the values obtained from photometry.

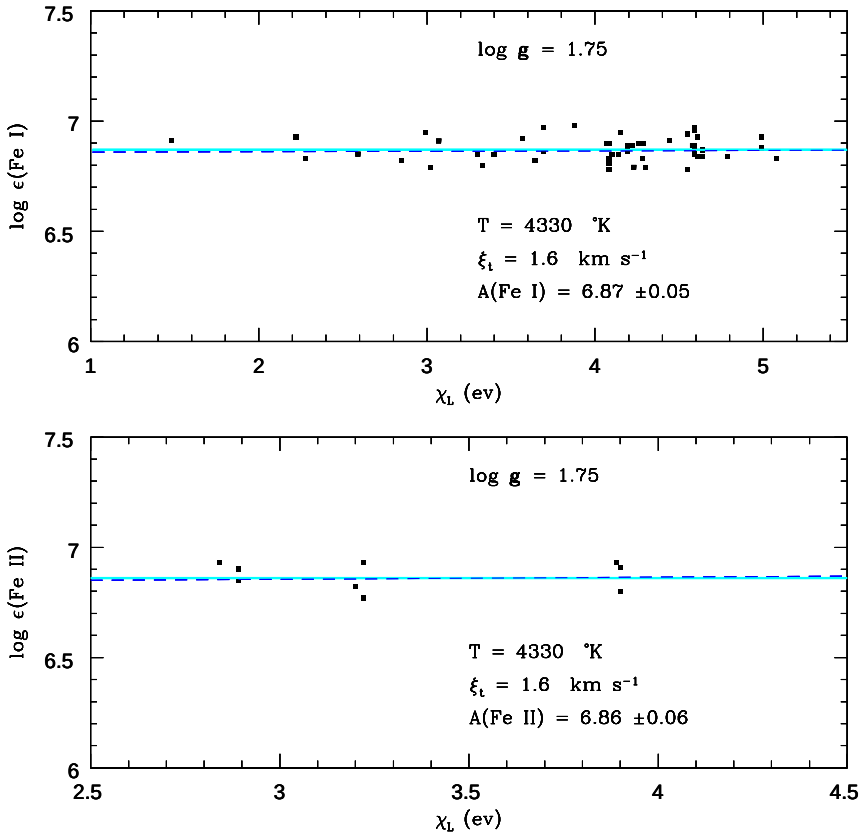

Figure 4.4: Ionization equilibrium of iron lines are shown in the determination of surface gravity of a sample star.

ROTATIONAL VELOCITIES

Rotational velocities or V_{rot} are used in this study for two purposes: one being V_{rot} is used as the input in the spectrum synthesis and other being the interpretation of V_{rot} with respect to high Li in K giants. The second aspect of V_{rot} is deferred to later chapters in this study. What we obtain from the spectra is basically the projected rotational velocity i.e *vsini* (i is the inclination angle). The *vsini* values were estimated by fitting synthetic spectra to small portions of spectrum of individual stars. Observed profiles were modeled as Gaussian distribution functions which include abundance of a particular element corresponds to particular line profile like macro turbulence (V_m which is 3 km s^{-1}, a typical value for K giants (Fekel 1997). The spectrum synthesis code MOOG (Sneden 1973) was used. The standard form of rotational broadening was assumed (Gray 1992), with a limb-darkening coefficient calculated using the relations from Diaz-Cordoves et al. (1995). Figure 4.5 shows fits to Fe I lines at 6703 Å and 6705 Å. Observed profiles are fitted by varying

Table 4.9: Derived spectroscopic atmospheric parameters from high resolution spectra

HD	T_{eff}	log$g$	ξ_t	log ϵ(Fe I)	log ϵ(Fe II)	[Fe/H]
124897	4330 ± 50	1.75 ± 0.15	1.60 ± 0.2	6.88 ± 0.05	6.86 ± 0.07	-0.65 ± 0.055
8676	4860 ± 75	2.95 ± 0.15	1.26 ± 0.2	7.51 ± 0.05	7.45 ± 0.05	0.0 ± 0.052
10437	4830 ± 75	2.85 ± 0.15	1.20 ± 0.2	7.61 ± 0.05	7.55 ± 0.08	0.05 ± 0.056
12203	4870± 75	2.65 ± 0.15	1.33 ± 0.2	7.22±0.06	7.19±0.06	-0.26 ± 0.064
37719	4650± 100	2.40 ± 0.2	1.5 ± 0.3	7.58 ± 0.12	7.55 ± 0.06	0.1 ± 0.13
51367	4650± 75	2.55 ± 0.15	1.44 ± 0.2	7.75 ± 0.09	7.71 ± 0.1	0.18 ± 0.1
77361	4580 ± 75	2.30 ± 0.15	1.40 ± 0.2	7.43 ± 0.07	7.43 ± 0.04	-0.02 ± 0.1
88476	5100± 100	3.10 ± 0.2	1.37 ± 0.3	7.38 ± 0.07	7.37 ± 0.07	-0.1 ± 0.098
107484	4640± 90	2.50 ± 0.15	1.40 ± 0.2	7.72±0.1	7.67 ±0.08	0.20 ± 0.11
118319	4700± 100	2.20 ± 0.2	1.45 ± 0.3	7.22±0.07	7.22±0.08	-0.25 ± 0.073
133086	4940 ± 80	2.95 ± 0.15	1.35 ± 0.2	7.53 ± 0.06	7.47 ± 0.03	0.03 ± 0.061
145457	4850 ± 70	2.75 ± 0.15	1.45 ± 0.3	7.41 ± 0.07	7.38 ± 0.05	-0.08 ± 0.073
150902	4690 ± 75	2.55 ± 0.15	1.30 ± 0.2	7.59 ± 0.05	7.54 ± 0.09	0.09 ± 0.1
167304	4860 ± 80	2.95 ± 0.15	1.48 ± 0.2	7.66 ± 0.07	7.65 ± 0.04	0.1 ± 0.072

only *vsini* and keeping macroturbulence, instrumental profile width (FWHM = 0.17 Å and 0.13Å for VBT and HJST spectra), and abundances constant. Note for some K giants the profiles are quite broad and the predicted profile with *vsini* = 2.0 km s^{-1} for normal K giants (De Medeiros et al. 2000) is far too sharp to match the observed profile. The *vsini* values of the best fit profiles are given in Table 4.10.

Table 4.10: Derived projected rotational velocities

Star	log(L/L$_\odot$)	T_{eff}	log$g$	[Fe/H]	v$_t$	u	v$_m$	vsin$i$
Arcturus	2.10	4340	1.75	-0.65	1.60	0.809	3.5	2.0
HD 145457	1.61	4850	2.75	-0.08	1.47	0.751	3.0	3.0
HD 77361	1.66	4580	2.35	-0.02	1.40	0.779	3.0	3.0
HD 10437	1.77	4830	2.85	+0.10	1.20	0.750	3.0	1.5
HD 167304	1.93	4860	2.95	+0.18	1.48	0.746	3.5	3.5
HD 8676	1.68	4860	2.95	0.02	1.26	0.746	3.5	2.0
HD 150902	1.83	4690	2.55	0.09	1.30	0.766	3.5	2.5
HD 88476	1.87	5100	3.10	-0.10	1.37	0.727	3.0	3.0
HD 133086	1.70	4940	2.975	0.02	1.34	0.740	3.0	2.5
HD 12203	1.69	4870	2.65	-0.27	1.33	0.751	3.5	2.5
HD 107484	1.78	4640	2.50	0.18	1.39	0.771	3.5	4.0
HD 51367	1.59	4650	2.55	0.20	1.44	0.769	3.5	3.5
HD 118319	1.68	4700	2.20	-0.25	1.45	0.772	3.5	3.5
HD 37719	1.76	4650	2.40	0.09	1.47	0.772	3.5	2.0
HD 170527	1.69	4810	2.85	0.00	1.40	0.752	4.5	25.0
HD 40168	2.10	4800	2.50	0.00	1.40	0.759	4.0	14.0

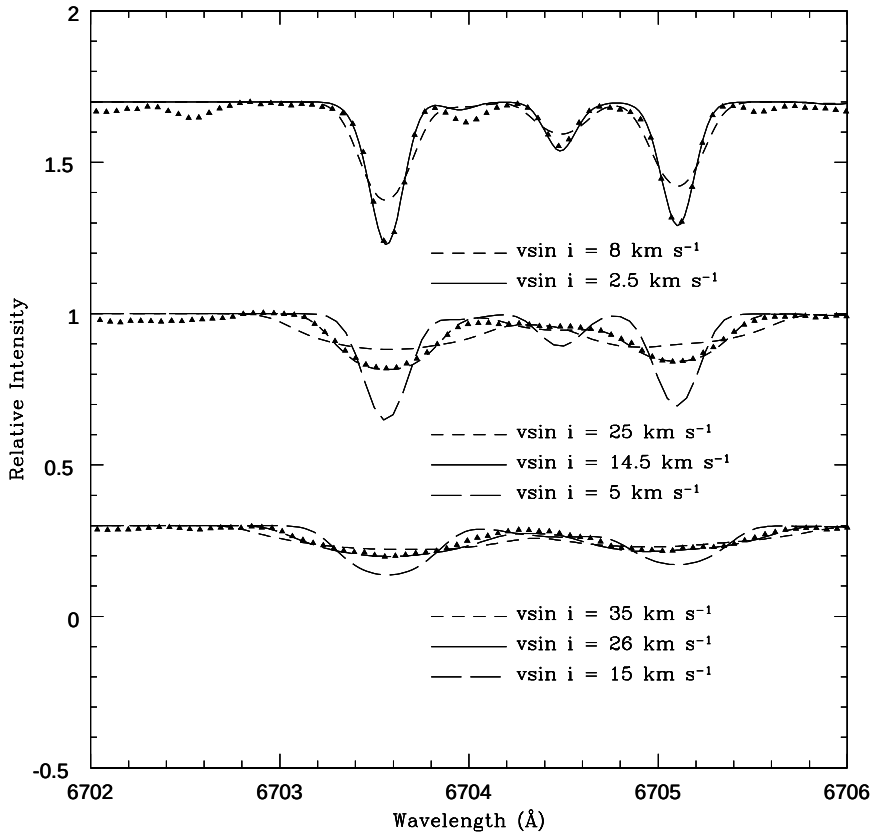

Figure 4.5: The figure shows the broadening of synthetic profile matching with observed ones in the determination of vsin i

4.4 ABUNDANCES

For this study we have adopted stellar models computed using an LTE code ATLAS9 by Kurucz (1993) and radiative transfer code MOOG developed by Sneden (1973) and updated. MOOG computes photospheric abundances for a given photospheric model and line equivalent widths for different elements. For a given stellar model MOOG predicts W_λ for each line and compares with the given observed strengths. MOOG also predicts a portion spectrum for a given model and the line list. The predicted spectrum is compared with the observed spectrum until it matches.

4.4.1 LITHIUM

Initial inspection of the spectra confirmed our identification that the 15 Li-rich candidates are infact as Li-rich K giants. The Li I 6707 Å resonance doublet is very strong, with

an equivalent width ranging from W_λ 100 - 600 mÅ. The resonance line is a blend of hyperfine and possibly isotopic components. In this study, we treat the profile as purely due to ^{7}Li isotope which is more abundant and also stable. Li also has another transition at 6103Å which is an excited line with LEP of 1.846 eV. In most cases this line is weak/absent. However, Li subordinate line at 6103 Å is measured for Li-rich K giants whose abundances are close to cosmic value. Measured W_λ of 6707 Å and 6103 Å are given in Table 4.11.

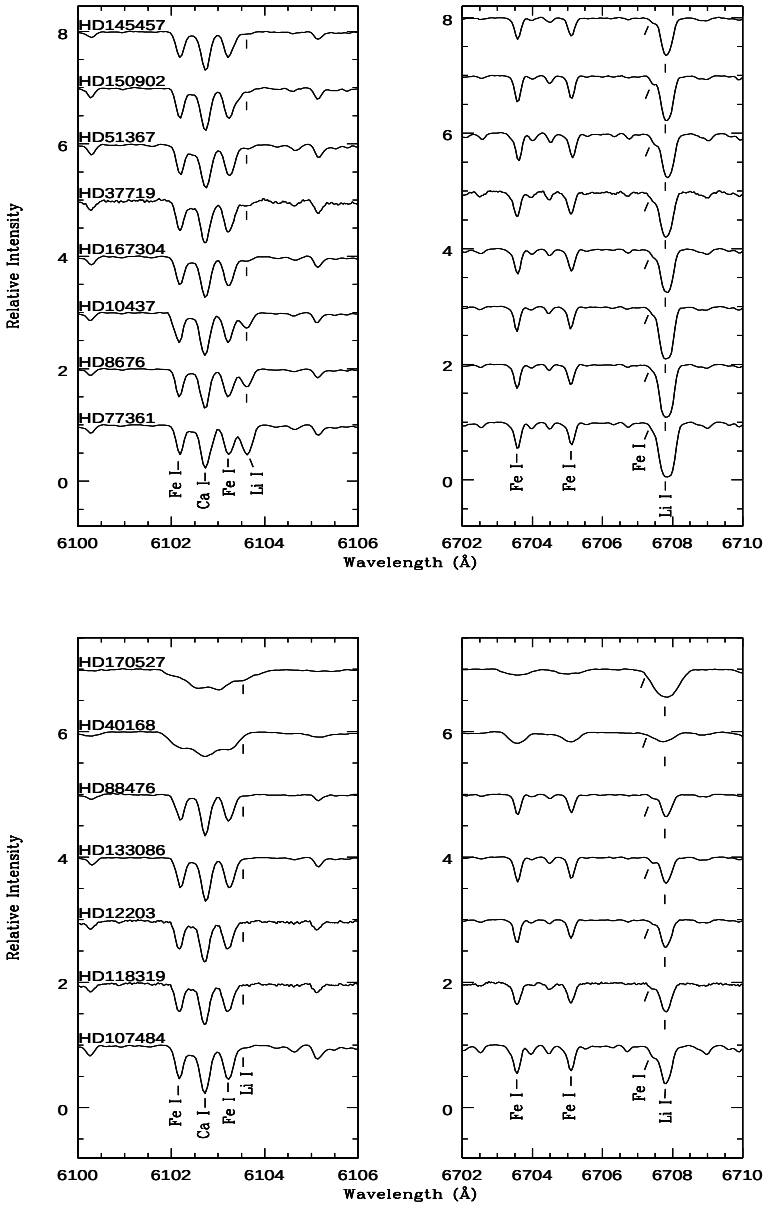

Figure 4.6: Spectra of new Li-rich giants showing the Li line at 6707 and 6103 .

The spectra of program stars in the two Li profile regions are shown in Figure 4.6. The spectra of HD 77361, HD 8676, HD 10437 show very strong Li lines at 6707Å and moderately strong 6103 Å. In some cases, the subordinate line at 6103Å is smeared out due to high rotation. This is particularly noticeable in the spectra of HD 170527 and HD 40168 (see top left panel of Figure 4.6). Li subordinate line sits at the red wing of a Fe I line. Other nearby Fe I and Ca I lines are marked (see bottom left Panel of Figure 4.6). Note subordinate line is very weak or absent in intermediate Li-rich stars.

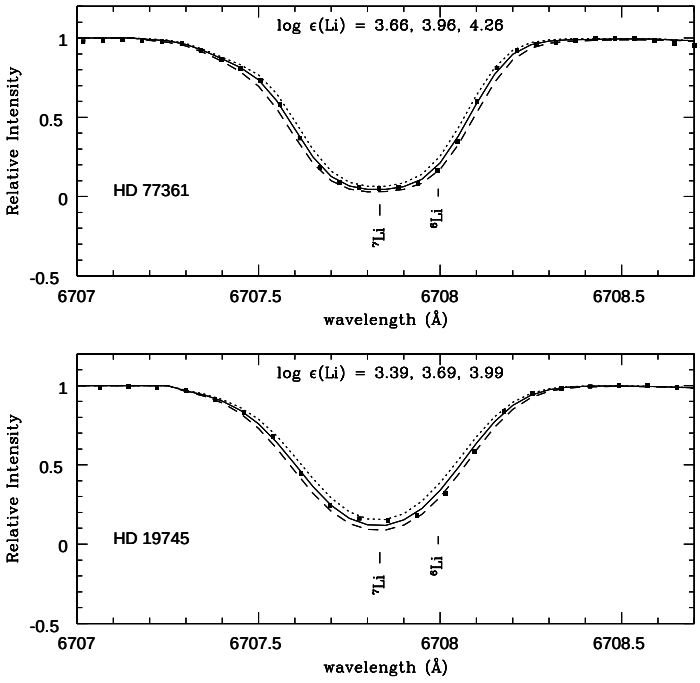

Figure 4.7: Observed (filled triangles) and synthetic spectra (lines) around the Li I lines at 6707 Å for HD77361 and HD 19745. The computed spectra for log ϵ(Li) = 3.96 and 3.69 matches very well with the observed spectra.

Li profile at 6707Å is quite strong and many of nearby weak lines get buried within the profile. For example the Fe I line at 6707Å which sits at the blue wing of the Li profile is difficult to separate out from the main Li profile. Also, Li profile at 6707Å is blended with hyperfine and possibly isotopic components. Apart from these, number of other weak lines of CN and atomic lines present (see Reddy et al. 2002) within the width of the profile which are significant in very cool spectra and where Li profile is not strong. For these reasons, Li profile at 6707Å must be analyzed using spectrum synthesis to derive accurate Li abundance. The wavelengths and line strengths of these components are taken from Smith et al. (1998), as corrected by Hobbs et al. (1999).

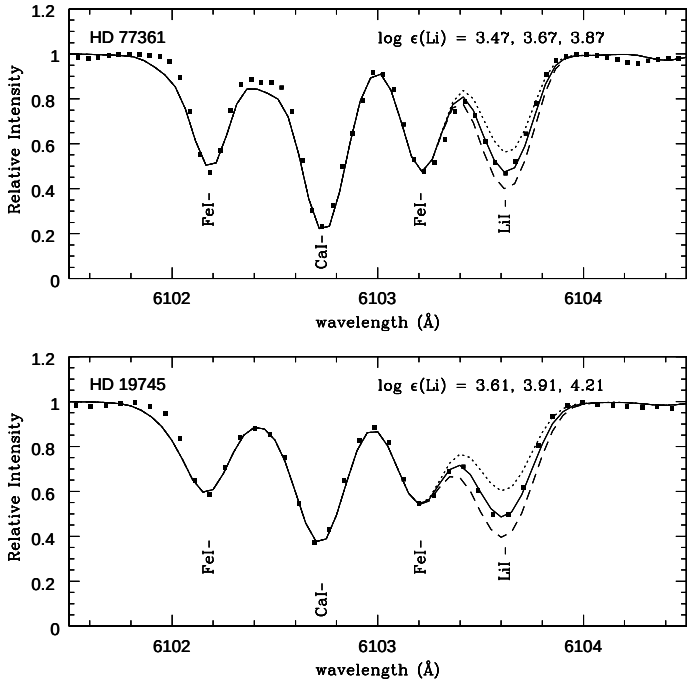

Figure 4.8: Observed (filled triangles) and synthetic spectra (lines) around the Li I lines at 6103 Å for HD77361 and HD 19745. The computed spectra for log ϵ(Li) = 3.67 and 3.96 matches very well with the observed spectra.

The line list for the 6707Å was adopted from Reddy et al. (2002) who have compiled lines in the vicinity of 6707Å primarily from Kurucz database. Entire line list was tested by reproducing the spectra of the Sun and Arcturus, both are Li-poor stars. In cases where the reproduction is satisfactory, they have modified log gf values. Now, for a given atmospheric model, spectrum was synthesized and broadened with the instrumental profile, derived $V_{\rm rot}$, and $V_{\rm m}$ (assumed to be 3 km s^{-1}). The spectra were computed for different values of Li abundance and were compared with the observed spectra. A similar procedure was followed for the synthesis of subordinate profile at 6103 Å. The line list for the Li line at 6103.6Å was compiled from Kurucz line database and tested with the Sun and Arcturus. Li abundances of the best fit computed spectra with the observed spectra for both the profiles are given in Table 4.11. In Figures 4.7 & 4.8, we have shown comparison of synthetic spectra with that of observed spectra for a couple of super Li-rich K giants: HD 77361 and HD 19745. As shown in Table 4.11, difference in abundances derived from 6103Å and 6707Å is quite significant. It is known that 6707Å line suffers from non-LTE effects much more severe compared to 6103Å line. Below we provide a brief description of non-LTE effect in Li which was studied by (Lind et al. 2009).

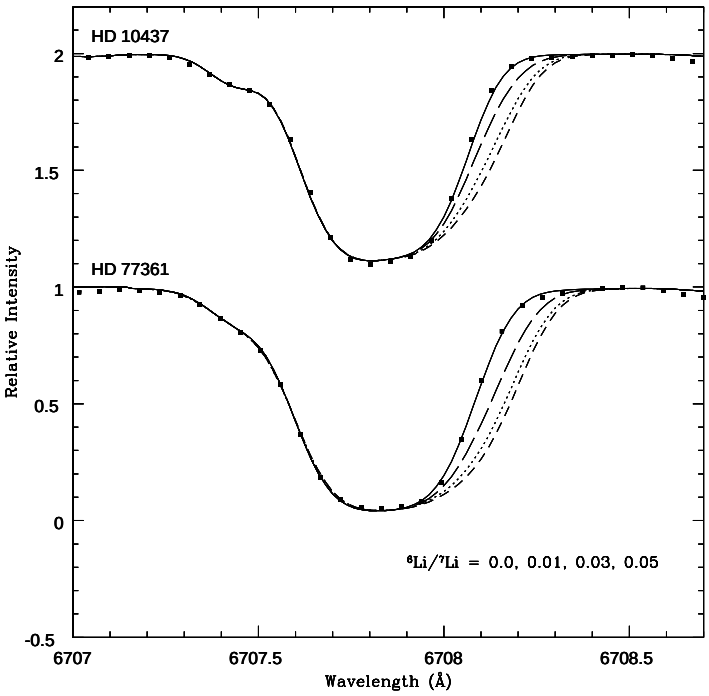

Figure 4.9: Synthetic spectra for four isotopic ratios ^{6}Li/^{7}Li = 0.0, 0.01, 0.03, and 0.05 for two Li-rich K giants, HD 77361 and HD 10437. The ^{6}Li/^{7}Li = 0.0 provides the best fit.

As noted earlier, we have made an assumption that the entire Li profiles are due to stable Li isotope which is ^{7}Li. However, there is a possibility for the presence of some amount of ^{6}Li. Here we investigate that possibility. The two profiles are separated by just 0.15Å and ^{6}Li components are at the red side of the main profile. Thus, addition of ^{6}Li will increase the asymmetry in red side and shifts the entire profile towards red. We have computed profiles for different ^{6}Li/^{7}Li ratios with varying total Li abundance and compared with the observed profiles. In all cases, our fittings showed that the profile computed for 6li/7li = 0.0 best matches the overall shape of the observed profile. Fitting has been done by fixing the observed Li profile position (6707.768 ± 0.02 Å), determined from the doppler shifts of symmetric Fe I and Ca I features for which accurate laboratory measurements are available. Within the measurement errors, the observed Li profile position matches with the predicted profile position λ_c = 6707.768 Å (for ^{7}Li only). Also, the Li abundances derived with the assumption of ^{7}Li only from 6707Å and 6103Å profiles agree very well after non-LTE correction (see Table 4.11). This is an indirect evidence that ^{6}Li is not present in detectable amount in any of these sample K giants.

Table 4.11: Derived Lithium abundance

HD	Li I 6707				Li I 6103			
	W_λ	A(Li)$_{LTE}$	NLTE$_{corr}$	A(Li)$_{NLTE}$	W_λ	A(Li)$_{LTE}$	NLTE$_{corr}$	A(Li)$_{NLTE}$
77361	495	3.96	−0.16	3.80	151	3.67	0.16	3.84
8676	410	3.86	−0.31	3.55	86	3.46	0.14	3.60
10437	405	3.76	−0.28	3.48	76	3.35	0.15	3.50
170527	360	3.31	−0.19	3.12	–	3.13	0.15	3.28
167304	315	2.95	−0.098	2.852	22	2.75	0.145	2.875
150902	315	2.64	0.01	2.65	18	2.56	0.17	2.73
51367	320	2.58	0.02	2.60	–	–	–	–
37719	305	2.70	0.01	2.71	–	–	–	–
145457	240	2.49	0.03	2.52	–	–	–	–
107484	238	2.04	0.10	2.14	–	–	–	–
118319	160	1.88	0.14	2.02	–	–	–	–
12203	157	2.01	0.083	2.093	–	–	–	–
133086	145	2.03	0.116	2.146	–	–	–	–
88476	114	2.12	0.089	2.209	–	–	–	–
40168	105	1.49	0.21	1.70	–	–	–	–

NON-LTE LI ABUNDANCES

The dominant NLTE effect is over-ionization of neutral lithium, which leads to small number populations in the ground (2s) and first excited (2p) states compared to LTE and to higher values of the line source functions. Both the effects on the source functions and the loss of line-opacity weaken the lines in non-LTE, making the abundance corrections positive. The corrections range from being close to zero for the hottest giants to a maximum of +0.45 dex for cool, metal-rich giants for the 6707Å line. For the 6103Å line, the corrections are slightly smaller, ≤ +0.3 dex. Lind et al. (2009) computed non-LTE and LTE Li abundances for both the profiles over a wide range of $T_{\rm eff}$ (4000 - 8000 K), log g (1.0 to 5.0), [Fe/H] (0.0 to -3.0) and for Li abundance (−0.3 to 4.2 dex). They have used LTE 1D MARCS model atmospheres with plane-parallel approximation and a radiative transfer code (MULTI) (Carlsson 1986, 1992). The model atom in this study includes 20 energy levels of neutral Li and ground state of singly ionized Li, six hyper-fine components of ^{7}Li by neglecting ^{6}Li for resonance line and 3 fine components for subordinate line.

In this study we have used the interpolation program provided by K.Lind (Private communication). For a given set of atmospheric parameters and LTE abundance the program interpolates values provided in the Tables 2 and 3 of Lind et al. (2009) and gives the

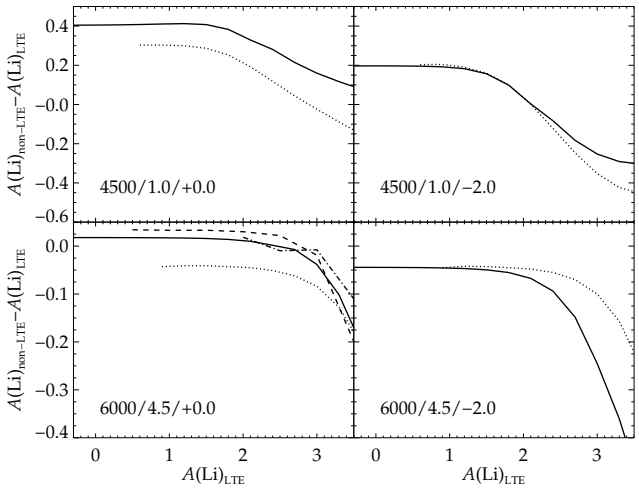

Figure 4.10: Non-LTE abundance corrections for 6707 Å as functions of LTE lithium abundance for the indicated stellar parameters in the lower left corner of each plot, to be read as $T_{\rm eff}/\log g/$[Fe/H]. *Solid*: Lind et al. (2009) corrections including charge transfer reactions with hydrogen as well as bound-bound transitions due to collisions with neutral hydrogen. The cross-sections are calculated with quantum mechanics (Belyaev & Barklem 2003; Croft et al. 1999). *Dotted*: Carlsson et al. (1994) corrections. *Dashed*: Takeda & Kawanomoto (2005) corrections. *Dash – dotted*: Pavlenko & Magazzu (1996)

correction for LTE abundance. The recipe works for models of microturbulence of 2 km/s with solar metallicity stars. The stars in our study are close to solar metallicity but with ξ_t from 1.3 to 1.6 km s^{-1}. Difference of 0.5 km s^{-1} may not be an issue as the difference corresponds to about 0.05 dex in the correction. The behavior of abundance corrections (non-LTE -LTE) are shown in Fig. 6. For cooler and supergiants corrections are positive ranging from 0.4 to 0.0 whereas for hotter and dwarf stars with high Li corrections are negative. The non-LTE corrected Li abundances are given in Table 4.11.

4.4.2 Carbon, Nitrogen, and Oxygen

Our approach to find the C and N abundances was by matching computed spectrum with the observed spectrum. Oxygen abundance was derived from equivalent widths. For carbon abundance, three indicators were used: the C I lines at 5380 and 5052 Å, and a C_2 Swan system triplet at 5135 Å, with lower weight given to another C_2 feature at 5141 Å. For some stars, we also have used carbon forbidden line [C I] at 8727Å as carbon abundance indicator. We took atomic and molecular data around the [C I] line

from Gustafsson et al. (1999). For the 5380 Å line we adopted the theoretical log = -1.57 (Biemont et al. 1993). For the spectrum syntheses near 5135 Å, we took data for C_2 lines from Querci, Querci, & Kunde (1971) and for MgH and the atomic lines from the Kurucz database. The derived carbon abundances from multiple indicators and the mean abundances are given in Table 4.12. All of them are found to have mild deficient in carbon except HD 12203 ([C/Fe] = 0.16), HD 107484 ([C/Fe] = 0.02), and HD 133086 ([C/Fe]=0.04) .

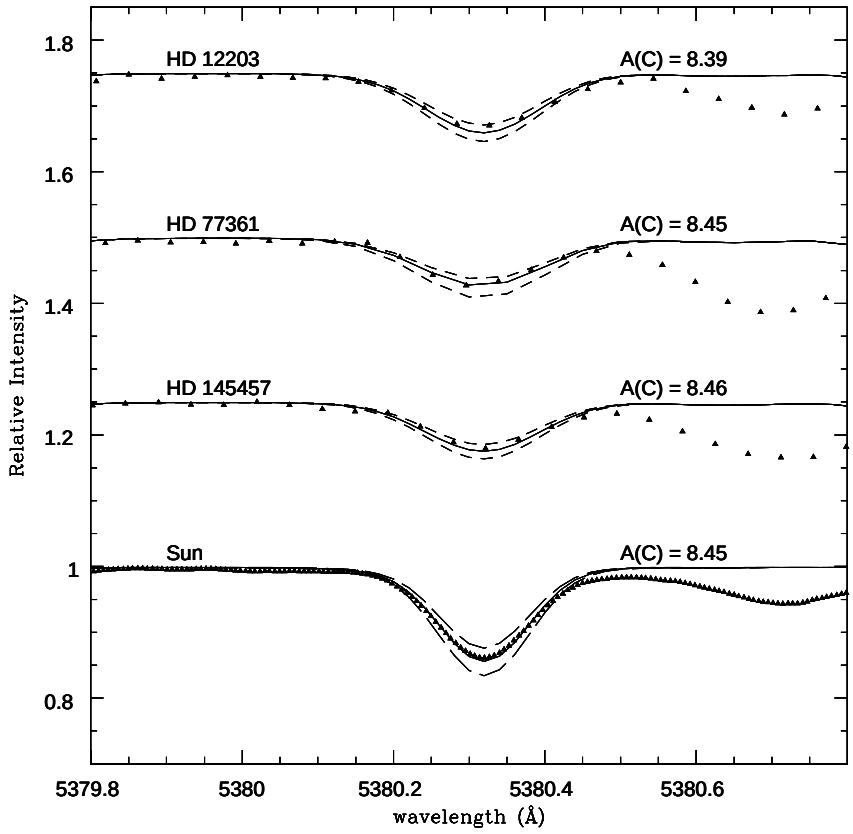

Figure 4.11: Sample spectra show the determination of Carbon abundance from the synthesis.

There are no detectable atomic transitions of N available in the spectra. The N I transitions in the visible range have LEP 7-10 eV which can't be excited in cool stars such as K giants. Our available option is CN Red system lines at 8005 Å. Basic data for the CN lines were taken from de Laverny & Gustafsson (1998) with a dissociation energy D_o = 7.75 eV (Lambert 1994). Spectra were computed for a given carbon abundance but for varying N abundances and we have adopted N abundance of the best fit comparison

with the observed spectra. Derived mean N abundances are given in Table 4.12. Oxygen abundances are obtained from the [O I] 6300 Å and 6363 Å lines. Allowance was made for a blending Ni I line Allende Prieto et al. (2001). A summary of the derived mean C, N, and O abundances and the ratios relative to Fe ([X/Fe]) are given in Table 4.12. The solar CNO abundances are derived in the same way as the abundances of our program stars. These are in good agreement with the solar CNO abundances found in literature (Luck & Heiter 2007).

4.4.3 The ^{12}C/^{13}C Ratio

The ^{12}C/^{13}C ratios were obtained from the CN Red system lines at 8005 Å. The CN line at 8004.7Å is a molecule of ^{13}C^{14}N. Once the abundances of ^{14}N and ^{12}C are derived, one can obtain ^{12}C/^{13}C ratio from 8003Å line by varying ^{12}C/^{13}C ratios for fixed C and N abundances. One needs to be cautious as the 8003 Å line is normally weak (a few mÅ) and close to telluric lines. In stars of red shifted lines, there is a possibility that these lines gets blended with weak telluric lines. We have inspected this region using Arcturus spectrum and also our own hot high rotating star spectra. In cases where we are not sure about the contamination by the telluric lines, we have divided program spectra with that of hot star spectra. The ^{12}C/^{13}C values derived from matching computing spectra with observed spectra are given in Table 4.12. The error on the isotopic ratio was estimated as a quadratic sum of the various uncertainties. The uncertainty in C and N abundances of ± 0.1 dex leads to an uncertainty of ± 2 in the ^{12}C/^{13}C ratio. The rms = 0.004 of the S/N ratio at the continuum yields approximately an uncertainty of 1 in the carbon ratio. The quoted uncertainties in the derived model parameters have an insignificant effect on the derived ^{12}C/^{13}C ratio.

4.5 DISCUSSION AND CONCLUSIONS

Li among K giants: We confirm that all the 15 Li-rich candidate K giants identified from our low resolution spectroscopic survey are Li-rich K giants based on high resolution spectroscopy. We found four as super Li-rich where log ϵ (Li) $\geq$= 3.2, a value derived for ISM, often referred to as cosmic Li abundance. Li abundances in the super Li-rich giants are about a factor of 100 (or two orders of magnitude) more than the maximum expected Li in normal K giants. Rest of the 11 giants are Li-rich with Li abundance ranging from 1.7 dex to 2.9 dex about a factor of 1.5 to 25 more than the expected values. This is the largest number of Li-rich K giants that have been found in any single study. With

Table 4.12: CNO abundances and $^{12}C/^{13}C$ ratios

HDno	[Fe/H]	C	N	O	[C/H]	[N/H]	[O/H]	[C/Fe]	[N/Fe]	[O/Fe]	CNO	[CNO/H]	[CNO/Fe]	CN	[CN/H]	[CN/Fe]	C/O	$^{12}C/^{13}C$
8676	0.02	8.30	8.39	9.10	-0.2	0.21	0.29	-0.22	0.19	0.27	9.231	0.191	0.171	8.648	-0.022	-0.042	0.158	5
10437	0.10	8.21	8.43	9.14	-0.29	0.25	0.33	-0.39	0.15	0.23	9.258	0.218	0.118	8.635	-0.035	-0.135	0.117	5
12203	-0.27	8.39	8.84	8.98	-0.11	0.66	0.17	0.16	0.93	0.44	9.277	0.237	0.507	8.972	0.302	0.572	0.257	7.5
51367	0.20	8.63	8.62	9.05	0.13	0.44	0.24	-0.07	0.24	0.04	9.293	0.253	0.053	8.926	0.256	0.056	0.380	8.5
77361	-0.02	8.45	8.37	8.89	-0.05	0.19	0.08	-0.03	0.21	0.1	9.111	0.071	0.091	8.713	0.043	0.063	0.363	4.3
88476	-0.10	8.08	8.38	8.97	-0.42	0.2	0.16	-0.32	0.3	0.26	9.112	0.072	0.172	8.556	-0.114	-0.014	0.129	9.0
107484	0.18	8.70	8.48	9.07	0.2	0.3	0.26	0.02	0.12	0.08	9.296	0.256	0.076	8.905	0.235	0.055	0.427	12.5
133086	0.02	8.02	8.54	9.05	-0.48	0.36	0.24	-0.5	0.34	0.22	9.197	0.157	0.137	8.655	-0.015	-0.035	0.093	7.0
145457	-0.08	8.46	7.95	8.86	-0.04	-0.23	0.05	0.04	-0.15	0.13	9.042	0.002	0.082	8.577	-0.093	-0.013	0.398	10.0
150902	0.09	8.26	8.30	8.90	-0.24	0.12	0.09	-0.33	0.03	0.03	9.070	0.030	-0.060	8.581	-0.089	-0.179	0.229	5.0
167304	0.18	8.35	8.60	9.13	-0.15	0.42	0.32	-0.33	0.24	0.14	9.295	0.255	0.075	8.794	0.124	-0.056	0.166	7.5
148293	0.08	8.53	8.30	9.04	0.03	0.12	0.23	-0.05	0.04	0.15	9.213	0.173	0.093	8.731	0.061	-0.019	0.309	16.0
90633	0.02	8.61	8.10	8.89	0.11	-0.08	0.08	0.09	-0.1	0.06	9.117	0.077	0.057	8.727	0.057	0.037	0.525	7.0
214995	0.00	8.43	8.19	8.87	-0.07	0.01	0.06	-0.07	0.01	0.06	9.066	0.026	0.026	8.627	-0.043	-0.043	0.363	13.0
40827	0.10	8.40	8.35	8.72	-0.1	0.17	-0.09	-0.2	0.07	-0.19	9.000	-0.040	-0.140	8.677	0.007	-0.093	0.479	10.0
63798	-0.10	7.89	8.60	8.62	-0.61	0.42	-0.19	-0.51	0.52	-0.09	8.951	-0.089	0.011	8.677	0.007	0.107	0.186	8.0
19745	-0.05	8.35	8.15	8.68	-0.15	-0.03	-0.13	-0.1	0.02	-0.08	8.926	-0.114	-0.064	8.562	-0.108	-0.058	0.468	15.0
183492	-0.08	8.33	8.22	8.73	-0.17	0.04	-0.08	-0.09	0.12	0.00	8.962	-0.078	0.002	8.580	-0.090	-0.010	0.398	9.0
108471	-0.01	8.33	8.22	8.83	-0.17	0.04	0.02	-0.16	0.05	0.03	9.024	-0.016	-0.006	8.580	-0.090	-0.080	0.316	10.0
120602	-0.08	8.26	8.21	8.83	-0.24	0.03	0.02	-0.16	0.11	0.1	9.009	-0.031	0.049	8.537	-0.133	-0.053	0.269	9.0
203136	0.05	8.18	8.43	8.70	-0.32	0.25	-0.11	-0.37	0.2	-0.16	8.965	-0.075	-0.125	8.624	-0.046	-0.096	0.302	16.0

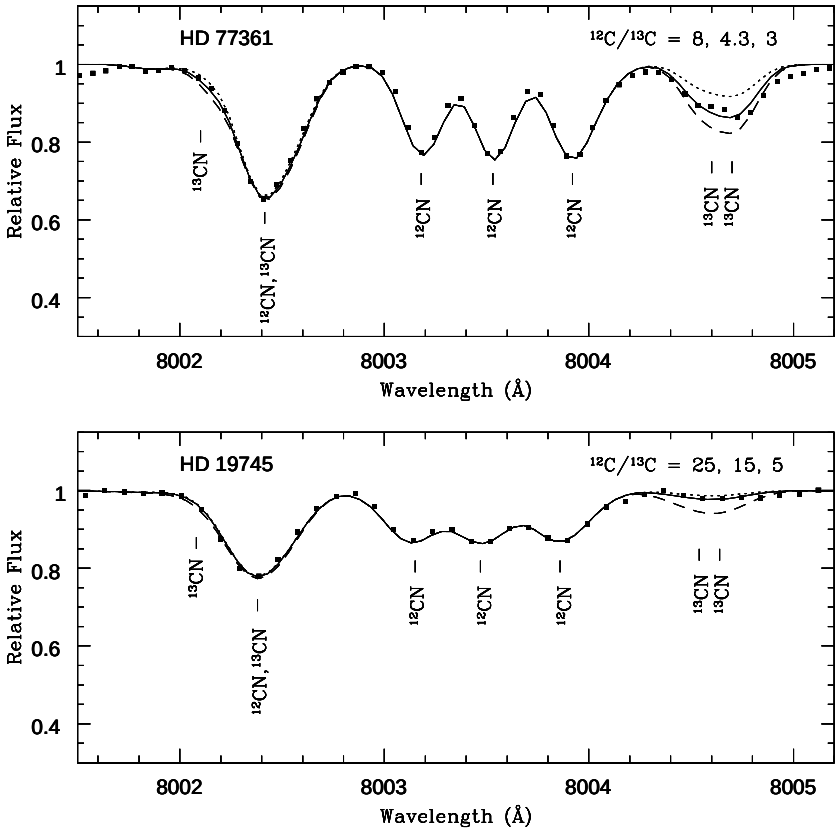

Figure 4.12: Comparison of synthetic and observed spectra for HD 77361 and the template star HD 19745 in the wavelength region of 8000 Å. Ratio of ^{12}C/^{13}C is derived using the ^{13}C^{14}N lines at 8004.6 Å.

these findings the current Li-rich sample goes up by a factor of 2. Importantly, the survey resulted four super Li-rich K giants which is by far the highest from a single study which increases the total number of super Li-rich giants to 12.

Another important factor is that our present survey confirms that the Li-rich K giants are rare. Our study suggests that just 15 out of 2000 stars are Li-rich implying that just under 1% of giants within mass range of 0.8 - 2.5M$_\odot$ (or late G- and K- spectral type RGB stars) show Li-richness in their photopheres. There are not many surveys that could be used for comparison with our results. The high resolution spectrsocopic survey on 644 sample giants by Brown et al. (1989) resulted in 11 Li-rich giants (G- and K-spectral type) which are about 2%. This discrepancy can be easily understood from the fact that Brown survey was undertaken much before the Hipparcos astrometry made available to the public in 1998. As a result, we expect chances of mixing with massive RGBs and

even AGB stars in their sample is very high. To understand the discrepancy, we have re-derived luminosities and temperatures and put them in HR diagram (see Figure **??**). We found many of their sample stars more massive and relatively more evolved on the RGB compared to our sample. Incidences of having more Li in more massive stars ($\geq 2.5 M_{\odot}$) may probably be due to insufficient mixing of original main sequence surface Li. Also, some of these stars could be early AGB stars where Li is known to be produced through hot bottom burning (see Sackmann & Boothroyd 1999).

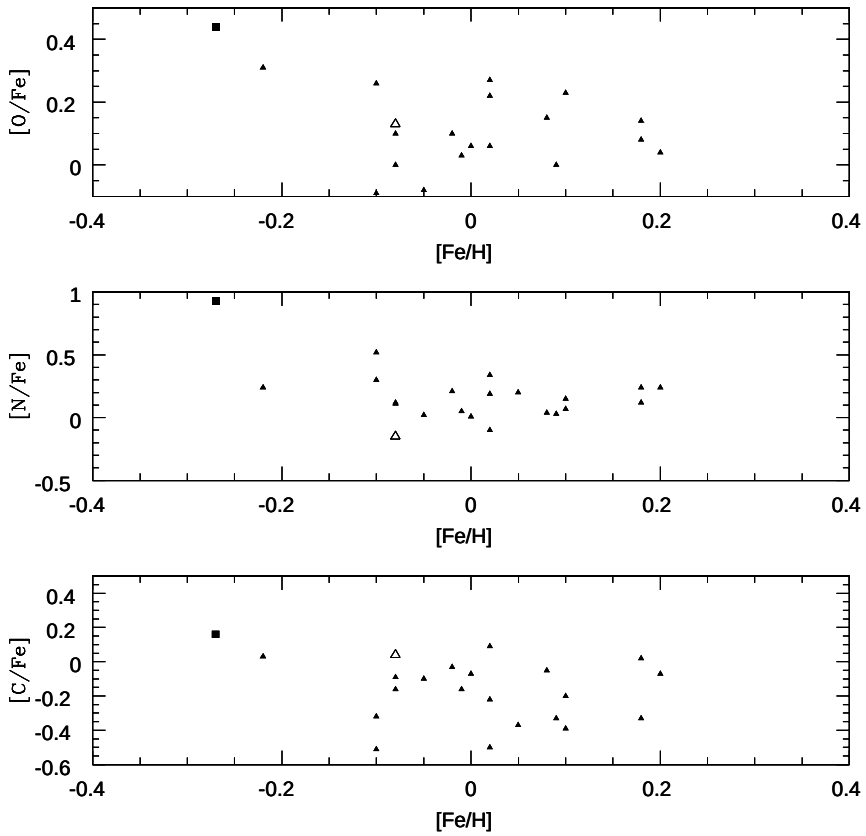

Figure 4.13: Carbon, Nitrogen,and Oxygen abundances with respect to iron abundance are plotted against Metallicity. Filled square represents HD 12203, a thick disk giant. Open triangle represents HD 145457, planet host giant.

C,N,O abundances : Abundances of CNO and carbon isotopic ratios for the entire new Li-rich K giants are given in Table 4.12. Also, the newly derived CNO and $^{12}C/^{12}C$ ratios for the known Li-rich giants are given. Along with Li, CNO and carbon isotopes are sensitive, and their composition get modified as stars evolve off the main sequence to RGB and to AGB. Standard models make predictions about the effects of first dredge-

up effects on the surface abundances of Li, C, N, and O. Observations of normal red giants confirm these predictions, qualitatively, if not always quantitatively. Interpretation of lithium abundances is assisted and possibly complicated just by knowledge of the C, N, and O abundances. In Table 4.12, we have given CNO abundances relative to solar abundances ((X/H]) as well as relative to Fe ([X/Fe]). Also, provided are C/O, [CN/Fe], [CNO/Fe] etc. These ratios will track abundance changes as a star evolves. Note the changes in values of the K giants from the values of main sequence dwarf, the Sun (in this case). As predictions and also observed in most of the RGB stars, the Li-rich K giants in this study show mild reduction in carbon and increase in N but preserving the total abundance of C and N, and also C, N and O. The C/O ratio for the K giants is down by a factor of two from the main sequence. In Figure 4.14, log ϵ(Li) versus CNO abundances with respect to Fe are shown. Figures suggesting no trend with the Li enhancement and Li abundance in Li-rich K giants seems to be independent of CNO changes. The CNO abundances are in conformity with the model predictions for the RGB stars.

However, among the new Li-rich giants, HD 12203 is the only RGB star which is an anomaly (see Figure 4.13). The anomaly being the large N and O abundances and the star has significantly large value of [CNO/Fe] = 0.51 (see Table 4.12). This means that the total abundance of CNO is not conserved as expected from CNO process. This suggests that some fresh N got dredged-up to the surface. Exact cause for such high amount of N abundance is not known but probably this can be attributed to those stars which have gone through the 2nd dredge-up process. The 2nd dredge-up further enhances N abundance and it is not clear whether this comes from the freshly synthesized C from 3α-reactions. In that case HD 12203 must be an early AGB star. As for the over abundance of O is concerned, this may be due to its population. HD 12203 is the only star whose kinematics show that its probability to belong to thick disk is P_{thick} = 83% (see Table 4.7). Thick disk stars are old ($\geq$ 10 Gyrs) and metal-poor ($-0.3 - 1.5$ dex or less) population stars which show enhancement in α-process elements (see Reddy et al. 2006).

Carbon isotopic Ratio $^{12}C/^{13}C$ and Li: ^{12}C/^{13}C is one of the most sensitive indicators of the stellar evolution. The ratio decreases as the star evolves off the main sequence value of ^{12}C/^{13}C $\approx$ 90 to 3, CN equilibrium value, towards the tip of the RGB. Some amount of the ^{13}C abundance produced through CN reaction in the H-burning shell gets dredged-up before getting converted to ^{14}N. During this process, the main isotope ^{12}C gets depleted as it gets converted to ^{13}C as well as ^{14}N (See Figure **??**). The reduced ^{12}C and enhanced ^{13}C would give the net result of a sharp reduction in ^{12}C/^{13}C ratio.

Thus the ^{12}C/^{13}C ratio traces the convection much more effectively. Information of

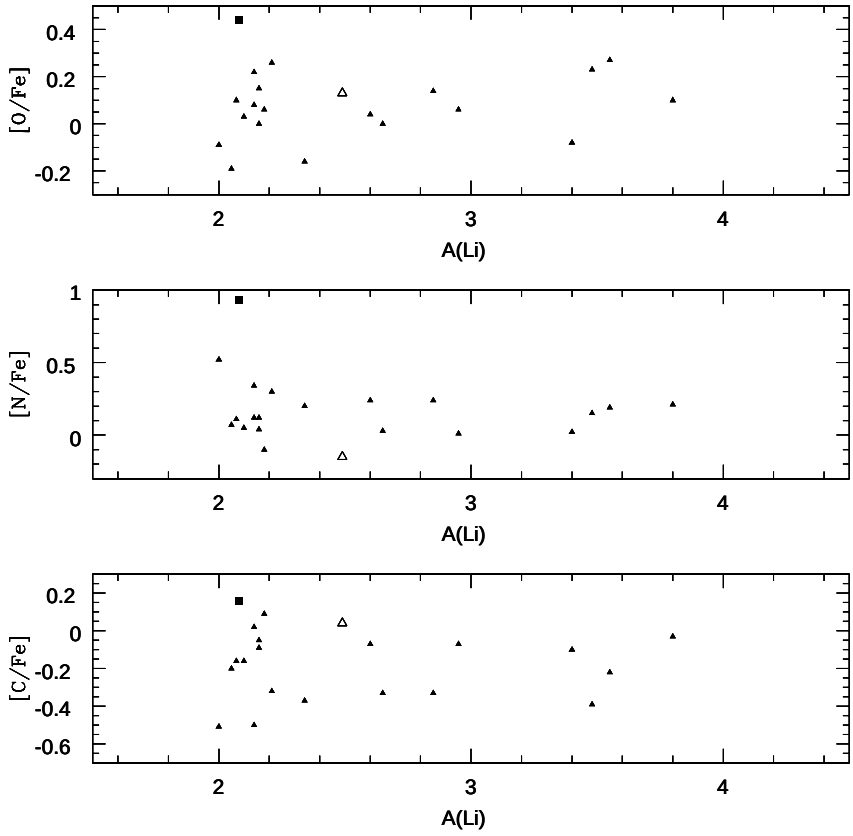

Figure 4.14: Carbon, Nitrogen,and Oxygen abundances with respect to iron abundance are plotted against Lithium abundance.

$^{12}C/^{13}C$ will certainly help us to understand the Li as this element is very fragile and highly sensitive to mixing. The derived ratios for both the new as well as know Li-rich K giants are given in Table 4.12. In general, $^{12}C/^{13}C$ values suggest that all the Li-rich K giants have gone through modest to severe mixing of material. In most cases, $^{12}C/^{13}C$ values are below 20 and in some cases below 10. Compared to vast majority of RGB stars and the standard stellar models these values are much lower. Standard models predict $^{12}C/^{13}C$ values of 25-35 (Boothroyd & Sackmann 1999). Among Li-rich K giants only five fall in that category and all of those are known ones. The recent theoretical models of extra mixing (see for example Eggleton et al. 2008) do predict lower values for low mass solar metallicity stars. Again, lowest $^{12}C/^{13}C$ they could predict are in the range of 10-15 towards the tip of RGB. The very low $^{12}C/^{13}C$ values (<10) found in many of the Li-rich K giants, that too not at the tip but near the RGB luminosity bump, is in fact a puzzle. To understand the Li behavior with the convection, we have plotted $^{12}C/^{13}C$ ratios versus

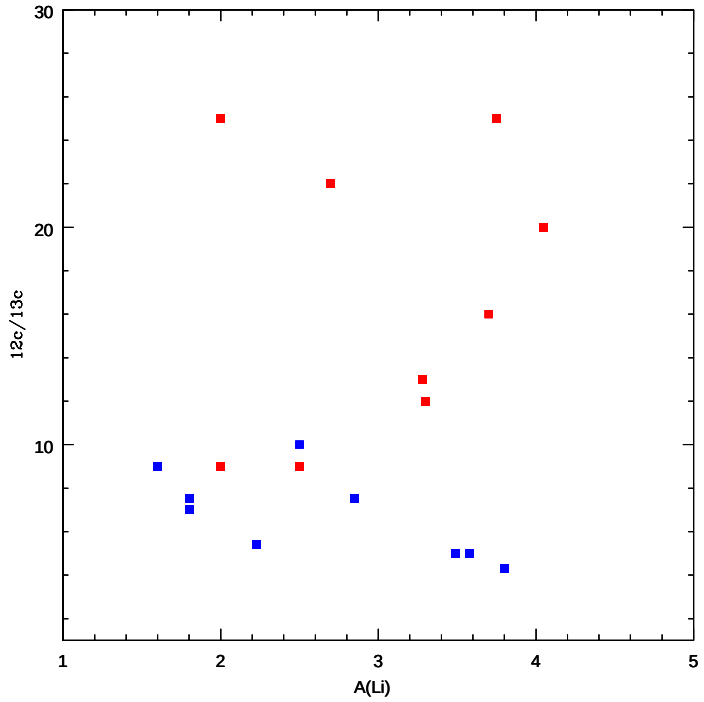

Figure 4.15: Carbon isotopic ratios against Li abundances

Li in Figure 4.15. Red symbols represent known Li stars and the blue ones are from this study. Two remarks can be made from the plot shown in Figure 4.15: a) if we consider them as all Li-rich K giants as one group we do not see any particular trend with Li enhancement, b) All of the new Li-rich K giants show very low ^{12}C/^{13}C and there seems to be a slight correlation between ^{12}C/^{13}C and Li abundances. In that ^{12}C/^{13}C gradually decreases with steep increase in Li. Two know Li-rich K giants (HD 183492, PDS 100) also fall in this trend. More discussions on very low ^{12}C/^{13}C and high Li abundances are given in Chapter 5.

CHAPTER 5

SUPER LI-RICH GIANTS WITH ANOMALOUS LOW $^{12}C/^{13}C$ RATIO

5.1 INTRODUCTION

Super Li-rich K giants are much more rare than Li-rich giants, and as of now there are just one dozen (de La Reza & da Silva 1995; Balachandran et al. 2000; Drake et al. 2002; Reddy & Lambert 2005; Luck & Heiter 2007; Carlberg et al. 2010), including the four being studied here. To understand the distribution of Li-rich stars in terms of their mass and luminosity, Charbonnel & Balachandran (2000) located all the known Li-rich stars on the Hertzsprung-Russell diagram, thanks to the accurate parallaxes from *Hipparcos* mission (Perryman et al. 1997). The study revealed that the ($M/M_{\odot} \leq 2.0$) super Li-rich (log ϵ(Li) $\geq$ 3.3 dex) K giants are confined to a small region on the HR diagram, the so called luminosity bump: log $L/L_{\odot}$ = 1.45 - 1.9; log T_{eff} = 4450 - 4650 K) (Girardi et al. 2000). Also, these stars are found to have lower $^{12}C/^{13}C$ ratios than the expected from the standard mixing theory. It is not well understood how the K giants with very deep convective envelope and efficient mixing, as suggested from the measured low values of $^{12}C/^{13}C$, possessed such high amounts of Li; almost 10 times larger than the ISM value. In the literature, a different class of super Li-rich stars were reported. They are either massive ($\geq$ 4 $M_{\odot}$) weak G- band stars (Lambert & Sawyer 1984) or AGB stars (Smith & Lambert 1989) or low mass metal-poor giants (Kraft et al. 1999; Monaco & Bonifacio 2008).

The high values of Li in the super Li-rich K giants are thought to be due to the stellar nucleosynthesis and some kind of extra mixing (Denissenkov & Weiss 2000; Palacios et al. 2001; Denissenkov & Herwig 2004). At the luminosity bump on the RGB, the hy-

drogen burning shell passes the μ-barrier or the mean molecular weight discontinuity that was created during the 1st dredge-up. This allows mixing between the cool outer layers and the hotter inner regions. This so called extra-mixing theory associated with cool bottom processing was invoked for Li enhancement. For low mass stars of solar metallicity at the luminosity bump, theoretical models (e.g., Denissenkov & Herwig 2004) are constructed to match the observed peak Li abundance of log ϵ(Li) $\geq$ 3 and low $^{12}C/^{13}C \approx$ 15 - 28. The theoretical results are, in general, in agreement with the observed values of super Li-rich K giants (Charbonnel & Balachandran (2000) and references there in). As star evolves from the bump region and moves up towards the tip of RGB, Li drops sharply with the $^{12}C/^{13}C$ ratio (Lambert et al. 1980).

The analysis of high resolution specra of new Li-rich giants resulted in four super Li-rich stars in which three are found to have anomalously low isotopic ratios of carbon, that are close to CN equilibrium value ($^{12}C/^{13}C \approx 3.5$). Determination of Li abundance and $^{12}C/^{13}C$ ratios are discussed extensively in Chapter 4. In this chapter, we discuss high Li and low $^{12}C/^{13}C$ in these three stars along with other super Li-rich giants. We also discuss the various other stellar parameters of these giants and their location in the H-R diagram.

5.2 SUPER LI-RICH GIANTS

The three program stars, HD 77361, HD 8676, and HD 10437, are bright field stars and no previous spectroscopic analysis of either low- or high resolution spectra is available. Li-richness of these stars are idenfied from the low resolution spectra using the line depth ratios of Li and nearby Ca line. The detail description of the line depth ratio technique was discussed in Chapter 3. The low resolution spectra in which strong Li lines are identified are shown in the Figure 5.1. Later, Li-richness is confirmed by obtaining series of high resolution spectra. Figure 5.2 shows the determination of Li from the sythesis tecnique, which confirms the super Li-richess in these giants. Figure 5.3 shows the determination of $^{12}C/^{13}C$ ratio for all these giants. Figures 5.2 & 5.3 also shown the known super Li-rich K giant, HD 19745, whose Li abundance and $^{12}C/^{13}C$ are rederived similar to program stars, for comparison.

Derived atmospheric parameters, non-LTE Li abundance values, $^{12}C/^{13}C$ ratios, and vsini of the program stars along with other super Li rich stars are summarized in Table **??**. Stellar masses are obtained from the evolutinary tracks. Radius is calculated from luminosity and temperature. Values of projected rotational velocity (*vsini*) are derived from the synthesis of few Fe I lines (See chapter 4 for details). Luminosities are derived from

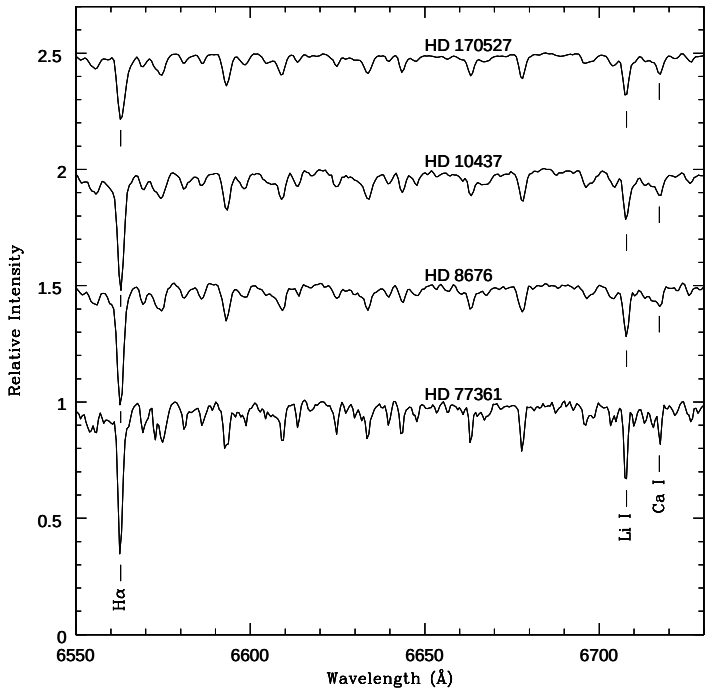

Figure 5.1: Detection of Strong Li line in Super Li-rich giant spectra are shown in the H-R diagram. Li and ca lines are marked

the hipparcos parallaxes and V magnitude. Few faint stars for which hipparcos parallaxes are not available, luminosities are derived from the spectroscopy. We have re-derived Li abundance, vsini, and carbon isotopic ratios for the known sample whose spectra were obtained along with the new Li-rich stars, also given in the same table. The values derived by previous studies are given in bracket. For HD 214995, we have derived the $^{12}C/^{13}C$ for first time as no attempts so far in literature. The spectra that are not available for few faint southern rapid rotators, IRAS 13313-5838 (Drake et al. 2002) and G 0928+73.2600 (Carlberg et al. 2010), for which values are taken from the original papers. Metallicity of most of the Li-rich stars are nearby solar values except for HDE 233517 and G 0928+73.2600 which are slightly metal poor (-0.3 dex). The masses of these stars are in the range of 1 to 2.5 $M_{\odot}$ indicates that all are low mass giants.

Figure 5.4 shows the location of super Li-rich giants in the H-R diagram. Magenta symbols are the new super Li-rich stars and blue symbols are the known ones. The location of these giants in the H-R diagram confirms that these are giants and not pre-main sequence stars. The appearance of these giants in the HRD suggests that they are clustered in two different groups, cooler and hotter. A group of cool (< 4700) super Li-rich

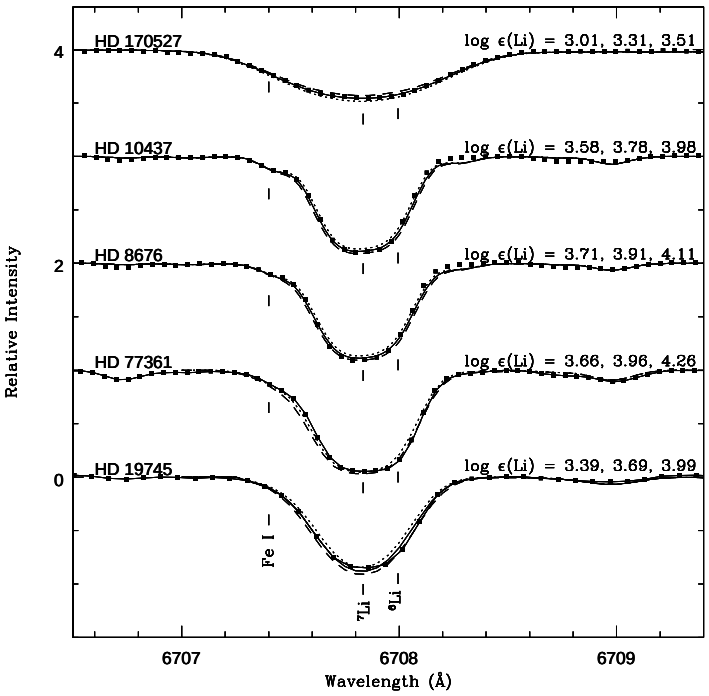

Figure 5.2: Confirmation of Li-richness in Super Li-rich giants are shown in the H-R diagram. Positions of ^{7}Li and ^{6}Li along with Fe I is marked

stars occupy near to the red kinks of evolutionary tracks. A group of hotter (> 4800) gaints are near to the black lines that are associated with the horizontal branch tracks.

5.3 DISCUSSION AND CONCLUSION

For the most Li-rich K giant HDE 233517 and new super Li-rich giant HD 170527, unfortunately, the $^{12}C/^{13}C$ ratio is not available, probably, due to its very high rotation of *vsini* = 17 km s^{-1} and 25 km s^{-1}, respectively. Generally, the $^{13}C^{14}N$ lines at 8004.6 Å, often used for the carbon isotopic ratio, is weak and gets smeared out in the spectra of high rotation stars. It is clear from the Table that these giants have a range of projected rotational velocities and isotopic ratios. Seven out of twelve are moderately high rotators ($\geq$ 5 km s^{-1}) and remaining are slow rotators similar to normal giants ($\leq$ 3 km s^{-1}). Note the rapid rotators have significantly higher $^{12}C/^{13}C$.

It is clear from the Table 5.1 that HD 77361 is a super Li-rich, and the 3rd most Li-rich K giant amongst twelve super Li-rich K giants known so far. The derived luminosity ($\log(L/L_{\odot})$ = 1.66) and $T_{\rm eff}$ = 4580 K places HD 77361 at the RGB luminosity bump.

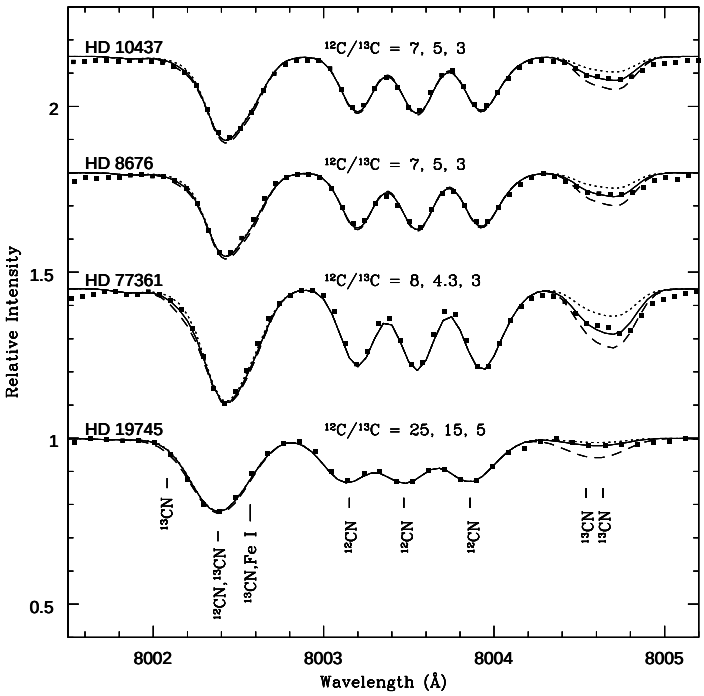

Figure 5.3: Determination of $^{12}C/^{13}C$ of new super Li-rich giants are shown along with the Known sample,HD 19745, for comparison.

The most striking from the results shown in Table 5.1 is that the lowest $^{12}C/^{13}C$ ratio of HD 77361 among all super Li-rich giants. The other super Li-rich stars have significantly higher values of $^{12}C/^{13}C$ ratios except HD 8676 and HD 10437. It is puzzling that HD 77361 has a $^{12}C/^{13}C$ ratio that is close to the CN equilibrium value, but continues to have peak value of Li on its surface. Another important point to be noticed is that the location of super Li-rich stars in the H-R diagram. The group of cool super Li-rich stars are very close to the expected luminosity bump region for a given stellar mass. Results of HD 77361 strengthens the argument that the changes to the stellar structure of low mass stars at the bump region are the main cause for the sudden reduction in $^{12}C/^{13}C$ ratio, and the enhancement of Li on the surface of first ascend giant branch stars.

5.3.1 LI AND $^{12}C/^{13}C$ AT THE RGB BUMP

It is known that at the RGB bump the hydrogen burning shell moves past the so called μ-barrier. In the absence of μ-barrier, convective zone reaches much deeper level dredging up the hydrogen burning products to the surface altering abundances of Li, C, N, and ^{13}C much more severely compared to the predictions of standard 1st dredge-up scenario. This

Table 5.1: Values of stellar parameters (Metallicity, $T_{\rm eff}$, Mass, luminosity) and the surface abundances values of log ϵ(Li) and carbon isotopic ratios of super Li-rich K giants.

Star	[Fe/H]	$T_{\rm eff}$	M$\star$/M$_\odot$	log L/L$_\odot$	R$\star$/R$_\odot$	log ϵ(Li)	$^{12}C/^{13}C$	*V sini*
HD 77361	−0.02	4580	1.5	1.66	10.75	3.82	4.3 ± 1	3
HD 8676	0.00	4860	2.4	1.67	9.66	3.58	5.0 ± 1	3
HD 10437	0.05	4830	2.5	1.77	10.97	3.49	5 ± 1	3
HD 170527	...	4811	2.3	1.69	10.11	3.20	...	25
HD 233517	−0.37	4475	1.7	2.0[a]	16.66	4.22	...	17.6
IRAS 13539-4153	−0.13	4300	0.8	1.60[a]	11.38	4.05	20	5
HD 9746	−0.06	4400	1.92	2.02	17.64	3.75	24(28±4)	8.7
HD 19745	−0.05	4700	2.2	1.90[a]	13.46	3.70	15(16±2)	2
HD 194937	−0.01	4863	1.73	1.57		3.41	...	1.0
IRAS 13313-5838	−0.09	4540	1.1	1.85[a]	13.62	3.3	12^{+8}_{-2}	20
HD 214995	−0.00	4737	1.80	1.54		3.28	13	4.5
G0928+73.2600	−0.25	4885		1.75		3.30	28±8	8.4

[a]Hipparcos astrometry is not available and values of luminosities and masses are derived from spectroscopy.

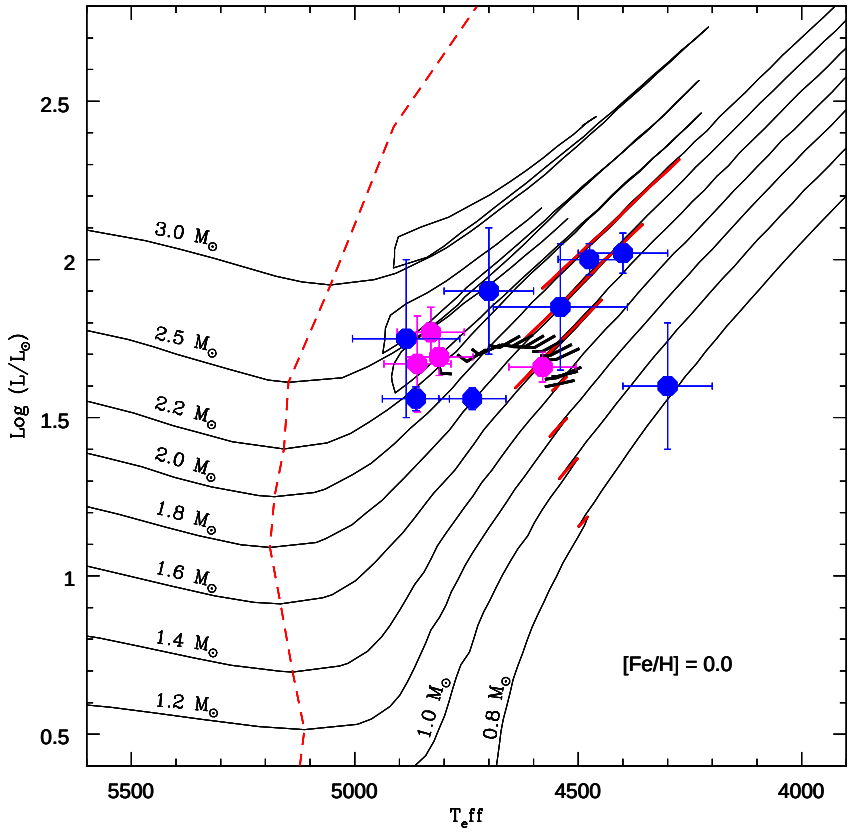

Figure 5.4: Super Li-rich giants are shown in the H-R diagram. Blue and magenta symbols are known and new sample giants, respectively.

is known as extra mixing (Sweigart & Mengel 1979; Charbonnel et al. 1998) which is different from the ordinary convective mixing. The extra mixing is invoked to explain the observed, in general, low values of Li and $^{12}C/^{13}C$ ratio at or above the RGB bump (Lambert et al. 1980; Gratton et al. 2000). The exact mechanism for the extra mixing is still an issue to be worked out.

For the Population I stars of low mass ($M/M_{\odot} \leq 2.5$) theoretical models of extra mixing predict final $^{12}C/^{13}C$ ratios as low as 10 when star evolves to the RGB tip. Boothroyd & Sackmann (1999) demonstrated that deep circulation mixing at the base of convective envelope and the associated cool bottom processing brings down the 1st dredge-up prediction of $^{12}C/^{13}C \approx 28$ to the lowest final value of 10 closer to the RGB tip for a star of 1.5 $M_{\odot}$ with solar metallicity. Similar results from the recent computations based on enhanced extra mixing triggered by external sources (Denissenkov & Herwig 2004) and mean molecular weight inversion or δ-mixing (Eggleton et al. 2008) predicted final values

of $^{12}C/^{13}C \approx$ 10-14 for low mass Pop I stars. However, in all the models, stars at the RGB bump region are expected to have $^{12}C/^{13}C$ ratios at about 15 or more.

Earlier suggestions of planet or dwarf companion merger (Alexander 1967; Brown et al. 1989; Siess & Livio 1999) with the parent stars or addition of Li rich material from the nearby novae ejections (Gratton & D'Antona 1989) cannot explain the localization of super Li-rich stars on the HR diagram. If the Li enhancement in the K giant is due to the external sources like planet engulfment or accretion of novae material, it could happen anywhere on the RGB phase. Absence of low mass super Li-rich giants below or above the RGB bump simply means that Li enhancement is related to changes in the internal stellar structure and the mixing process that are associated with the luminosity bump. Depletion of Li starts once again, from the peak Li abundance at the RGB bump, as stars evolve towards the RGB tip. Observations show, in general, very low Li abundances (log ϵ(Li) = -1.0 - 1.5 dex) in K giants between the bump and the RGB tip. As discussed by de La Reza et al. (1997) and calculated by Denissenkov & Herwig (2004) the super Li-rich phase on the RGB seems to be very short (a few million years), and all the low mass stars, perhaps, experience this phase.

Another suggestion one can infer from the results shown in Table 2 is that the absence of correlation between Li enhancement and the $^{12}C/^{13}C$ ratio at the bump. It seems Li enhancement in the K giants at the bump is independent of the $^{12}C/^{13}C$ ratio, and hence longevity or the extent of the deep mixing process. Sackmann & Boothroyd (1999) suggest that Li can be enhanced on the surface as long as fast deep mixing is ensured, and in fact they have predicted high values of Li towards the RGB tip (not at the RGB bump) where $^{12}C/^{13}C$ values are low. On the other hand, Palacios et al. (2001) hypothesized that the surface ^{7}Li enhancement is the precursor for the extra mixing. Given the very low value of $^{12}C/^{13}C$ ratio for the HD 77361, one may suggest that erasing the μ-barrier, and hence the free mixing of material between hydrogen burning shell and the bottom of convective outer layer seems to be providing conducive environment for the enhancement of surface Li abundance.

It is understood that Li is produced in the inner layers of the stars through Cameron & Fowler (1971) mechanism. Sustaining the Li production and dredging up the Li rich material to outer layers to the observed levels is still an unsolved problem. For safe transportation of ^{7}Be produced in the inner layers via $^{3}He(\alpha,\gamma)^{7}$Be to cooler regions, so that ^{7}Li could be produced and mixed up with the photosphere, a few possibilities were explored. Palacios et al. (2001) suggested Li-flash scenario for high Li-abundance. In this scenario, ^{7}Be diffuses outward where Li can be produced via $^{7}Be(e^{-},\nu)^{7}$Li and forms the

so called Lithium burning shell. Energy release from the destruction of ^{7}Li by proton as well as from production of ^{7}Li destabilize the Li burning shell leading to runway situation. This in turn leads to the enhanced meridional circulation and hence the observed Li enhancements. In this scenario Li enhancement precedes the ^{12}C/^{13}C reduction. This explains the localization of super Li-rich K giants at the bump and also the relatively high values of carbon isotopic ratios (Charbonnel & Balachandran 2000). As K giants evolve away from the bump Li starts decreasing with the decreasing ^{12}C/^{13}C ratio. A totally different approach was suggested from the computations by Denissenkov & Herwig (2004). An enhanced extra mixing triggered by spinning up of the K giants with the external angular momentum can produce the required mixing coefficients. Source of the external angular momentum could be either by the synchronization of K giant's spin with the orbital motion of close binary or engulfment of massive planet. This mechanism will enhance K giant's angular momentum by 10-fold, and explains high rotation velocity observed in some of the Li-rich K giants. But, as stated earlier, fails to explain the presence of all the twelve super Li-rich at the bump and the absence of super Li-rich stars any where along the RGB path. In all of these models, Li peak was achieved when the ^{12}C/^{13}C ratios are around 15 - 28 which are in general agreement with the six of the twelve super Li-rich stars shown in the Table 5.1.

CHAPTER 6

INFRARED EXCESS VS LITHIUM

6.1 INTRODUCTION

Low mass K giants are known to loose mass through stellar winds which are driven by stellar radiation. Mass-loss creates circumstellar dust around stars which absorbs part of star's radiation in visual wavelengths and re-emits in longer wavelengths. This is seen as infrared (IR) excess (Zuckerman et al. 1995). The connection between Li enhancement in K giants and the IR excess was first discussed by Gregorio-Hetem et al. (1993) based on the results obtained from the survey called Pico Dias Survey (hereafter PDS) which was originally meant for searching T-Tauri stars using far-IR color criteria. The survey led to discover a couple of Li-rich K giants whose IR colors overlapped with those of T-Tauri stars. The so called connection between IR excess and the high Li in K giants prompted more surveys to look for new Li-rich K giants based on IRAS color criteria (Gregorio-Hetem et al. 1993; de La Reza et al. 1997; Castilho et al. 1998). The number of K giants with IR excess obviously increased partly due to the bias in the criteria.

However, there are K giants with large Li but without IR excess, and K giants with significant IR excess but with normal Li. In the literature, there are many models connecting the Li-enhancement with the infrared excess. For example, the model developed by de La Reza et al. (1996) supported such a relation between Li enhancement and IR excess, and the observed IR excess is interpreted as due to expanding dust shell. The model suggest that all the normal K giants become Li-rich during a short interval of a few thousand years during the RGB phase, and the RGB phase lasts for about a few tens of million years. Various models were developed to understand the underlying physical process that are responsible to create excess as well as Li. Palacios et al. (2001) study provided a mechanism for such a scenario where rotation-induced mixing would cause

Li-enhancement as well as increase in mass-loss at the luminosity bump due to thermal instability in the lithium burning shell which they called as Li flash. Another interesting model was by Denissenkov & Herwig (2004) who proposed the Li enrichment due to enhanced extra mixing triggered by an external source like plunging of massive planets or a brown dwarf. According to them, the IR excess can be due to an orbiting dusty disk formed due to planet engulfment (e.g; Jura 2003) instead of an expanding dust shell.

However, the above models and observational inferences are based on a handful number of Li-rich K giants. To draw meaningful conclusions we require a study of substantial number of K giants with or without Li as well as K giants with or without IR-excess. In this chapter, we aim to study the infrared properties of a large number of K giants along the red giant branch. The data of excess of IR radiation was from *IRAS* measurements. The mass-loss rates were derived by modeling their spectral energy distribution (SED) using a radiative transfer code DUSTY. Using this approach, we have investigated the relation between Li enhancement and mass-loss for the first time for such a large sample.

6.2 SAMPLE SELECTION

The sample for our study consists of 2000 low mass (0.8 to 3.0 $M_{\odot}$) normal giants and the updated list of Li-rich giants. Normal giants are the survey sample taken from Chapter 3 and the entire list of Li-rich giants are taken from Chapter 4. Selected candidates occupy the RGB track beginning from the base of the RGB to beyond the post luminosity bump. The entire sample is divided into four bins in the HR diagram based on temperature, luminosity, and mass. The four bins are the pre-bump, bump, clump and post-bump. Sample stars with superposed evolutionary tracks are shown in Figure 6.1. Solid blue lines are evolutionary tracks for 0.8 to 3.0 $M_{\odot}$ stars computed for solar metalliciy, [Fe/H]=0.0 (Bertelli et al. 2008). Red dashed lines represent the base of RGB where the convective envelope deepens to a maximum extent. Red solid lines are the kinks in luminosity representing the amplitude of the luminosity bump or known as RGB bump. Yellow solid lines represent the red clump, where post He-core flash objects settle. These are core He burning stars. Cross symbols are the Li-normal giants, whose Li abundances, derived in this study from low resolution spectra (see Chapter 3), are below 1.4 dex. Green, cyan, black, and magenta crosses are pre-bump, bump, clump and post-bump giants, respectively. Obviously, the number of giants are relatively large in bump and clump regions. Blue filled circles are Li-rich K giants, whose Li abundances were derived from the high resolution spectral analysis (see Chapter 4 for details). The size of the circle represents

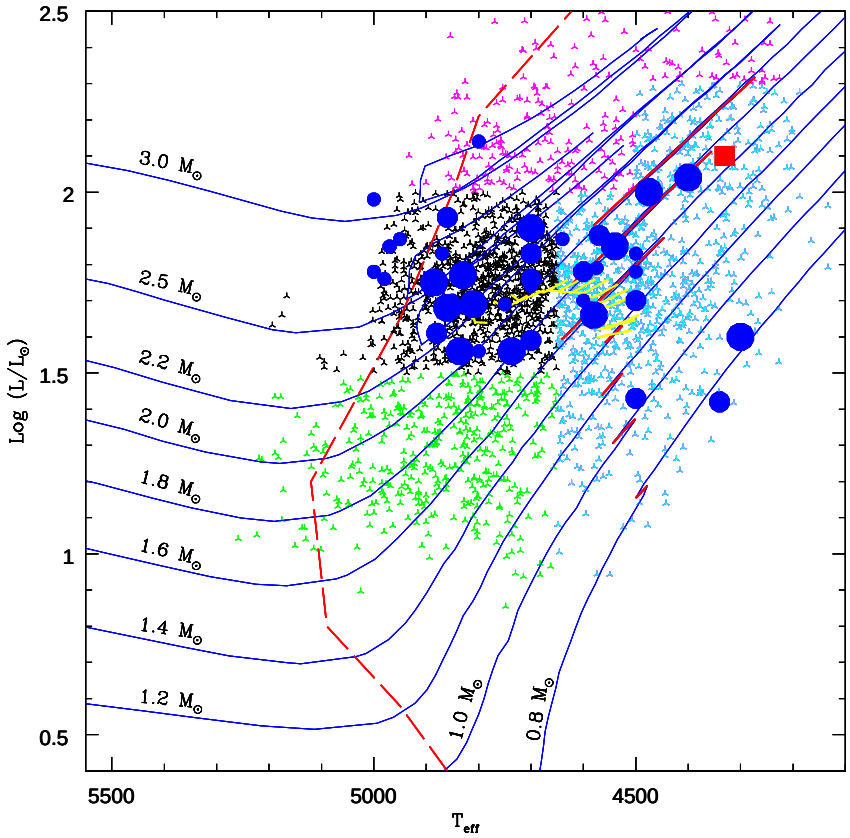

Figure 6.1: Li-rich and normal K giants are on the HR-diagram. Evolutionary tracks for low mass (0.8 - 3M$_\odot$) stars are superposed. Blue circles represents the Li-rich K giants and the size indicates the relative amount of lithium. Green, black, cyan, and magenta crosses represent pre-bump, red clump, bump, and post-bump giants, respectively.

the amount of Li. We find all the Li-rich K giants in the bins of bump and clump, and none in the other two bins of pre-bump and post-bump.

6.3 INFRARED EXCESS

Excess infrared radiation from a star indicates the presence of circumstellar dust. The hot and warm dust emits in near-infrared (NIR) wavelengths and cooler dust emits in far-infrared (FIR) wavelengths. Color-Color diagram (CCDm) is one of the tools often used in astronomy to study the excess radiation coming from a star. The diagram consists of color indices in both the axes. Color indices between two bands are derived from the intrinsic magnitudes at the two bands. As the star light passes through the interstellar

matter, the observed color needs to be corrected for interstellar reddening to get the intrinsic color of the star. The entire sample stars are checked for the existence of excess in NIR and FIR wavelengths.

6.3.1 NEAR-INFRARED CCDM

NIR CCDm helps to detect the warm and hot dust in the circumstellar orbiting disks and expanding shells. The typical colors used in NIR studies are (J-H) and (H-K). We have taken the NIR magnitudes in J, H, and K_s for the entire sample of stars from 2MASS catalog (Cutri et al. 2003). The quality of the data in the catalog varies from good to upperlimits. The sample consists of cooler red giants, so most of them have upperlimit fluxes in Ks band. Observed (J-H) and (H-K) colors are converted into the Koornneef

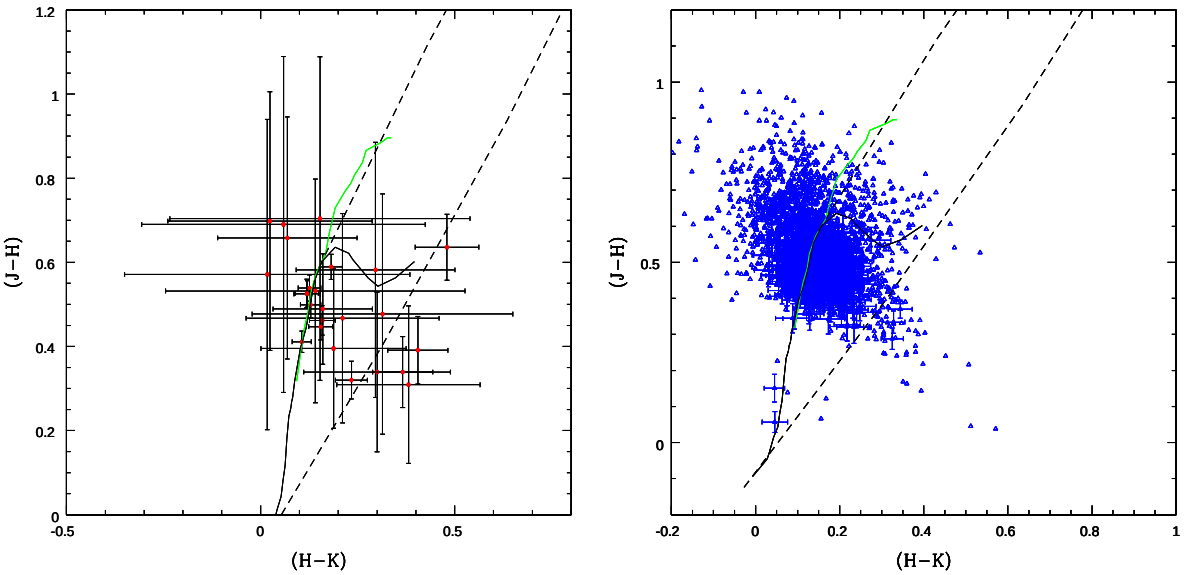

Figure 6.2: Li-rich and Li-normal giants are on Near IR color-color diagram.

(1983) system using transformation relations given in Carpenter (2001). The location of main-sequence (MS) stars, giants, and reddening vector in the NIR CCDm are taken from (Koornneef 1983). NIR colors with the error bars of Li-rich giants are plotted in NIR CCDm in the left panel of Figure 6.2 and the Li-normal giants are plotted in right panel. Red circles are Li-rich giants and blue open triangles are Li-normal giants. The dashed line indicates the reddening vector. Black solid line is the location of dwarfs. Green line indicates the location of giants. Many of the giants are well inside the reddening vector, indicating that no excess emission is found in NIR. The stars which are falling left side on

the diagram is due to large errors in the magnitudes. A few of them are having excess. We restrict our NIR study here to find the excess from CCDm. A detail study using spectra energy distribution (SED) will be discussed later in this chapter.

6.3.2 FAR-INFRARED CCDM

The excess radiation in FIR from the star indicates the presence of cool circumstellar dust, which can be detected using FIR CCDm. The colors, [12-25] and [25-60], used in the FIR CCDm are based on the IRAS fluxes at 12μ, 25μ, and 60μ bands and using Equation 6.1. The general definition to calculate colors for λ_1 and λ_2 are :

$$[\lambda_1 - \lambda_2] = log\lambda_2 f_{\lambda_1} - log\lambda_1 f_{\lambda_2} \tag{6.1}$$

where λ_1 and λ_2 are the central wavelength of the bands 1 and 2, f_{λ_1} and f_{λ_2} are the fluxes at λ_1 and λ_2, respectively.

IRAS fluxes along with the quality code of the data and calculated colors of Li-rich giants are given in Table 6.1 . The location of Li-rich K giants are shown on *IRAS* color-color diagram (see Figure 6.3). The quality of the data in this catalog varies from good, moderate, and upper limits. The quality of the data are shown in red, blue, and black symbols for good, moderate and upper limits, respectively. The size of open hexagons represents the amount of Li. Red square is Arcturus, a typical K giant with very low Li (A(Li)∼-0.6) and no infrared excess, which is shown for reference. There are three regions seen in the diagram and are named as region I, region II, and region III. The stars in the region I do not show 25μ and 60μ excesses indicating the absence of circumstellar dust. For these stars, the dust might not have formed or it might have formed and dissipated into interstellar space. The region II is where the star shows excess in both 25μ and 60μ indicating clearly the presence of a warmer and extended dust. Region III is where the excess is seen only at 60μ indicating the presence of an extended cool dust shell. In the diagram, Li-rich giants are showing excess emission either in 25μ or 60μ, indicating the presence of a dusty region around the central star. However, the quality of fluxes are upperlimits for a few candidates. The position of the giants in the diagram whose upper-limit fluxes at only 60μ will come vertically down and the objects with upperlimit fluxes at both 25μ and 60μ will come down diagonally. This indicates that they are associated with lesser excess in 60μ than the present estimation.

FIR colors also derived for prebump, bump, clump and post-bump giants. Most of the 60 μ fluxes and significant number of 25μ fluxes have upper limits. Prebump giants have

Table 6.1: IRAS fluxes of Li-rich giants from IPAC 1986

Star	F12 Jy	Qual	F25 Jy	Qual	F60 Jy	Qual	F100 Jy	Qual	[25-12]	[60-25]
HD108471	0.869	3	0.361	1	0.4	1	1	1	-0.700	-0.335
HD118319	1.04	3	0.287	1	0.4	1	1	1	-0.877	-0.236
HD120602	1.129	3	0.278	1	0.4	1	1	1	-0.927	-0.222
HD12203	0.793	3	0.409	1	0.4	1	1	1	-0.606	-0.389
HD133086	0.706	3	0.25	1	0.4	1	1	1	-0.769	-0.176
HD203251	0.416	3	0.369	1	0.4	1	1	1	-0.370	-0.345
HD217352	0.701	3	0.308	1	0.4	1	1	1	-0.675	-0.266
HD63798	0.865	3	0.347	1	0.4	1	1	1	-0.715	-0.318
HD88476	0.638	3	0.29	1	0.4	1	1	1	-0.661	-0.240
HD21018	0.859	3	0.285	1	0.4	1	1.01	1	-0.797	-0.232
HD150902	0.298	3	0.25	1	0.4	1	1.07	1	-0.396	-0.176
HD37719	0.376	3	0.25	1	0.4	1	1.37	1	-0.496	-0.176
HD40168	0.759	3	0.25	1	0.4	1	2.33	1	-0.801	-0.176
HD203136	0.444	3	0.305	1	0.584	1	22.6	1	-0.482	-0.098
HD112127	0.979	3	0.290	2	0.4	1	1	1	-0.846	-0.241
HD31993	0.785	3	0.291	2	0.4	1	1	1	-0.748	-0.243
HD40827	1.51	3	0.368	2	0.4	1	1	1	-0.931	-0.343
HD170527	0.873	3	0.264	2	0.4	1	1.02	1	-0.837	-0.200
HD51367	0.705	3	0.246	2	0.4	1	5.22	1	-0.774	-0.170
HD10437	1.12	3	0.304	2	0.4	1	8.38	1	-0.884	-0.261
HD145457	0.988	3	0.316	3	0.4	1	1	1	-0.813	-0.278
HD167304	1.28	3	0.281	3	0.4	1	1	1	-0.977	-0.226
HD214995	1.84	3	0.438	3	0.4	1	1	1	-0.942	-0.419
HD90633	1.41	3	0.346	3	0.4	1	1	1	-0.928	-0.317
HD148293	3.52	3	0.78744	3	0.4	1	1.47	1	-0.969	-0.674
HD116292	2.51	3	0.661	3	0.4	1	1.97	1	-0.898	-0.598
HD9746	2.74	3	0.712	3	0.4	1	4.38	1	-0.904	-0.630
HD77361	1.58	3	0.427	3	0.4	1	5.12	1	-0.886	-0.408
HD214714	1.12	3	0.314	3	0.4	1	6.12	1	-0.870	-0.275
HD205349	6.75	3	1.68	3	0.419	1	3.36	1	-0.922	-0.983
HD787	9.33	3	2.37	3	0.485	1	1	1	-0.913	-1.069
IRAS17596-3952	0.482	3	1.11	2	0.637	2	12.7	1	0.044	-0.621
HD19745	0.332	3	0.777	3	0.612	3	1	1	0.050	-0.483
IRAS13539-4153	0.491	3	0.821	3	0.644	3	1	1	-0.095	-0.485
HD146850	6.91	3	1.78	3	1.93	3	5.99	2	-0.907	-0.345
IRAS13313-5838	1.88	3	6.04	3	3.3	2	22.5	1	0.188	-0.642
PDS100	4.74	3	6.53	3	3.38	3	10.6	1	-0.179	-0.666
HD219025	17.1	3	10.3	3	3.86	3	1.7	3	-0.538	-0.806
HD233517	0.502	3	3.6	3	7.6	3	5.1	3	0.536	-0.055

1 = Upper limits; 2 = Moderate; 3 = High

more data with upperlimits in 25μ and 60μ than other giants, implying that these stars do not emit strongly in far-infrared. The giants in all the 4 bins are Li-normal. For our analysis, we considered the sources with good and moderate quality of fluxes in all the IRAS bands to derive their IR properties. Li-normal and Li-rich giants with only good and moderate quality of data are shown in *IRAS* color-color diagram (see Figure 6.4).

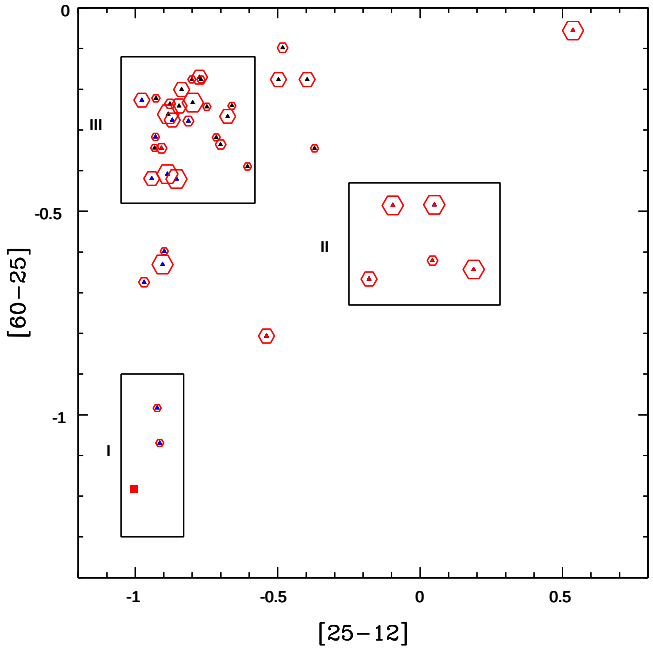

Figure 6.3: Location of Li-rich giants on the far infrared color-color diagram. Triangles are the Li-rich giants. Size of the open hexagons represents the relative amount of lithium, $1.4 \leq$ A(Li) < 2.0, $2.0 \leq$ A(Li) < 2.5, $2.5 \leq$ A(Li) < 3.3, and A(Li) ≥ 3.3, respectively. Red square is the Arcturus, a typical K giant with A(Li) < 0.0 . Black color indicates the upper limits of fluxes at 25μ and 60μ. Blue color is for the upper limit flux at 60μ. Red color is for the high and moderate quality fluxes at 12, 25, and 60μ

Red filled triangles are Li-rich giants and open symbols are Li-normal giants. Triangles, squares, pentagons, and hexagons represent pre-bump, bump, clump, and postbump giants respectively. In the diagram, most of the Li-normal giants are in the region where there is no excess in colors indicating the absence or negligible amount of circumstellar dust. A few of them are showing more excess in 60μ. Only a little fraction of giants are showing excess in both 25μ and 60μ bands.

The above analysis suggests that most of the Li-rich giants and a few Li-normal giants are associated with the circumstellar dust and the giants which are associated with the infrared excess are occupying the regions which are at or above the bump and the clump luminosity in the HR diagram. Most of the Li-normal giants are occupying the region I, indicating that the normal giants, in general, are not associated with infrared excess. A few Li-normal giants at region III (bump, clump and post-bump) have extended cool dust, which may be due to additional mass-loss encountered on the RGB. Li-rich giants in the bump and clump region in the HR diagram are located in region II in the FIR CCDm, which indicates more excess compared to normal giants.

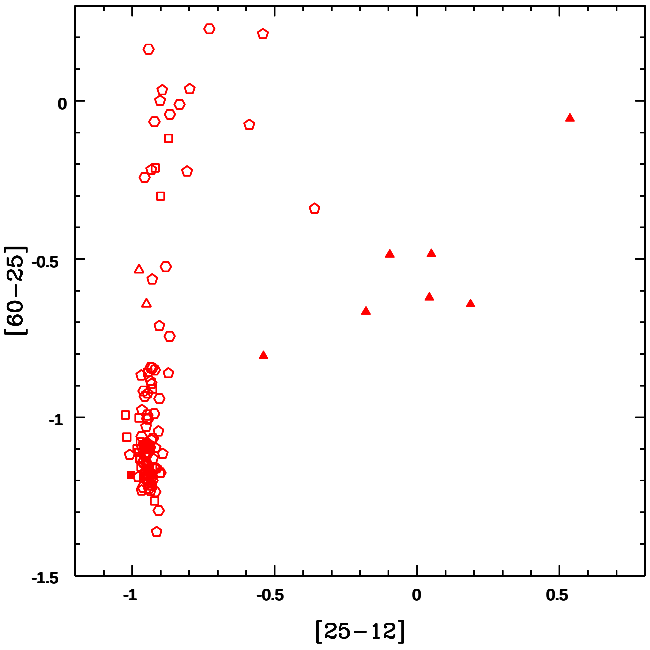

Figure 6.4: Li-rich and normal giants with only good quality of data are presented. Filled triangles are the Li-rich K giants. Open symbols are normal giants. Triangles, squares, pentagons and hexagons represent pre-bump, bump,clump, and postbump, respectively

6.4 GEOMETRY OF THE CIRCUMSTELLAR DUST

The geometrical distribution of dust around a star, spherical or non-spherical, gives an information regarding the origin of the dust formation. The geometry of the dusty region around the sample giants can be obtained using the dust emissivity index (α). For a dust cloud of uniform temperature, the ratio of emitted flux at two wavelengths λ_1 and λ_2 in the optically thin limit is

$$\frac{F_{\lambda_1}}{F_{\lambda_2}} = \left(\frac{\lambda_2}{\lambda_1}\right)^{\alpha} \frac{B_{\lambda_1}(T_d)}{B_{\lambda_2}(T_d)} \tag{6.2}$$

where α is the dust opacity index and $B_\lambda(T_d)$ is the Planck's function at λ for dust temperature T_d.

$$B_\lambda(T_d) = \frac{2hc}{\lambda^3}\left(\frac{1}{e^{\frac{hc}{\lambda k T_d}} - 1}\right) \tag{6.3}$$

Flux ratios, (F_{12}/F_{25}) and (F_{25}/F_{60}), are calculated from the moderate and good quality of fluxes at 12μ, 25μ, and 60μ bands of IRAS. Dust temperature (T_d) and dust opacity index (α) are obtained simultaneously by fitting flux ratios (F_{12}/F_{25}) and (F_{25}/F_{60}) described in above equations and shown in Figure 6.5.

The equations used in this analysis are adopted from Muthumariappan et al. (2006)

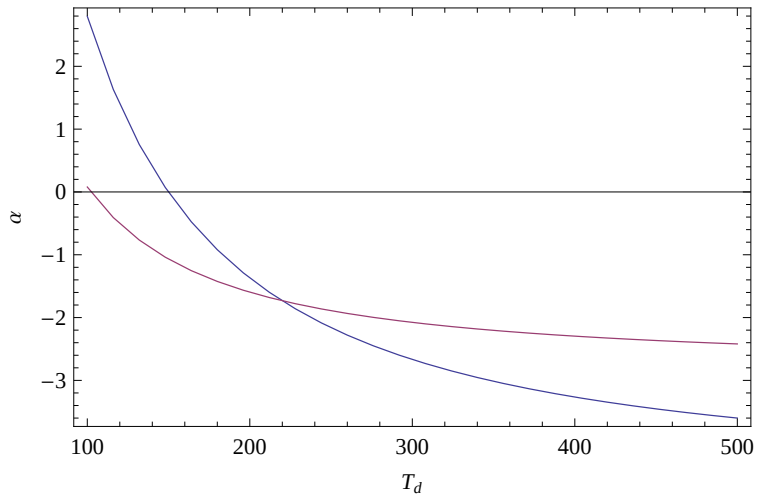

Figure 6.5: A plot of dust temperature (T_d) against the dust opacity index (α) for observed flux ratios of HDE 233517. Blue and pink colors represent the combination for (F_{12}/F_{25}) and (F_{25}/F_{60}), respectively. The intersection point represents the dust temperature and α for the dust shell (T_d = 219 and α = -1.73).

and using a program written in *MATHEMATICA*, the parameters were derived. The input parameters in the program are flux ratios, wavelengths, and ranges for dust temperature (T_d). We considered a minimum T_d of 10 K (the interstellar dust temperature) and a maximum T_d of 1500 K, a sublimation temperature of silicates. Many combinations of T_d and α will fulfill a given flux ratio however there will be only one set of values that fit both the ratios simultaneously. We have plotted T_d against α for the above ratios. The intersection point is taken as the best value of T_d and α which represents the average temperature and opacity index of the circumstellar dust. For cross checking, the resultant combination of T_d and α used to reproduce both the flux ratios. The plot of T_d against α for the values taken make an intercept as shown in Figure 6.5. In some cases, we did not find any intersection point for the given flux ratios which indicate the absence of the dusty region (flux ratios represent a blackbody) For example, Arcturus, which does not show IR excess, the interception may be seen at the photospheric temperature with α = 0 (See Figure 6.6).

The best fit values of T_d and α for Li-rich and Li-normal giants are given in Table 6.2, where $(F_{12}/F_{25})_p$ and $(F_{25}/F_{60})_p$ are the back calculated flux ratios. In the Table 6.2, α is positive for all the Li-normal giants, and most of the Li-rich giants have its value negative. The significance of the α is that it is a measure of the sphericity of the dusty region (Lynden-Bell & Pringle 1974). Positive α means that the dust around the star is spherically distributed and negative α meaning the non spherical distribution of circumstellar

Table 6.2: Dust Temperature and dust opacity index of Li-rich and Li-normal K giants

Star	(F_{12}/F_{25})	(F_{25}/F_{60})	T_d	α	$(F_{12}/F_{25})_p$	$(F_{25}/F_{60})_p$
IRAS17596-3952	0.43423	1.74124	225.9	-0.28025	0.43422	1.74122
IRAS13313-5838	0.31126	1.8303	183.5	0.08539	0.31124	1.83023
HD19745	0.42781	1.26961	268.0	-0.84076	0.4278	1.2696
IRAS13539-4153	0.59852	1.27484	362.1	-1.09788	0.59852	1.27484
PDS100	0.72588	1.93195	310.2	-0.50061	0.72588	1.93194
HD233517	0.13944	0.47368	219.8	-1.73122	0.13944	0.47367
hd219025	1.6602	2.6684	699.1	-0.5789	1.6602	2.6684
hd213930	2.02213	8.21488	265.6	1.30176	2.0221	8.21483
hd143107	3.87574	8.20926	564.8	0.78369	3.87571	8.20922
hd113226	3.94107	9.59364	464.0	1.05437	3.94105	9.59363
hd202109	3.98496	7.16338	801.0	0.50802	3.98497	7.16341
hd2261	4.0073	7.65363	695.1	0.62655	4.00729	7.65361
hd163588	4.08213	6.86089	993.5	0.40543	4.08212	6.86087
hd148387	4.13621	7.12426	924.1	0.46495	4.13622	7.12428
hd12929	3.83251	6.26543	1050.2	0.28996	3.83251	6.26542
hd135722	3.94521	6.03306	1455.4	0.19046	3.9452	6.03304
hd75691	4.075	6.58979	1147.8	0.33022	4.075	6.5898
hd180711	4.08478	6.28329	1462.1	0.23622	4.08477	6.28327
hd102224	4.08898	6.39566	1339.9	0.26956	4.08898	6.39566
hd9927	4.17457	6.43468	1479.7	0.26172	4.17457	6.43468
hd96833	4.18354	6.99057	1031.2	0.41884	4.18354	6.99057
hd127665	4.21569	6.71789	1259.9	0.33572	4.21569	6.71789
hd4128	4.40441	6.92641	1403.0	0.35357	4.40441	6.92642
hd197989	4.45141	7.08889	1329.2	0.38838	4.45142	7.08891
hd188114	3.75	5.43119	1924.5	0.0345	3.74079	5.42518
hd214868	3.81757	6.23516	1050.9	0.28429	3.81757	6.23517
hd8512	4.	6.04259	1587.6	0.18034	3.99993	6.04254
hd85503	4.17143	6.11426	2027.8	0.163	4.14982	6.09998

dust. The presence of non spherical distribution represents the expanding shell with truncated polar caps formed due to mass-loss from central star or it could be a disk like structure formed due to the evaporation of planetesimals and accretion of nearby companion (if the value of α is extremely negative). Jura (2003) and Jura et al. (2006) studied HDE 233517 extensively and suggested that flaring, orbiting, dusty disk is present in it. The high resolution spectra of HDE 233517 shows the features of weak emission at the blue wing of asymmetric Hα and variation in satellite lines of Na D (Drake et al. 2002;

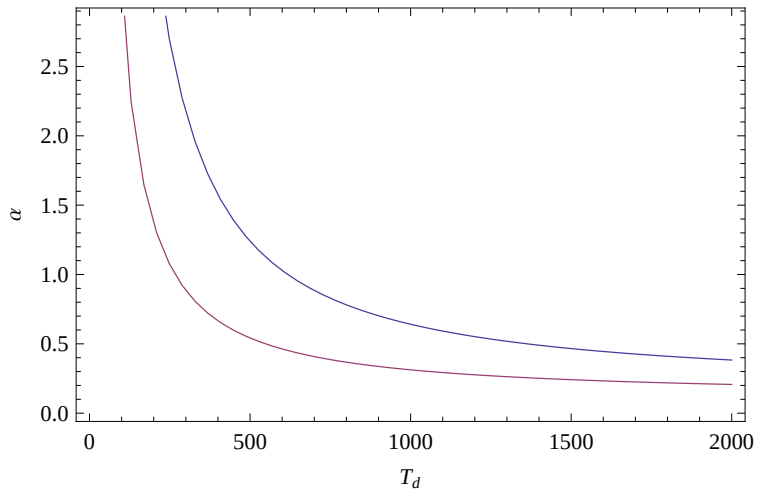

Figure 6.6: Combinations of dust temperature (T_d) and dust opacity index (α) for observed flux ratios of Arcturus. Blue and pink colors represent the combinations for (F_{12}/F_{25}) and (F_{25}/F_{60}), respectively. Both curves are diverging.

Balachandran et al. 2000), which are the significance of mass-loss. This suggests that the dusty region may be formed due to mass-loss and hence having an expanding circumstellar shell. Similarly, a few LRKG with non-spherical geometry of dusty regions have similar features like HDE 233517 in their spectra (See Figure 6.7) which indicates mass-loss (Drake et al. 2002). The geometrical analysis of dusty region around our samples suggests that most of the normal giants have spherically distributed circumstellar dust and hence the normal K giants follow the Reimer's mass-loss. The dusty region with non spherical distribution around Li-rich giants can be due to the presence of expanding shells with truncated polar caps.

6.5 CIRCUMSTELLAR SHELL MODELING

Study of circumstellar shell gives information about the dust shell formation, chemical composition of the dust grains, dust evolutionary timescales, and the rate of mass-loss from central star. The modeling of spectral energy distribution (SED) from far-UV to the sub-mm of cool giant stars is one of the important diagnostic tools to obtain the dust parameters of the circumstellar shell. Such modeling requires the photospheric parameters of a central star and its observed SED with which radiative transfer code can generate synthetic SED for a set of physical and chemical properties of dust shell. The atmospheric parameters of Li-rich giants are taken from Chapter 3 & 4. Optical (UBVRI), near-infrared (JHK_s) magnitudes and far-infrared (IRAS) fluxes are taken from the respective catalogs

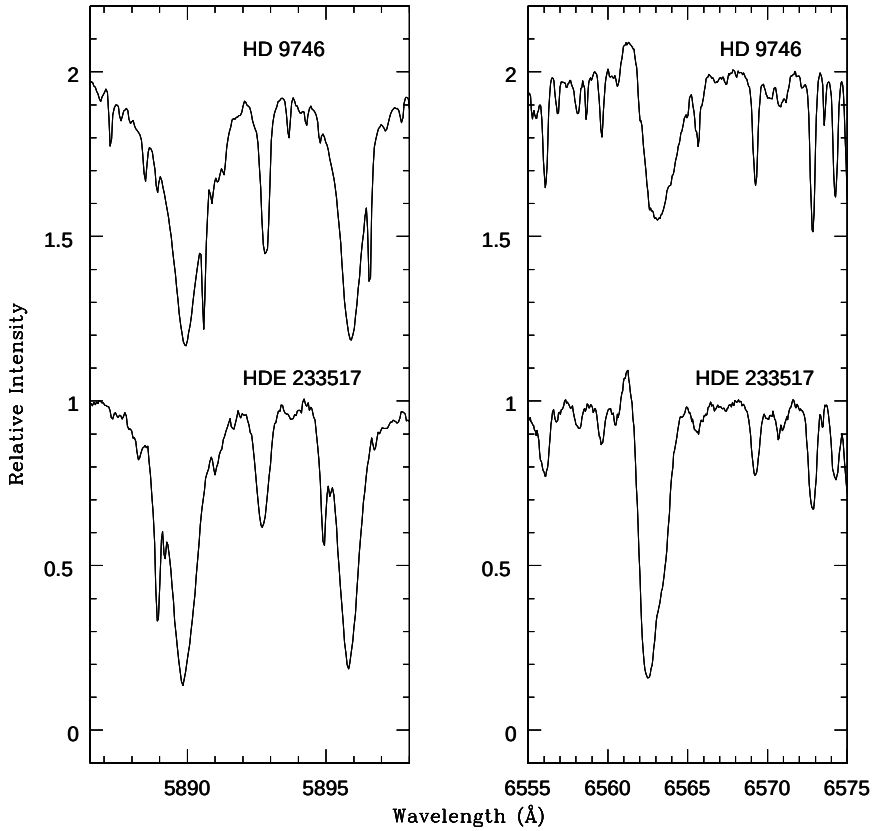

Figure 6.7: Sample spectra showing the Hα emission in blue wing. It also show the satellite lines of Na D1 and D2.

and SIMBAD collection. Mid-infrared fluxes observed by MSX were taken for the stars for which data is available. Magnitudes are converted into fluxes using their respective zero point fluxes. The fluxes are normalized to K band flux to construct the observed SED of all the Li-rich giants. We have used a radiative transfer code, DUSTY, to model the SEDs obtained for our investigation.

DUSTY is an one dimensional radiative transfer code used to solve the problem of radiative transport through the the dusty region in the circumstellar environment. The code was developed by Zeljko Ivezic and his group at the university of Kentucky (Ivezic et al. 1999). The geometry of the regions that can be handled are plane parallel and centrally-heated spherical density distribution. The SED of the source can be either Planckian or broken power law. It has built in optical properties for the common types of the most of the astronomical dust grains. The solution is obtained through an integral equation for the spectral energy density, spatial temperature profiles which is found from the radiative

equilibrium at every point in the dusty region, and does not introduce any approximations. The dust temperature (T_d) at the inner shell boundary, the optical depth (τ) at 0.55μ, and the relative shell thickness (ratio of the shell thickness to the inner shell radius, Δr/r) are given as input parameters. The output of the code gives the inner shell radius (r_{in}) for the specified T_d and luminosity (L), mass-loss rates and also the IR colors .

In our case, we considered the central star is a point source and dust is spherically distributed around it. The spherical density distribution follows the inverse square law with radial distance. Stellar atmospheric parameters are required as input parameters in modeling the photosphere. It can be given in two ways in the program: (i) Provide the effective temperature of star and the code assumes a blackbody SED described by the temperature (ii) Insert the suitable model atmospheres consisting of surface temperature, gravity, and metallicity. The model atmospheres are publicly available in the literature. Kurucz model atmospheres are used in our analysis. The shell is assumed to have astronomical silicate dust grains as most of the Li-rich giants are oxygen-rich.

The dust temperature, optical depth, and relative shell thickness are iterated in such a way that the theoretical SED matches with observed SED. We found that the excess emission is well reproduced with the warm silicate dust grains (Ossenkopf et al. 1992). For example, the SED of a Li-rich giant is shown in Figure 6.8. The dust parameters obtained from the modeling are listed in Table 6.4.

6.5.1 MASS-LOSS RATES

The dust parameters obtained from the SED model are used to derive the mass-loss rates of a central star. Considering the velocity of the wind is constant, the rate of mass-loss is given by de La Reza et al. (1996)

$$\dot{M} = 7.9\times10^{-28}\tau_v R'_{in} V_s \tag{6.4}$$

where, τ_v is the optical depth at visible band, R'_{in} is inner dust shell radius corrected for the stellar radius, and V_s is the shell expansion velocity. We assumed that the shell is expanding with a constant velocity of 2 km s^{-1}, typical for low mass giants (de La Reza et al. 1996). The age of the shell by assuming constant shell expansion velocity can written as below,

$$t = \frac{R'_{in}}{V_s} \tag{6.5}$$

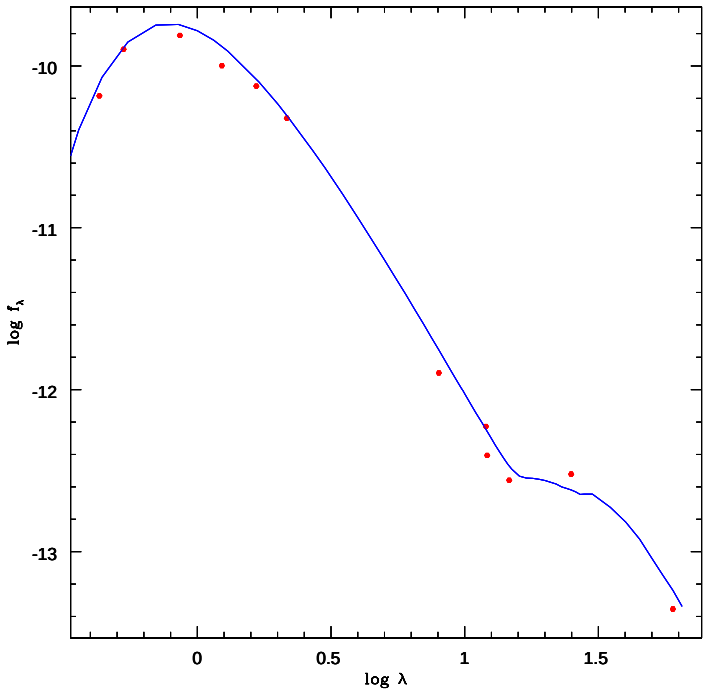

Figure 6.8: Spectral energy distribution of observed fluxes superposed with the theoretical fluxes modeled from DUSTY.

where t is the time taken to shell expanding to $R_{in}^{'}$. The age of the shell and mass-loss rates of Li-rich giants are derived and are given in Table 6.4. In the table, most of the giants are having mass-loss rates in the range of 10^{-10} to 10^{-8} $M_{\odot}$ yr^{-1}. The age of the shells are in the range of 10^3 to 10^5 years.

Luminosity driven mass-loss rates for normal giants in all the 4 bins (viz pre-bump, bump, clumps, post bump) are derived using the modified version of the Reimer's law (Schröder & Cuntz 2005)

$$\dot{M} = \frac{\eta L_{\star} R_{\star}}{M_{\star}} (\frac{T_{eff}}{4000})(1 + \frac{g_{\odot}}{4300 g_{\star}}) \tag{6.6}$$

Where η = 8±1×10^{-14} $M_{\odot}$ yr^{-1}. $L_{\star}$, $R_{\star}$, $M_{\star}$, $g_{\star}$ are Luminosity, Radius, Mass, and surface gravity of star, respectively. T_{eff} is the surface temperature of the star and we took a value of solar gravity, log $g_{\odot}$ = 4.44. Radius for the stars are calculated from their luminosities and temperatures. Parallax based gravities are obtained using the above parameters and the following equation:

$$logg = log\frac{L}{L_{\odot}} + log\frac{M}{M_{\odot}} + 4logT_{eff} - 10.61 \tag{6.7}$$

Table 6.3: Mass-loss rates derived from Reimer's law

Bin	T_{eff}	log(L/L$_\odot$)	M$_\star$	R$_\star$	log g	$\dot{M}_R$	$\dot{M}_S$
Pre-Bump	4650	0.9	1.0	4.3501	3.163	4.83757e-12	4.70296e-12
	4650	1.5	1.6	8.67958	2.76712	2.40163e-11	2.35003e-11
	5200	1.0	1.9	3.903	3.53596	2.87589e-12	4.12425e-12
	5200	1.5	2.5	6.94062	3.15514	1.2291e-11	1.76722e-11
	4800	1.3	1.8	6.47027	3.07343	1.0041e-11	1.09199e-11
Bump	4500	1.0	0.8	5.2117	2.90913	9.12048e-12	7.93285e-12
	4500	1.6	1.2	10.3987	2.48522	4.82977e-11	4.25529e-11
	4650	1.0	1.0	4.88089	3.063	6.83324e-12	6.65064e-12
	4650	2.0	2.5	15.4347	2.46094	8.64344e-11	8.55152e-11
	4200	2.0	0.8	18.9193	1.78928	3.31089e-10	2.47776e-10
	4600	1.75	1.8	11.8274	2.54949	5.17303e-11	4.90827e-11
Clump	4650	1.5	1.4	8.67958	2.70913	2.74472e-11	2.68991e-11
	4650	2.0	2.2	15.4347	2.40543	9.8221e-11	9.74637e-11
	5000	1.5	2.5	7.50697	3.08701	1.32939e-11	1.66752e-11
	5000	2.0	3.5	13.3495	2.73314	5.3398e-11	6.74193e-11
	4750	1.75	2.3	11.0922	2.71169	3.7968e-11	4.00836e-11
Post-Bump	4200	2.0	1.0	18.9193	1.88619	2.64871e-10	1.94484e-10
	4200	2.5	2.1	33.6439	1.70841	7.09275e-10	5.41037e-10
	5000	2.0	3.0	13.3495	2.66619	6.22976e-11	7.88092e-11
	4800	2.4	4.0	22.9574	2.32022	2.01832e-10	2.25006e-10
	4300	2.1	1.8	20.252	2.08234	1.983e-10	1.53688e-10
	4500	2.2	2.5	20.7482	2.20398	1.84148e-10	1.65278e-10

The mass-loss rates obtained for all Li-normal giants from the above method are all in the range of 10^{-12} to 10^{-10} M$_\odot$ yr^{-1} (see Table 6.3). From the above analysis, it is clear that the mass-loss rates of Li-rich giants are higher compared to the normal K giants, which indicates the extra mass-loss apart from Reimers mass-loss which normally occur in red Giants.

6.5.2 MASS-LOSS RATE VS LITHIUM

Mass-loss rates of Li-rich giants are plotted against derived Li abundances which are shown in Figure 6.9. There seems to be a weak correlation between Li and mass-loss indicating a common phenomena governing both the enhancement of Li and ejection of mass. However, we caution the reader over-interpreting of this result as it shows a large scatter. This could be due to the fact that the maximum Li seen at the time of shell ejection (large mass-loss) gets depleted with time due to convection. Another important aspect that is not very clear is the phase in which the Li is: enhancing phase or in the depletion phase. Also, other possibility for the scatter in the relation of mass-loss versus Li in RGB stars

Table 6.4: Photospheric and dust parameters of Li-rich K giants.

Star	A(Li)	T_{eff}	Log(L/L$_\odot$)	R/R$_\odot$	$\dot{M}$	T_{dust}	t
hd40168	1.50	4800	2.14	17.0185	8.20300e-10	55	4120.46
hd116292	1.50	4870	1.83	11.5704	7.35389e-11	95	615.656
hd40827	1.60	4575	1.79	12.5205	1.29562e-10	110	371.889
hd88476	1.60	4950	1.87	11.7272	3.57581e-10	75	1330.5
hd63798	1.75	5000	1.78	10.3625	5.12552e-09	28	20596.8
hd787	1.80	4180	2.71	43.2566	2.48527e-11	180	249.675
hd12203	1.80	4850	1.69	9.92936	4.23622e-10	65	1576.22
hd133086	1.80	4850	1.70	10.0443	3.54807e-09	30	16202.1
hd90633	1.85	4800	1.56	8.72815	4.39417e-11	100	367.873
hd120602	1.90	5000	1.98	13.0456	2.77807e-10	70	1860.6
hd183492	2.00	4700	1.74	11.1998	7.02149e-10	110	352.697
hd148293	2.00	4640	1.87	13.3465	4.75923e-13	250	47.8122
hd107484	2.00	4500	1.78	12.7932	2.19865e-09	63	1840.68
hd118319	2.00	4750	1.69	10.3518	6.25045e-10	40	6279.33
hd146850	2.00	4200	2.90	53.322	4.50029e-09	60	6458.69
hd108471	2.00	4970	1.85	11.3682	8.82667e-10	65	2955.82
hd203136	2.23	4980	1.76	10.2081	3.83363e-09	80	962.838
I17596	2.30	4600	1.70	11.1658	2.37905e-08	190	85.3588
hd145457	2.40	4880	1.61	8.94469	4.64719e-11	80	466.867
hd51367	2.50	4700	1.59	9.42343	3.43837e-10	60	1727.13
pds100	2.50	4500	1.70	11.6676	1.48663e-08	250	29.87
hd217352	2.64	4600	1.78	12.243	1.03377e-10	105	399.44
hd112127	2.70	4340	1.42	9.0871	9.77463e-11	60	1309.31
hd150902	2.70	4700	1.83	12.4225	6.67202e-10	90	670.286
hd37719	2.80	4700	1.76	11.4606	2.62341e-07	20	52710.6
hd39853	2.80	3900	2.66	46.9111	9.44113e-11	110	948.476
hd167304	2.85	4860	1.93	13.0356	3.31485e-08	20	66603.3
hd6665	2.92	4500	1.43	8.55027	4.39517e-10	95	339.653
hd219025	3.00	4570	1.88	13.9179	6.02185e-09	275	40.3312
hd170527	3.28	4810	1.69	10.0952	1.60569e-10	65	1613.11
hd214995	3.28	4737	1.56	8.96186	4.21595e-08	20	42354.3
I13313	3.30	4540	1.85	13.6236	1.29749e-07	260	46.553
hd10437	3.49	4830	1.77	10.9777	1.12186e-08	27	22541
hd8676	3.58	4860	1.68	9.77535	3.45143e-10	100	433.422
hd19745	3.70	4700	1.90	13.4651	3.50690e-09	170	117.437
hd9746	3.75	4400	2.04	18.0509	3.42073e-08	22	49093.3
hd77361	3.80	4580	1.66	10.7566	7.70440e-09	30	12900
I13539	4.05	4300	1.60	11.3885	3.27951e-08	230	47.0666
hd233517	4.22	4475	2.00	16.6655	1.88577e-07	75	1262.99

is the greater uncertainty of original Li in K giants from which Li enhanced.

Further, one would expect some sort of a relation between Li and T_d. Plot of Li versus T_d is shown in Figure 6.9 (right panel). Exception comes from the assumption that stars that have dust shells close to the photospheres have higher T_d and not much time elapsed since the ejection. Therefore, those K giants should have much higher Li as there was not much time for the depletion to occur. With time Li gets depleted and the dust shell moves away from the star and gradually becomes cool. However, results shown in Figure 6.9 do not suggest any such relation. This may be due to multiple reasons such as faster depletion of Li compared to dust cooling or multiple episodes of mass ejections.

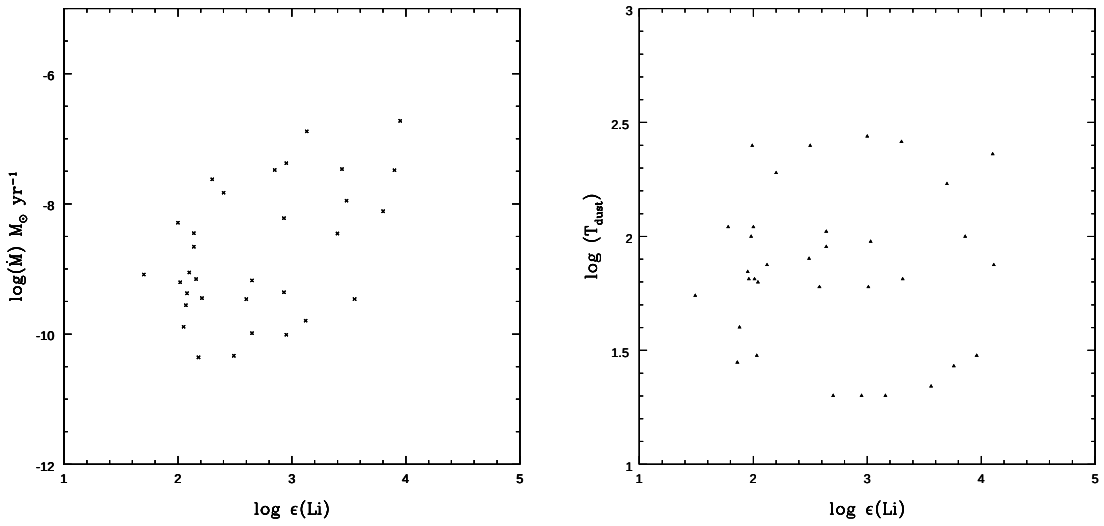

Figure 6.9: Li abundance against mass-loss rates of Li-rich K giants are plotted in left panel. Li abundance against dust temperatures of Li-rich K giants are plotted in left panel. Li abundance was derived from the high resolution spectra. Mass-loss rates and dust temperatures are obtained from this work.

6.5.3 SHELL EVOLUTIONARY MODELS

The model *IRAS* colors of the dust shell for selected ranges of photospheric temperature, radius, and mass-loss rates were computed for different ages of the shell to investigate their evolutionary paths in the *IRAS* color-color diagram. For our study, we chose four combinations of central star parameters typically found for the K giants: $T_\star$ = 4000 K, $R_\star$ = 10 $R_\odot$, $T_\star$ = 4000 K, $R_\star$ = 20 $R_\odot$, $T_\star$ = 5000 K, $R_\star$ = 10 $R_\odot$, and $T_\star$ = 5000 K, $R_\star$ = 20 $R_\odot$. The maximum mass-loss rates that are possible by Reimers law are in the order of 10^{-10} $M_\odot$ yr^{-1}. However, the mass-loss rates for most of the Li-rich giants are

in between 10^{-10} and 10^{-8} $M_\odot$ yr^{-1}. We have made our computations for a set of four mass-loss rates of 10^{-10}, 10^{-9}, 5×10^{-9}, and 3×10^{-8} $M_\odot$ yr^{-1}. Further, we assume that the star has encountered mass-loss for a duration of around 1000 yrs to calculate the physical thickness of the shell (as we found from the models of SED of known LRKG). The relative thickness of the shell varies from 35 to 0.017. The hottest dust considered is at 1500 K (at Age = 0) which is the sublimation temperature for silicates, and the coolest dust around 10 K which is almost near the ISM dust temperature. At first, we have estimated the photospheric colors by assuming no dust around it. In all our models, we considered the colors at dust formation temperature as the starting point and stellar photospheric color as the ending points of the evolutionary loop. This point represents cases where the shell might not have formed yet or it is expanded and fully dissipated into interstellar medium. Intense mass-loss creates a thick shell with peak dust temperature of 1500 K, with time, as the shell expands it becomes thinner and cooler and finally the shell will dissipate into the interstellar medium.

Table 6.5: Dust parameters and evolutionary timescales for different photospheric parameters

$\dot{M}$	$T_\star$	$R_\star$	T_d	Age
$M_\odot yr^{-1}$	°K	$R_\odot$	°K	yr
1×10^{-10}	4000	10	25	16548
		20	28	23641
	5000	10	27	37802
		20	31	50164
1×10^{-9}	4000	10	17	52163
		20	19	74736
	5000	10	19	107675
		20	20.5	171636
5×10^{-9}	4000	10	15	75957
		20	16	125070
	5000	10	15.5	198868
		20	17	300273
3×10^{-8}	4000	10	13	116681
		20	13.5	208958
	5000	10	13.5	299198
		20	14	537481

The evolutionary paths of the dust shell in the *IRAS* color-color diagram are shown in Figure 6.10. In the models, the colors are less effected due to the change in temperature but significant changes in colors are observed due to increasing radius. The dust parame-

ters including the evolutionary timescales for all the models are given in Table 6.5 & **??**, where T_{dust} is the dust temperature and age represents the duration of dust shell evolution. The looping timescales for all the models are in between 1.65×10^4 and 5.37×10^5 yrs. The evolutionary timescales are increased more than 50% with increasing radius of $20R_\odot$ and 25% increased with increasing temperature of 1000 K.

6.6 DISCUSSION AND CONCLUSIONS

FIR colors of Li-rich giants with all available data are presented on dust evolutionary models and is shown in Figure 6.10. All the giants taken for the study are fitted well inside the modeled loops, except one star HDE 233517, whose mass-loss rate is of the order of 10^{-7} $M_\odot$ yr^{-1}. Red square is Arcturus, a typical K giant, which is inside the smallest loop which corresponds to very little mass-loss of the order of 1×10^{-10} $M_\odot$ yr^{-1}. The Li-rich giants occupy regions at the hotter side of the loops indicating these have

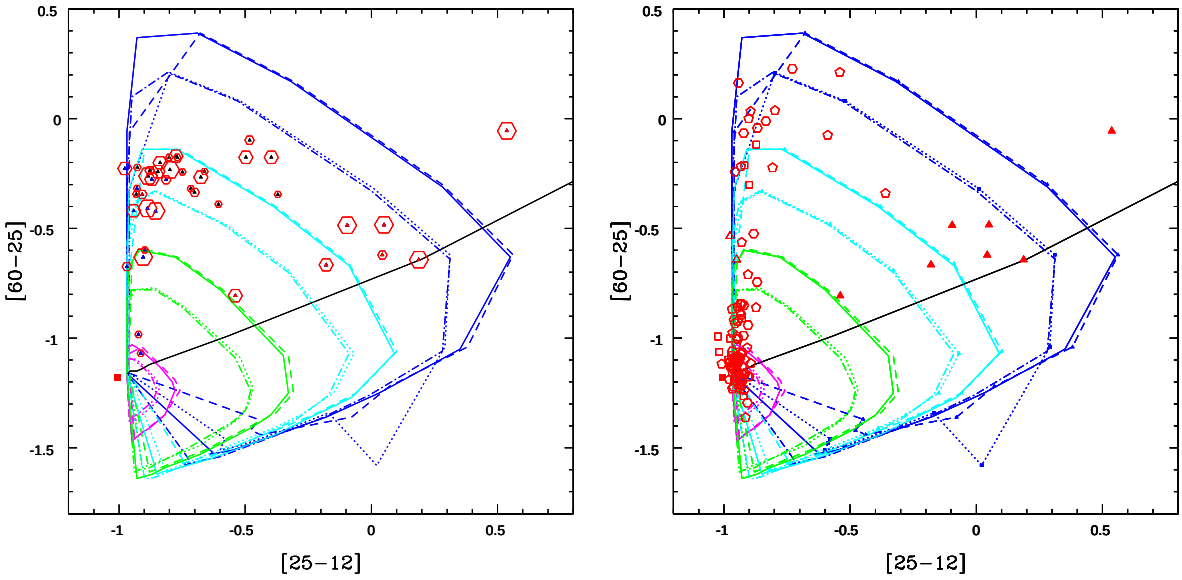

Figure 6.10: Sample giants and dust shell evolutionary models are on color-color diagram. Li-rich giants with various quality data are presented on left panel. On the right panel, Li-rich and normal giants with only good quality of data are presented. Different colors, magenta, green, cyan and blue represents the loops of the evolution of a dust shell with mass-loss rates, 1×10^{-10}, 1×10^{-9}, 5×10^{-9}, and 3×10^{-8}, respectively. Four varieties of lines in each color indicate the different photospheric temperatures and radius, T_{eff} = 5000 K, R = 20 $R_\odot$, T_{eff} = 4000 K, R = 20 $R_\odot$, T_{eff} = 5000 K, R = 10 $R_\odot$, T_{eff} = 4000 K, R = 10 $R_\odot$ of the dust shell hosting stars, radially outwards, respectively.

relatively warmer shells and the mass-loss episode occured recently. The mass-loss rates correspond to the loops are in between 1×10^{-9} and 3×10^{-8} $M_\odot$ yr^{-1}. The dust temperatures are in between 100 to 80 K and the respective timescales are 300 to 550 yrs. Li-rich and normal giants with only good quality data are shown in Figure 6.10 (right panel). Most of the normal giants in the Figure 6.10 are occupying the smallest loop (magenta), corresponding to little or no mass-loss or the mass-loss rate is comparable to Remer's mass-loss which is about 1×10^{-10} $M_\odot$ yr^{-1}. Interestingly, all the Li-rich K giants are in the loops of higher mass-loss rates. As shown in Figure 6.10, they have mass-loss rates of about 1×10^{-9} $M_\odot$ yr^{-1} to 3×10^{-8} $M_\odot$ yr^{-1} and have dust temperatures ranging from from 80 to 100 K. Also, there a few Li-normal giants that do lie in the high mass-loss loops but the giants show cooler T_d in the range of 30 K to 60 K. As shown in the Figure 6.10, the super-Li rich K giants have T_d around 100 K. The giants with peak Li values have the dust temperature around 100 K but they are in different loops meaning they have range of mass-loss. The scatter in the earlier plot of T_d versus Li (Figure 6.9) perhaps due to this situation. The corresponding timescale for dust evolution for K giants with $T_d \sim 100$ K is about 1000 years and they have mass-loss rates ranging from 10^{-9} $M_\odot$ yr^{-1} to 10^{-8} $M_\odot$ yr^{-1}. Considering that the mass-loss begins at the center of inner most loop (small loop), depending on mass and radius, their dust shells evolve along the loops with corresponding mass-loss rates and finally join the same inner most loop after losing most of the dust shell into space. Evolutionary periods correspond to a range of periods starting for a few thousand years in the case of stars of least mass-loss rates to five hundred thousand years for giants of high mass-loss rates (see Table 6.5). Given the good data for a very small fraction of stars and the other uncertainties described above it is not very straightforward to suggest a one-to-one correlation with Li evolution with that of dust evolution.

However, by combining the IR CCDm and the HR diagram, we could infer some gross relations between Li and the dust evolution. As shown in FIR CCDm (Figure 6.3), the Li-rich K giants that are occupying bump position in the HR diagram show excess flux at 25μ and 60μ. The Li-rich giants that occupy clump region whose excess flux only at 60μ. This is an interesting result. Based on the dust cooling one may argue that the mass-loss was perhaps began during its bump evolution. The star evolved and passed through RGB tip and settled at the clump region where one naturally expects some cooler dust. If the Li enhancement too began during the bump evolution and one would expect a very little Li by the time it settles at the clump. However, we do have super Li-rich giants both at the clump and at the bump though the clump and bump giants, in this case, could not be separated for sure. Assuming that all the Li-rich giants are located at the

bump and the non detection of Li-rich K giants above the bump, one would argue that the Li evolutionary period is quite small or comparable to the bump evolutionary periods (see Table 6.6). Our modeling of dust shells suggest the periods are of the order of a few thousand to hundred thousand years. The model results are given in Table 6.5.

Table 6.6: Evolutionary timescales from bump to clump

$M/M_{\odot}$	t_{bump}	$t_{bumpbegin-tip}$	$t_{bumpend-tip}$	t_{clump}
1.0	1.525000e+07	1.278400e+08	1.125900e+08	9.492500e+07
1.2	1.117600e+07	9.879300e+07	8.761700e+07	7.988305e+07
1.4	8.128000e+06	7.503300e+07	6.690500e+07	7.613281e+07
1.6	6.856000e+06	5.685500e+07	4.999900e+07	8.077742e+07
1.8	4.070000e+06	3.547000e+07	3.140000e+07	9.170689e+07
2.0	2.450000e+06	1.955300e+07	1.710300e+07	1.032371e+08

The timescales of important stages along the RGB are derived from evolutionary tracks (Bertelli 2008) which are given in Table 6.6. In Table 6.6, t_{bump} is the duration of time star spends at the luminosity bump, $t_{bumpbegin-tip}$ is the time taken from the beginning of bump to the RGB tip, $t_{bumpend-tip}$ is the time duration that star takes to reach the RGB tip from the end of bump, and t_{clump} is the time duration that star spends at the red clump. The results suggest an upper limit for Li evolution which is the t_{bump}. This is much smaller value compared to the dust evolution which is of the order of a few hundred thousand years.

Now the issue is the whether it is same dust that originated at the bump that is cooling off at the red clump? The timescales that require for a star to go from bump to the clump are of the order of 10^8 years. Since the dust evolutionary time scales are much smaller compared to star's evolution, one would not expect any IR excess on the giants at the clump. The IR excess perhaps could be the result of core He-flash at the RGB tip and one can suspect that even Li could have been synthesized at that time. Since evolutionary timescales from the tip to the clump are small one would expect very large amounts of Li at clump giants. Also, since the clump timescales are of the order of a few million years, one would expect to see giants with a range of IR excess from very little to strong excess. The fact that there are a very few Li-rich giants even at the clump, we suggest that Li enhanced during the core He-flash is getting depleted rapidly.

Table 6.7: Circumstellar shell evoltuionary models

$T_\star$	$R_\star$	$\dot{M}$	T_{dust}	τ	R_{in}	r1/rc	θ	δr/r	t
4000	10	1e-10	1500	1.38e-1	9.49e13	6.45	7.08e-1	34.3	0.724
			500	1.48e-2	8.89e14	61.3	6.63	4.5	6.78
			250	3.87e-3	3.40e15	235	25.4	1.93	25.93
			200	2.28e-3	5.77e15	397	43.0	1.54	44.00
			100	3.61e-4	3.64e16	2510	271	1.087	277.6
			50	4.00e-2	2.76e17	19000	2060	1.017	2104.8
			30	1.04e-5	1.26e18	86900	9410	1.017	9609.0
			25	6.06e-6	2.17e18	1.49e5	1.62e4	1.017	16548.9
		1e-9	1500	1.25	1.05e14	7.25	7.85e-1	31.0	0.80
			500	1.44E-01	9.13E+14	6.30E+01	6.82E+00	4.45	6.96
			250	3.82E-02	3.44E+15	2.37E+02	2.57E+01	1.916	26.23
			200	2.26E-02	5.81E+15	4.00E+02	4.34E+01	1.54	44.30
			150	1.09E-02	1.21E+16	8.34E+02	9.03E+01	1.28	92.27
			100	3.60E-03	3.65E+16	2.51E+03	2.72E+02	1.086	278.35
			50	4.77E-04	2.76E+17	1.91E+04	2.06E+03	1.017	2104.83
			30	1.04E-04	1.26E+18	8.69E+04	9.41E+03	1.017	9609.00
			20	3.12E-05	4.21E+18	2.90E+05	3.14E+04	1.017	32106.3
			17	1.92E-05	6.84E+18	4.71E+05	5.10E+04	1.017	52163.2
		5e-9	1500	5.57E+00	1.18E+14	8.17E+00	8.84E-01	27.7	0.899892
			1000	2.31E+00	2.85E+14	1.97E+01	2.13E+00	12.0	2.17347
			500	6.69E-01	9.84E+14	6.78E+01	7.34E+00	4.2	7.50419
			250	1.84E-01	3.58E+15	2.47E+02	2.67E+01	1.876	27.3018
			200	1.10E-01	5.99E+15	4.13E+02	4.47E+01	1.526	45.69
			150	5.35E-02	1.23E+16	8.50E+02	9.20E+01	1.256	93.8023
			100	1.79E-02	3.68E+16	2.54E+03	2.75E+02	1.086	280.644
			80	9.48E-03	6.94E+16	4.79E+03	5.18E+02	1.045	529.259
			60	4.09E-03	1.61E+17	1.11E+04	1.20E+03	1.020	1227.82
			50	2.37E-03	2.77E+17	1.91E+04	2.07E+03	1.017	2112.46
			30	5.22E-04	1.26E+18	8.70E+04	9.41E+03	1.017	9609.02
			20	1.56E-04	4.21E+18	2.90E+05	3.14E+04	1.017	32106.3
			15	6.61E-05	9.96E+18	6.86E+05	7.43E+04	1.017	75957.0
		3e-8	1500	2.80E+01	1.41E+14	9.69E+00	1.05E+00	23.30	1.07529
			1250	1.93E+01	2.05E+14	1.41E+01	1.53E+00	16.35	1.56337
			1000	1.21E+01	3.27E+14	2.25E+01	2.44E+00	10.60	2.49377
			500	3.49E+00	1.13E+15	7.80E+01	8.45E+00	3.800	8.61761
			250	9.84E-01	4.01E+15	2.76E+02	2.99E+01	1.785	30.5811
			200	5.97E-01	6.61E+15	4.55E+02	4.93E+01	1.477	50.4092
			150	2.96E-01	1.33E+16	9.18E+02	9.94E+01	1.237	101.429
			100	1.02E-01	3.85E+16	2.65E+03	2.87E+02	1.080	293.609
			80	5.52E-02	7.15E+16	4.93E+03	5.34E+02	1.044	545.274
			60	2.41E-02	1.64E+17	1.13E+04	1.22E+03	1.019	1250.7
			50	1.41E-02	2.80E+17	1.93E+04	2.09E+03	1.017	2135.34
			30	3.13E-03	1.26E+18	8.72E+04	9.44E+03	1.017	9609.02
			20	9.38E-04	4.21E+18	2.90E+05	3.14E+04	1.017	32106.3
			13	2.58E-04	1.53E+19	1.06E+06	1.14E+05	1.017	116681
4000	20	1e-10	1500	7.01E-02	9.39E+13	6.47E+00	7.00E-01	34.54	1.4322
			1000	2.73E-02	2.41E+14	1.66E+01	1.80E+00	14.07	3.67583
			500	7.41E-03	8.88E+14	6.12E+01	6.62E+00	4.54	13.5441
			300	2.87E-03	2.29E+15	1.58E+02	1.71E+01	2.37	34.928
			250	1.94E-03	3.40E+15	2.34E+02	2.54E+01	1.926	51.8582

Continued on next page

Table 6.7 – continued from previous page

$T_\star$	$R_\star$	$\dot{M}$	T_{dust}	τ	R_{in}	r1/rc	θ	δr/r	t
			200	1.14E-03	5.76E+15	3.97E+02	4.30E+01	1.54	87.8539
			150	5.48E-04	1.20E+16	8.30E+02	8.98E+01	1.26	183.029
			100	1.81E-04	3.64E+16	2.51E+03	2.71E+02	1.086	555.188
			80	9.53E-05	6.90E+16	4.75E+03	5.14E+02	1.045	1052.42
			60	4.08E-05	1.61E+17	1.11E+04	1.20E+03	1.020	2455.64
			50	2.38E-05	2.76E+17	1.90E+04	2.06E+03	1.017	4209.67
			40	1.23E-05	5.36E+17	3.70E+04	4.00E+03	1.017	8175.29
			30	5.22E-06	1.26E+18	8.69E+04	9.41E+03	1.017	19218
			28	4.24E-06	1.55E+18	1.07E+05	1.15E+04	1.017	23641.2
		1e-9	1500	6.51E-01	1.01E+14	6.95E+00	7.52E-01	32.18	1.54049
			1000	2.63E-01	2.50E+14	1.73E+01	1.87E+00	13.6	3.8131
			500	7.31E-02	9.00E+14	6.21E+01	6.72E+00	4.50	13.7272
			300	2.85E-02	2.31E+15	1.59E+02	1.72E+01	2.363	35.2331
			250	1.92E-02	3.42E+15	2.36E+02	2.55E+01	1.921	52.1632
			200	1.14E-02	5.79E+15	3.99E+02	4.32E+01	1.544	88.3115
			150	5.44E-03	1.21E+16	8.32E+02	9.00E+01	1.26	184.554
			100	1.81E-03	3.64E+16	2.51E+03	2.72E+02	1.087	555.188
			80	9.53E-04	6.90E+16	4.76E+03	5.15E+02	1.046	1052.42
			60	4.09E-04	1.61E+17	1.11E+04	1.20E+03	1.020	2455.64
			50	2.38E-04	2.76E+17	1.91E+04	2.06E+03	1.017	4209.67
			40	1.23E-04	5.37E+17	3.70E+04	4.00E+03	1.017	8190.54
			30	5.22E-05	1.26E+18	8.69E+04	9.41E+03	1.017	19218
			25	3.03E-05	2.17E+18	1.49E+05	1.62E+04	1.017	33097.7
			19	1.34E-05	4.90E+18	3.38E+05	3.66E+04	1.017	74736.8
		5e-9	1500	2.95E+00	1.12E+14	7.74E+00	8.38E-01	29.10	1.70827
			1000	1.21E+00	2.72E+14	1.88E+01	2.03E+00	12.58	4.14866
			500	3.48E-01	9.46E+14	6.52E+01	7.06E+00	4.32	14.4288
			300	1.38E-01	2.38E+15	1.64E+02	1.77E+01	2.32	36.3007
			250	9.40E-02	3.50E+15	2.41E+02	2.61E+01	1.90	53.3834
			200	5.59E-02	5.88E+15	4.05E+02	4.39E+01	1.535	89.6842
			150	2.70E-02	1.22E+16	8.40E+02	9.10E+01	1.258	186.079
			100	8.99E-03	3.66E+16	2.52E+03	2.73E+02	1.086	558.238
			80	4.75E-03	6.92E+16	4.77E+03	5.16E+02	1.046	1055.47
			60	2.04E-03	1.61E+17	1.11E+04	1.20E+03	1.020	2455.64
			50	1.19E-03	2.77E+17	1.91E+04	2.06E+03	1.017	4224.92
			40	6.13E-04	5.37E+17	3.70E+04	4.00E+03	1.017	8190.54
			30	2.61E-04	1.26E+18	8.69E+04	9.41E+03	1.017	19218
			25	1.52E-04	2.17E+18	1.49E+05	1.62E+04	1.017	33097.7
			20	7.81E-05	4.21E+18	2.90E+05	3.14E+04	1.017	64212.6
			18	5.71E-05	5.76E+18	3.97E+05	4.30E+04	1.017	87853.9
			16	4.01E-05	8.20E+18	5.65E+05	6.12E+04	1.017	125070
		3e-8	1500	1.51E+01	1.31E+14	9.00E+00	9.74E-01	25.00	1.99807
			1000	6.39E+00	3.09E+14	2.13E+01	2.31E+00	11.19	4.71299
			500	1.84E+00	1.07E+15	7.35E+01	7.96E+00	3.95	16.3201
			300	7.53E-01	2.62E+15	1.80E+02	1.95E+01	2.20	39.9613
			250	5.18E-01	3.81E+15	2.63E+02	2.84E+01	1.826	58.1117
			200	3.13E-01	6.31E+15	4.35E+02	4.71E+01	1.50	96.2427
			150	1.54E-01	1.28E+16	8.83E+02	9.56E+01	1.246	195.231
			100	5.26E-02	3.75E+16	2.59E+03	2.80E+02	1.084	571.965
			80	2.81E-02	7.04E+16	4.85E+03	5.25E+02	1.045	1073.77
			60	1.21E-02	1.63E+17	1.12E+04	1.21E+03	1.019	2486.14

Continued on next page

Table 6.7 – continued from previous page

$T_\star$	$R_\star$	$\dot{M}$	T_{dust}	τ	R_{in}	r1/rc	θ	δr/r	t
			50	7.10E-03	2.78E+17	1.92E+04	2.08E+03	1.017	4240.17
			30	1.57E-03	1.26E+18	8.70E+04	9.42E+03	1.017	19218
			20	4.69E-04	4.21E+18	2.90E+05	3.14E+04	1.017	64212.6
			18	3.42E-04	5.77E+18	3.97E+05	4.30E+04	1.017	88006.4
			15	1.98E-04	9.96E+18	6.86E+05	7.43E+04	1.017	151914
			13.5	1.44E-04	1.37E+19	9.42E+05	1.02E+05	1.017	208958
5000	10	1e-10	1500	4.87E-02	1.15E+14	1.24E+01	8.60E-01	28.4	2.06034
			1000	1.89E-02	2.96E+14	3.19E+01	2.21E+00	11.6	5.30315
			800	1.19E-02	4.69E+14	5.06E+01	3.50E+00	7.71	8.40262
			500	5.14E-03	1.09E+15	1.17E+02	8.12E+00	3.88	19.5285
			300	1.99E-03	2.81E+15	3.02E+02	2.10E+01	2.12	50.3441
			250	1.34E-03	4.17E+15	4.49E+02	3.11E+01	1.755	74.7099
			200	7.93E-04	7.06E+15	7.60E+02	5.27E+01	1.446	126.487
			150	3.81E-04	1.47E+16	1.59E+03	1.10E+02	1.214	263.366
			100	1.26E-04	4.46E+16	4.80E+03	3.32E+02	1.071	799.055
			80	6.63E-05	8.45E+16	9.10E+03	6.30E+02	1.037	1513.90
			60	2.84E-05	1.97E+17	2.12E+04	1.47E+03	1.017	3529.46
			50	1.66E-05	3.38E+17	3.65E+04	2.53E+03	1.017	6055.62
			40	8.53E-06	6.57E+17	7.08E+04	4.90E+03	1.017	11770.8
			30	3.64E-06	1.54E+18	1.66E+05	1.15E+04	1.017	27590.7
			27	2.65E-06	2.11E+18	2.27E+05	1.58E+04	1.017	37802.8
		1e-9	1500	4.45E-01	1.26E+14	1.36E+01	9.39E-01	25.00	2.25742
			1000	1.81E-01	3.10E+14	3.34E+01	2.31E+00	11.16	5.55397
			800	1.15E-01	4.85E+14	5.23E+01	3.62E+00	7.50	8.68928
			500	5.05E-02	1.11E+15	1.19E+02	8.27E+00	3.80	19.8868
			300	1.97E-02	2.84E+15	3.05E+02	2.12E+01	2.10	50.8815
			250	1.33E-02	4.20E+15	4.52E+02	3.13E+01	1.75	75.2473
			200	7.89E-03	7.10E+15	7.64E+02	5.29E+01	1.44	127.204
			150	3.78E-03	1.48E+16	1.59E+03	1.10E+02	1.21	265.157
			100	1.26E-03	4.46E+16	4.81E+03	3.33E+02	1.071	799.055
			80	6.63E-04	8.45E+16	9.10E+03	6.31E+02	1.037	1513.9
			60	2.84E-04	1.97E+17	2.12E+04	1.47E+03	1.017	3529.46
			50	1.65E-04	3.39E+17	3.65E+04	2.53E+03	1.017	6073.54
			40	8.53E-05	6.57E+17	7.08E+04	4.90E+03	1.017	11770.8
			30	3.64E-05	1.54E+18	1.66E+05	1.15E+04	1.017	27590.7
			25	2.11E-05	2.65E+18	2.86E+05	1.98E+04	1.017	47477.5
			20	1.09E-05	5.16E+18	5.55E+05	3.85E+04	1.017	92446.7
			19	9.32E-06	6.01E+18	6.47E+05	4.48E+04	1.017	107675
		5e-9	1500	1.99E+00	1.41E+14	1.52E+01	1.05E+00	23.30	2.52616
			1250	1.32E+00	2.12E+14	2.28E+01	1.58E+00	15.85	3.7982
			1000	8.19E-01	3.42E+14	3.68E+01	2.55E+00	10.21	6.12728
			800	5.29E-01	5.29E+14	5.70E+01	3.95E+00	6.95	9.47758
			500	2.37E-01	1.18E+15	1.27E+02	8.78E+00	3.66	21.1409
			300	9.53E-02	2.94E+15	3.17E+02	2.20E+01	2.070	52.6731
			250	6.48E-02	4.32E+15	4.66E+02	3.23E+01	1.729	77.3973
			200	3.86E-02	7.25E+15	7.81E+02	5.41E+01	1.434	129.891
			150	1.87E-02	1.50E+16	1.62E+03	1.12E+02	1.210	268.74
			100	6.24E-03	4.49E+16	4.84E+03	3.35E+02	1.070	804.43
			80	3.30E-03	8.49E+16	9.14E+03	6.33E+02	1.037	1521.07
			60	1.42E-03	1.97E+17	2.13E+04	1.47E+03	1.017	3529.46
			50	8.26E-04	3.39E+17	3.65E+04	2.53E+03	1.017	6073.54

Continued on next page

Table 6.7 – continued from previous page

$T_\star$	$R_\star$	$\dot{M}$	T_{dust}	τ	R_{in}	r1/rc	θ	δr/r	t
			40	4.26E-04	6.58E+17	7.08E+04	4.91E+03	1.017	11788.7
			30	1.82E-04	1.54E+18	1.66E+05	1.15E+04	1.017	27590.7
			25	1.06E-04	2.65E+18	2.86E+05	1.98E+04	1.017	47477.5
			18	3.97E-05	7.06E+18	7.60E+05	5.27E+04	1.017	126487
			15.5	2.52E-05	1.11E+19	1.19E+06	8.25E+04	1.017	198868
		3e-8	1500	6.46E+00	2.60E+14	2.81E+01	1.94E+00	13.10	4.65817
			1000	4.35E+00	3.86E+14	4.16E+01	2.88E+00	9.160	6.91559
			800	2.80E+00	6.01E+14	6.47E+01	4.49E+00	6.250	10.7675
			500	1.25E+00	1.34E+15	1.44E+02	1.00E+01	3.350	24.0075
			400	8.62E-01	1.95E+15	2.10E+02	1.45E+01	2.600	34.9363
			300	5.09E-01	3.30E+15	3.55E+02	2.46E+01	1.954	
			250	3.50E-01	4.80E+15	5.17E+02	3.58E+01	1.656	85.9970
			200	2.12E-01	7.93E+15	8.54E+02	5.92E+01	1.397	142.074
			150	1.05E-01	1.60E+16	1.72E+03	1.19E+02	1.195	286.657
			100	3.61E-02	4.65E+16	5.00E+03	3.47E+02	1.068	833.096
			80	1.94E-02	8.68E+16	9.35E+03	6.47E+02	1.036	1555.11
			60	8.40E-03	2.00E+17	2.15E+04	1.49E+03	1.017	3583.21
			50	4.93E-03	3.41E+17	3.68E+04	2.55E+03	1.017	6109.37
			40	2.55E-03	6.60E+17	7.11E+04	4.92E+03	1.017	11824.6
			30	1.08E-03	1.55E+18	1.67E+05	1.15E+04	1.017	27769.9
			25	6.32E-04	2.66E+18	2.86E+05	1.98E+04	1.017	47656.6
			18	2.38E-04	7.06E+18	7.61E+05	5.27E+04	1.017	126487
			14	1.12E-04	1.50E+19	1.62E+06	1.12E+05	1.017	268740
			13.5	1.01E-04	1.67E+19	1.80E+06	1.25E+05	1.017	299198
5000	20	1e-10	1500	2.46E-02	1.14E+14	1.23E+01	8.54E-01	28.6	4.08486
			1250	1.58E-02	1.77E+14	1.91E+01	1.32E+00	18.7	6.34228
			1000	9.49E-03	2.95E+14	3.18E+01	2.20E+00	11.06	10.5705
			800	5.97E-03	4.69E+14	5.05E+01	3.50E+00	7.700	16.8052
			500	2.57E-03	1.09E+15	1.17E+02	8.11E+00	3.88	39.057
			300	9.97E-04	2.81E+15	3.02E+02	2.09E+01	2.12	100.688
			250	6.73E-04	4.16E+15	4.48E+02	3.11E+01	1.756	149.061
			200	3.97E-04	7.06E+15	7.60E+02	5.27E+01	1.446	252.974
			150	1.91E-04	1.47E+16	1.59E+03	1.10E+02	1.214	
			100	6.28E-05	4.46E+16	4.80E+03	3.32E+02	1.070	
			80	3.32E-05	8.44E+16	9.09E+03	6.30E+02	1.037	
			60	1.42E-05	1.97E+17	2.12E+04	1.47E+03	1.017	
			50	8.29E-06	3.38E+17	3.65E+04	2.53E+03	1.017	12111.2
			40	4.26E-06	6.57E+17	7.08E+04	4.90E+03	1.017	23541.7
			35	2.87E-06	9.77E+17	1.05E+05	7.29E+03	1.017	35007.9
			31	2.00E-06	1.40E+18	1.51E+05	1.05E+04	1.017	50164.9
		1e-9	1500	2.31E-01	1.21E+14	1.30E+01	9.02E-01	27.00	4.33568
			1250	1.52E-01	1.84E+14	1.98E+01	1.37E+00	18.10	6.5931
			1000	9.24E-02	3.03E+14	3.26E+01	2.26E+00	11.39	10.8571
			800	5.87E-02	4.77E+14	5.14E+01	3.56E+00	7.60	17.0919
			500	2.55E-02	1.10E+15	1.18E+02	8.18E+00	3.86	39.4153
			300	9.93E-03	2.82E+15	3.04E+02	2.10E+01	2.11	101.046
			250	6.70E-03	4.18E+15	4.50E+02	3.12E+01	1.75	149.778
			200	3.96E-03	7.08E+15	7.62E+02	5.28E+01	1.44	253.691
			150	1.89E-03	1.48E+16	1.59E+03	1.10E+02	1.21	530.315
			100	6.28E-04	4.46E+16	4.80E+03	3.33E+02	1.07	1598.11
			80	3.31E-04	8.45E+16	9.10E+03	6.30E+02	1.037	3027.81

Continued on next page

Table 6.7 – continued from previous page

$T_\star$	$R_\star$	$\dot{M}$	T_{dust}	τ	R_{in}	r1/rc	θ	δr/r	t
			60	1.42E-04	1.97E+17	2.12E+04	1.47E+03	1.017	7058.92
			50	8.26E-05	3.39E+17	3.65E+04	2.53E+03	1.017	12147.1
			40	4.26E-05	6.57E+17	7.08E+04	4.90E+03	1.017	23541.7
			30	1.82E-05	1.54E+18	1.66E+05	1.15E+04	1.017	55181.4
			25	1.06E-05	2.65E+18	2.86E+05	1.98E+04	1.017	94955.0
			21	6.28E-06	4.46E+18	4.80E+05	3.33E+04	1.017	159811.0
			20.5	5.85E-06	4.79E+18	5.16E+05	3.57E+04	1.017	171636.0
		5e-9	1500	1.04E+00	1.34E+14	1.44E+01	1.00E+00	23.50	4.8015
			1250	6.93E-01	2.02E+14	2.17E+01	1.51E+00	16.60	7.23808
			1000	4.30E-01	3.26E+14	3.51E+01	2.43E+00	10.60	11.6813
			800	2.77E-01	5.06E+14	5.45E+01	3.77E+00	7.20	18.131
			500	1.23E-01	1.14E+15	1.22E+02	8.48E+00	3.76	40.8486
			300	4.86E-02	2.88E+15	3.10E+02	2.15E+01	2.09	103.196
			250	3.29E-02	4.25E+15	4.57E+02	3.17E+01	1.74	152.286
			200	1.96E-02	7.16E+15	7.71E+02	5.34E+01	1.44	256.558
			150	9.40E-03	1.49E+16	1.60E+03	1.11E+02	1.211	533.898
			100	3.13E-03	4.47E+16	4.82E+03	3.34E+02	1.070	1601.69
			80	1.65E-03	8.47E+16	9.12E+03	6.32E+02	1.037	3034.98
			60	7.11E-04	1.97E+17	2.12E+04	1.47E+03	1.017	7058.92
			50	4.13E-04	3.39E+17	3.65E+04	2.53E+03	1.017	12147.1
			40	2.13E-04	6.57E+17	7.08E+04	4.90E+03	1.017	23541.7
			30	9.09E-05	1.54E+18	1.66E+05	1.15E+04	1.017	55181.4
			25	5.28E-05	2.65E+18	2.86E+05	1.98E+04	1.017	94955.0
			18	1.98E-05	7.06E+18	7.60E+05	5.27E+04	1.017	252974.0
			17	1.67E-05	8.38E+18	9.02E+05	6.25E+04	1.017	300273.0
		3e-8	1500	5.56E+00	1.51E+14	1.63E+01	1.13E+00	21.81	5.41064
			1250	3.68E+00	2.28E+14	2.46E+01	1.70E+00	14.81	
			1000	2.28E+00	3.69E+14	3.98E+01	2.75E+00	9.53	13.222
			800	1.47E+00	5.73E+14	6.17E+01	4.27E+00	6.49	20.5318
			500	6.62E-01	1.27E+15	1.37E+02	9.49E+00	3.48	45.5067
			300	2.68E-01	3.13E+15	3.37E+02	2.34E+01	2.00	112.154
			250	1.84E-01	4.57E+15	4.92E+02	3.41E+01	1.689	163.753
			200	1.11E-01	7.58E+15	8.16E+02	5.66E+01	1.415	271.607
			150	5.42E-02	1.55E+16	1.66E+03	1.15E+02	1.204	555.397
			100	1.84E-02	4.56E+16	4.91E+03	3.40E+02	1.069	1633.94
			80	9.80E-03	8.57E+16	9.22E+03	6.39E+02	1.037	3070.81
			60	4.24E-03	1.98E+17	2.14E+04	1.48E+03	1.017	7094.75
			50	2.47E-03	3.40E+17	3.66E+04	2.54E+03	1.017	12182.9
			40	1.27E-03	6.59E+17	7.09E+04	4.91E+03	1.017	23613.3
			30	5.42E-04	1.55E+18	1.66E+05	1.15E+04	1.017	55539.7
			25	3.16E-04	2.66E+18	2.86E+05	1.98E+04	1.017	95313.3
			18	1.19E-04	7.06E+18	7.60E+05	5.27E+04	1.017	252974.0
			15	6.89E-05	1.22E+19	1.31E+06	9.10E+04	1.017	437151.0
			14	5.60E-05	1.50E+19	1.62E+06	1.12E+05	1.017	537481.0

CHAPTER 7

ORIGIN OF LI ENHANCEMENT IN K GIANTS

The origin of Li anomaly in a small number of K giants are discussed here in the context of two prominent suggestions given in literature, (i) external origin by engulfment of planets or brown dwarfs, (ii) internal synthesis of Li and associated mixing process. In order to understand these issues, we study the evolution of Li and infrared excess in large number of sample giants starting from the base to well beyond the post luminosity bump in the H-R diagram.

In this chapter, we discuss the results from a large survey of K giants designed to find additional Li-rich examples, locate their appearance in the HR diagram and so provide essential material for testing hypotheses about Li-enrichment. For example, Li production may be associated with the bump in the luminosity function for stars on the RGB as suggested from observations by Charbonnel & Balachandran (2000). Depending on mass and composition the bump occures on RGB between luminosities, log ($L/L_{\odot}$) = 1.5 - 2.2, and this has been predicted (Iben 1968) as a region where evolution of a giant is slowed down creating a bump in the luminosity function of stars along the RGB. Internally, the bump is associated with the H-burning shell crossing over of H-discontinuity. Additionally or alternatively, the He-core flash may be the trigger for Li production and the creation of Li-rich red clump (horizontal branch) stars. Discrimination between bump and clump is possible because the two groups appear in somewhat different places in the HR diagram. Our 2000 giants provide a reference sample comfortably spanning the luminosity of the clump and the bump. Also, the survey designed to test the suggestion of planet engulfment scenario by including giants from all the way from the base of RGB to well above the clump/bump luminosities. With Brown et al.'s survey, a total of 2644

giants covering a wide range of luminosities and effective temperatures represent a potent database in which to search for clues to the origin of the Li enrichment in K giants.

7.1 THE HERTZSPRUNG-RUSSELL DIAGRAM

7.1.1 SAMPLE GIANTS

The sample consists of 2000 giants from our survey and 644 giants from Brown's survey (B89). Luminosity and temperature of B89 samples are rederived in the similar fashion to our survey samples that are described in the Chapter 3. The distribution of luminosity and temperature of these samples are shown in Figure 7.1. Note the samples are peaking at luminosity around 1.7 - 1.8 , which is well a known clump luminosity. However, sample stars peak in temperature at two places; 4500 K and 4850 K, which corresponds to bump and clump regions, respectively.

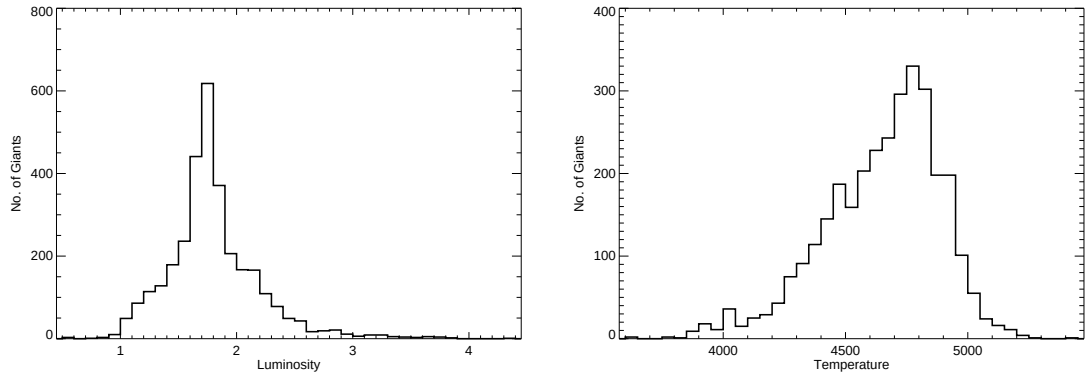

Figure 7.1: Distribution of samples from our survey and Brown et al.'s survey. Luminosities are in left panel and Temperatures are in right panel.

The giants from our and B89 surveys are shown on the HR diagram in Figure 7.2 along with evolutionary tracks (Bertelli et al. 2008) computed for solar metallicity, [Fe/H] = 0.0, and stellar masses ranging from $0.8M_{\odot}$ to $3M_{\odot}$. our sample, shown in blue symbols, occupy from the base of RGB to post luminosity bump whereas B89 sample starts from clump luminosity to well beyond the post-luminosity bump region. Combined sample from both the surveys covers from all the way from the base of RGB to well above the post clump/bump luminosities in the H-R diagram. All stars observed at low resolution are assumed to have solar metallicity. For Li-rich K giants and B89 sample actual metallicities are available from the high resolution spectra and most of them are turned out to

be close to solar values. Errors derived from the quoted uncertainties in the parallaxes and in the derivation of temperatures for the Li-rich K giants are marked in Figure 7.3

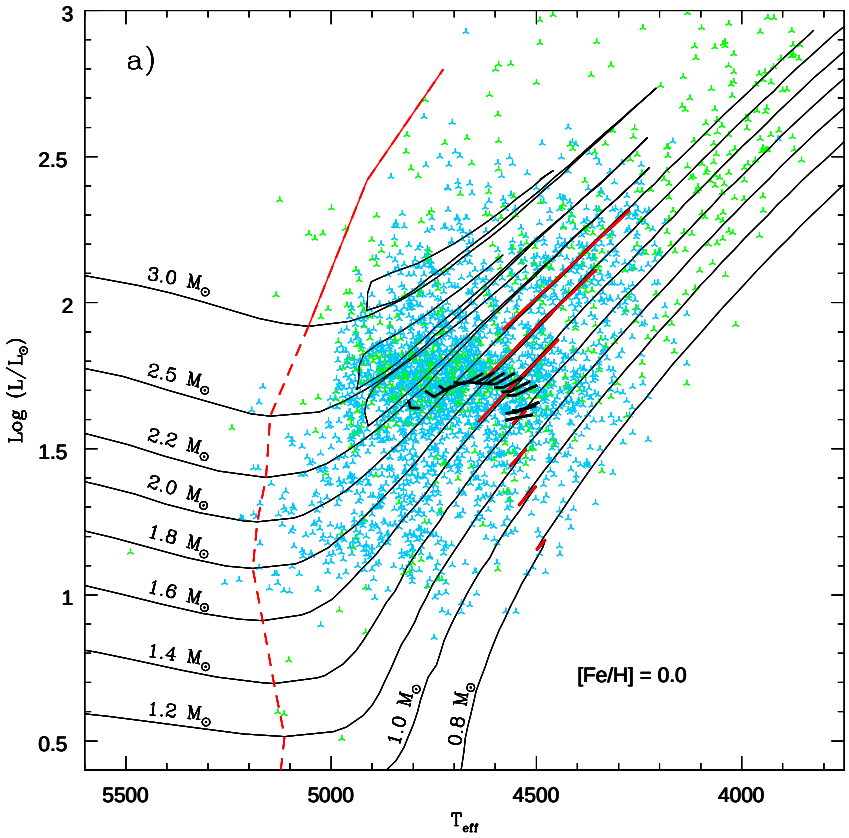

Figure 7.2: Sample stars of our survey in blue symbols and from B89 survey in green symbols are shown in the HR diagram. Evolutionary tracks of stars of masses from 0.8 to 3.0$M_\odot$ and of solar metallicity, [Fe/H]=0.0, computed by Bertelli et al. (2008) are also shown. The base of the RGB and the extent of RGB bump are marked as broken and solid red lines, respectively. The RGB clump region is shown as a thick yellow line.

Vast majority of stars in the two samples have evolved beyond the base of the RGB (the red dashed line in Figure 7.2) and, therefore, their surface Li abundance must have been greatly diluted. In Figure 7.2, there is the expected concentration of stars with luminosities of about $\log(L/L_\odot) \simeq 1.7$. This population in the HR diagram are red clump stars (horizontal branch) with He-core burning core that have evolved from the tip of the RGB: the thick black line in Figure 7.2 shows the predicted locations of clump stars. Extension of the $\log(L/L_\odot) \simeq 1.7$ concentration to cooler temperatures may include stars at the bump luminosity of the first ascent RGB stars (see red portions of the evolutionary tracks). Dominance of the HR diagram by clump stars is expected because the lifetime

of a clump star is typically one to two orders of magnitude longer than for a bump star. This argument is not strictly applicable to the Li-rich stars because their frequency is also dependent on the probabilities that clump and bump stars produce lithium.

Except for five luminous examples, the Li-rich stars are either at the luminosity of the clump or within the range of expected values for the bump, a range spanning the clump's luminosity. The five luminous exceptions must owe their Li richness to different phenomena than those accounting for the majority of the Li-rich stars. For example, HD 39853 (Gratton & D'Antona 1989) in Figure 7.3 is a Li-rich K giant but with $\log(L/L_{\odot}) = 2.7$ is probably a post-clump early AGB candidate where, as discussed by Charbonnel & Balachandran (2000), Li-production by the Cameron-Fowler mechanism has occurred by a variant of its operation in bump stars (see below). In contrast, the high luminosity warm ($T_{\rm eff}$ = 5150K) Li-rich star HD 21018 is, as suggested by Charbonnel & Balachandran (2000), caught prior to dilution of lithium by the convective envelope, i.e., it is a Li-normal star exhibiting a Li abundance close to its in initial abundance. We focus here on the Li-rich giants at bump and clump luminosities.

7.2 LI-EXCESS IN K GIANTS

7.2.1 EXTERNAL ORIGIN AN UNLIKELY SCENARIO

The idea of a planet or a brown dwarf engulfment scenario for explaining the Li-excess in the K giants has been there for quite a long time (Alexander 1967; Brown et al. 1989). They argued that sufficient amount of earth-like planetary mass with devoid of H may enhance the Li abundance to the observed levels. Recent findings of exo-solar planetary systems of main sequence as well as giants, and in some cases planets orbiting closer to the central star, further raised such a possibility. Siess & Livio (1999) , inspired by these recent findings, computed the possible effects of such mergers on the RGB phase, and proposed that accretion of a planet or a brown dwarf is responsible for high Li enhancement in the envelops of K giants and also the mass loss. And to a certain extent high rotation observed among the Li-rich K giants was attributed to the imparting of angular momentum to the K giants by the merger events (see also Carlberg et al. 2010). In the recent observational finding Carlberg et al. (2010) interprets the super Li-richness in a K giant G0928+73.2600 and its high rotation as due to the planet engulfment. Observational studies of individual Li-rich candidates (Reddy et al. 2002; Drake et al. 2002; Reddy & Lambert 2005) explored the possibilities of planet engulfment scenarios to simultaneously explain rotation, infrared excess and also high amount of Li.

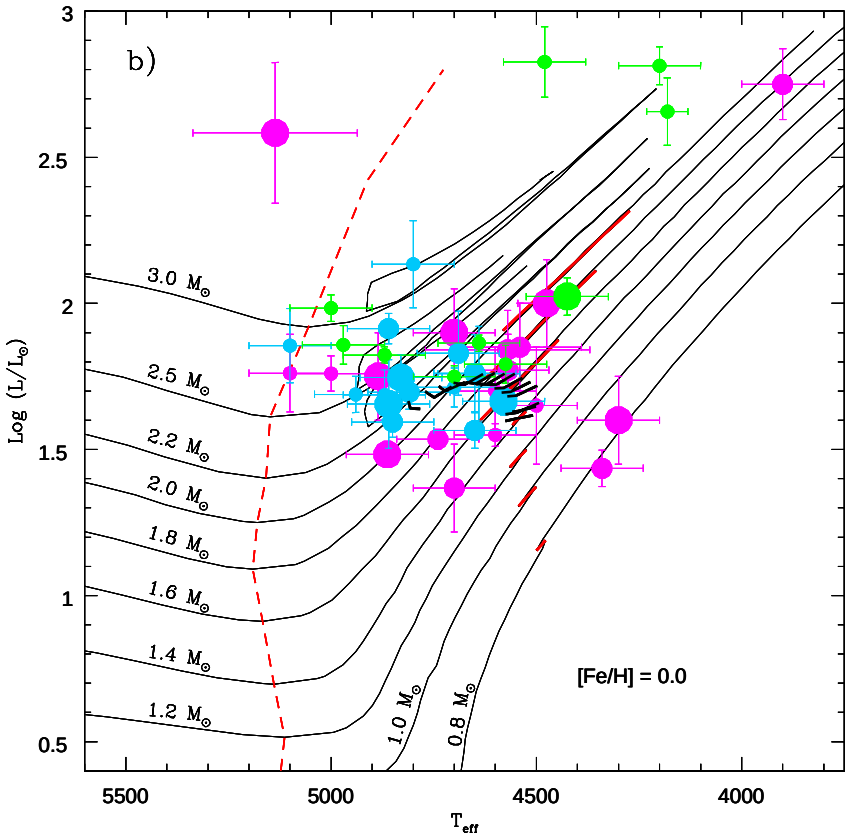

Figure 7.3: Same as Figure 7.2. New Li-rich giants are in blue symbols and green symbols are from Brown and magenta symbols are other known Li-rich giants.

Siess & Livio (1999) engulfment model suggests accretion mass of more than $0.12M_{\odot}$ is required to replenish Li to the observed level. To put this in perspective a K giant envelope needs to be mixed-up with planetary material of mass more than 30,000 earth-like planets or 100 Jupiter-like planets. In case of brown dwarfs, one may require at least 5 - 10 brown dwarfs as massive as 10 - 20 Jupiter masses. Engulfment of very massive brown dwarfs won't be helpful as Li gets destroyed due to higher central temperatures and convection. It is not clear whether such events have to occur at once or in some intervals. Based on our current observational evidence shown in Figures 7.2 & 7.3 , we argue that the engulfment is very unlikely scenario. If planet engulfment is the reason either directly or indirectly to the Li enhancement, one may expect Li-rich K giants all along the RGB phase. However, examination of the HR diagram, as shown in Figure 7.2, reveals otherwise. All of the Li-rich K giants in the mass range of 0.8 - $3.0M_{\odot}$, within uncertainties, occupy a narrow region on the HR diagram: $1.4 \geq \log(L/L_{\odot}) \leq 2.2$ and

$4300 \geq T_{eff} \leq 5100$ K. This narrow luminosity region is overlapped with bump and clump which has an important consequence in our quest for searching clues for origin of excess Li in the K giants.

7.2.2 LITHIUM-SYNTHESIS AT THE BUMP AND/OR CLUMP?

Since the Li-rich K giants are concentrated within a narrow luminosity range, one may suppose a significant event must be associated directly or indirectly with this range. One suspects that the significant event is either the bump on the first ascent of the RGB and/or associated with the red clump formed of He-core burning giants that have experienced the He-core flash at the tip of the RGB.

The observed luminosity range is crossed by first ascent RGB stars in which the H-burning shell passes into the region that previously was the maximum extent reached by the convective envelope. When the outward moving H-burning shell, as a result of increasing He-core mass, first encounters this region, a star reacts to the increased availability of H by lowering the surface luminosity. After a while, the giant continues its ascent of the RGB. This creates a kink on the evolutionary tracks for stars of masses up to $2M_{\odot}$ (Iben 1968; Bertelli et al. 2008) and a bump in the luminosity function along the RGB. As shown in Figure 7.2, the kink on the evolutionary tracks (Bertelli et al. 2008) is visible only up to $2M_{\odot}$ for solar metallicity stars.

Internally, the kink is associated with an inversion in the run of mean molecular weight with distance from the stellar center. This inversion is linked to destruction of ^{3}He by the reaction ^{3}He(^{3}He,$2p$)^{4}He which lowers the mean molecular weight, and the homogenization of the composition within the convective enevelope. Eggleton et al. (2008) show that this inversion leads to 'compulsory' mixing and changes to the surface abundances of C,N, and O isotopic abundances, i.e., the ^{12}C/^{13}C ratio is lowered relative to its value before the bump. Charbonnel & Lagarde (2010) recognize too that mixing occurs as a result of the molecular weight inversion but include the effects of rotationally-induced mixing to drive the mixing. This mixing referred to as $\delta\mu$-mixing by Eggleton et al. (2008) or thermohaline mixing by Charbonnel & Lagarde (2010) is observationally confirmed by measurements of the ^{12}C/^{13}C ratio in giants along the RGB showing a decrease in the ratio at and above the luminosity of the bump.

As p-captures on ^{12}C create ^{13}C, the reservoir of primordial and main-sequence synthesized ^{3}He is depleted. It is this reservoir that is a potential source of ^{7}Li from the Cameron-Fowler (Cameron & Fowler 1971) mechanism (^{3}He(^{4}He,γ)^{7}Be(e^{-}, ν)^{7}Li) but in order for the ^{7}Li to enrich the stellar atmosphere and its progenitor ^{7}Be must be swept

quickly to temperatures too cool for proton captures to occur. Eggleton et al. (2008) calculations show that more than about 80% of the ^{3}He is destroyed in stars of masses less than about $1.5M_\odot$. This destruction seems unlikely to produce lithium because the mixing is too slow for the ^{7}Be and ^{7}Li to avoid destruction by protons (Lattanzio et al. 2008). However, the initial subsurface ^{3}He reservoir is such that only a minor fraction of the ^{3}He need be converted with moderate efficiency to provide a Li-rich giant. It is anticipated that the lithium produced as the star crosses the bump's luminosity may be destroyed as the star with its convective envelope evolves to the tip of the RGB.

The evidence from Figure 7.3 is that few of the Li-rich stars are aligned along the run of bump stars in the HR diagram. Although the cooler Li-rich stars are likely to be bump stars, many Li-rich stars are too warm to be so identified. Thus, we suggest that Li-rich stars cannot be identified exclusively with the bump. Rather the colocation of the Li-rich stars in Figure 7.3 with the high concentration of observed (Li-normal) giants and the theoretical location of the clump suggests that they are clump stars. If Li produced at the bump on the RGB survives a star's evolution from the bump to the clump, such Li-rich stars may appear predominantly as clump stars because the lifetime at the clump is similar to or longer than the time to evolve through the bump and to the clump via the tip of the RGB. Since Li, if produced at the bump on the RGB, may be destroyed by the time the star has evolved up the RGB to experience the He-core flash, the speculation is that the Cameron-Fowler mechanism may also operate at the He-core flash in at least some stars, i.e.,in stars of $M < 2.25M_\odot$. Since Eggleton et al. (2008) predict survival of ^{3}He in stars with $M > 1.5M_\odot$, there seems in principal the possibility that the He-core flash may be the key to synthesis of lithium in stars in a narrow mass range centered at about $2M_\odot$ with the range's the upper limit set by the maximum mass for a He-core flash and the lower limit set by survival of sufficient ^{3}He following $\delta\mu$ or thermohaline mixing on the RGB. Evidently, the concentration of Li-rich stars at the clump implies that the synthesized Li is swiftly destroyed as a clump star evolves along the early reaches of the AGB. If all stars evolving through the He-core flash synthesize copious amounts of Li, they survive as a Li-rich giant for about one per cent of their horizontal branch lifetime, i.e., about 2 Myr. (The four luminous Li-rich stars in Figure 7.3 have a mass in excess of those experiencing the He-core flash. Charbonnel & Balachandran (2000) suggest that these tap their ^{3}He to produce Li as the He-burning shell evolves outward.)

7.3 BUMP AND CLUMP

To understand the Li-rich association with bump and/or clump, we studied the infrared properties of Li-rich giants and giants without Li from bump and clump region in the HR-diagram. The infrared study of these sample stars suggested that mass-loss rates are higher for Li-rich giants compare to normal giants. Li-rich stars on theoretical IRAS color-color diagram revealed that Li-rich bump stars are associated with slightly warmer dust shells compare to Li-rich clump stars. The location of Li-rich giants in the IRAS diagram and the relation obtained between mass-loss rates and Li abundances suggested that Li timescales are in the order of 10^3 to 10^5 years.

Li timescales compared with the timescales of bump, clump and bump to clump, given in Table 6.6, suggested that Li timescales are less than bump timescales ($\approx 10^6$), clump timescales ($\approx 10^7$), evolutionary timescales from RGB tip to clump ($\approx 10^6$), and evolutionary timescales from bump to clump ($\approx 10^7$).

As the dust evolutionary timescles are comparable to Li timescales and are lesser compare to the timescales of a star that travel from bump to clump, which are in the order of ten million years for stellar masses above 2 $M_\odot$, it is impossible to see the dust around clump stars that is surviving from the bump and hence Li produced at bump can not survives to clump. In this case, the dust around clump stars may be due to their strong stellar winds or mass-loss occurs due to the structural changes during He core flash at RGB tip. However, the mass-loss at He-core flash at RGB tip is neglected because the enormous amount of energy releases at the time of flash wont reach to the surface. In case the dust forms at RGB tip, shell evolutionary timescales must be higher than the timescales of a star to settle in red clump from the RGB tip, to see the signatures of the dust around clump stars. The proportion of Li-rich clump stars should be equal to the stars associated with the circumstellar dust at clump, to relate the Li enhancement with massloss at core He flash.

7.4 CONCLUSIONS

The principal novel result here is that the majority of Li-rich K giants have a luminosity and effective temperature combination suggesting that Li production may occur at the He-core flash in those stars. Although this speculation about the He-core flash has yet to be supported by calculations, the nuclear physics of Li production is surely that described by the Cameron-Fowler mechanism, i.e., conversion of ^{3}He to ^{7}Li by α-capture with ^{7}Be as a radioactive intermediary. An earlier suggestion that Li production, also by the

Cameron-Fowler mechanism, occurs at the luminosity bump of the RGB (Charbonnel & Balachandran 2000) is required to account for cooler Li-rich stars but may, if the Li produced at the bump survives evolution from there to the clump, account for some or all of the Li-rich clump stars. Infrared study of Li-rich giants suggesting that Li produced at the bump can not survives to clump, therfore, high Li seen in clump stars may be accounted for production of Li during He-core flash. Our discovery of that Li-rich giants are concentrated within a narrow luminosity range does not support a view that Li-rich giants result from the swallowing by the giant of a gaseous planet (Alexander 1967) or some other external origin.

CHAPTER 8

CONCLUSIONS AND FUTURE WORK

8.1 SUMMARY OF RESULTS

In this study we dealt with the long standing problem of unexpectedly high amount of Li in K giants. This was done in three parts. In part one we made a comprehensive survey for Li-rich K giants among K giants using low resolution spectroscopy. A sample of 2000 K giants of brightness and volume limited were chosen from the Hipparcos catalog which contains one hundred thousand stars with accurate astrometry. Sample was chosen in such a way that it covers the RGB all the way from the base of RGB to well above the luminosity bump in the HR diagram. Entire low resolution spectra were obtained with the IIA facilities located at Vainu Bappu Observatory (VBO), Kavalur and Indian Astronomical Observatory, Hanle, Ladak. Telescopes used were 1-m CZT and 2.3-m VBT at VBO and 2.3-m HCT at IAO. We note that this is the largest survey of its kind in the literature. Observations were carried over the period of three years from 2006 to 2009. Spectra were analyzed for finding Li enhanced K giants. In the phase I of our study we measured core strengths of Li resonance line at 6707.7 Å and the nearby Ca I line at 6717.6 Å. For given metallicity and $T_{\rm eff}$, the ratio of Li line to Ca I line would indicate the level of Li enhancement in a given star. An empirical relation between the actual Li measured from high resolution and the ratio of line strengths from low resolution spectra was derived. In deriving the relation, we used number of known Li-rich K giants as well as normal K giants. This way, we found 15 Li-rich K giant candidates . Some are super Li-rich. Also, the survey confirmed the rarity of Li-rich K giants i.e., 1% among the K giants in the Galaxy.

In the second part of this study, we focused on the high resolution spectroscopic study of the new and old Li-rich K giants. We have performed spectral analysis to derive quan-

titative abundances of Li, C, N, and O and carbon isotopic ratio $^{12}C/^{13}C$. With the high resolution spectroscopy, we have confirmed all the 15 Li-rich giant candidates as Li-rich K giants. Four among them are super Li-rich with log ϵ (Li) $\geq$ 3.3 dex, about a factor of 100 more than the expected Li in K giants. The current study resulted in highest number of K giants in any one single study. With this findings, the total number of Li-rich K giants in the literature went up by a factor of two. The total number of super Li-rich K giants to twelve. The study also threw-up some new interesting results. Three Li-rich K giants are found to have anomalous low $^{12}C/^{13}C$, very close to CN equilibrium value. Such low values are expected very close to the RGB tip or in the very metal-poor stars. It is puzzling that such low values are found to be at the RGB bump in solar metallicity stars and they are super Li-rich and this suggests severe mixing process must be somehow related to Li enhancement.

Results show that all the Li-rich K giants lie in a narrow luminosity range of log $(L/L_{\odot})$ = 1.4 - 2.2 spanning in $T_{\rm eff}$ = 4300 - 5100 K. The region overlaps with the luminosity bump and also the red clump region in the HR diagram. However, no Li-rich giants were found either too below the luminosity bump or too above the bump. This is an important result which rules out the frequent suggestions of planet engulfment scenario for the Li enrichment in K giants. Since the bump region is associated with important structural changes in the interior, we suggest that somehow this is linked to the high Li. Absence of high Li before or after the bump indicates that Li phenomenon in giants is very short, and, utmost, it lasts for the duration of the bump evolution. This is estimated from the evolutionary tracks as few thousand years depending on mass. Amount of Li in super-Li rich stars clearly rules out the earlier suggestion of preservation of main sequence Li. From this study we reinforce ideas of internal nucleosynthesis for Li-origin in K giants.

We have searched for clues for Li origin question in terms of Li enhancement patterns with other elemental abundances which are sensitive to mixing on RGB. Abundances of C and N in all of the Li-rich giants follow the theoretical predictions i.e., carbon is modestly depleted and N is modestly enhanced. These are the byproducts of CN cycle in H-burning cycle. However, O remained constant as ON cycle requires much higher central temperatures. However, HD 12203 is an exception for its C, N, and O abundances which are significantly different from the rest of Li-rich K giants. It's kinematics show that the star is a member of Galactic thick disk, and all others are thin disk members. Its C and N abundances are attributed to either its mass or its status as early AGB stars. The decrease in C and increase in N abundances show no dependency with the Li enhancement

in K giants. The $^{12}C/^{13}C$ ratios show some interesting results. The $^{12}C/^{13}C$ ratios of the combined sample do not indicate correlation with Li abundance in K giants. However, the new sample of K giants do show a correlation between $^{12}C/^{13}C$ and Li. The K giants that have lower $^{12}C/^{13}C$ values have much higher Li abundances. This is a surprising result which suggests some sort of extra mixing that is responsible for reducing $^{12}C/^{13}C$ and enhancing Li abundance.

Another aspect of K giants is the rotation. Rotational velocities for all the Li-rich K giants were obtained. Results indicate that there is no particular trend of high rotation with high Li. There are just six Li-rich giants (out of total 24 that are known) which show anomalous high rotation ($\geq$ 8 km s^{-1}). From the current results we suggest that having slightly higher rotation among a small fraction of K giants is normal. In fact, this particular result is drawn from our study of rotational velocity distribution among dwarfs and giants (this study is not included in the thesis).

In the third part of this thesis we dealt with infrared excess and the Li abundances. The study does not throw any definite results related to our quest for Li origin. However, we found K giants that are at the bump showing higher mass loss rates and warmer dust temperatures relative to other regions such as clump and pre-bump regions. This means that recent mass loss occurrence at the bump. Whether this is related to the Li enrichment is an important question. Also, modeling of dust shells using DUSTY suggests that the Li-rich K giants have non-spherical dust shells with truncated polar caps, and the normal K giants have spherical dust shells. Again, these results hint likely association of mass ejections at the bump with Li enhancement.

8.1.1 IMPACT OF THIS STUDY

The principal results that will impact the field in this particular area are:

- Finding of large number of Li-rich K giants includes four super Li-rich K giants. With this study total number of Li-rich K giants went up by a factor of two i.e. about 25 and the number of super-Li rich K giants went up to 12. These results significantly improved the statistical significance of the sample and interpretation of their properties

- Fractional content of Li-rich K giants are $\leq$ 1% among K giants in the Galaxy from an unbiased survey of brightness and volume limited sample

- Another important result is finding of very low $^{12}C/^{13}C$ values among three super

Li-rich K giants. Results of C,N, O and $^{12}C/^{13}C$ for a full set of Li-rich K giants and their trends with Li would help to constrain theoretical modeling

- Results suggest that high rotational property of the Li-rich K giants seems to be coincidental and is also seen among normal K giants

8.2 FUTURE PLANS

Several interesting issues came to light in this study. For example it is not very clear how the Li-rich K giants are distributed, in the HR diagram, among the clump and/or bump regions. In our study, almost 50% of K giants occupy the bump regions and the rest occupy a region called the red clump. Giants at the red clump are the ones that have evolved off the RGB tip. On the other hand, stars at the bump are climbing the RGB for the first time towards RGB tip. Discrimination of these regions would help in identifying the physical process that are associated with Li-rich K giants. Unambiguous identification is quite difficult among field RGB stars. However, this could be achieved in clusters where the bump and clump regions are well defined and separated from each other. Globular clusters are ideal for such studies. However, stars in the globular clusters are quite faint, and requires 8 - 10-m class telescopes with multi-object spectrographs and this will be investigated at a later point of time.

Another important aspect that we could right away initiate is that variability study of Li-rich K giants. It is not clear whether binarity is some how related to the Li-richness. Though such a possibility is remote, given the results in this study, it would be an important exercise to take up 2 to 3 years of continuous monitoring of all the Li-rich K giants and eliminate that possibility. As of now, no such studies are initiated, as they need modest size telescopes.

In this study we mostly concentrated on extracting results from observations and interpreting them with the help of standard stellar mixing theory and the recently developed extra mixing models of RGB stars. One of the bigger pictures that we had envisaged at the time of embarking on the survey was to estimate RGB stars contribution to the total Li in the Galaxy. This would have put some real constraints on the Li evolution in the Galaxy. We are hoping to carry out such studies in due course of time.

REFERENCES

Alexander, J. B. 1967, The Observatory, 87, 238

Allende Prieto, C., Asplund, M., López, R. J. G., & Lambert, D. L. 2002, ApJ, 567, 544

Allende Prieto, C., Lambert, D. L., & Asplund, M. 2001, ApJ, 556, L63

Alonso, A., Arribas, S., & Martínez-Roger, C. 1999, A&AS, 140, 261

Andrievsky, S. M., Gorlova, N. I., Klochkova, V. G., Kovtyukh, V. V., & Panchuk, V. E. 1999, Astronomische Nachrichten, 320, 35

Aoki, W., Barklem, P. S., Beers, T. C., et al. 2009, ApJ, 698, 1803

Arnould, M. & Norgaard, H. 1975, A&A, 42, 55

Asplund, M., Lambert, D. L., Nissen, P. E., Primas, F., & Smith, V. V. 2006, ApJ, 644, 229

Balachandran, S. C., Fekel, F. C., Henry, G. W., & Uitenbroek, H. 2000, ApJ, 542, 978

Bellazzini, M., Gennari, N., & Ferraro, F. R. 2005, MNRAS, 360, 185

Belyaev, A. K. & Barklem, P. S. 2003, Phys. Rev. A, 68, 062703

Bertelli, G., Girardi, L., Marigo, P., & Nasi, E. 2008, A&A, 484, 815

Bidelman, W. P. 1951, ApJ, 113, 304

Biemont, E., Hibbert, A., Godefroid, M., & Vaeck, N. 1993, ApJ, 412, 431

Boesgaard, A. M. 1970, ApJ, 161, 1003

Boesgaard, A. M. & Tripicco, M. J. 1986, ApJ, 302, L49

Bonifacio, P., Molaro, P., Sivarani, T., et al. 2007, A&A, 462, 851

Bonifacio, P., Pasquini, L., Spite, F., et al. 2002, A&A, 390, 91

Boothroyd, A. I. & Sackmann, I.-J. 1999, ApJ, 510, 232

Brown, J. A., Sneden, C., Lambert, D. L., & Dutchover, E. J. 1989, ApJS, 71, 293

Cameron, A. G. W. & Fowler, W. A. 1971, ApJ, 164, 111

Carlberg, J. K., Smith, V. V., Cunha, K., Majewski, S. R., & Rood, R. T. 2010, ApJ, 723, L103

Carlsson, M. 1986, Uppsala Astronomical Observatory Reports, 33

Carlsson, M. 1992, in Astronomical Society of the Pacific Conference Series, Vol. 26, Cool Stars, Stellar Systems, and the Sun, ed. M. S. Giampapa & J. A. Bookbinder, 499–+

Carlsson, M., Rutten, R. J., Bruls, J. H. M. J., & Shchukina, N. G. 1994, A&A, 288, 860

Carpenter, J. M. 2001, AJ, 121, 2851

Castelli, F., Gratton, R. G., & Kurucz, R. L. 1997a, A&A, 324, 432

Castelli, F., Gratton, R. G., & Kurucz, R. L. 1997b, A&A, 318, 841

Castelli, F. & Hack, M. 1990, Mem. Soc. Astron. Italiana, 61, 595

Castilho, B. V., Gregorio-Hetem, J., Spite, F., Spite, M., & Barbuy, B. 1998, A&AS, 127, 139

Charbonnel, C. 1995, ApJ, 453, L41+

Charbonnel, C. & Balachandran, S. C. 2000, A&A, 359, 563

Charbonnel, C., Brown, J. A., & Wallerstein, G. 1998, A&A, 332, 204

Charbonnel, C. & Lagarde, N. 2010, ArXiv e-prints

Clarke, D. 1964, The Observatory, 84, 28

Cottrell, P. L. & Norris, J. 1978, ApJ, 221, 893

Cox, A. N. 2000, Allen's astrophysical quantities, ed. Cox, A. N.

Croft, H., Dickinson, A. S., & Gadea, F. X. 1999, MNRAS, 304, 327

Cutri, R. M., Skrutskie, M. F., van Dyk, S., et al. 2003, 2MASS All Sky Catalog of point sources., ed. Cutri, R. M., Skrutskie, M. F., van Dyk, S., Beichman, C. A., Carpenter, J. M., Chester, T., Cambresy, L., Evans, T., Fowler, J., Gizis, J., Howard, E., Huchra, J., Jarrett, T., Kopan, E. L., Kirkpatrick, J. D., Light, R. M., Marsh, K. A., McCallon, H., Schneider, S., Stiening, R., Sykes, M., Weinberg, M., Wheaton, W. A., Wheelock, S., & Zacarias, N.

Cyburt, R. H., Fields, B. D., & Olive, K. A. 2008, J. Cosmology Astropart. Phys., 11, 12

D'Antona, F. & Matteucci, F. 1991, A&A, 248, 62

Dantona, F. & Mazzitelli, I. 1982, ApJ, 260, 722

de La Reza, R. & da Silva, L. 1995, ApJ, 439, 917

de La Reza, R., Drake, N. A., & da Silva, L. 1996, ApJ, 456, L115+

de La Reza, R., Drake, N. A., da Silva, L., Torres, C. A. O., & Martin, E. L. 1997, ApJ, 482, L77+

de Laverny, P. & Gustafsson, B. 1998, A&A, 332, 661

De Medeiros, J. R., do Nascimento, Jr., J. D., Sankarankutty, S., Costa, J. M., & Maia, M. R. G. 2000, A&A, 363, 239

de Medeiros, J. R., Melo, C. H. F., & Mayor, M. 1996, A&A, 309, 465

Dehnen, W. & Binney, J. J. 1998, MNRAS, 298, 387

Della Valle, M., Pasquini, L., Daou, D., & Williams, R. E. 2002, A&A, 390, 155

Denissenkov, P. A. & Herwig, F. 2004, ApJ, 612, 1081

Denissenkov, P. A. & Weiss, A. 2000, A&A, 358, L49

Di Cecco, A., Bono, G., Stetson, P. B., et al. 2010, ApJ, 712, 527

Diaz-Cordoves, J., Claret, A., & Gimenez, A. 1995, A&AS, 110, 329

Domínguez, I., Abia, C., Straniero, O., Cristallo, S., & Pavlenko, Y. V. 2004, A&A, 422, 1045

Drake, N. A., de la Reza, R., da Silva, L., & Lambert, D. L. 2002, AJ, 123, 2703

Dunkley, J., Komatsu, E., Nolta, M. R., et al. 2009, ApJS, 180, 306

Eggleton, P. P., Dearborn, D. S. P., & Lattanzio, J. C. 2008, ApJ, 677, 581

Fekel, F. C. 1997, PASP, 109, 514

Fekel, F. C. & Marschall, L. A. 1991, AJ, 102, 1439

Fekel, F. C. & Watson, L. C. 1998, AJ, 116, 2466

Frankowski, A., Jancart, S., & Jorissen, A. 2007, A&A, 464, 377

Fuhr, J. R. & Wiese, W. L. 2006, Journal of Physical and Chemical Reference Data, 35, 1669

Gilroy, K. K. 1989, ApJ, 347, 835

Girardi, L., Bressan, A., Bertelli, G., & Chiosi, C. 2000, A&AS, 141, 371

Gonzalez, O. A., Zoccali, M., Monaco, L., et al. 2009, A&A, 508, 289

Gratton, R. G., Bragaglia, A., Carretta, E., et al. 2003, A&A, 408, 529

Gratton, R. G. & D'Antona, F. 1989, A&A, 215, 66

Gratton, R. G., Sneden, C., Carretta, E., & Bragaglia, A. 2000, A&A, 354, 169

Gray, D. F. 1992, The observation and analysis of stellar photospheres., ed. Gray, D. F.

Gregorio-Hetem, J., Castilho, B. V., & Barbuy, B. 1993, A&A, 268, L25+

Guillout, P., Klutsch, A., Frasca, A., et al. 2009, A&A, 504, 829

Gustafsson, B., Karlsson, T., Olsson, E., Edvardsson, B., & Ryde, N. 1999, A&A, 342, 426

Haakonsen, C. B. & Rutledge, R. E. 2009, ApJS, 184, 138

Hanni, L. 1984, Soviet Astronomy Letters, 10, 51

Harris, M. J., Lambert, D. L., & Smith, V. V. 1988, ApJ, 325, 768

Hartoog, M. R., Persson, S. E., & Aaronson, M. 1977, PASP, 89, 660

Hauck, B. & Mermilliod, M. 1998, A&AS, 129, 431

Hekker, S. & Meléndez, J. 2007, A&A, 475, 1003

Hernanz, M., Jose, J., Coc, A., & Isern, J. 1996, ApJ, 465, L27+

Herwig, F. 2005, ARA&A, 43, 435

Hill, V. & Pasquini, L. 1999, A&A, 348, L21

Hinkle, K., Wallace, L., Valenti, J., & Harmer, D. 2000, Visible and Near Infrared Atlas of the Arcturus Spectrum 3727-9300 A, ed. Hinkle, K., Wallace, L., Valenti, J., & Harmer, D.

Hobbs, L. M., Thorburn, J. A., & Rebull, L. M. 1999, ApJ, 523, 797

Hosford, A., Ryan, S. G., García Pérez, A. E., Norris, J. E., & Olive, K. A. 2009, A&A, 493, 601

Houdashelt, M. L., Bell, R. A., & Sweigart, A. V. 2000, AJ, 119, 1448

Houk, N. 1982, Michigan Catalogue of Two-dimensional Spectral Types for the HD stars. Volume 3. Declinations -40 to -26., ed. Houk, N.

Hoyle, F. & Schwarzschild, M. 1955, ApJS, 2, 1

Iben, I. 1968, Nature, 220, 143

Iben, Jr., I. 1973, ApJ, 185, 209

Iben, Jr., I. & Renzini, A. 1983, ARA&A, 21, 271

Iben, I. J. 1967a, ApJ, 147, 650

Iben, I. J. 1967b, ApJ, 147, 624

Ivezic, Z., Nenkova, M., & Elitzur, M. 1999, ArXiv Astrophysics e-prints

Jasniewicz, G., Parthasarathy, M., de Laverny, P., & Thévenin, F. 1999, A&A, 342, 831

Jeans, J. H. 1928, Astronomy and cosmogony, ed. Jeans, J. H.

Jose, J. & Hernanz, M. 1998, ApJ, 494, 680

Jura, M. 2003, ApJ, 582, 1032

Jura, M., Bohac, C. J., Sargent, B., et al. 2006, ApJ, 637, L45

Keenan, P. C. 1967, AJ, 72, 808

Kirkman, D., Tytler, D., Suzuki, N., O'Meara, J. M., & Lubin, D. 2003, ApJS, 149, 1

Knauth, D. C., Federman, S. R., & Lambert, D. L. 2003, ApJ, 586, 268

Knauth, D. C., Federman, S. R., Lambert, D. L., & Crane, P. 2000, Nature, 405, 656

Koen, C. & Eyer, L. 2002, MNRAS, 331, 45

Koornneef, J. 1983, A&A, 128, 84

Korn, A. J., Grundahl, F., Richard, O., et al. 2006, Nature, 442, 657

Kraft, R. P., Peterson, R. C., Guhathakurta, P., et al. 1999, ApJ, 518, L53

Kumar, Y. B. & Reddy, B. E. 2009, ApJ, 703, L46

Kurucz, R. L. 1970, SAO Special Report, 309

Kurucz, R. L. 1993, in Astronomical Society of the Pacific Conference Series, Vol. 44, IAU Colloq. 138: Peculiar versus Normal Phenomena in A-type and Related Stars, ed. M. M. Dworetsky, F. Castelli, & R. Faraggiana, 87–+

Kurucz, R. L. 1994, `www.kurucz.harvard.edu`

Kurucz, R. L. & Bell, B. 1995, Atomic line list, ed. Kurucz, R. L. & Bell, B.

Lambert, D. L. 1994, in Lecture Notes in Physics, Berlin Springer Verlag, Vol. 428, IAU Colloq. 146: Molecules in the Stellar Environment, ed. U. G. Jorgensen, 1–+

Lambert, D. L., Dominy, J. F., & Sivertsen, S. 1980, ApJ, 235, 114

Lambert, D. L. & Reddy, B. E. 2004, MNRAS, 349, 757

Lambert, D. L. & Sawyer, S. R. 1984, ApJ, 283, 192

Lattanzio, J. C., Dearborn, D. S. P., & Eggleton, P. P. 2008, in American Institute of Physics Conference Series, Vol. 1001, Evolution and Nucleosynthesis in AGB Stars, ed. R. Guandalini, S. Palmerini, & M. Busso, 279–286

Lemoine, M., Vangioni-Flam, E., & Casse, M. 1998, ApJ, 499, 735

Lind, K., Asplund, M., & Barklem, P. S. 2009, A&A, 503, 541

Lodders, K. 2003, ApJ, 591, 1220

Luck, R. E. 1982, PASP, 94, 811

Luck, R. E. & Heiter, U. 2007, AJ, 133, 2464

Luck, R. E. & Lambert, D. L. 1992, ApJS, 79, 303

Lynden-Bell, D. & Pringle, J. E. 1974, MNRAS, 168, 603

Maggio, A., Vaiana, G. S., Haisch, B. M., et al. 1990, ApJ, 348, 253

Makarov, V. V. & Kaplan, G. H. 2005, AJ, 129, 2420

Mallik, S. V. 1999, A&A, 352, 495

Matteucci, F. 2010, in IAU Symposium, Vol. 268, IAU Symposium, ed. C. Charbonnel, M. Tosi, F. Primas, & C. Chiappini, 453–461

McClure, R. D. & Forrester, W. T. 1981, Publications of the Dominion Astrophysical Observatory Victoria, 15, 439

Meneguzzi, M., Audouze, J., & Reeves, H. 1971, A&A, 15, 337

Mishenina, T. V., Bienaymé, O., Gorbaneva, T. I., et al. 2006, A&A, 456, 1109

Mishenina, T. V., Soubiran, C., Kovtyukh, V. V., & Belik, S. I. 2010, in IAU Symposium, Vol. 268, IAU Symposium, ed. C. Charbonnel, M. Tosi, F. Primas, & C. Chiappini, 343–344

Möhler, S. 2004, in IAU Symposium, Vol. 224, The A-Star Puzzle, ed. J. Zverko, J. Ziznovsky, S. J. Adelman, & W. W. Weiss, 395–402

Monaco, L. & Bonifacio, P. 2008, Mem. Soc. Astron. Italiana, 79, 524

Monaco, L., Villanova, S., Moni Bidin, C., et al. 2011, ArXiv e-prints

Monet, D. G., Levine, S. E., Canzian, B., et al. 2003, AJ, 125, 984

Muthumariappan, C., Kwok, S., & Volk, K. 2006, ApJ, 640, 353

Olive, K. A. & Schramm, D. N. 1992, Nature, 360, 439

Ossenkopf, V., Henning, T., & Mathis, J. S. 1992, A&A, 261, 567

Pakhomov, Y. V., Antipova, L. I., & Boyarchuk, A. A. 2011, Astronomy Reports, 55, 256

Palacios, A., Charbonnel, C., & Forestini, M. 2001, A&A, 375, L9

Palacios, A., Charbonnel, C., Talon, S., & Siess, L. 2006, A&A, 453, 261

Pallavicini, R., Spanò, P., Prisinzano, L., Randich, S., & Sestito, P. 2006, Multi-Object Spectroscopy of Open Clusters with FLAMES: Preliminary GTO Results, ed. Randich, S. & Pasquini, L., 181–+

Parthasarathy, M. & Rao, N. K. 1980, Ap&SS, 73, 251

Pavlenko, Y. V. & Magazzu, A. 1996, A&A, 311, 961

Perryman, M. A. C., Lindegren, L., Kovalevsky, J., et al. 1997, A&A, 323, L49

Piau, L., Beers, T. C., Balsara, D. S., et al. 2006, ApJ, 653, 300

Pilachowski, C. 1986, ApJ, 300, 289

Pilachowski, C., Saha, A., & Hobbs, L. M. 1988, PASP, 100, 474

Plez, B., Smith, V. V., & Lambert, D. L. 1993, ApJ, 418, 812

Prabhu, T. P., Anupama, G. C., & Surendiranath, R. 1998, Bulletin of the Astronomical Society of India, 26, 383

Randich, S., Bragaglia, A., Pastori, L., et al. 2005, The Messenger, 121, 18

Randich, S., Pallavicini, R., Meola, G., Stauffer, J. R., & Balachandran, S. C. 2001, A&A, 372, 862

Rao, N. K. 1978, MNRAS, 185, 585

Rao, N. K., Sriram, S., Jayakumar, K., & Gabriel, F. 2005, JApA, 26, 331

Reddy, B. E. & Lambert, D. L. 2005, AJ, 129, 2831

Reddy, B. E., Lambert, D. L., & Allende Prieto, C. 2006, MNRAS, 367, 1329

Reddy, B. E., Lambert, D. L., Hrivnak, B. J., & Bakker, E. J. 2002, AJ, 123, 1993

Reddy, B. E., Tomkin, J., Lambert, D. L., & Allende Prieto, C. 2003, MNRAS, 340, 304

Reeves, H. 1970, Nature, 226, 727

Richard, O., Michaud, G., & Richer, J. 2005, ApJ, 619, 538

Romano, D., Matteucci, F., Ventura, P., & D'Antona, F. 2001, A&A, 374, 646

Ryan, S. G., Beers, T. C., Olive, K. A., Fields, B. D., & Norris, J. E. 2000, ApJ, 530, L57

Sackmann, I. & Boothroyd, A. I. 1992, ApJ, 392, L71

Sackmann, I.-J. & Boothroyd, A. I. 1999, ApJ, 510, 217

Sackmann, I.-J., Smith, R. L., & Despain, K. H. 1974, ApJ, 187, 555

Salaris, M., Cassisi, S., & Weiss, A. 2002, PASP, 114, 375

Sato, B., Omiya, M., Liu, Y., et al. 2010, PASJ, 62, 1063

Scalo, J. M., Despain, K. H., & Ulrich, R. K. 1975, ApJ, 196, 805

Schild, R. E. 1973, AJ, 78, 37

Schröder, K. & Cuntz, M. 2005, ApJ, 630, L73

Sestito, P. & Randich, S. 2005, A&A, 442, 615

Siess, L. & Livio, M. 1999, MNRAS, 308, 1133

Smith, V. V. & Lambert, D. L. 1989, ApJ, 345, L75

Smith, V. V. & Lambert, D. L. 1990, ApJ, 361, L69

Smith, V. V., Lambert, D. L., & Nissen, P. E. 1993, ApJ, 408, 262

Smith, V. V., Lambert, D. L., & Nissen, P. E. 1998, ApJ, 506, 405

Smith, V. V., Plez, B., Lambert, D. L., & Lubowich, D. A. 1995, ApJ, 441, 735

Sneden, C., Lambert, D. L., Tomkin, J., & Peterson, R. C. 1978, ApJ, 222, 585

Sneden, C. & Pilachowski, C. A. 1984, PASP, 96, 38

Sneden, C. A. 1973, PhD thesis, AA(The University Of Texas at Austin.)

Spite, F. & Spite, M. 1982, A&A, 115, 357

Starrfield, S., Truran, J. W., Sparks, W. M., & Arnould, M. 1978, ApJ, 222, 600

Surendiranath, R., Vivekananda Rao, P., & Sarma, M. B. K. 1978, Acta Astron., 28, 231

Sweigart, A. V. & Mengel, J. G. 1979, ApJ, 229, 624

Takeda, Y. & Kawanomoto, S. 2005, PASJ, 57, 45

Torres-Peimbert, S. & Wallerstein, G. 1966, ApJ, 146, 724

Travaglio, C., Randich, S., Galli, D., et al. 2001, ApJ, 559, 909

Tull, R. G., MacQueen, P. J., Sneden, C., & Lambert, D. L. 1995, PASP, 107, 251

van Leeuwen, F., ed. 2007, Astrophysics and Space Science Library, Vol. 350, Hipparcos, the New Reduction of the Raw Data

Voges, W., Aschenbach, B., Boller, T., et al. 1999, A&A, 349, 389

Wallerstein, G. & Morell, O. 1994, A&A, 281, L37

Wallerstein, G. & Sneden, C. 1982, ApJ, 255, 577

Woosley, S. E., Hartmann, D. H., Hoffman, R. D., & Haxton, W. C. 1990, ApJ, 356, 272

Woosley, S. E. & Weaver, T. A. 1995, ApJS, 101, 181

Yi, S. K., Kim, Y.-C., & Demarque, P. 2003, ApJS, 144, 259

Zuckerman, B., Kim, S. S., & Liu, T. 1995, ApJ, 446, L79+